Bioinspired Nanometal Synthesis and Applications in Catalysis

Yani Pan

Department of Chemistry, McGill University

Montreal, Quebec, Canada

December 2021

A thesis submitted to McGill University

in partial fulfillment of the requirements of the degree of

Doctor of Philosophy

Abstract

Electrocatalysis, which facilitates the interconversion between electric and chemical energy, has been considered as an efficient and green route to produce clean energy and chemical feedstocks. Nevertheless, conventional chemical protocols for synthesizing nanosized metallic electrode materials frequently involve the use of non-natural stabilizing additives, hazardous solvents and high temperature, which requires high energy input and raise some environmental concerns. Searching for green catalysts with excellent catalytic performances are highly desired. In this regard, bioinspired syntheses are emerging as greener and more energy-efficient alternatives, since they enable fabrication of well-patterned hierarchical micro and nanostructures under mild reaction conditions. Among the different biological scaffolds, proteins are characterized by their diverse architectures, abundant binding sites and engineerable amino acid residues.

This thesis presents the utilization of a tobacco mosaic virus coat protein (TMVCP) as a versatile platform to synthesize a series of metallic nanomaterials and their applications in energy related electrocatalytic reactions. Taking advantage of the self-assembly properties of TMVCP under different solution conditions, nanoparticles can be embedded onto the disk protein surface or capped by protein subunits. We show that in addition to the eco-friendly synthesis merit, the as prepared materials are superior catalysts in electrocatalytic reactions. While the nanosized silver rings exhibit significant enhancement towards catalyzing electrochemical carbon dioxide reduction reaction, the two TMVCP-templated platinum catalysts are promising candidates for methanol oxidation reaction. Besides electrocatalysis, potential applications of protein-metal hybrid systems in heterogeneous organic synthesis are also described. Gold and palladium nanoparticles capped by the bulky protein subunits are employed for two organic reactions and also showed remarkable kinetics. Possible origins for the improved catalytic behaviors brought by these materials are explored. This thesis is expected to stimulate more research on employing natural ligands to protect nanostructures and discover their applications in catalysis and energy related areas.

Abrégé

L'électrocatalyse, facilitant l'interconversion entre l'énergie électrique et chimique, a été considérée comme une voie efficace et verte pour produire de l'énergie propre et des matières premières chimiques. Néanmoins, les protocoles chimiques conventionnels pour la synthèse de matériaux d'électrodes métalliques nanométriques impliquent fréquemment l'utilisation d'additifs stabilisants non naturels, de solvants dangereux et de hautes températures, qui sont plutôt énergivores et soulèvent des problèmes environnementaux. La recherche de catalyseurs verts avec d'excellentes performances catalytiques est fortement désirée. À cet égard, les synthèses bio-inspirées apparaissent comme des alternatives plus vertes et plus économes en énergie, car elles permettent la fabrication de micro et nanostructures hiérarchiques bien structurées dans des conditions de réaction douces. Parmi les différents échafaudages biologiques, les protéines se caractérisent par leurs architectures diverses, leurs sites de liaison abondants et leurs résidus d'acides aminés manipulables.

Cette thèse présente l'utilisation d'une protéine d'enveloppe du virus de la mosaïque du tabac (TMVCP) comme plate-forme polyvalente pour synthétiser une série de nanomatériaux métalliques et leurs applications dans les réactions électrocatalytiques liées à l'énergie. Profitant des propriétés d'auto-assemblage du TMVCP dans différentes conditions de solution, les nanoparticules peuvent être intégrées à la surface de la protéine du disque ou coiffées par des sous-unités protéiques. Nous montrons qu'en plus de la synthèse verte, les matériaux tels que préparés sont des catalyseurs supérieurs dans les réactions électrocatalytiques. Alors que les anneaux d'argent nanométriques présentent une amélioration significative vers la catalyse d'une réaction de réduction électrochimique du dioxyde de carbone, les deux catalyseur au platine à matrice TMVCP sont des candidats prometteur pour la réaction d'oxydation du méthanol. Outre l'électrocatalyse, les applications potentielles des systèmes hybrides protéine-métal dans la synthèse organique hétérogène sont également décrites. Des nanoparticules d'or et de palladium coiffées par les sous-unités protéiques volumineuses sont utilisées pour deux réactions organiques et ont également montré une cinétique remarquable. Les origines possibles des comportements catalytiques

améliorés apportés par ces matériaux sont explorées. Cette thèse devrait stimuler davantage de recherches sur l'utilisation de ligands naturels pour protéger les nanostructures et découvrir leurs applications dans les domaines de la catalyse et de l'énergie.

Table of Contents

Acknowledgements

I would like to take this opportunity to express my gratitude to many people who have helped me during my PhD study and accomplish this thesis.

First and foremost, I'd like to thank my supervisor, Prof. Janine Mauzeroll. Dating back to five years ago while I was browsing the department research page to see which group would be a good fit for me, I did not realize that somehow I would ended up starting my PhD in an electrochemistry group, since I had zero research background in electrochemistry. I thought it was my first meeting with Janine and my chat with Dr. Lisa Stephens that made me want to join this research group. Now looking back, I'm happy that I made a correct decision. Thank you to Janine for leading me into this fun research field. Janine is an amazing supervisor who has helped shape my scientific thinking, guided my research projects with great patience, looked for potential collaborators to solve problems, and supported my ideas of conducting the experiments. Her scientific intuitions, attitude towards academy and life, have inspired me a lot, not only in the research aspect, but also how to become a better person.

I'd like to express my thanks to Dr. Amy Blum, for her numerous help on our collaboration projects. It is with the materials provided by her group that I began the first project in this thesis. Dr. Blum also gave a lot of scientific insights on my research projects and helpful discussion on manuscript writing. I have also had a chance to collaborate with Dr. Lena Simine in our department. Thank you to Lena for letting me have a general idea of how to do simulation and I was grateful to have some actual practices. The talk with Lena is always constructive and it has been a delightful collaboration experience. I am also thankful to Dr. Steen Schougaard at UQAM, who provided guidance on the lithium ion battery project that I worked on during my first and half year PhD.

I would also like to thank my former supervisor at Zhejiang University, Prof. Simon Duttwlyer. I learned a lot from Simon, in both research and personal aspects. It is the experience with Simon that have prepared me for my PhD journey. I look forward to seeing you when I visit Hangzhou.

My sincere thanks go to all the Mauzeroll team members, past and present. It is definitely a happy and unforgettable research experience to work with you guys.

To our former postdoc Dr. Waldemir Paschoalino, who co-authored my first and second chapters. Thank you for giving me helpful advice on electrocatalysis experiment and structure building in manuscript writing. To another former postdoc, Dr. Mohammadreza Ghavidel, thank you for mentoring me on the battery project, and your jokes made working in the lab more fun. To a postdoc in Amy's group, Dr. Serene Bayram. Thank you for teaching me how to synthesize nanomaterials and useful suggestions on the silver nanoring project.

Lisa, you were the first person that I talked to when I entered the students' office. Thank you for a lot of things, like bringing me into Matlab world and helping me troubleshoot software problems. You were always warmhearted when I approached you with a question to ask. Nick, thank you for being willing to share your scientific thoughts. I appreciate that your depth of thinking can usually bring the research to a higher level. It was a pity we did not have a collaborative project together. Also thanks for your time on making the journal cover. Siba, we entered the PhD program in the same year, you have a great attitude towards study, I mean, you are always eager to learn new things. Thank you for your encouragement when I was down in spirit. Jeremy, you are an awesome guy. It is the battery project that I had more contact with you and found you are a great colleague to work with and talk to. I admire your creativity in science, daily life, and talent in giving a speech. Also from a personal note, you are a good friend and I have learned a lot from you about the Canadian culture. Yuanjiao, you are my first Chinese labmate in the group, thank you for those favors in the lab, and I will certainly miss the days when we were hanging out together. Hu, it is a great pleasure to have you as a labmate. We have had many discussions on various topics not limited to chemistry, thanks for those time spent together, also I appreciate your kind help in the lab every time I ask you for a favor on wechat. Isa, thanks so much for your input on keeping our lab running efficiently with a strong sense of responsibility. I feel so lucky to have great labmates Dr. William Odette, Dr. Andrew Danis, Dr. Malak Dayeh, Dr. Emmanuel Mena, Dr. Danny Chhin, Nathaniel, Sarah, Changyue and Malsha. Thank you all for making my lab life a wonderful one.

My research projects involve use of various characterization techniques, I appreciate the technical stuffs who provided me instrumental training with great patience, and they are Dr. Robin Stein,

Dr. Xuedong Liu, Dr. Kelly Sears, Dr. Lihong Shang, Dr. Kim Munro, Dr. Hatem Titi, Dr. Petr Fiurasek.

Finally, I would like to express my gratefulness to my family members and friends. Your unconditional love and support bring me happiness in my life and have encouraged me to pursue what I want.

Author Contributions

The work presented in this thesis was performed under the supervision of Professor Janine Mauzeroll at McGill University. Professor Mauzeroll provided guidance on all project work, reviewed all manuscripts and gave corrections. Associate Professor Amy Szuchmacher Blum (A. Blum) at McGill University was our collaborator in several studies. She provided insightful advice on Chapter 1, 3, 4 and 5, where she is a co-author on the published papers. Assistant Professor Lena Simine (L. Simine) is our collaborator in Chapter 5 for computational studies, where she is a co-author in the published paper.

Chapter 1. The author wrote this chapter in collaboration with Dr. Waldmir Junior Paschoalino (W. Paschoalino). The author and W. Paschoalino conceived the idea and outlined the structure of the manuscript. W. Paschoalino drafted the bio-templated nanomaterial synthesis section and the author modified this section. The electrocatalytic applications of bio-templated nanomaterials section was written by the author. A. Blum provided feedback and assisted in manuscript editing.

Chapter 2. The author wrote this chapter. The author summarized the experimental methodology for material synthesis, characterizations and electrochemical measurements.

Chapter 3. The author designed, carried out experimental work, analyzed data and wrote the manuscript. Dr. Serene Bayram provided guidance on the material synthesis and did TEM characterizations on the silver nanorings. W. Paschoalino and A. Blum gave helpful discussion on manuscript writing.

Chapter 4. The author conceived the idea, performed all the experiments and data analysis. The author also wrote the manuscript. A. Blum reviewed the manuscript and assisted in editing.

Chapter 5. The author conceived the idea, performed all the experimental work, analyzed data and wrote the manuscript. L. Simine performed the molecular dynamic simulation and wrote the

corresponding simulation section in the manuscript. A. Blum reviewed the manuscript and assisted in editing.

Chapter 6. The author designed all the experimental work, carried out data analysis, and wrote this chapter.

Chapter 7. The author summarized the thesis and wrote this chapter.

List of Figures

List of Schemes

List of Tables

List of Abbreviations

Abbreviation	Full Name
AC	Alternating current
ADT	Accelerated durability test
Ag/AgCl	Silver/silver chloride reference electrode
Ag NR	Silver nanoring
BET	Brunauer-Emmett-Teller
CA	Chronoamperometry
CD	Circular dichroism
CO_2 RR	Carbon dioxide reduction reaction
CO OR	Carbon monoxide oxidation reaction
CE	Counter electrode
CPMV	Cowpea mosaic virus
CTAB	Cetrimonium bromide
CV	Cyclic voltammetry
DAFCs	Direct alcohol fuel cells
DC	Direct current
DMAB	Dimethylamine borane complex
DNA	Deoxyribonucleic acid
ECSA	Electrochemical surface area
EOR	Ethanol oxidation reaction
DFAFCS	Direct formic acid fuel cells
DFT	Density functional theory
EDS	Energy dispersive spectroscopy
EIS	Electrochemical impedance spectroscopy
ESM	Eggshell membrane
EXAFS	Extended x-ray absorption fine structure

Abbreviation	Full Name
FAOR	Formic acid oxidation reaction
Fcc	Face centered cubic
FE	Faradaic efficiency
FTIR	Fourier transform infrared
GC	Gas chromatography
GCE	Glassy carbon electrode
GR	Glutathione reductase
HAADF-STEM	High-angle annular dark-field scanning transmission electron microscopy
HER	Hydrogen evolution reaction
Hsp	Heat shock protein
HR-TEM	High resolution transmission electron microscopy
ICP-OES	Inductively coupled plasma-optical emission spectrometry
INSAFs	Insulin amyloid fibrils
LSV	Linear sweep voltammetry
MA	Mass activity
MOR	Methanol oxidation reaction
MNMS	Metallic nanostructured materials
MTNN	Multiple-twinned nanowire networks
NADPH	Nicotinamide adenine dinucleotide phosphate
NC	Nanocluster
NMR	Nuclear magnetic resonance
NM	Nanomaterial
NP	Nanoparticle
NR	Nanoring
NW	Nanowire
OER	Oxygen evolution reaction
ORR	Oxygen reduction reaction
PDF	Pair distribution function

Abbreviation	Full Name
PEMFCs	Proton exchange membrane fuel cells
Prx	Peroxiredoxin
RDS	Rate determining step
RHE	Reversible hydrogen electrode
RMC	Reverse Monte Carlo
RNA	Ribonucleic acid
RRDE	Rotating ring disk electrode
r.t.	Room temperature
SA	Specific activity
SAED	Selected area electron diffraction
SCE	Saturated calomel electrode
SWNT	Single-wall carbon nanotube
TEM	Transmission electron microscopy
TMV	Tobacco mosaic virus
TMVCP	Tobacco mosaic virus coat protein
TEA	Triethanolamine
TOF	Turnover frequency
Tris-HCl	Tris (hydroxymethyl) aminomethane hydrochloride
UME	Ultramicroelectrode
UPD	Underpotential deposition
UV	Ultraviolet
UV/Vis	Ultraviolet/visible
WE	Working electrode
XAFS	X-ray absorption fine-structure spectroscopy
XPS	X-ray photoelectron spectroscopy
XRD	X-ray power diffraction
0D	Zero-dimensional
1D	One-dimensional

Abbreviation	Full Name
2D	Two-dimensional
3D	Three-dimensional

List of Symbols

Symbol	Meaning	Usual Unit
A	Pre-exponential factor	None
C_0	Concentration at time zero	mol/L
C_t	Concentration at time t	mol/L
C	Charge of monolayer coverage of the atoms onto a clean electrode	coulomb/cm^2
E	Applied potential	V
E_a	Activation energy	kJ/mol
E_0	Standard potential	V
E_{onset}	Onset potential	V
F	Faraday constant (9.649×10^4)	C/mol of e^-
ħ	Plank's constant (6.626×10^{-34})	Js
I	Current	mA
J	Current density	mA/cm^2
J_0	Exchange current density	mA/cm^2
k	Rate constant	s^{-1}
M	Molarity	mol/L
Q	Charge	coulomb
R	Resistance	Ω
R_{ct}	Charge transfer resistance	Ω
R_g	Gas constant	J $(K\ mol)^{-1}$
S	Surface area	cm^2
T	Temperature	K
t	Time	s
v	Scan rate	mV/s
Z	Impedance	Ω

Symbol	Meaning	Usual Unit
Z_{Im}	Imaginary part of the complex impedance	Ω
Z_{Re}	Real part of the complex impedance	Ω
λ_{max}	Maximum absorbance wavelength	nm
η	Overpotential	V
ε	Molar extinction coefficient	ml (mg cm)$^{-1}$
ν	Frequency of light	1/s

Chapter 1

Bio-Templated Metallic Nanomaterial Synthesis and Electrocatalytic Applications

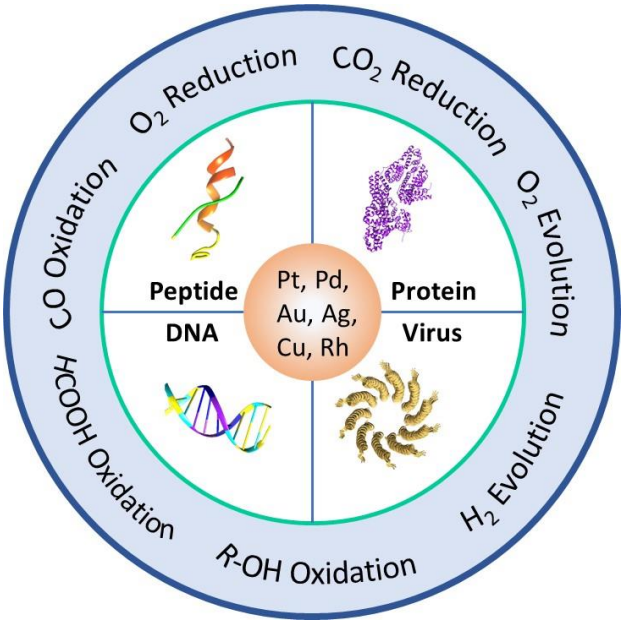

Chapter Preface

Scientific Contributions:

Chapter 1 serves as an introduction to the entire thesis. This chapter summarizes the state-of-art synthetic methods of nanometals templated by biological scaffolds, which include peptide, protein, DNA and virus. The advantages and disadvantages of each template for nanomaterial fabrications are discussed. A comprehensive literature review is provided on the applications of biological-templated nanometals in various electrocatalytic reactions, such as oxygen reduction, hydrogen evolution, carbon dioxide reduction, etc. Additionally, the structure-property correlations to elucidate the mechanism for enhanced catalytic performances are proposed. We also provide perspectives on the current challenges to suggest possible future research directions in electrocatalysis using bio-templated catalysts.

Public Information:

This chapter is adapted from a previously published review article with permission from:

Y. Pan, W. J. Paschoalino, A. S. Blum, J. Mauzeroll. Recent advances in bio-templated metallic nanomaterial synthesis and electrocatalytic applications. *ChemSusChem* **2021,** 14, 758-791.

Chapter Abstract

Developing metallic nanocatalysts with high reaction activity, selectivity and practical durability is a promising and active subfield in electrocatalysis. In the classical “bottom-up” approach to synthesize stable nanomaterials by chemical reduction, stabilizing additives such as polymers or organic surfactants must be present to cap the nanoparticle to prevent material bulk aggregation. In recent years, biological systems have emerged as green alternatives to support the uncoated inorganic components. One key advantage of biological templates is their inherent ability to produce nanostructures with controllable composition, facet, size and morphology under ecologically friendly synthetic conditions, which are difficult to achieve with traditional inorganic synthesis. In addition, through genetic engineering or bioconjugation, bio-templates can provide numerous possibilities for surface functionalization to incorporate specific binding sites for the

target metals. Therefore, in bio-templated systems, the electrocatalytic performance of the formed nanocatalyst can be tuned by precisely controlling the material surface chemistry. With controlled improvements in size, morphology, facet exposure, surface area and electron conductivity, bio-inspired nanomaterials often exhibit enhanced catalytic activity towards electrode reactions. This chapter mainly reviews recent research developments in bio-approaches for metallic nanomaterial synthesis and their applications in electrocatalysis for sustainable energy storage and conversion systems. As an introduction section in this thesis, Chapter 1 provides comprehensive background knowledge for bioinspired nanoelectrocatalyst in terms of preparation methods and applications. Chapter 1 also discusses current challenges and possible future directions. The outline of each chapter is also provided.

1.1 Introduction

Fossil fuel combustion is still the most widely adopted method for producing energy, which is both unsustainable and environmentally detrimental. Among the various technologies aimed at developing clean and renewable energy carriers to alleviate the reliance on fossil fuels, electrocatalysis has proven itself to be a facile and ecological route to transform electrical energy into chemical energy in the form of useful feedstocks.[1,2] For example, hydrogen, as one of the cleanest energy sources, can be obtained through water electrolysis with the assistance of efficient electrocatalysts.[3–5] In electrocatalysis, the reactant in the electrolyte diffuses to the electrode surface, gaining or losing electrons to experience a series of transformations to form the product, which then desorbs and gradually diffuses away from the electrode into the electrolyte.[6] Although extensive effort has been devoted towards searching for electrode materials with high catalytic activity and selectivity, there are still significant challenges in improving catalyst's performance (i.e., activity, selectivity, and durability) such as complicated material synthetic processes, the high cost of noble metals, stability problems and difficulty in commercialization.[1]

In recent years, nanosized metallic materials have become a key component in various chemistry research areas such as sensing[7–10], drug delivery,[11–13] and electronics,[14–16] and also have stood out as excellent electrocatalysts for renewable energy applications.[2,17–19] Electrocatalysis plays a critical role in the interconversion of electrical and chemical energy, with the ultimate goal of

reducing rising environmental concerns with continuing the use of fossil fuels. Compared to their bulk counterparts, nanomaterials (NMs) feature a much higher surface-to-volume ratio, exposing larger numbers of catalytically active sites, thus lowering the kinetic barriers and boosting the efficiency of electrode reactions.[20] In electrocatalysis specifically, since the catalytic properties of the NMs are highly dependent on the surface composition, size and morphology, tremendous research attention has been focused on developing materials with optimized structure that can significantly increase the rate of the target electrode reaction.

One classical method for NM synthesis is via "bottom-up" chemical reduction, in which a metal salt precursor is reduced to its metallic form by a reductant in the presence of a capping agent to stabilize the formed nanostructure.[21,22] However in many cases, this technique involves the use of organic capping agent, organic solvent and high temperature to obtain target structures, requiring a high energy input.[23] In this sense, biologically-inspired synthesis represents a greener and more sustainable approach. For instance, these reactions generally use water as the solvent and are carried out at room temperature. In addition, some natural organisms contain reducing components that can eliminate the necessity of auxiliary reductants such as $NaBH_4$, N_2H_4 and hydrogen gas.[24] To date, a series of biological materials such as peptides,[25] proteins,[26] DNA,[27] and viruses[28] have been extensively exploited as templates for the construction of metallic nanomaterials (MNMs) with different structures and properties. Besides the environmentally-benign synthetic process, some bioinspired methods also have an inherent advantage in patterning when these biological templates contain motifs that hold specific binding affinities for target metal substrates, thereby directing the nucleation and growth of nanoparticles (NPs) into a well-defined structure.[20] In addition, some biomolecules are able to self-assemble into diverse shapes that expose different binding sites under various solution conditions such as pH or concentration. With such templates, the NPs can be organized into the corresponding pattern with precise control over size, shape, facet and location. Furthermore, with the assistance of genetic modification or bioconjugation,[28] the surface of the bio-templates can be designed with specific functional groups, providing numerous possible nucleation sites and resulting in nanostructures with desired characteristics. The as prepared MNMs have emerged as potential heterogeneous catalysts with excellent electrocatalytic performances.

Previously, there have been reviews on the synthesis of MNMs inspired by bio-templates and their wide applications,[20,29–31] in which electrocatalytic applications were only briefly mentioned. In recent years, there is an increase research interest in developing bio-templated nanocatalysts for electrochemical reactions involved in energy storage/conversion systems, which we will address in this review chapter. Herein, we first attempt to summarize bio-templated (peptides, proteins, DNA and viruses) synthesis of MNMs (including several metal oxide nanomaterials). Afterwards, a more detailed discussion will be focused on the most recent results to date of their electrocatalytic applications, which mainly includes oxygen reduction reactions (ORR), hydrogen evolution reactions (HER), methanol/ethanol oxidation reactions (MOR/EOR), formic acid oxidation reactions (FAOR), carbon dioxide reductions (CO_2 RR) and carbon monoxide oxidations (CO OR). Specifically, the catalytic performances of the material for each target electrocatalytic reaction will be involved, as well as explorations of possible mechanisms that might explain their performances. Finally, current issues and prospects in the catalytic applications of bioinspired NMs will be presented.

1.2 Bio-Templates for the Synthesis of MNMs

Various functional groups on bio-templates such as hydroxyl, carboxyl, amine, thiol groups can act as the binding and nucleation sites for MNM formation. Table 1.1 presents the associated functional groups for some representative MNM fabrications and the corresponding synthetic methods for the reported examples. Based on the general scale of bio-templates, the following discussion is reviewed from the smallest peptide to largest virus.

Table 1.1: Examples of bio-templated MNM fabrications.

Bio-Template	Binding Functional Groups	MNMs	Synthesis Method
Peptide	COOH	Ag NP[32]	Aldehyde Reduction
	COOH/OH	Pt NP[33]	Glow Discharge
	NH_2	Au Nrib[34]	Biomineralization
		Au NW[35]	AA Reduction
		Au NP[36]	Glow Discharge
		Au, Pd NPNs[37,38] Pt NP,[39] Cu NC[40]	$NaBH_4$ Reduction
	SH	Pd NP,[41] Ag NC[42]	$NaBH_4$ Reduction
		Ag NP[43]	HEPES Reduction
		Au, Ag, Cu NCs[44]	Biomineralization
	Phenyl ring	Pt NP	$NaBH_4$/AA Reduction[45] Glow Discharge[46]
Protein	COOH	Ag NP[47]	UV Radiation
	NH_2	Au NR[48] Pt/CNT[49]	Self-assembly $NaBH_4$ Reduction
	NH_x (His)	NiPd, CoPd NPs[50]	Electroless Deposition
	SH	Au NP[51]	NADPH Reduction
	NH_2 and COOH	Au NP/NW[52]	$NaBH_4$ Reduction
DNA	SH	Au NW[53]	Electroless Deposition
		Pt, Au NPs[54,55]	Self-assembly
	Purine/pyrimidine	Ag NP[56]	Electrodeposition
		Ag NC[57]	$NaBH_4$ Reduction
Virus	COOH	Co, Ni, Cu, CuNi, AuCo, AuNi, AuCu NFs[58] Pt-$Ni(OH)_2$ NP[59]	Electroless Deposition
		Co NP[60]	$NaBH_4$ Reduction
	NH_2	Co, Ni, Fe, Pt CoPt, NiFe NPs[61] Co, Ni NTs[62]	Electroless Deposition
		Pt NT[63]	Methanol Reduction
	SH	Ni, Co NWs[64,65]	Electroless Deposition
		Au NP[66]	Self-assembly
	OH	Au, Au@Pt NWs[67]	AA Reduction

1.2.1 Peptides

Peptides are well known for their excellent biomimetic properties as templates for the controlled growth of different NPs.[68–70] Peptides are composed of short chains of amino acids, which provide chemical diversity such as –COOH, –SH, –OH and $–NH_2$ groups. These groups have strong and flexible binding affinities for specific metallic surfaces. In addition, the presence of hydrophobic and hydrophilic motifs as well as secondary structures can lead to stronger interactions between peptide and nucleated metal nanocomposite, which play important roles in determining the final structure of the formed MNMs.[71] Herein, we present an overview of the recent literature in using peptides for preparing MNMs.[41,72,73]

Biomineralization is a process in nature, by which living organisms fabricate minerals such as $CaCO_3$, $Ca_3(PO_4)_2$ to form materials like shells, bone and teeth with hierarchical architectures.[74] Inspired by this widespread phenomenon, some peptide sequences have been artificially programmed to synthesize metallic nanoclusters (MNCs, generally containing two to tens of metal atoms) such as Ag NC,[75]Au NC[76] and Cu NC[77] without the use of adventitious reductants. In this process, the metal precursors are first introduced to the peptide solution and then, the pH of the mixture is adjusted by adding NaOH to the desired alkaline conditions, as some amino acid residues such as tyrosine in peptide possess reduction capability in a basic environment. To obtain these MNCs, most peptides are designed such that at least one domain contains a CCY (cysteine-cysteine-tyrosine) sequence, which is responsible for binding and reducing metal ions. For example, Cui et al.[75] used an artificial peptide (CCYTAT) to biomineralize serial Ag NCs with different sizes. Under alkaline conditions, the phenolic hydroxy group of tyrosine has the ability to reduce Ag^+ into metallic Ag NCs, which is then anchored by the thiol group of cysteine. Noteworthily, it was suggested that the reductive ability of tyrosine is dependent on the pH values (Scheme 1.1). At higher pH, the phenolic peptides are more readily converted to phenoxide, which can strongly reduce Ag^+ to Ag atoms and result in larger clusters. In addition, circular dichroism measurements suggested that the solution alkalinity could likewise tune peptide secondary structure, which may also affect the Ag NC size.

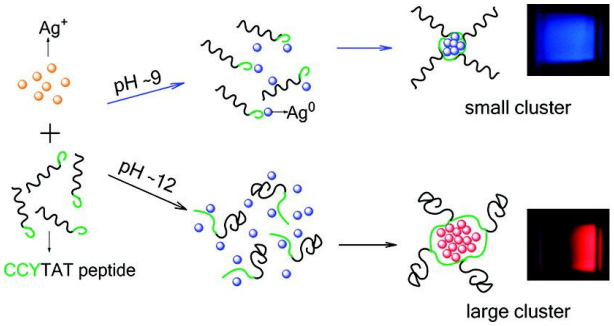

Scheme 1.1: Illustration of peptide–Ag cluster formation. The peptide can biomineralize Ag^+ in situ and produce Ag clusters in aqueous solution. At pH values of ~9 and ~12, Ag clusters with blue and red emission are formed, respectively. Reprinted with permission from ref 75. Copyright 2011 American Chemical Society.

To date, chemical reductant-based methods are the most widely adopted for peptide-metal synthesis. The process usually consists of two steps. First, the material-binding peptide is incubated with metal precursors in water or a buffer solution for a specific time at room temperature. Then a reducing agent such as $NaBH_4$ or ascorbic acid is added to the mixture to reduce the metal ions to their zerovalent nanoforms while the solution is stirred. Sometimes, a reducing buffer such as HEPES is used as the reductant instead.[43] Chemical reduction methods usually generate a random distribution of NP sizes/shapes and give relative low stability to the formed material – without the presence of an additional capping agent.[78–80] In the case of peptide derived synthesis, the peptide drives the nucleation process at a site where the nanoparticle growth starts and is then captured by the template, providing monodisperse size distribution and particle stability in the colloid solution.[41] In this regard, the stability is due to the strong affinity of the amino acid residues for metals.[69]

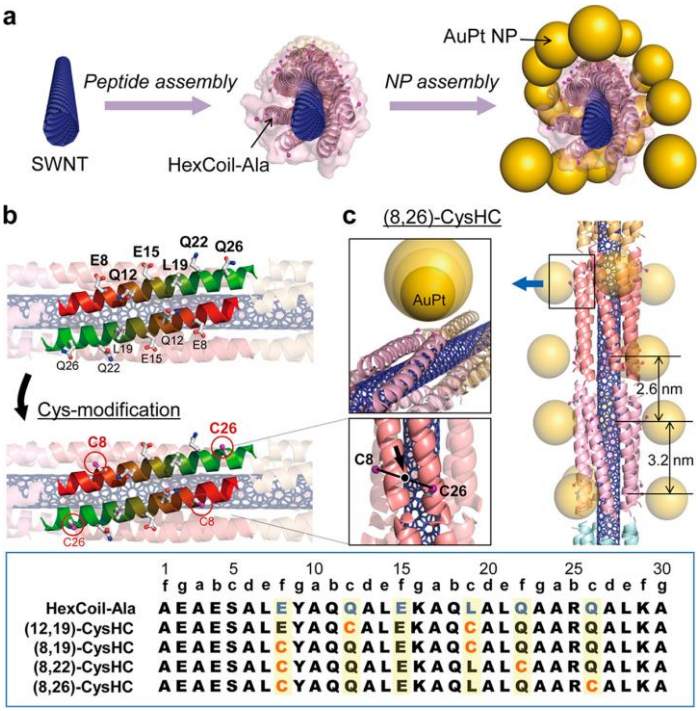

Figure 1.1: Synthesis of AuPt NP superstructures on a SWNT linked by peptide. (a) Fabrication scheme; (b) Genetic modification of outward-facing sites in peptide sequences (red-to-green colour indicates the N-to-C termini) with Cysteine (Cys) residues to specifically nucleate NPs. One of the modified peptides, with E8 and Q26 changed to Cys, is shown (bottom box: peptide sequence); (c) Computational model simulating the assembly geometry of (8, 26) NPs. NP position is indicated at the midpoint between two adjacent Cys residues (inset figures). Reprinted with permission from ref 69. Copyright 2018 American Chemical Society.

Using the chemical reduction method, Kang et al.[69] employed a programmed HexCoil-Ala (HC) peptide to construct a superstructure of AuPt NPs on single wall carbon nanotubes (SWNTs) with tailored electrocatalytic activity (Figure 1.1). In the synthesis, the peptide first formed a suprahelical structure via assembly into an antiparallel hexameric bundle along a SWNT axis. Next, the metal precursors $HAuCl_4$ and H_2PtCl_6 were successively added to the peptide/SWNT suspension, followed by the injection of $NaBH_4$ after ~30 min. Different reaction time led to particles of different sizes. In this case, the peptide was programmed such that it had bifunctional specific recognition properties, with 1) a nanotube-specific inner face that interacted with the aromatic moieties of the conductive SWNT; and 2) an outer metal-specific face that was engineered to bind NPs at predefined anchoring sites. This was realized by systematically revising

the amino acid compositions of the peptide to replace the original residues with cysteine residues at selected sites, which resulted in well-organized NP superstructures at precise positions.

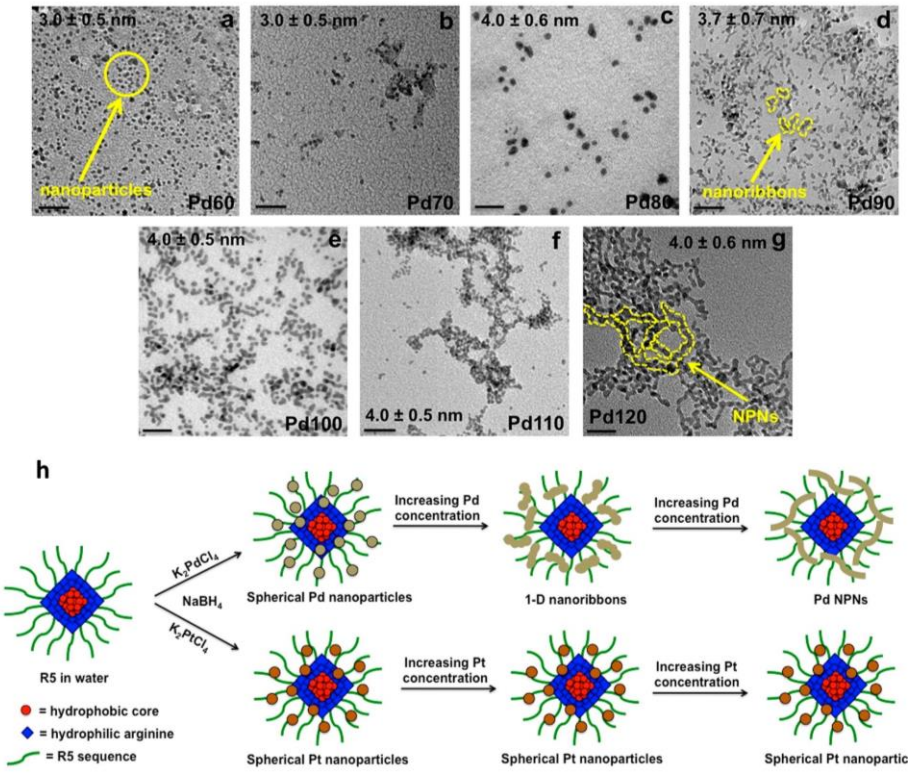

Figure 1.2: TEM analysis of the (a) Pd60; (b) Pd70; (c) Pd80; (d) Pd90; (e) Pd100; (f) Pd110; and (g) Pd120 materials generated using the R5 peptide template. All scale bars equal 20 nm. (h) Proposed mechanism for the formation of Pd and Pt nanostructures on R5 peptide template. Reprinted with permission from ref 39. Copyright 2013 American Chemical Society.

The final size, shape and facets of the prepared MNMs are dependent on a number of factors including peptide structure, peptide/metal ratio, metal ion reduction rate, reaction time and the buffer pH. Bhandari and co-workers synthesized Pd,[39] Pt,[39] and Au[37] nanostructures of varying morphologies using a $NaBH_4$ reduction method with an R5 peptide, which was able to self-assemble in solution. Metal-peptide complexes, such as Pd^{2+}-peptide binding, have interactions between amine moieties and metal sites at favorable pH conditions.[81] It was found that the morphology of the encapsulated MNMs depended on the inorganic composition and the metal/peptide ratio. Particularly, for Pd nanostructures at low Pd/peptide ratio, spherical NPs were

produced; at intermediate and high ratios linear ribbons and branched nanoparticle networks (NPNs) were the products respectively (Figure 1.2a-g). As shown in Figure 1.2h, at low Pd/peptide ratio, Pd ions are sufficiently spaced and upon reduction, spherical NPs nucleate and grow, with large interparticle distance to prevent aggregation. As Pd loading increases, more nucleation sites develop during the reduction process, leading to decreased particle distance within the template to allow for controlled aggregation to form nanoribbons. For even higher ratios, branched NPNs form as a result of more extensive aggregation. Interestingly, this structure evolution phenomenon did not apply to Pt[39] and Au nanostructures.[37] For Au, only NPNs formed at all tested ratios, while Pt formed only spherical NPs regardless of the metal loadings. The results were attributed to the different peptide-metal binding affinities and the rate of metal ion complex reduction, particle nucleation, growth and aggregation.

Besides reducing metal ions by chemical reagents, argon glow discharge, which uses cold plasma as the electron source, recently appeared as an effective and simple method for preparing nanoparticle-peptide biofilms. In two reports by Liu's group,[33,36] ultrathin and uniform biofilms fabricated from cold-plasma-assisted peptide assembly were applied to support noble metal NPs (Au, Pt, Pd NPs). The metal salts were mixed with $A\beta_{16-20}$ peptide molecules in distilled water, and then treated by glow discharge for 10 min, followed by incubation at 37 °C. With the assistance of hydrated electrons produced from the interactions between plasma and water, the peptide assembled into the biofilm and simultaneously, the metal ions also adsorbed electrons to form highly dispersed NPs on the film. Figure 1.3 shows the fabrication process of an Au-peptide nanofilm, representative photographs and TEM images.

Amino acid sequences are important for NP nucleation, since they are related to the total binding energy between the metal ion and the chain sequence of the peptide.[43,44] It is clear that supramolecular driving forces affect the structure of the NPs and how they stabilize the interactions between metal and peptide.[82] However, peptide-based synthesis also presents some challenges related to spatial and structural control in three dimensions that must be overcome.[71] In this sense, protein-based materials have emerged as an alternative for peptide-based structures, since proteins are multi-stacked structures and can provide a more complex template architecture for NP deposition/growth. The generated bio-interface between the peptide molecules and NPs can modify the surface property of the metal, which further tunes the electrocatalytic activity and

selectivity. It is therefore imperative to fully characterize the bio-interface and elucidate detailed structure/property relationships to avoid endless trial-and-error experimentation. Nevertheless, studies revealing this relationship are rather limited to date due to the high complexity of probing binding events and the resulting interfacial structure.

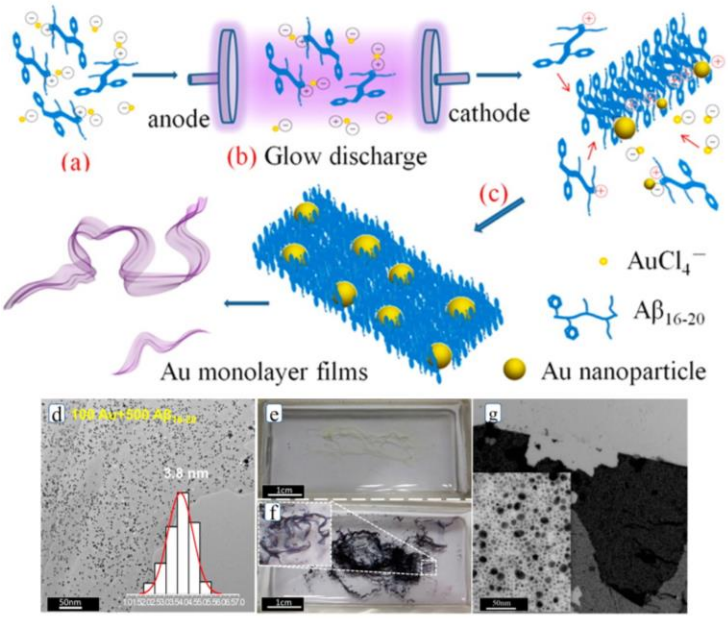

Figure 1.3: (a-c) Process of synthesizing peptide-based Au monolayer film: (a) Peptide interacts with $AuCl_4^-$ through the positive charge on the K residue; (b) Glow discharge plasma reduces Au ions to Au NPs, and the peptide monomers self-assemble into fibrils; (c) Au nanoparticles and peptide fibrils assemble into well-distributed nanofilms; (d) TEM image of P-Au/$A\beta_{16–20}$ films prepared using 100 μM $HAuCl_4$ with 500 μM $A\beta_{16–20}$; Photograph of (e) P-$A\beta_{16–20}$ and (f) P-Au/$A\beta_{16–20}$ in the quartz boat after the glow discharge treatment (P–Au/$A\beta_{16–20}$ sample using 100 μM $A\beta_{16–20}$ and 500 μM $HAuCl_4$ hybrid aqueous solutions) and (g) representative TEM micrographs of the film formed. Reprinted with permission from ref 36. Copyright 2013 American Chemical Society.

1.2.2 Proteins

Compared to peptides, proteins have larger structural diversity, assembling into rods,[83] disks,[48] cages,[84] and barrels,[85] for example. They also possess more abundant binding sites for metal ion complexation with high selectivity and efficiency,[86] making them promising building blocks for MNM construction.

Different approaches have been applied in order to combine MNMs and protein templates. One of them is the biomimetic mineralization process, where the deposition is based on the interaction between the metal ion and the template site, followed by reduction using the functional groups of the protein, with final structures affected by metal/protein ratio, pH values and incubation time.[40,87–90] Using biomineralization, a series of metal clusters of Au, Cu and alloys on the model protein BSA (bovine serum albumin) were prepared under optimized conditions.[26,91,92] The metal salts were mixed with BSA at an appropriate temperature (37~55 °C) with the pH adjusted to ~12 by NaOH. Under this optimized temperature and pH, the reduction capability of Tyr residues is greatly enhanced, turning metal ions into zerovalent nanoclusters. Other types of protein such as ferritin and some enzymes have also been used as templates to biomineralize metal clusters.[44] Besides biomineralization, external reducing agents like $NaBH_4$ have also been used to synthesize noble metal nanoarchitectures in aqueous solution under room temperature.[49,52]

Eggshell membrane (ESM) is a naturally multiple protein-based (mainly collagens and glycoproteins) waste material with interconnected fiber framework,[93] and has been widely explored as a cost-effective template for constructing 3D nanoarchitectures.[94–97] For example, Yang's group developed ESM-templated porous and uniform CuO-ZnO nanocomposites via a simple biomineralization process followed by calcination.[94] Similarly, Au nanonetworks were also reported through biomineralization.[95] The microporous ESM has a rigid structure to stabilize Au nanoparticle with large surface area.[95] In addition, the reduction process to form Au nanoparticle can be accelerated by hydrazine reduction at room temperature.[96] The large amount of functional groups on the protein make it an excellent platform with high metal loading capacity.[96]

Tobacco mosaic virus coat protein (TMVCP) is the capsid protein of the plant virus TMV. This RNA free protein is a good example to demonstrate how protein structure affects NP deposition.[98,99] Under the pH range from 5.5 to 7.5, TMVCP self-assembles predominantly into disk forms with a diameter of 18 nm and an inner channel of 4 nm. The disks have an organized charge distribution, with negative charge arising from carboxyl groups and positive charge arising from nitrogen containing groups. This charge distribution facilities the selective binding of gold NPs by electrostatic interaction.

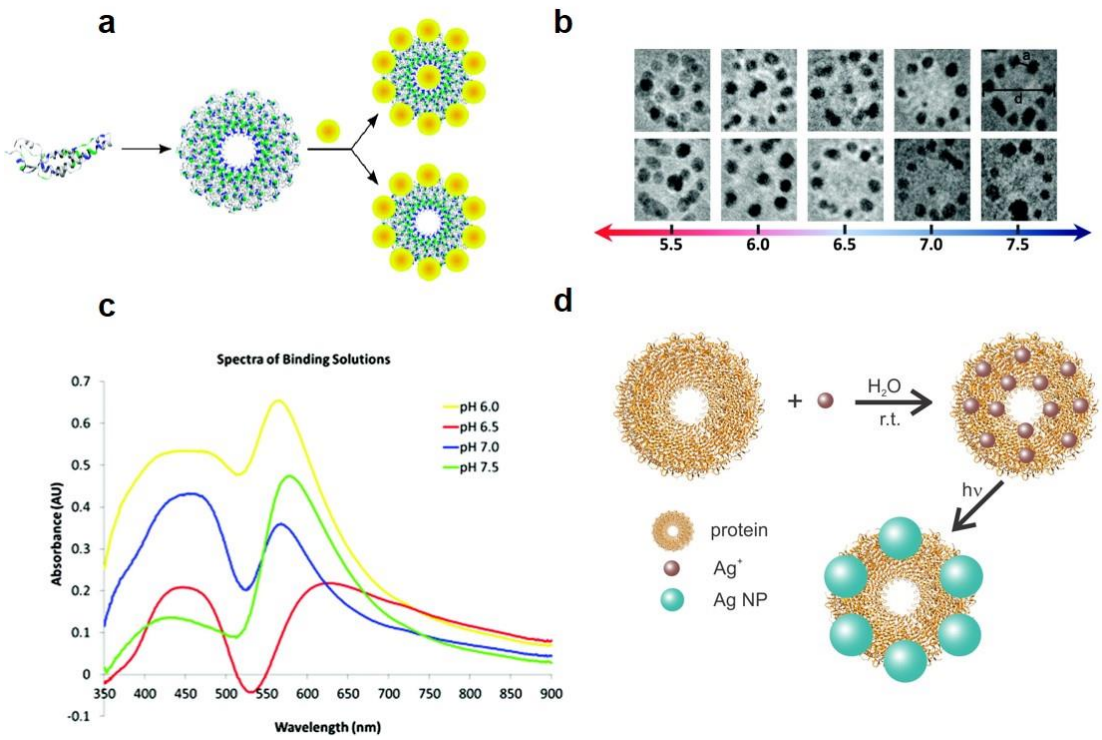

Figure 1.4: (a) Process of Au nanoring assembly with and without a central particle; (b) TEM images with different pH conditions; (c) Spectra of binding solutions at each pH studied. Identical solutions with buffer instead of TMVCP are used for blank correction; (d) TMVCP–mediated photoreduction of silver ions into silver rings. (a-c) were reprinted with permission from ref 48. Copyright 2012 American Chemical Society. (d) was adapted with permission from ref. 99. Copyright 2019 Royal Society of Chemistry.

Using a mutant TMVCP as the template, Blum's group successfully fabricated Au nanoparticle rings with sub-23 nm diameters on the outer surface of the disk shaped protein,[48] which may have potential impact in optical applications. As illustrated in Figure 1.4a-c, preformed Au NPs were incubated with the protein. Thorough electrostatic attraction to the arginine residues on the protein, the Au NPs are attached to the top edges of the disk. Interestingly, a nanoparticle will also bind to arginine groups in the central pore when the pH is carefully adjusted to protonate the carboxyl groups surrounding the pore. The results have shown that the size distribution of NPs is uniform and particle agglomeration was avoided. The same group also synthesized Ag nanorings surrounding the outer surface of TMVCP by a fast photoreduction method.[47,100] Ag precursors were first incubated with protein in water at room temperature. Under UV light illumination, Ag^+

were reduced to Ag^0 atomic clusters, which then grew and assembled on outer surface of the protein, forming a disk-templated nanoring (Figure 1.4d). The formation mechanism was believed to be radical based, with carboxylates hosting and stabilizing the photogenerated radicals.

Protein's chemical and topological properties play a critical role in MNM synthesis, since the chemical groups can control the nucleation sites and the topology can determine the features of the NPs due to spatial confinement.[50,98,101] To make it easier for metallization to generate target structures, proteins are often engineered to functionalize certain sites by genetic or direct surface chemistry modification. In a pioneering work by McMillan et al.,[50] a loop that occludes the central pore of chaperonin was genetically removed and a polyhistidine (His10) sequence was then added, which enhanced solvent accessibility and metallization potential in the hollow core region. Using electroless deposition activated by Pd^{2+} (Pd^{2+} tightly binds to the imidazole side chains of the histidine), Ni-Pd and Co-Pd bimetallic NPs were patterned with dimensions defined by the chaperonin. Following this work, another protein, peroxiredoxin (Prx), in its toroidal form was also chemically decorated by histidine residues around its central core.[102] Prx is a protein that assembles into different forms such as stacks, tubes, toroids under certain solution environment.[103]

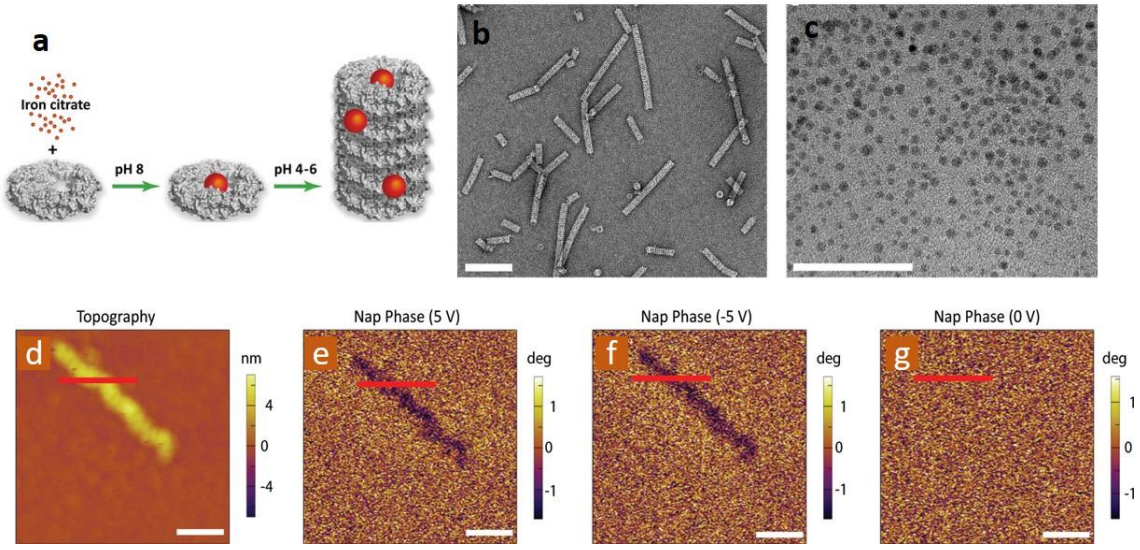

Figure 1.5: (a) Schematic illustration of the Iron oxide 1D NP assembly; TEM images of Fe-Prx dialyzed to pH 6.0 with (b) negatively stained (scale bar of 100 nm) and (c) unstained image (scale bar of 50 nm); Electron force microscopy data of Fe-Prx dialyzed to pH 6.0 and deposited on a p-doped silicon wafer with (d) the first pass topography and (e-g) the second-pass phase with a lift height of 30 nm with applied biases of 5, -5, or 0 V, respectively. Reprinted with permission from ref 101. Copyright 2018 American Chemical Society.

In their study, Fe^{2+} was sequestered into the pore and underwent oxidation in the presence of atmospheric oxygen to form an iron oxyhydroxide NP in the confined space.[102] Upon changing pH to 4~6, the mineralized toroids were able to organize into stacks and release some particles to the outer surface of the protein, resulting in a one-dimensional (1D) NP assembly, as shown in Figure 1.5.

From a catalysis point of view, nanomaterial size, shape, crystallinity and distribution pattern are factors that can directly affect the catalytic response of the material, and thus are the focus of many studies. These properties can be exquisitely controlled by choosing appropriate protein candidates and optimizing the reaction conditions. For example in electrochemistry, protein has often been used to promote the formation of NPs on carbon-based materials, focusing on increasing the NP distribution and size control to improve electrochemical results.[49,104,105] Due to the functional groups presented in the carbon-based materials and the proteins, the binding between these two structures is favorable. Once this interaction is established, NP deposition can be realized by a simple sodium borohydride reduction. As mentioned above, the size and distribution of the NPs are also controlled by the incubation time of the metal ion, metal/protein ratio and the concentration of the reducing agent. Alternatively, protein-NP structures can first be prepared then immobilized on carbon materials to improve electrocatalytic activity. For example, Bagheri et al.[106] fabricated a biocompatible nanocomposite containing BSA, Cu NCs and SWCNT (Figure 1.6a, e). In this case, the Cu NCs were first assembled on BSA by biomineralization under alkaline condition. The as prepared CuNCs@BSA were then coated on the SWCNT to improve the electrocatalytic activity for sensing purpose. The UV-vis, fluorescence and FTIR (Fourier transform infrared) indicated that the BSA entrapped in the composite film had been changed in its secondary structure (Figure 1.6b-d).[106]

Protein can also act as the sole support for NPs in catalysis where, unlike a passivating layer formed in most traditional synthesis, the protein does not coat the entire surface of the NPs while maintaining structural stability. For example, Varpness et al.[107] used a small heat shock protein (Hsp) to immobilize Pt metal clusters as a H_2 catalyst. Hsp is a cage protein with 24 subunits assembled into a 12 nm cage with a 6.5 nm interior cavity. In the synthesis, purified Hsp was incubated with $PtCl_4^{2-}$ and reduction was realized by DMAB (dimethylamine borane complex),

forming a Pt NC in the interior cavity. In this case the protein cage is able to maintain the integrity of the Pt clusters, prevent agglomeration, and control H_2 molecular access to Pt.

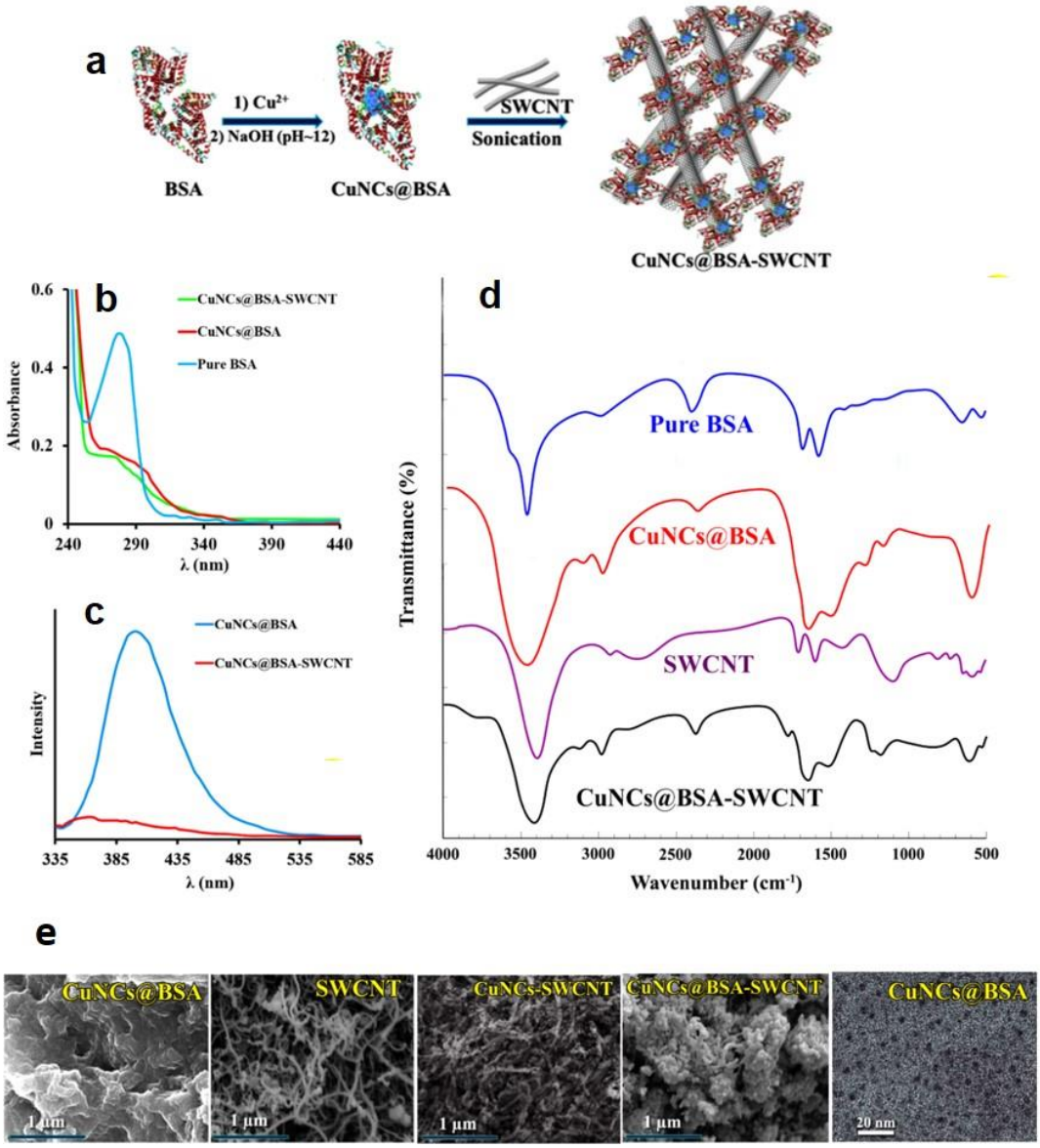

Figure 1.6: (a) Synthesis of Cu/BSA/SWNT conjugate; (b) UV–vis absorption spectra of free BSA, CuNCs@BSA and CuNCs@BSA-SWCNT nanocomposite; (c) Fluorescence emission spectra of CuNCs@BSA and CuNCs@BSA-SWCNT at λ_{exc}: 325 nm; (d) FT-IR spectra of free BSA, CuNCs@BSA, SWCNT and CuNCs@BSA-SWCNT; (e) SEM images of CuNCs@BSA, SWCNT, CuNCs-SWCNT and CuNCs@BSA-SWCNT nanocomposite, respectively and TEM images of CuNCs@BSA. Reprinted with permission from ref 105. Copyright 2017 Elsevier.

In electrocatalysis, it is important to avoid material agglomeration, which decreases the surface area, and in turn affects the electrochemical activity. One way to avoid agglomeration is by functionalizing the surface of the catalyst with a species that is able to keep uniform distribution of the formed NPs. The application of enzymes either as a support or as a catalyst mediator is an interesting focus of study, since enzyme can provide specificity to certain reactions and controllability (protect and stabilize) to NP growth.[108,109] For example, Scott et al.[51] used a redox-active enzyme glutathione reductase (GR) to prepare Au NPs at the enzyme's active site, which can electrocatalyze the borohydride oxidation reaction. The synthesis was achieved by incubation of GR with NADPH and $AuCl_4^-$ in buffers. It was established that the GR catalysis was NADPH-dependent, and the reduced gold binds to enzyme by cysteine.

NPs can also be obtained by employing reducing agents produced from enzyme catalyzed reactions, which is a straightforward and greener way. By generating reducing agents throughout these reactions the metal ion can be reduced in a more controllable manner.[110] One example would be the formation of H_2O_2 from glucose oxidase, which then promotes the reduction of gold ions and leads to gold deposition.[111] Prussian blue NPs were also synthesized in the presence of an enzyme (peroxidase), where the presence of H_2O_2 also leads to the formation of NPs.[112]

Like all of the bioinspired supports cited previously, the structure of the enzymes is important as the functional groups and chains can modulate coordination and expose active sites.[113] Hydrophilic and hydrophobic motifs can directly affect the interaction between enzyme and metal ions, changing the incubation residence time and the interaction strength. Suitable environments are essential for enhancing electrostatic interactions between substrates and metal precursors, which is critical to stabilize the NP and improve its electrocatalytic performance.[114]

1.2.3 DNA

Using DNA as a platform for NP assembly is a powerful strategy to create an organized structure that is able to perform different functions, such as enhancing sensing signals[115,116] or create plasmonic effects.[117,118] DNA architecture provides the desired controllability and programmability as a building block.[119] Its surface is fully addressable and can be easily modified to incorporate different chemical species/structures such as nanoparticles, with high positional precision.[120]

Composed of a phosphate backbone and four types of nucleobases, DNA is highly negatively charged under a wide pH range. Therefore, electrostatic interaction is often exploited to direct the assembly of preformed NPs on DNA molecules. For example, DNA-functionalized gold nanostructures are key reagents in a variety of fields such as drug delivery, sensing and directed assembly. Many DNA/Au NP conjugates have been prepared by mixing DNA with Au NPs, which are capped by ligands possessing positively charged head groups. Furthermore, if the Au NPs are capped by ligands like citrate, salt is needed to help DNA overcome the long-ranged electrostatic repulsion.[121] The assembly is realized by DNA replacing the citrate ligands, since Au NPs have much stronger affinity to DNA than to citrate. To further enhance binding affinity to metals, DNA is often thiolated before mixing with NPs.[122] DNA is able to arrange NPs with high regularity and density in 2D or even 3D structures, which can be useful for electrocatalytic applications.[55] A review article from 2013 gave an overview of how gold NPs can interact with DNA strands and how the NPs can be organized on the DNA structure.[123]

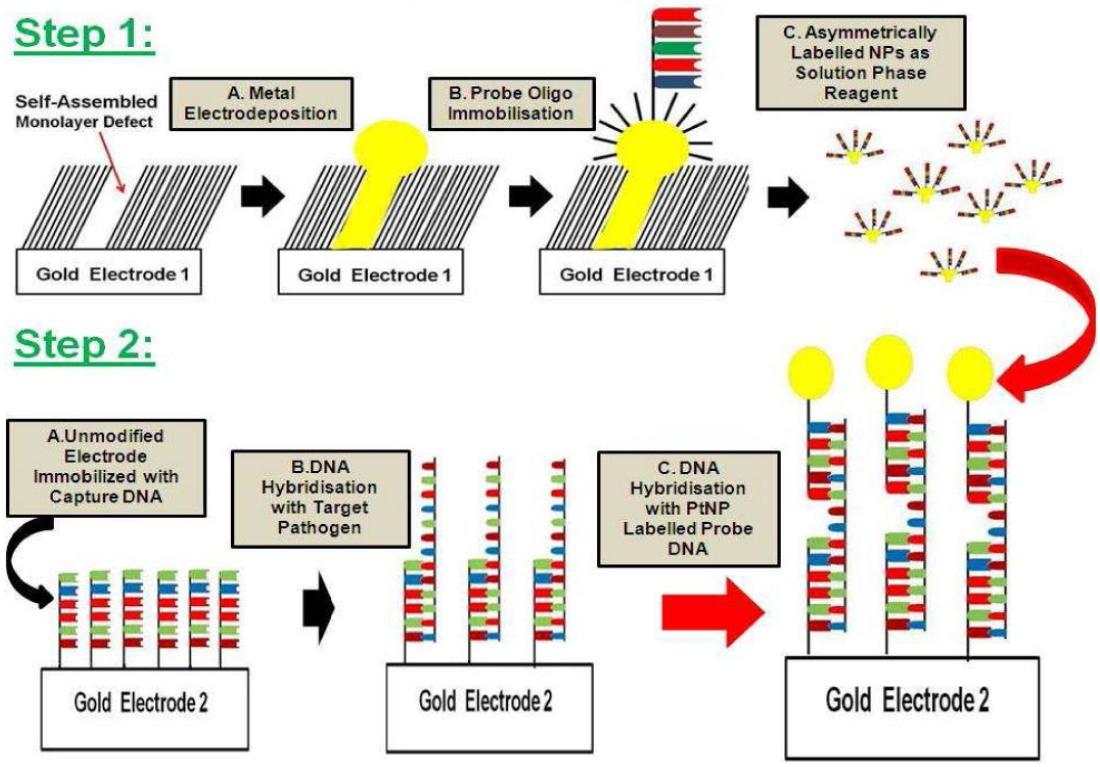

Figure 1.7: Overview of Pt NP formation and sensor fabrication. Reprinted with permission from ref 54. Copyright 2012 American Chemical Society.

DNA has been used in electrochemical measurements due to its self-assembled structure, which helps the organization of NP distribution to improve electrochemical performance,[124,125] such as increasing detection limits for sensors applications.[53] Spain and co-workers[54] developed a DNA detection system with high sensitivity by using probe DNA decorated Pt NPs, as shown in Figure 1.7. In this case, the Pt NPs were first electrodeposited onto a self-assembled monolayer on the gold electrode, followed by immersion in a thiol terminated probe DNA solution. These DNA labeled electrocatalytic particles were then used to determine the target DNA concentrations, which shows wide dynamic range and high detection sensitivity. A platinum-DNA system was also used to modify a gold ultramicroelectrode (UME) looking to enhance the electrochemical sensing.[126] In this work, preformed Pt NPs were incubated with a detection DNA probe, and the gold UME was modified with a capture probe. With the target oligonucleotide hybridizing with both probes, a Pt NP bound to the UME surface, which was able to electrooxidize hydrazine to give signals.

Like other templates discussed, DNA-metal complexes can also be prepared in situ by using reductants like $NaBH_4$, citrate, or ascorbic acid. Unmodified DNA or SH-DNA is first mixed with metal precursor and incubated for a defined time period, then followed by adding reducing agents. For example, Ag^+ has affinity to DNA through interaction with the nitrogen of purine or pyrimidines, enabling the creation of short oligonucleotide-encapsulated Ag NCs. A 12-base oligonucleotide was mixed with $AgNO_3$ in buffer solutions. After reduction by $NaBH_4$, Ag NCs with 1-4 atoms grew on the template, as indicated by mass spectra.[57] Fluorescent Cu NPs have also been fabricated on DNA by sodium ascorbate reduction, and later served as nucleic acid amplification nanoprobes for tuberculosis diagnosis.[127] Silver-DNA NPs can also be prepared by electrodeposition in which a potential is applied in the presence of DNA and Silver precursor.[56] In this case, the presence of DNA controls the silver electrodeposition, which acts as a barrier, avoiding stronger agglomeration processes and resulting in a narrow size distribution.

DNA is a green template to organize and control NP size and distribution. With the development of DNA-origami, the functionalization and programmability of DNA-metal nanomaterials could pave the way for future developments based on well-patterned bioinspired electrocatalysts.

1.2.4 Virus

As a building block that is able to self-assemble and promote specific arrangements that can be applied in different areas, viruses emerge as interesting templates for NM deposition. Viruses consist of a DNA or RNA chain surrounded by a number of coat protein subunits that assemble into monodisperse particles. They come with a variety of sizes and shapes such as filaments, icosahedra, tubes, and head-to-tail structures, which provide great diversity for NM fabrication.[128] In addition, some viruses have evolved to withstand even harmful environmental stimuli in nature, making them durable scaffolds for required chemical modifications to be applied for specific purposes. Viruses contain a considerable number of functional groups displayed on their capsid proteins, which can promote NP growth by specific and nonspecific interactions.[129] Particularly, these capsid protein sequences and structures are determined by the genetic code contained in the DNA or RNA, thereby offering great promise in controlling the structure and surface chemistry precisely.

Different strategies have been applied to enhance the metallization potential of the virus. One method is to activate the virus surface through electroless deposition. Wild type TMV is a rod-shaped virus with a helical RNA encapsulated in 2130 coat proteins. The single virion has a high aspect ratio, it is 300 nm long, with an outer diameter of 18 nm and an inner diameter of 4 nm.[130–132] In a pioneering work by Knez et al.,[62] it was experimentally demonstrated that TMV has extraordinary physiochemical stability towards treatment with different solvents, solution pH change and relatively high temperature, which has attracted extensive research attention on utilizing it as a robust template for directing nanostructure assembly. They successfully metallized TMV in the central channel with continuous 3-nm nickel and cobalt nanowires (NWs) by electroless deposition. In this process, the metallization was done with palladium salt in order to activate the nonconductive surface and enhance the interaction with the substituent metals. Basically, Pd^{2+}-virus was firstly created. This new structure was then submitted to a plating bath containing nickel or cobalt salt and a mild reductant DMAB. The structure of the virus helps the NP growth and keeps its shape and size distribution.[130] Furthermore, it allows to obtain ultra-small and organized structure, which can be interesting for electrocatalysis studies. Inspired by this work, a series of studies have investigated TMV mineralization.[65,133–135]

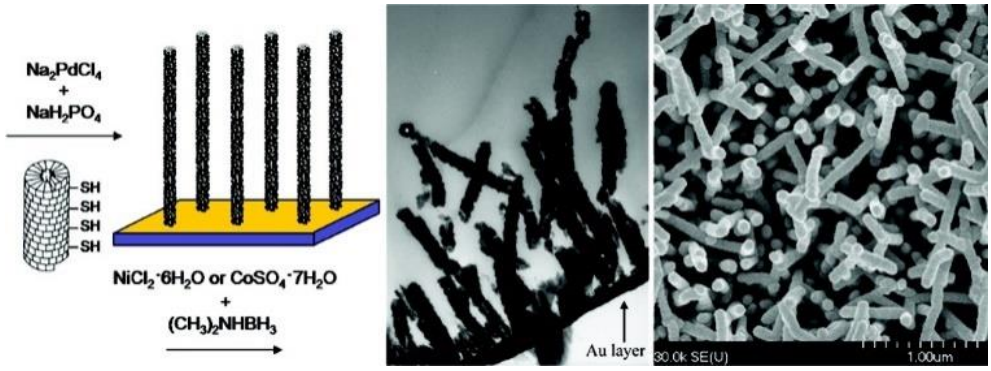

Figure 1.8: Ni and Co NWs assembly on TMV-cys by electroless deposition. Reprinted with permission from ref 132. Copyright 2008 American Chemical Society.

Another method to increase metallization potential is by genetic modification. For example, Culver's group genetically engineered wild type TMV to express cysteine residues on its outer surfaces.[65] The thiol group on cysteine has high affinity to gold and palladium. To apply it in battery applications, the virus was firstly vertically patterned on gold surfaces. Next, it was subjected to electroless plating process to coat the virus with uniform high surface area Ni and Co electrodes (Figure 1.8).

Besides TMV, filamentous bacteriophage M13 is also a widely employed virus template for 3D nanoarchitecture organization.[59,67,136] Owing to its material-specific binding capability as identified by a biopanning process,[137] M13 allows control over its surface chemistry for metallization. The phage is 880 nm in length and ~8 nm in diameter, which can serve as a long and thin material building block with high surface area. Wild type M13 is composed of a single-stranded DNA encapsulated by around 2700 copies of major p8 proteins along its body, 5-7 copies each of p3 and p6 proteins at one end, 5-7 copies of p7 and p9 at the other end.[138] These proteins can be either chemically decorated via bioconjugation to add new functionalities, or genetically engineered to display certain peptide sequences. M13 and its variants have been incorporated into different energy applications including Li-ion batteries,[139–141] solar cells[142,143] and electrocatalysis.[59,144]

A bioconjugation approach was used to fix thiol groups at the p8 proteins by reacting the amino groups with N-succinimidyl S-acetylthiopropionate, followed by deprotection.[144] This surface

modified virion demonstrated good templating to nucleate and grow Au, Ag and Pt NPs on its outer surface. Likewise, Au and Pt NPs were created on a mesoporous silica structure, which was also prepared on M13.[145] Interestingly, the Au and Pt NPs were formed by reduction of the Try and/or Phe residues on the protein, without the need of external reductants.

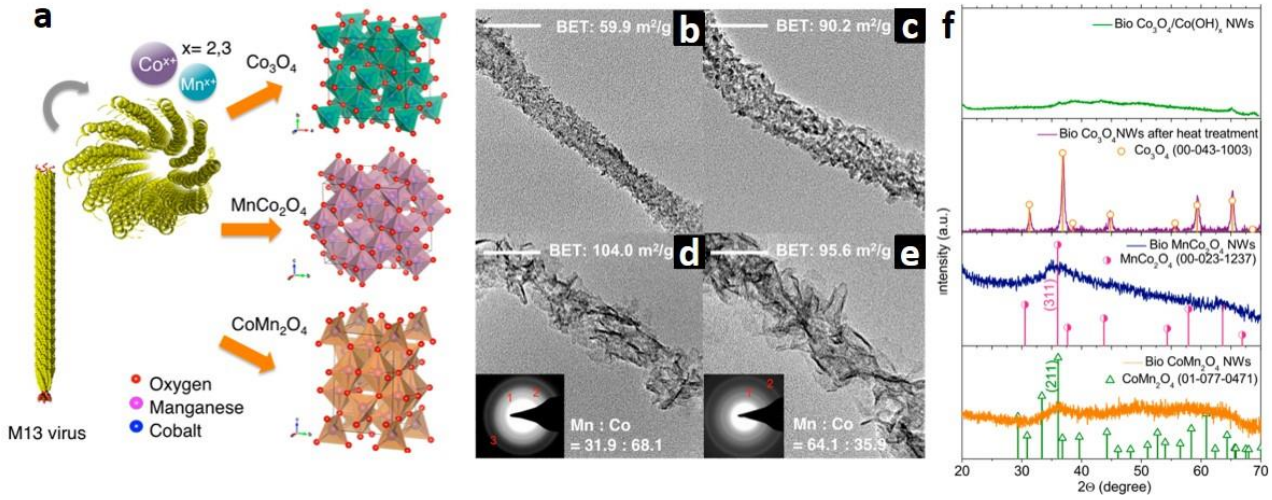

Figure 1.9: (a) M13 virus-templated fabrication of multi-components Co/Mn oxide NWs. Left: Synthesis schematic showing the interaction between transition metal ions (Co^{x+}, Mn^{x+}) and the p8 major coat protein of M13 virus (cross sectional view on the right side). Right: Crystal structures of $Mn_xCo_{3-x}O_4$ (x = 0, 1, 2) templated along M13 virus; (b-f) Material characterizations of M13 virus-templated $Mn_xCo_{3-x}O_4$ NWs: TEM images and BET data of bio-templated MCO NWs with a scale bar of 50 nm; (b) Bio Co_3O_4/$Co(OH)_x$ NWs; (c) Heat-treated (400 °C for 10 min) bio Co_3O_4 NWs; (d) Bio $MnCo_2O_4$ NWs with EDS data of Co and Mn, corresponding selected area electron diffraction (SAED) pattern with three rings approximately matching to 1, (311), 2, (400), and 3, (440) planes; (e) Bio $CoMn_2O_4$ NWs with EDS data of Co and Mn, corresponding SAED pattern with two rings close to 1, (211) and 2, (400) planes; (f) XRD patterns of bio Co_3O_4/$Co(OH)_x$ NWs (green), heat-treated bio Co_3O_4 NWs (violet), bio $MnCo_2O_4$ NWs (dark blue), and bio $CoMn_2O_4$ NWs (orange) with reference patterns. Reprinted with permission from ref 136. Copyright 2014 American Chemical Society.

For genetic modification, the E3(EEAE)/E4(EEEE) virus clone of M13 has been used to direct the synthesis of a variety of metal oxides, such as TiO_2,[146] Co_3O_4,[147] $Mn_xCo_{3-x}O_4$ (x = 0-2).[136] Figure 1.9a shows the fabrication of cobalt manganese spinel oxide NWs on the E3 clone. In this clone, the N-terminus of each p8 protein contains a sequence of triple glutamate.[136] The negatively charged p8 proteins bind to the positively charged metal complexes through electrostatic interactions. After reduction by H_2O_2, highly porous and homogenous NWs were deposited on the

virus, as evidenced by BET (Brunauer-Emmett-Teller) data and TEM images (Figure 1.9b-e). XRD characterization indicated the materials were amorphous/nanocrystalline (Figure 1.9f), which could play an important role in OER or ORR.[136]

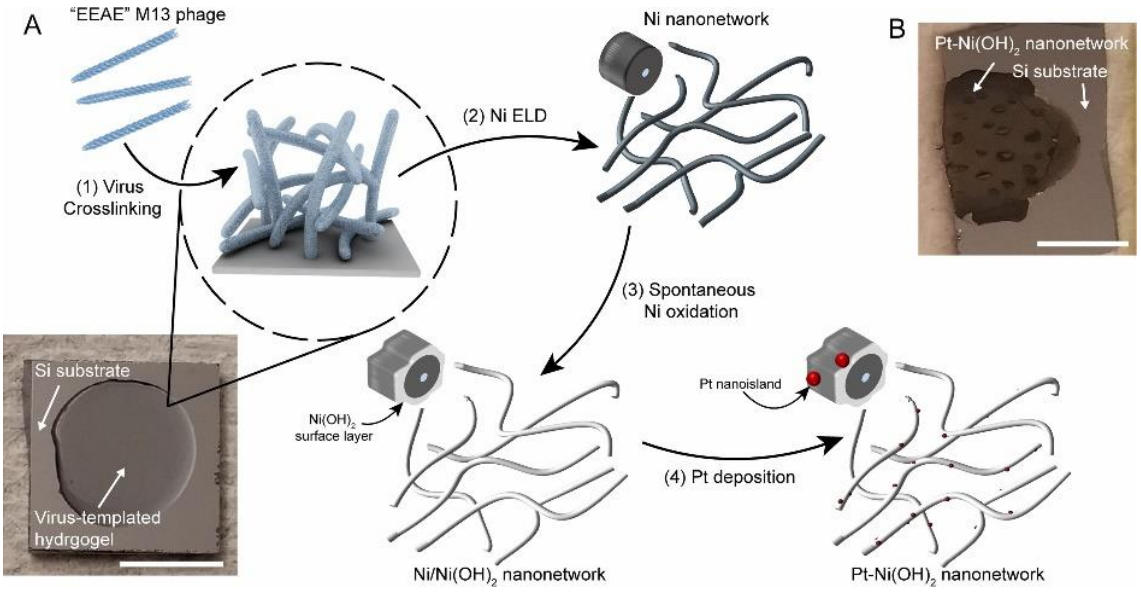

Figure 1.10: (A) Synthesis of Pt–$Ni(OH)_2$ nanonetworks: EEAE M13 virus particles are (1) crosslinked and (2) metallized. (3) Nickel spontaneously oxidizes to $Ni(OH)_2$ in aerobic conditions, and (4) platinum is deposited on the surface of the phage-templated scaffold; (B) Macroscopic view of a Pt–$Ni(OH)_2$ nanonetwork. Scale bars in (A) and (B) are 5 mm. Reprinted with permission from ref 59. Copyright 2019 Elsevier.

Using this same M13 virus clone, Belcher's group reported the facile design of a 3D nanostructured Pt-$Ni(OH)_2$ nanonetworks for alkaline HER.[59] As shown in Figure 1.10, the phage particles were first cross-linked to hydrogels on a titanium substrate. Next, nickel was coated onto the phage scaffold by electroless deposition and then formed a $Ni(OH)_2$ shell under aerobic conditions. Samples were then immersed in Pt salts to form Pt^0 by galvanic deposition. Material characterizations (Figure 1.11) showed that the Pt-$Ni(OH)_2$ featured interconnected NWs, decorated with platinum nanoislands on the order of 200 nm. The island size was dependent on the Pt precursor concentration, with higher concentration leading to higher metal loadings. The thickness of $Ni(OH)_2$ oxide layer was less than 10 nm.

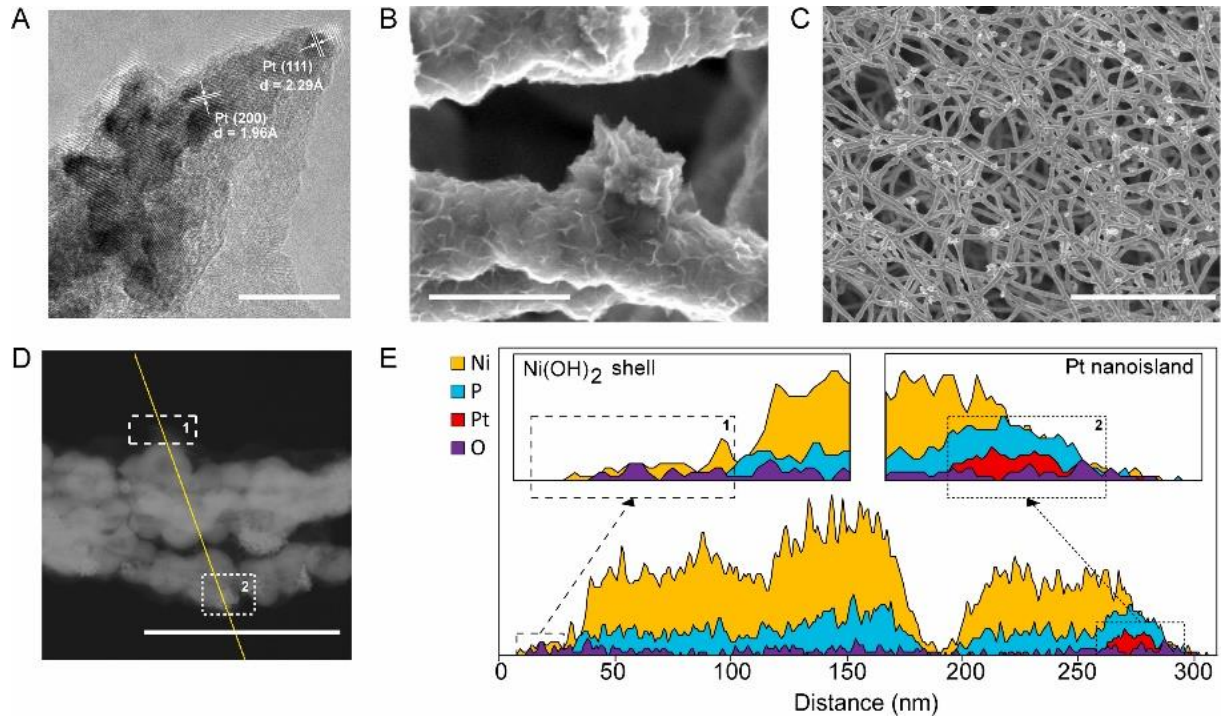

Figure 1.11: (a) HR-TEM; (b) High-magnification SEM; (c) Low-magnification SEM; and (d) HAADF-STEM images of a Pt–Ni(OH)$_2$ nanonetwork with 35.5 μg_{Pt} cm^{-2}geo; (e) EDX line scan identifying the (1) Ni(OH)$_2$ shell and (2) platinum nanoisland. Scale bars are 5 nm, 200 nm, 5 µm, and 200 nm for (a), (b), (c), and (d), respectively. Reprinted with permission from ref 59. Copyright 2019 Elsevier.

Virus-MNMs can also be obtained via direct reduction by agents like $NaBH_4$, ascorbic acid and methanol, etc. Previous work by Belcher's group reported the formation of uniform Au NWs on a genetically engineered M13 phage.[67] The phage was modified so that a peptide sequence with high affinity to Au was expressed on 100% of the copies of the p8 major coat protein (denoted as p8#9 phage), which provided strong adsorption sites along the long dimensions for Au and Au ions. Figure 1.12 shows the fabrication process of Au NWs over the time frame of 0 to 9 h. The growth progress was monitored by color changes, UV-vis and TEM characterizations of reaction mixture, which suggested that the formation of Au NWs arose from smoothing of Au NPs along the phage. Incubation of Au^{3+} with p8#9 in the presence of surfactant CTAB (cetyl trimethylammonium bromide) for 3 h lead to the formation of Au^{+}. This was followed by addition of ascorbic acid to nucleate Au NPs assisted by Ag^{+}. The advantage of using p8#9 includes generation of homogenous Au NWs without the need for size selection and side product removal, the high conversion yield

of at least 98%, and the long-term stability of as-prepared material. In addition, the thickness of the NWs can be controlled by changing the concentration of phage, Au^{3+} precursor and CTAB.[67]

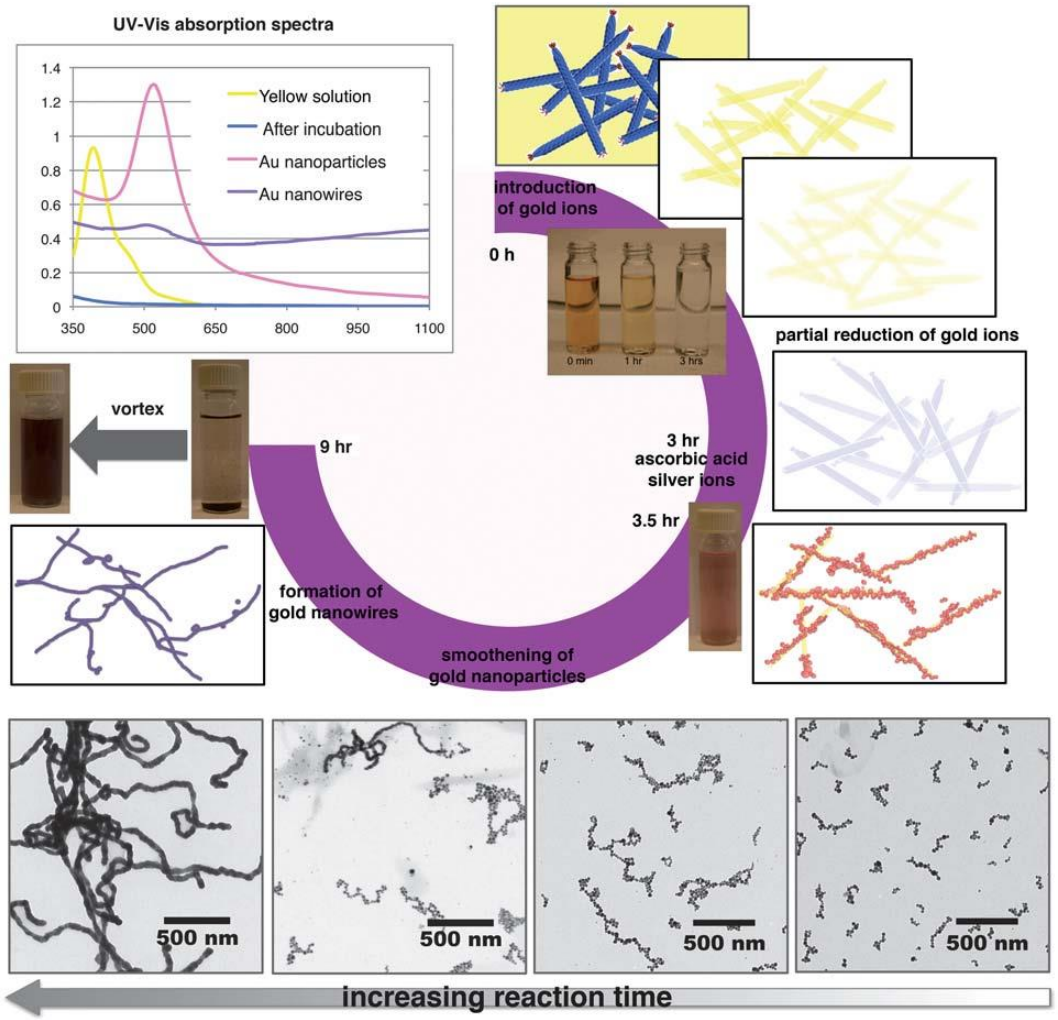

Figure 1.12: Fabrication of Au NWs with time frame. When Au^{3+} ions were introduced to the dispersion of p8#9 phage in CTAB solution (0 h), the solution color was initially orange-yellow and gradually lightened (three solutions in small vials) over time as Au^{3+} partially reduced to Au^{+} (3 h). The addition of ascorbic acid followed by Ag^{+} initiated the nucleation of Au NPs along the p8#9 phage (3.5 h). The solution started to become pale pink in color and became deeper with time and finally yielding a dark violet precipitate on the bottom of the tube due to the weight of Au NWs. These precipitates were easily re-dispersed into a homogeneous solution due to CTAB molecules on the surface of Au NWs. TEM analysis verified the increase in Au NPs with time eventually yielding Au NWs (9 h). Reproduced from with permission from ref 67. Copyright 2012 Royal Society of Chemistry.

In another report by Alaa et al.,[60] wild type cowpea mosaic virus (CPMV) empty particles (eVLPs, devoid of RNA) were metallized by Co and Fe_3O_4 NPs. CPMV has an icosahedral shape with diameter about 28 nm and contains 60 copies of its coat protein. By incubating eVLPs with cobalt salt followed by $NaBH_4$ reduction, Co NPs were formed and organized in the central cavity. The template can also be metallized with iron oxide through hydrolysis. Using an electroless deposition process, CPMV has also been used as a support for forming MNMs.[60,61,66]

Many studies have applied virus-based materials as a platform to improve electrochemical signal and affinity with different systems, especially in the sensors field. Two recent reviews exploring the electrochemical applications of bacteriophage-based electrodes give a good overview of how virus have been used in this field.[30,148] The combination of NPs and virus-templates for electrocatalysis has not been as well explored as peptide templates previously, but more reports have come in recent years, especially with M13. In the same way as other templates, the structure of the M13 plays an important role in NP deposition, affecting their size and distribution, which in turn influences the catalytic behavior of the catalyst.

1.2.5 Others

Besides the above four templates, other biological scaffolds such as lipids,[149,150] plant biomass,[151,152] and microorganisms[153,154] have also been discovered as effective candidates for the MNM synthesis. For example, lipid molecules can functionalize NP surface using their charged hydrophilic head groups. NP is often loaded into the supported bilayers by mixing the preformed NP and the corresponding lipids.[155,156] The lipid uses its polar heads to interact with the NP via electrostatic and van der Waal forces, and then arrange into a typical bilayer structure. For plant biomass and microorganisms, biomineralization is frequently used to mediate NP growth.[31] In terms of applications, these biotemplate-NP systems are rarely used in electrocatalysis up to date, readers are thus kindly referred to the reviews more focused on these material syntheses and specific applications.[150,157–159] While lipid-NP structures are most implemented in biomedical fields (drug delivery, diagnosis, therapy, etc.), plant and microorganism-mediated NPs found wide applications in organic catalysis, sensing, and antimicrobial.

1.3 Applications of Bio-Templated MNMs for Different Electrocatalytic Reactions

In previous sections we discussed how MNMs with interesting and complex structures could be fabricated under the guidance of biological systems using green and mild synthetic conditions. Although impressive research progress has been achieved in this synthetic area, applications of the as prepared MNMs in catalysis, especially electrocatalysis, have attracted great interest only in recent years. Table 1.2 summarizes the different electrocatalytic reaction types that have been demonstrated with the corresponding bioinspired MNMs. Table 1.3 compares some advantages and disadvantages for MNM electrocatalyst supported on each template.

Table 1.2: Electrocatalytic reactions catalyzed by metallic nanostructures on different bio-templates.

Electrocatalytic Reaction	Bio-Template Type	Bio-Template Name	MNMs	Year
Oxygen reduction	Peptide	BP7A	Pt NW[160]	2013
		AFP fibrils	Pt NP/NW[161,162]	2019, 2013
		Aβ_{16-20}	Pt(111)/C NP[46]	2016
		Aβ-sheet	Pt NP[163]	2019
		Z1	AuPt alloy NP[72]	2018
		R5	Au and Pt NP/NW[164]	2016
		FLA3	Au@Pd core-shell[73]	2018
		A4	AuAg alloy NP[68]	2017
		HexCoil-Ala on SWNT	AuPt NP[69]	2018
Oxygen evolution	Virus	DOPA-fd-tet	$Co(OH)_2$[165]	2018
		TMV	Co_3O_4 tube[166]	2017
Hydrogen evolution	Peptide	Z1	AuPt alloy NP[72]	2018
		FLA3	Au@Pd core-shell[73]	2018
	Virus	M13	Pt-$Ni(OH)_2$[59]	2019
Methanol/ethanol oxidation	Peptide	BP7A	Pt NW[160]	2013
		Pd4/AuBP1/H1	PdAu NP[167]	2016
	Protein	Polyhedrin	Pd NP/NW[70]	2016
		Polyhedrin	PdCu alloy NP[168]	2017
		Insulin amyloid fibril	Pt NW,[169] PtRh NW[170]	2012, 2019
	Virus	P8#9 M13	Au@Pt core-shell[67]	2012
		M13-SH	Pt/Au/Ag NPs[144]	2013
Formic acid oxidation	DNA	Calf thymus DNA	Pd NP[171]	2012
		Salmon sperm DNA	Pd NP[172]	2014
Carbon dioxide reduction	Protein	TMV coat protein	Ag NR[100]	2019
Carbon monoxide oxidation	Virus	P8#9 M13	Au NW[67]	2012

Table 1.3: Comparison of MNM electrocatalyst assembled on different bio-templates.

Bio-Template	Advantages	Disadvantages	Refs
Peptide	Low cost; Widely commercially available; High sequence control; Higher electronic conductivity; Wide reaction scope.	Simple architecture (mostly 0D or 1D); Risk of denaturation; Fewer binding sites.	46, 72-73, 69, 160-164, 167
Protein	Low/medium cost; Abundant binding sites; Broad architecture scope.	Limited commercial availability; Sequence control via mutagenesis; Risk of denaturation; Medium/low electronic conductivity; Narrower reaction scope.	70, 99, 168-170
DNA	Widely commercially available; Medium risk of denaturation; High sequence control; Direct 2D/3D architectures; Abundant binding sites.	High cost; Medium/low electronic conductivity; Narrow reaction scope.	55, 123, 171-172
Virus	Controlled architecture; Abundant binding sites; Low risk of denaturation; High electronic conductivity; Wide reaction scope.	Medium/high cost; Limited commercial availability; Sequence control via mutagenesis; Surface treatment required for activation.	59, 67, 144, 165-166

1.3.1 Oxygen Reduction Reaction (ORR)

As a promising technology to solve the energy crisis, proton exchange membrane fuel cells (PEMFCs) transform chemical energy into electricity through electrochemical reactions at the cathode and anode.[173,174] However, due to the sluggish kinetics of the ORR at the cathode, fuel cells face a critical barrier to realize large scale commercialization.[175,176] In principal, ORR can occur under both acidic and alkaline conditions. A simplified reaction mechanism suggests that one oxygen molecule either experiences a direct four-electron transfer process to form the final product H_2O, or else it accepts two electrons to form a H_2O_2 intermediate, which is then further reduced to H_2O,[177] as shown in scheme 1.2.

acidic medium

$O_2 + 4H^+ + 4e^- \longrightarrow 2H_2O$ (direct pathway)

$O_2 + 2H^+ + 2e^- \longrightarrow H_2O_2$ (indirect pathway)

$H_2O_2 + 2H^+ + 2e^- \longrightarrow 2H_2O$

alkaline medium

$O_2 + 2H_2O + 4e^- \longrightarrow 2H_2O$ (direct pathway)

$O_2 + H_2O + 2e^- \longrightarrow HO_2^- + OH^-$ (indirect pathway)

$H_2O + HO_2^- + 2e^- \longrightarrow 3OH^-$

Scheme 1.2: Direct and indirect pathways for oxygen reduction in acid and alkaline media.

Currently, Pt-based NMs have been demonstrated to be the most effective catalyst type for the ORR.[174] One state-of-art material consists of platinum NPs supported on carbon (Pt/C). However, the carbon support suffers from oxidation and stability problems, resulting in gradual electrochemical surface area (ECSA) loss and a decrease in catalytic activity.[178,179] Searching for electrode materials with enhanced efficiency and stability is thus highly desirable for improving cell performance. In the literature for the ORR, only peptides have been used as bio-templates to construct NMs. These peptides can be either synthetic peptides or purified from natural sources.

1.3.1.1 Monometallic Pt NMs

It is known that ORR activity of Pt nanostructures strongly depends on the size, morphology and surface crystalline features. Theoretical and experimental findings have shown that Pt NPs with 2.2 nm in size have the optimal binding affinity to oxygen species, making the reactive sites less blocked by adsorbed intermediates (such as OH*) and thus increase the ORR mass activity.[180] In particular, oxygen binding on Pt (111) is weaker than on other Pt facets. Synthesizing Pt NPs with smaller size and exclusively (111) facets would thus be very helpful to understand the structure-property relationship and improve catalytic activity toward ORR. Wang et al.[46] developed a method to prepare 2 nm Pt NPs with predominantly (111) facets (Figure 1.13a-b), in which Pt precursors were incubated with $A\beta_{16-20}$ peptide solution and then reduced to Pt NPs by glow discharge (a cold plasma phenomenon with highly energetic electrons, that can produce mainly (111) facets[181]). The Pt NPs-peptide was then loaded on carbon support (denoted as Pt-P/C). Peptide $A\beta_{16-20}$ was chosen as the additive, as Pt (111) can be effectively exposed on the phenyl ring of phenylalanine. The authors claimed that the combination of electron reduction by glow discharge and peptide assistance is the reason for the exclusive (111) facet formation, as well as both the control of NP size to 2 nm and effective particle dispersion.[46] Numerous $-NH_2$ groups from the peptide can further improve the hydrophilic property of the material, which could enhance adsorption of dissolved O_2 in water.[182] In addition, the binding energy between Pt and C atoms can be increased in the presence of N atoms existing on the carbon support, thus stabilizing the formed Pt NPs.[183] Besides, the authors claimed that the peptide in Pt-peptide structure is electron-sensitive and has a high conductivity, which may come from the π-π stacking between the aromatic rings.[46] OH and COOH on the peptide groups may also contribute to enhanced electron transfer. ORR LSV results showed that Pt-P/C was much better than that of commercial Pt/C catalyst in terms of mass activity (Figure 1.13c) and specific activity (Figure 1.13d). Although the Pt-P/C experienced greater activity loss than the Pt/C after durability tests for 10000 cycles, its mass activity was still higher than the latter one, demonstrating an enhanced oxygen reduction capability.[46]

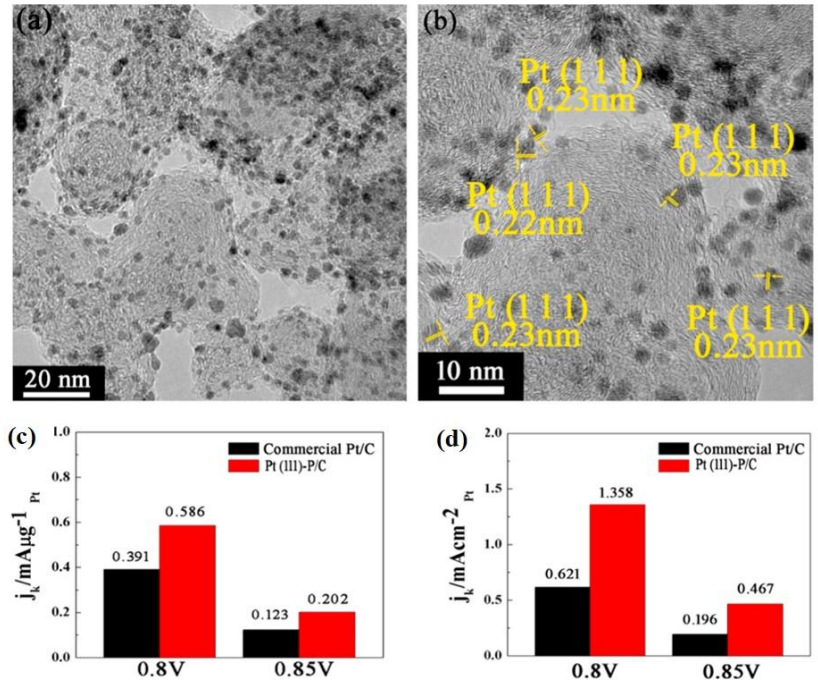

Figure 1.13: (a-b) TEM images of Pt(111)-Pt/C catalyst; (c) Mass activity and (d) Specific activity at 0.8 V and 0.85 V vs. RHE. Reprinted with permission from ref 46. Copyright 2016 Elsevier.

Another peptide, peptide BP7A, was also demonstrated by Huang's group to be a good template for the synthesis of twinned Pt NPs.[184] They further exploited this observation,160 and reported the successful preparation of ultrathin 1D Pt multiple-twinned nanowire networks (MTNN) (Figure 1.14A-B) on the peptide and compared it to the commercial Pt/C for ORR. It was found that Pt MTNN showed higher ECSA than Pt/C (Figure 1.14C). For ORR in acidic conditions (O_2 saturated 0.1 M $HClO_4$), the two materials gave similar onset potentials, but Pt MTNN exhibited higher mass activity (0.144 mA/μg vs. 0.091 mA/μg) and specific activity (0.139 mA/cm^2 vs. 0.116 mA/cm^2) at 0.9V (vs. RHE) (Figure 1.14D). More importantly, accelerated durability test (ADT) results (Figure 1.14E, F) showed that Pt MTNN had an ECSA loss of 14.2% after cycling for 6000 cycles, which was much more stable than Pt/C (56.7% loss of ECSA). It was suggested that the enhanced stability of the NWs likely originates from its unique structure. Compared to zero-dimensional (0D) counterparts, the ultrathin 1D NW could experience slower ripening and dissolution process because of the structural anisotropy. In addition, atomic migration can also be prevented in nanotwins to some extent.[185] The abundant twin defects in Pt MTNN are the result of

enhanced lattice-mismatched attachment during nanowire growth, which is possibly due to the stabilization of twin sites provided by the BP7A peptide molecule.[160]

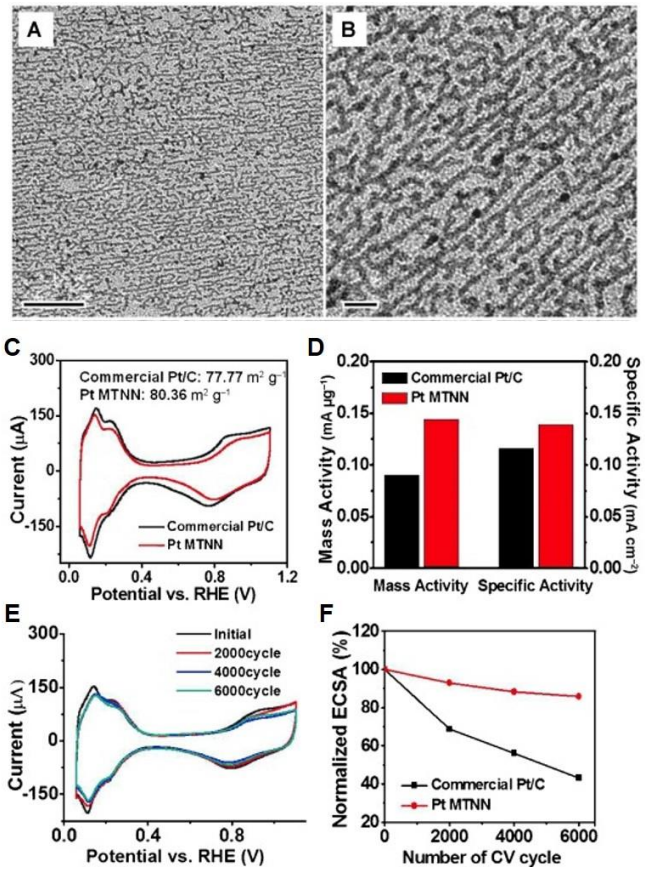

Figure 1.14: (A) Low and (B) high magnification TEM images of Pt MTNN; (C) CV curves of Pt MTNN and commercial JM Pt/C catalysts in a deoxygenated 0.1 M $HClO_4$ solution at a scan rate of 50 mV s^{-1}; (D) Corresponding mass activities and specific activities at 0.9 V of JM Pt/C and Pt MTNN, respectively; (E) CV curves of Pt MTNN before and after an accelerated durability test at room temperature in O_2-saturated 0.1 M $HClO_4$ solution with cyclic potentials sweeping between 0.6 and 1.1 V at a sweep rate of 50 mV s^{-1}; (F) Loss of ECSA of JM Pt/C and Pt MTNN as a function of the cycling number. Reprinted with permission from ref 185. Copyright 2013 WILEY Publishing.

Besides the in situ growth of Pt nanostructures on peptides, Pt-peptide hybrids can also be constructed through immobilization of pre-synthesized NPs on peptides. In a report by Zhou et al.,[162] citrate-capped Pt NPs (negatively charged) were deposited on AFP peptide (positively charged) via electrostatic interaction. The AFP peptide is able to self-assemble into amyloid-like fibrils, which can drive the formation of a Pt-AFP nanocomposite with Pt NPs evenly distributed

along the fibril structure (Figure 1.15a). ORR tests in air-saturated H_2SO_4 showed that the peak for catalytic reduction current occurred at more positive potential with a Pt-AFP fibril modified electrode than with Pt NPs modified and bulk Pt electrodes.[162] Based on this work, Bandak et al.[161]

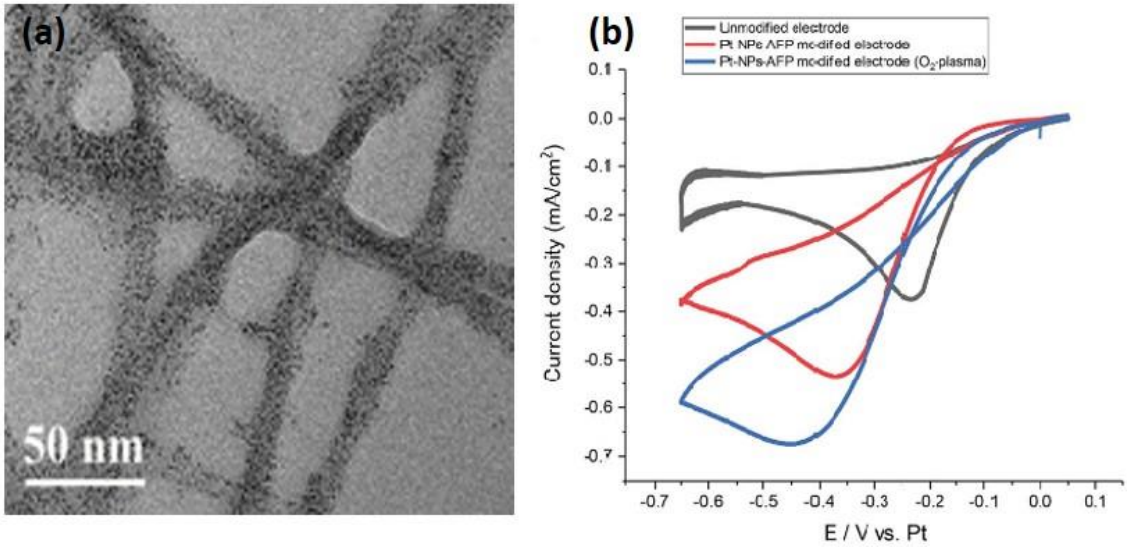

Figure 1.15: (a) TEM image of Pt-AFP fibrils; (b) Cyclic voltammograms of oxygen reduction at the unmodified electrode (black line) Pt-NPs-AFP modified electrode (red line) and O_2-plasma treated Pt-NPs-AFP modified electrode (blue line). (a) was reprinted with permission from ref 162. Copyright 2013 Royal Society of Chemistry. (b) was reprinted with permission from ref 161. Copyright 2019 Royal Society of Chemistry.

used O_2-plasma to remove the peptide and the organic stabilizer to further investigate the effect of the capping agent and the peptide on the catalytic performance of the hybrid system, resulting in an interconnected Pt nanonetwork. The material showed slightly higher ORR current density compared to the one without O_2-plasma treatment (Figure 1.15b), suggesting that the capping agent and peptide may block some reaction sites. However, the durability of the material needs to be tested to demonstrate the utility of this method, since removing the peptide support may lead to particle aggregation after extended operation.

In another work, a laser ablation method was used to synthesize surfactant-free Pt NPs 6 nm in size, which were then mixed with a β-sheet peptide.[163] The resulting material displayed sheet-like morphology with Pt NPs well dispersed on the peptide due to the rich distribution of amino groups on the peptide chains (Figure 1.16a-c). Unlike the previously described materials that use

electrostatic interactions to construct the Pt-peptide system, this material is abundant in Pt-N bonds, as confirmed by XPS results. For ORR in O_2-saturated KNO_3 solution, it was found that the onset potential and current density were well correlated with Pt content (Figure 1.16d), indicating that Pt-N moiety is essential for higher ORR activity.[163] The optimized $PtNP_{12.5}$/βP displayed slightly better onset and half-wave potential compared to commercial Pt/C. In addition, kinetics studies (Tafel slope and exchange current density) also indicated its higher reaction activity. The mass activity value was more than 25 times higher than the previously mentioned citrate-stabilized PtNP/peptide hybrid system.[162] The authors claimed this was possibly due to better O_2 access to the surfactant free Pt NPs. The interaction between amine and Pt was thought to be an important reason for the enhanced electrocatalytic performance, as material with higher percentage of Pt-N moieties showed decreased overpotential towards ORR. After a stability test of 1000 cycles, the material maintained 89% of its initial mass activity, which needs further improvement.

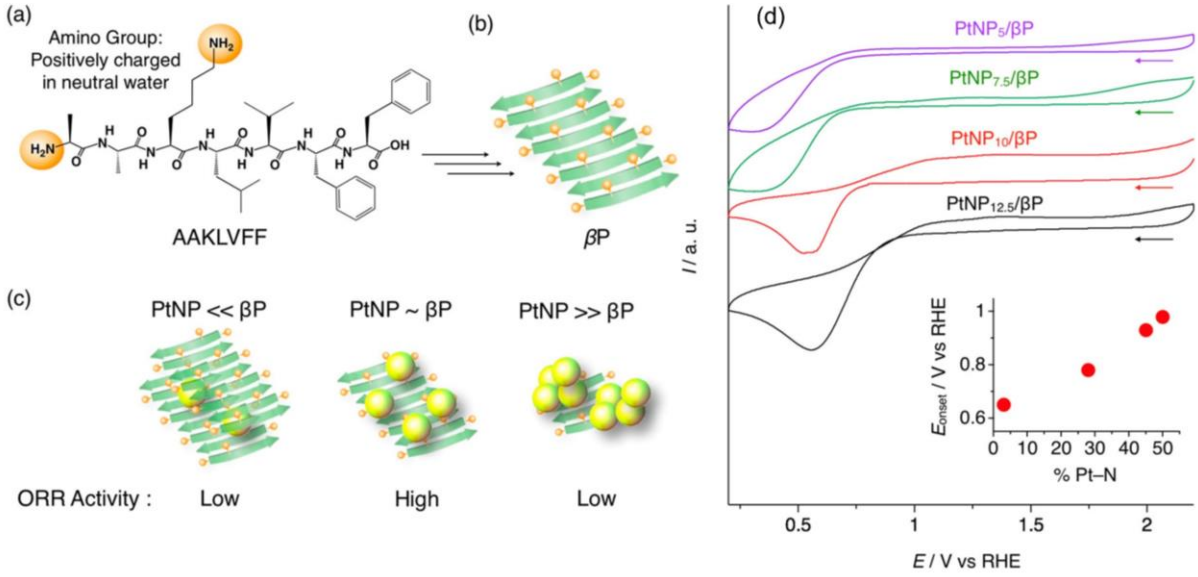

Figure 1.16: (a) A schematic description of the molecular structure of the NH_2-AAKLVFF-COOH peptide; (b) Schematic illustration of the self-assembled β-sheet peptide (βP); (c) Schematic representations of PtNP/βP hybrids with low (left), middle (center), and high (right) PtNP contents; (d) CV profiles of PtNP5/βP, PtNP7.5/βP, PtNP10/βP, and PtNP12.5/βP on a glassy carbon electrode in O_2-saturated 1 M KNO_3 solution at a scan rate of 0.1 V s^{-1}. Inset: Plot of E_{onset} versus the percentage of Pt–N. Reprinted from ref 163. Copyright 2019 American Chemical Society.

One important factor that determines the final MNM structure and the corresponding catalytic behavior is the metal-to-peptide ratio. A study using R5 peptide for fabricating MNMs demonstrated that differently shaped Au and Pt NMs could be synthesized by tuning the metal-to-peptide ratio.[164] Spherical NPs were obtained for both Au and Pt with lower metal-to-peptide ratios, while higher ratios led to the formation of nanoribbons and/or networked nanochains. ORR results suggested that R5-Au-90 networked chains and R5-Pt-90 nanoribbons were the optimized compositions in their own series, as manifested by onset potential and specific activity. Their enhanced activities were explained by the higher ECSA values of the network chains compared to the spherical particles formed with lower metal loadings, and aggregated particles with too high metal ratios.[164]

1.3.1.2 Pt-based bimetallic NMs

One efficient approach to engineer MNMs as electrocatalysts is thorough constructing a bimetallic platform, which integrates the physicochemical properties of the two metals and can reduce the loading amount of the metal of higher cost.[186] In bimetallic systems, the introduction of a second metal generally gives a number of new effects:[187] 1) different Fermi levels of the two metals can lead to charge transfer and alter the electronic properties of the material,[188,189] 2) the intimate interactions between the two components may affect the final size, shape and spatial arrangement of surface atoms,[190] which will further impact the catalyst performance. One good example of bimetallic catalysts is AuPt NMs, which have been discovered to be effective electrocatalysts in a series of applications such as ORR,[191–193] HER[194–196] and MOR.[197–199] However, precise control of the surface properties in such systems still presents a large challenge in bimetallic nanostructures. In pursuit of this goal, different bio-templates such as peptide[69,72] and virus[67] have been explored to serve as potential supports to construct AuPt with well-defined morphology under mild synthetic conditions.

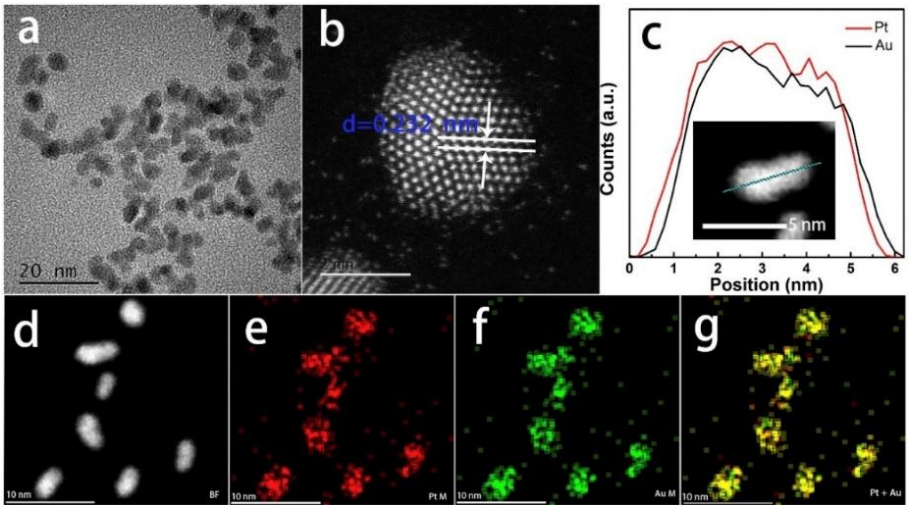

Figure 1.17: (a) Representative TEM image and (b) HR-TEM image of the $Au_{33}Pt_{67}$ sample; (c) Cross-sectional compositional line-scan profiles of a single $Au_{33}Pt_{67}$ NP (inset: HAADF-STEM image); (d) Dark field-TEM image of the $Au_{33}Pt_{67}$ sample and EDS elemental mapping of (e) Pt, (f) Au and (g) Pt plus Au elements in the NPs. Reprinted with permission from ref 72. Copyright 2018 Elsevier.

Wu et al.[72] used Z peptide as a template to prepare peanut shaped $Au_{33}Pt_{67}$ alloy nanoparticles (spherical particles with other Au-to-Pt ratios). Au and Pt had a homogenous elemental distribution in the synthesized alloy, as confirmed by HR-TEM and EDS (Figure 1.17). Different Au-Pt alloy ratios were tested for ORR (Figure 1.18), and it was found that the reaction activity of the alloy varied with content ratio, but all measured alloy ratios showed comparable or more positive onset potential compared to Pt/C. In addition, the alloy with best ratio ($Au_{33}Pt_{67}$) exhibited higher stability than Pt/C in ADT and long time chronoamperometry tests in both alkaline and acidic media, demonstrating the effectiveness of this peptide method in improving performance. The enhanced reaction activity and stability may be attributed to the alloying effects and the peptide template.[72] For the alloy effect, introducing a second metal can lead to formation of hetero-atom bond and generate new catalytic active site.[186] In addition, under alkaline conditions the presence of Au could reduce the strength of the formation of Pt-OH and thus provided more sites for O_2 adsorption.[200] Furthermore, the peptide support can prevent the metal-metal aggregation and/or coalescence between the NPs, which improves the stability of the catalyst.[201]

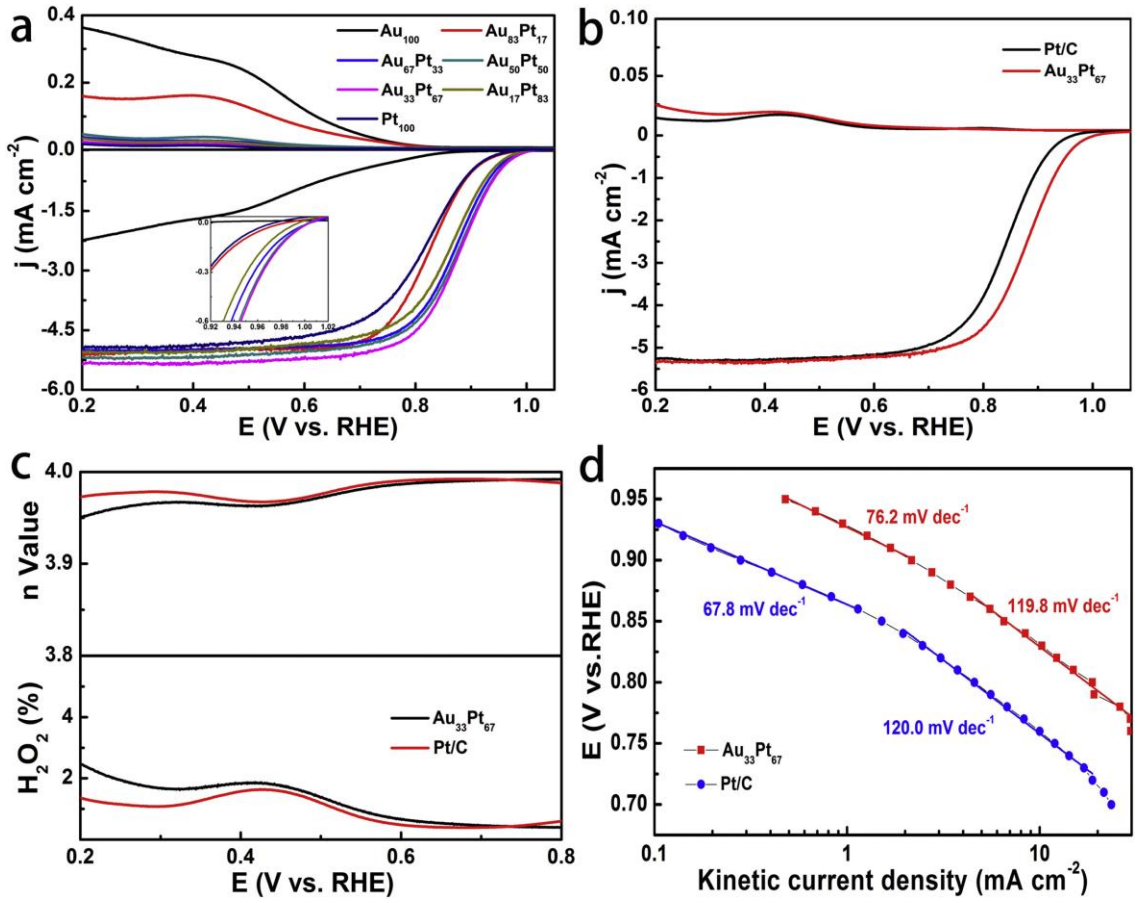

Figure 1.18: (a) RRDE voltammograms of a glassy carbon electrode of the AuPt alloyed NPs in O_2-saturated 0.1 M KOH solution (inset is the amplified graph with the potential ranging from 0.92 V to 1.02 V). Potential scan rate is 10 mV s^{-1} and the rotation rate is 1600 rpm; (b) RRDE voltammograms; (c) Plots of H_2O_2 yield and electron transfer numbers and (d) the corresponding Tafel plots of the $Au_{33}Pt_{67}$ sample and Pt/C catalyst. Reprinted with permission from ref 72. Copyright 2018 Elsevier.

One newly developed method for peptide mediated MNM synthesis is using programmable peptides. This rational approach enables precise manipulation on the geometric position of NPs instead of relying on random distribution, which can promote electrocatalytic performance towards ORR. In the report mentioned previously in section 2.1,[69] HexCoil-Ala (HC) peptides were programmed to assemble into an antiparallel hexameric bundle along a single-wall carbon nanotube (SWNT). As a model system, a fibrous AuPt alloy (Figure 1.19a-c) with different NP sizes was assembled on the HC/SWNT hybrids by incubating the two corresponding precursors with the peptide/SWNT suspension then followed by reduction with $NaBH_4$. It was expected from

the simulated model that the specific activity would not change upon reaching the NP size where coalescence is predicted to occur. The experimental ORR activity agrees with the theoretical predictions (Figure 1.19d), with the diffusion-limited current increasing as NP size grew from 1.6 to 2.4 nm (in diameter), then decreasing for larger NP size, which was due to NP coalescence.[69] The AuPt displayed higher activity than Pt/C, which was due to the synergistic effect of the bimetallic system.

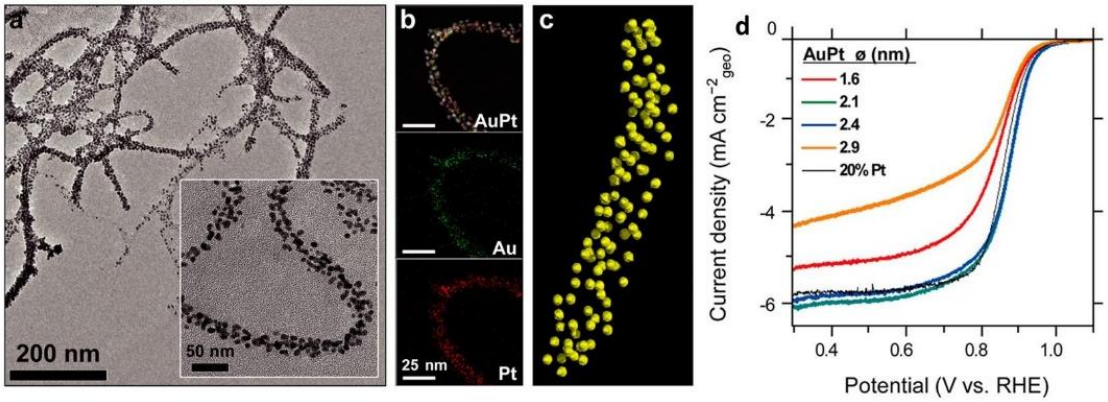

Figure 1.19. (a) TEM and HR-TEM and (b) STEM-EDS mapping of one modeled AuPt/HC/SWNT; (c) 3D reconstructed model of rendered tomographic volume through electron tomography; (d) ORR polarization curves of the (8,26)-catalysts with different particle sizes and a commercial Pt/C catalyst on a rotating disk electrode in an O_2-saturated 0.1 M KOH solution at a sweep rate of 10 mV s^{-1} and a rotation rate of 1600 rpm. Reprinted with permission from ref 69. Copyright 2018 American Chemical Society.

1.3.1.3 Non-Pt based bimetallic NMs

Although Pt-based materials are regarded as state-of-art catalysts for ORR, the limited earth abundance of Pt, its high cost and the poisoning of the catalyst by carbon monoxide make it challenging to realize large scale commercialization of PEMFCs. Developing cost effective electrocatalysts with outstanding activity and stability to reduce our dependence on Pt is thus an active area of research. Wang et al.[68] took the advantage of AuAg bimetallic system for ORR application. Through a phage display technique,[202,203] an A4 peptide with strong binding for Ag was selected to stabilize an AgAu intercrossed nanoparticle network. Similar to the previously described experiments with PtAu alloys, AgAu materials with different metal-to-peptide ratios and Au-to-Ag ratios resulted in different onset potentials and diffusion-limited current densities

(Figure 1.20). The optimized composition (Au:Ag:A4 = 10:30:1) exhibited a larger diffusion limited current density and remarkably higher durability when compared to Pt/C.[68]

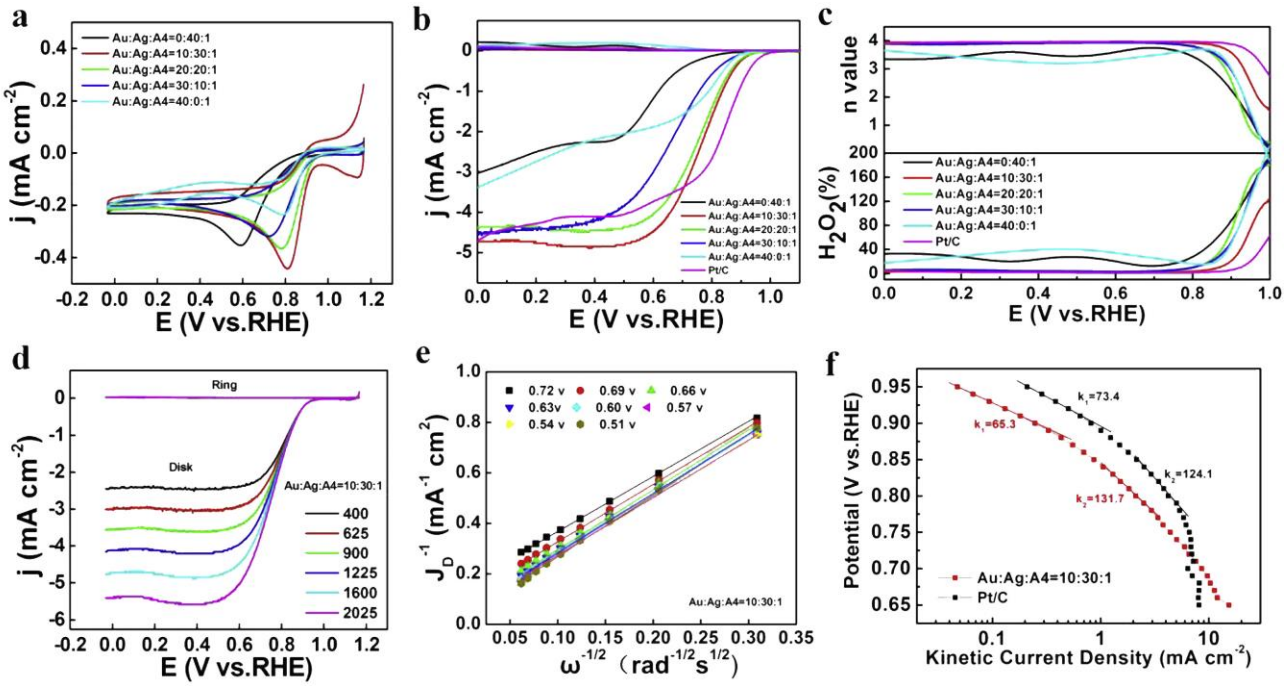

Figure 1.20: The electrochemical performance of the glassy carbon electrode (GCE) modified with the samples of different Au-to-Ag ratio and same metal-to-peptide ratio (40:1) and Pt/C in O_2-saturated 0.1 M KOH solution: (a) Cyclic and (b) rotating disk electrode (RDE) voltammograms at a rotation speed of 1600 rpm with 10 mV/s potential sweep rate; (c) Plots of number of electron transfer and H_2O_2 (%) yield; (d) Voltammetric current of Au:Ag:A4 = 10:30:1 at the rotation rate of 400–2025 rpm with 10 mV/s potential sweep rate; (e) Corresponding Koutecky–Levich plots of Au:Ag:A4 = 10:30:1 catalyst at different potentials; (f)The corresponding Tafel plots of Au:Ag:A4 = 10:30:1 and commercial Pt/C. All measurements were conducted with a catalyst loading of 80.8 μg cm^{-2} in an O_2-saturated 0.1 M KOH aqueous solution at a potential scan rate of 10 mV s^{-1}. Reprinted with permission from ref 68. Copyright 2017 Elsevier.

In addition to alloy particles with homogeneous metal distribution, core-shell nanostructures are another form of bimetallic materials, which often display enhanced electrocatalytic performance due to lattice strain between the core and shell region and the synergistic effect of the two metals.[73] One classical way to make Au@Pd core-shell NPs is to first prepare Au@Ag in organic solvent, then add Pd precursor to displace the sacrificial Ag shell.[204,205] To make the synthetic process less sophisticated and energy consuming, Zong et al.[73] introduced a FlgA3 peptide template for

$Au@Pd_x$ (x is the molar ratio of Pd-to-Au) formation. The synthesis eliminated the requirements of sacrificial reagent and organic solvent. While the A3 domain of the peptide can stabilize the Au surface and form Au NPs, the Flg domain binds to Pd. TEM results suggested that the nanoparticle core consisted of a large Au particle (~50 nm in diameter) with several much smaller Pd particles (7-8 nm) surrounding it (Figure 1.21a-b). Cyclic voltammetry tests showed that with increasing Pd content, the ORR activity first increased then decreased, which peaked at $Au@Pd_{1.0}$. LSV (linear sweep voltammetry) curves obtained from RRDE (rotating ring disk electrode) measurements also demonstrated that the half-wave potentials and diffusion-limited current densities both varied dramatically with different Pd-to-Au ratios, with $Au@Pd_{1.0}$ giving comparable values to Pt/C in alkaline condition (Figure 1.21c). For core-shell structures, the shell thickness plays an important role in tuning the core metal surface electronic property and thus affect the material electrocatalytic activity.[206,207] In this study, relatively higher Pd content would form more Pd NPs on Au surface and showed enhanced catalytic activity.[73] However, further increase of Pd resulted in particle coalescence and aggregation, which blocked some electrocatalytically active sites and decreased the ORR performance.[73] In addition, chronoamperometric and long-term stability tests suggested $Au@Pd_{1.0}$ had superior stability than Pt/C and Pd/C. The excellent ORR performance from $Au@Pd_{1.0}$ compared to some other AuPd bimetallic catalysts has been attributed to lattice strain induced by the well-defined core-shell

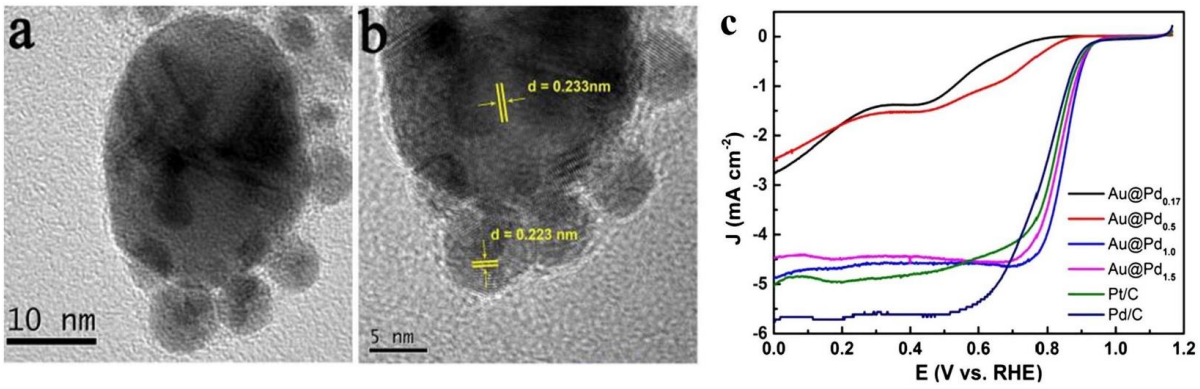

Figure 1.21: (a) TEM image of the $Au@Pd_{1.0}$ sample; (b) HR-TEM image; (c) LSV curves of $Au@Pd_{0.17}$, $Au@Pd_{1.0}$, $Au@Pd_{1.5}$, Pt/C and Pd/C in an O_2-saturated 0.1 M KOH solution at a sweep rate of 10 mV/s and electrode rotation speed of 1600 rpm. Reprinted with permission from ref 73. Copyright 2018 Elsevier.

structure, which was caused by lattice mismatch between the core Au NP and shell Pd NP as observed by HR-TEM.[73] This strain in crystal lattice led to the shift in the d-band center, which could affect the molecule-adsorption and thus altering the catalytic activity.[208,209]

1.3.2 Oxygen Evolution Reaction (OER)

Hydrogen is one of the most environmentally friendly energy carriers. Water electrolysis driven by green electricity is potentially a sustainable and promising method to produce hydrogen compared to the reforming of fossil fuels, which emits the green house gas CO_2. However, water electrolysis currently represents only ~4% of current hydrogen production due to its high cost.[174] To make water electrolysis economically viable, researchers must develop cost-effective electrocatalysts that can replace noble metals while retaining excellent catalytic performance. For the water splitting reaction in an electrochemical cell, compared to HER on the cathode, the other half reaction OER on the anode involves a more complex four-electron/four-proton mechanism, leading to high energy barrier and poor reaction kinetics.[210] Therefore, efficient and stable OER catalysts are desired to reach excellent overall efficiency for water splitting.

For economic purposes, nonprecious metal-based oxides such as Co-based materials have been used as attractive alternatives to replace Ir and Ru for OER in recent years.[211,212] Attempts have also been made to utilize bio-templates for constructing nanosized cobalt oxides and hydroxides. For instance, in work by Rho et al.,[165] catechol groups and triglutamates were introduced onto the major coat proteins to form a DOPA(3,4-dihydroxy-L-Phenylalanine)-phage. The catechol group is known for strong interactions with various kinds of inorganic materials such as Au, Ag, FePt.[213,214] Amorphous $Co(OH)_2$ was adhered to the phage through electroless deposition, resulting in one-dimensional entangled wires along the long axis of the virus particles.[165] Characterization by cyclic voltammetry showed that $Co(OH)_2$ on the DOPA-phages can be electrochemically oxidized to CoOOH and then further to CoO_2 during the water oxidation reaction. Compared to Ed-Co (electrodeposited cobalt oxide based oxygen evolution catalyst), the Co/DOPA-phage showed improved stability and slight catalytic enhancement in the low overpotential region. The authors attributed the improved performance to assistance from the catechol group, which might be able to stabilize Co^{2+} and lower the thermodynamic potential of the proton-coupled electron-transfer pre-equilibrium.[215] The OER performance of this new material may be further improved

through optimizing the organization of the catechol group pattern, as well as the material conductivity.

In another study by Schenk et al.,[166] cobalt carbonate was first precipitated on the surface of a tobacco mosaic virus (TMV) bio-template via ammonium carbonate decomposition and diffusion (Figure 1.22a). The mineral product was then calcinated at 400 °C to form spinel-type Co_3O_4 arranged in rod-like superstructures around TMV, with the virus gross morphology remaining intact (Figure 1.22b). The OER performance of the material was compared to commercially available Co_3O_4 powder and Co_3O_4 synthesized using same procedure except without the TMV template.[166] Cyclic voltammetry results showed that compared to the other two materials, the virus directed Co_3O_4 exhibited smaller overpotential to reach 10 mA/cm^2, which demonstrated the critical role of the catalyst surface structure (Figure 1.22c). The tubular structure of TMV-Co_3O_4 has a high surface area, which enhances the transport process between the reactants and gaseous products. It is also possible that TMV affects the morphology of the individual Co_3O_4 nanograins formed after calcination, forming a high density of catalytic centers on the surface, which lowers the activation energy for the reaction.

1.3.3 Hydrogen Evolution Reaction (HER)

HER is known to be drastically affected by a change of pH from acidic to alkaline conditions.[216] For the market-driven purpose in industry, alkaline media holds the advantage of less corrosive environment and safety concerns compared to highly acidic conditions. Although there has been much progress in developing materials that are comparable to platinum benchmark in performance, they typically showed 2~3 times lower activity in alkaline conditions than in acidic conditions due to mechanistic changes that are not fully elucidated.[59,217] Alkaline electrolytes have fewer available protons, which makes water dissociative adsorption the dominating step in HER.[218] Some reports demonstrated that bimetallic systems comprised of Pt and oxophilic materials such as metal hydroxides are promising in improving alkaline HER.[219,220] One example is Pt-Ni$(OH)_2$, which combines the advantage of strong affinity to water adsorption from Ni$(OH)_2$ with the high HER activity from Pt. As mentioned in section 2.4, the M13 phage clone templated, binder-free Pt-Ni$(OH)_2$ nanonetworks were successfully applied to HER (Figure 1.23).[59] In HER tests, the templated Pt-Ni$(OH)_2$ with an optimized Pt loading (40.8 ± 10.4 μg_{pt} cm^{-2}_{geo}) showed nearly an

order of magnitude higher current density than most reported Pt-Ni(OH)$_2$ systems with similar Pt loading. In addition, its mass activity is the highest reported Pt mass activity to date in 1M KOH. The current density, mass activity, TOF (turnover frequency) value and electrocatalytic stability all demonstrated that the Pt-Ni(OH)$_2$ nanonetwork is a highly efficient catalyst in alkaline HER. Its performance was attributed to enhanced Pt dispersion on the high surface area Ni(OH)$_2$ framework. In addition, the nanostructure may also experience morphology changes due to interactions with the coat protein, contributing to improved catalytic activity.[59]

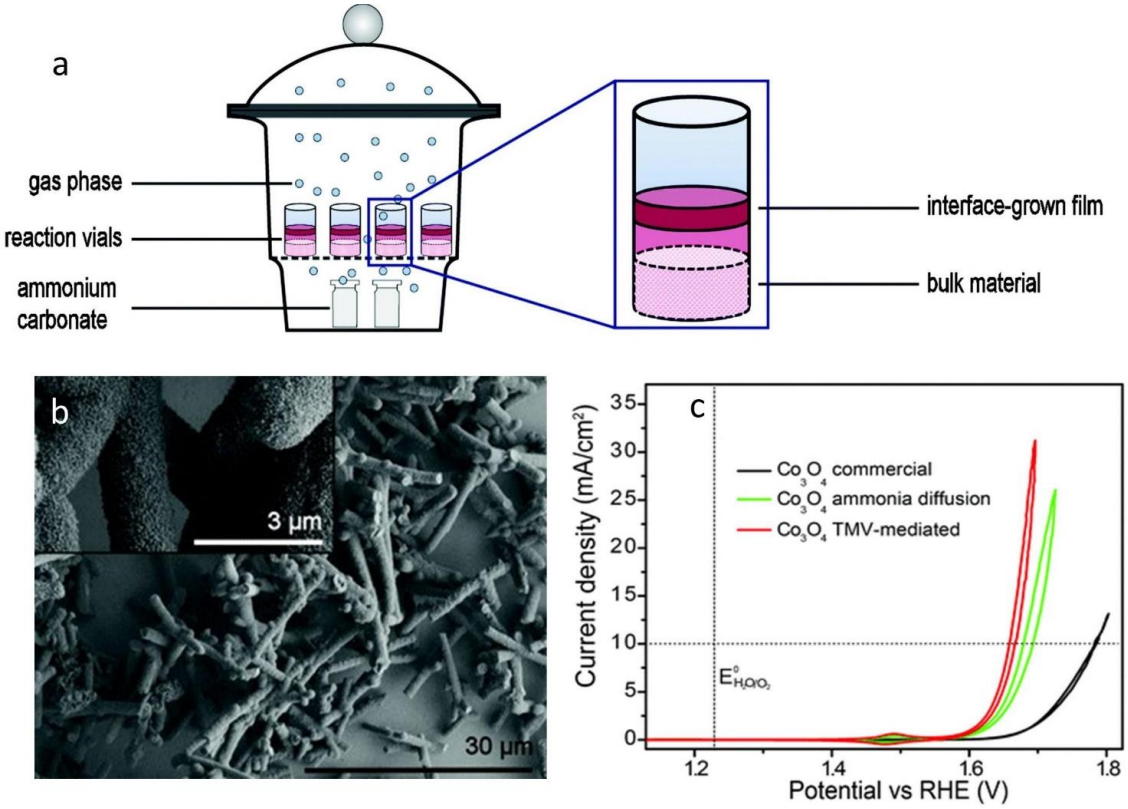

Figure 1.22: (a) Schematic illustration of the experimental setup highlighting the origin of bulk and interface materials within the reaction vial; (b) SEM images of Co_3O_4 mineral rods and tubes formed by annealing the TMV/mineral precursor (400 °C, 2 hours), showing the preservation of the overall morphology. Inset: Higher magnification image of the surface structure; (c) OER performance of cobalt oxide materials with different morphologies. Cyclic voltammograms (I/E-curves) are presented for a commercial Co_3O_4 nanopowder (black curve), Co_3O_4 prepared by ammonia diffusion in the absence of additives (green curve) and TMV-directed Co_3O_4 (red curve). Data were recorded in 0.1 M NaOH electrolyte at a scan rate of 10 mV s^{-1} at 2000 rpm. The vertical dashed line indicates the position of E° (H_2O/O_2) and the horizontal dashed line marks the current density of 10 mA cm^{-2}, at which the overpotentials η = 10 mA cm^{-2} were determined. Reproduced from with permission from ref 166. Copyright 2017 Royal Society of Chemistry.

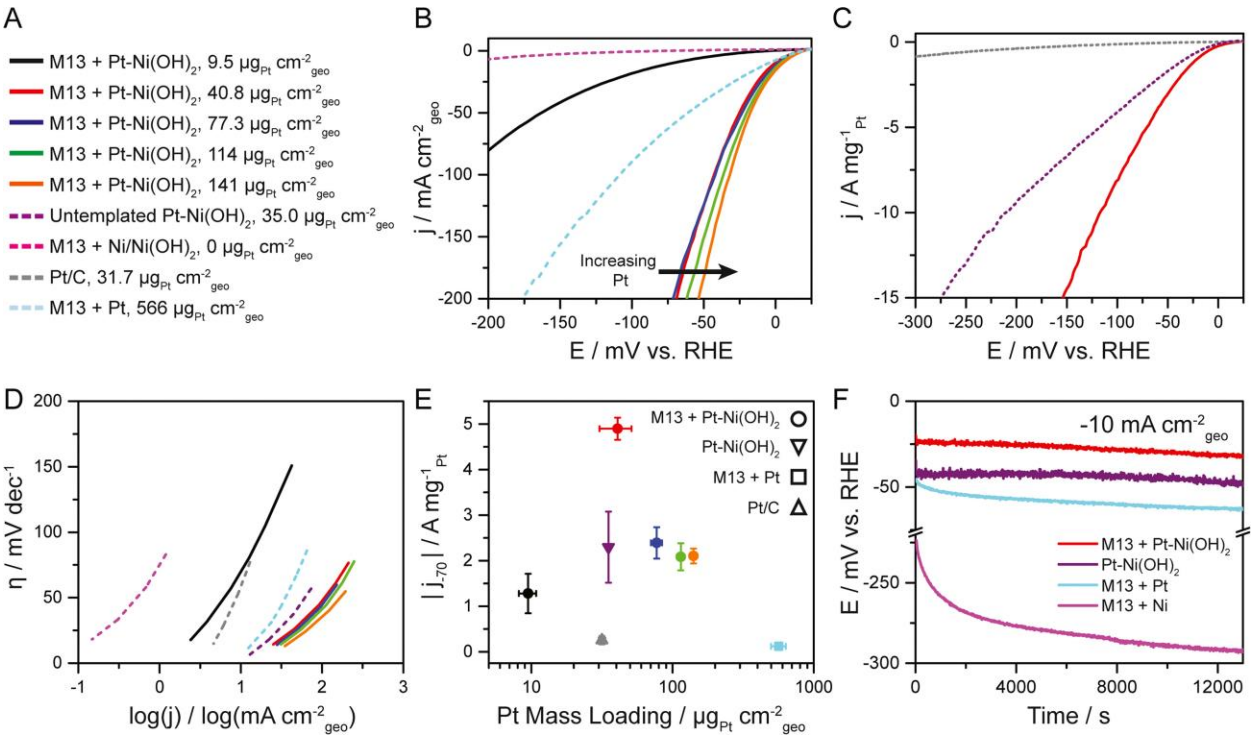

Figure 1.23: (a) Legend entries for tested samples in (b)–(d); (b) CV scans at comparing Ni and Pt nanonetworks with Pt–Ni(OH)$_2$ nanonetworks at several platinum loadings; (c) Mass-normalized CV scans comparing Pt–Ni(OH)$_2$ nanonetworks to Pt/C and untemplated Pt–Ni(OH)$_2$ controls; (d) Tafel plots at several platinum loadings; (e) Mass activity benchmarks at −70 mV vs. RHE; (f) Galvanostatic stability of Pt–Ni(OH)$_2$ nanonetworks with the optimal platinum loading versus untemplated Pt–Ni(OH)$_2$, Pt nanonetwork, and Ni nanonetwork controls at a current density of -10 mA cm^{-2}geo. Reprinted with permission from ref 59. Copyright 2019 Elsevier.

Besides virus, peptides are another facile template class for constructing bimetallic nanosystems for HER application. AuPt alloy on Z1 peptide and Au@Pd core-shell on FLA3 peptide are not only excellent catalysts for ORR as discussed in the previous section (section 1.3.1),[72,73] but they also demonstrated high activity towards HER. For the bimetallic AuPt on Z1 peptide, different Au-to-Pt ratios were tested in both acid and alkaline electrolytes. In both cases, $Au_{33}Pt_{67}$ displayed the best HER activity among the series, as indicated by the smallest overpotentials. While the activity of $Au_{33}Pt_{67}$ is close to the Pt/C, it possessed higher stability in both acid and alkaline conditions. The enhanced durability was attributed to the alloying effect and the peptide template.[72]

1.3.4 Methanol/Ethanol Oxidation Reaction (MOR/EOR)

Direct alcohol fuel cells (DAFCs) are power sources characterized of low operating temperature, easy storage and high energy density when compared to hydrogen fuel cells.[221] They work by oxidizing various alcohols (eg. methanol, ethanol, and glycerol) to CO_2 (MOR: $CH_3OH + H_2O \rightarrow CO_2 + 6H^+ + 6e^-$) on the anode with the protons diffusing to the cathode to react with O_2 to form H_2O. However, despite their potential advantages, DAFCs generally have slow kinetics.[222] In addition, various intermediates such as CO, aldehyde could be strongly adsorbed on the electrode surface and poison the active sites of the Pt catalyst.[223] It is thus vital to develop materials with fast kinetics and high durability. In the available literature, peptides, proteins and viruses are all found to function as excellent supports for MNMs (mainly noble-metal Pt and Pd-based catalysts) with applications in DAFCs.

1.3.4.1 Peptides as templates

Peptides are good supports for synthesizing metallic nanostructures that are active for methanol oxidation. In a report by Bedford et al.,[167] a Pd4 peptide that binds strongly to palladium, an AuBP1 peptide that binds strongly to gold, and an H1 peptide that contains anchoring motifs from the N-terminal half of AuBP1 and the C-terminal half of Pd4 were all employed to synthesize AuPd alloy NPs with different Au-to-Pd molar ratios. The NPs were then analyzed by XAFS (X-ray absorption fine-structure spectroscopy), PDF (pair distribution function) and computational modelling. The detailed XAFS and PDF analysis revealed PdAu phase separation in the peptide-capped alloy particle, which was significantly affected by the peptide used. In addition, the capping peptide could directly influence bimetallic miscibility and final atomic-scale structural differences, which means that the peptides could be used to regulate surface disorder and surface composition.[167] As shown in the RMC (reverse Monte Carlo) simulated models (Figure 1.24A-I), different peptide templates led to different surface compositions. Take a PdAu NP at 3:1 (Pd:Au) ratio as an example, the NP capped by peptide AuBP-1 displayed a larger fraction of surface Au atoms compared to the other two peptides, which was due to higher affinity of AuBP-1 to gold.[167]

This property further affected the electrocatalytic activity of PdAu NPs as demonstrated by MOR (Figure 1.24J-L). For MOR, the PdAu (3:1) alloy capped by Pd4 exhibited substantially improved activity compared to the ones capped by AuBP1 and H1, suggesting that the peptide sequence

plays a key role in determining the NP electrocatalytic performance.[167] The biotic/abiotic interface of the peptide can affect the PdAu surface composition/structure, with Pd4 more effectively resisting an undesirable amount of Au surface migration that would reduce catalytic activity. In addition, the capping peptide orientation on the NP may also partially block active surface sites and prevent methanol oxidation.[167]

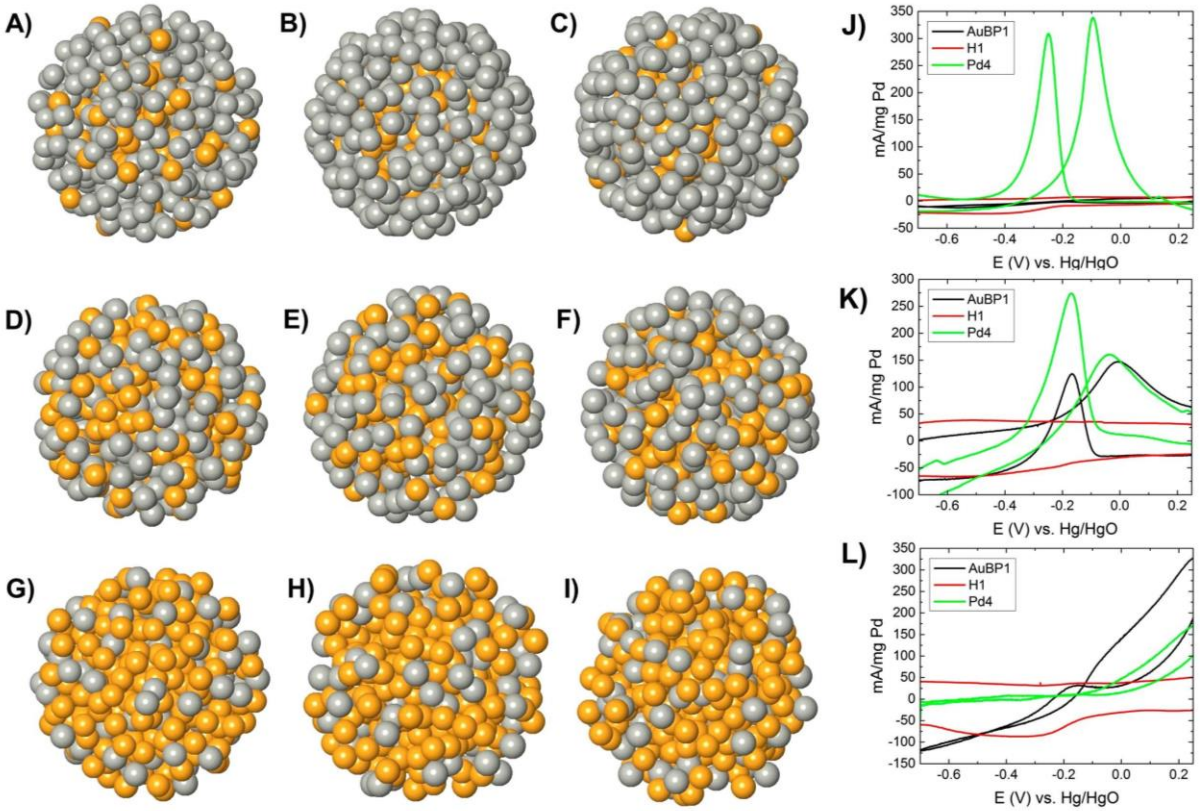

Figure 1.24: Bimetallic nanoparticle configurations generated from RMC simulations of atomic PDFs for (A) AuBP1, 3:1 Pd:Au; (B) H1, 3:1 Pd:Au; (C) Pd4, 3:1 Pd:Au; (D) AuBP1, 1:1 Pd:Au; (E) H1, 1:1 Pd:Au; (F) Pd4, 1:1 Pd:Au; (G) AuBP1, 1:3 Pd:Au; (H) H1, 1:3 Pd:Au; and (I) Pd4, 1:3 Pd:Au; Background subtracted CVs of peptide-caped PdAu bimetallic nanoparticles in 1.0 M NaOH, 1.0 M MeOH at 20 mV/s for (J) 3:1 Pd:Au; (K) 1:1 Pd:Au; and (L) 1:3 Pd:Au. Reprinted with permission from ref 167. Copyright 2016 American Chemical Society.

1.3.4.2 Proteins as templates

In two reports by Gao's group,[169,170] insulin amyloid fibrils (INSAFs) were successfully employed as sacrificial templates for the fabrication of ultrathin Pt nanowires and vine-tree-like PtRh bimeta-

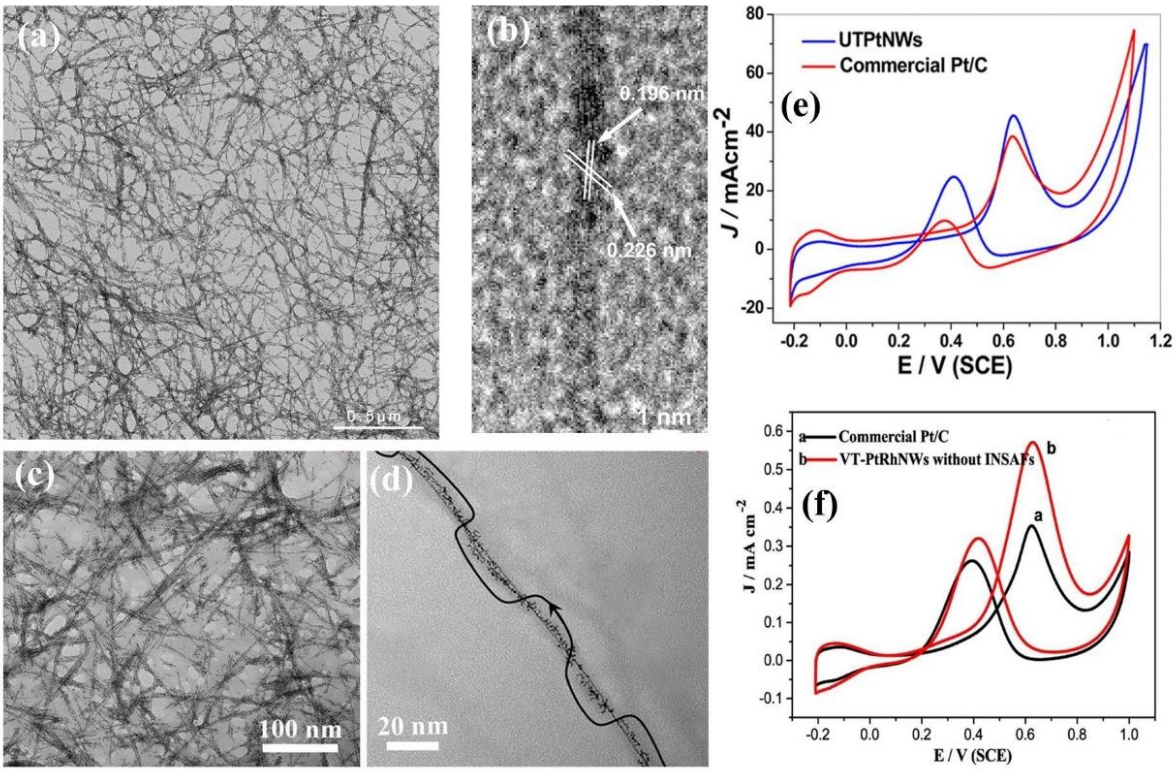

Figure 1.25: (a) TEM image of UTPt NWs; (b) HR-TEM image of a single Pt nanowire; (c) Low magnification TEM image of VT-PtRh NWs; (d) TEM image of a single VT-PtRh nanowire; (e) CVs of UTPt NWs and a commercial Pt/C catalyst in a mixture of 0.5 M H_2SO_4 and 1 M CH_3OH solution at a scan rate of 50 mV/s; (f) Specific activity for MOR of commercial Pt/C and VT-PtRh NWs without INSAFs in 0.5 M H_2SO_4 + 1 M CH_3OH at a scan rate of 50 mV/s. (a), (b) and (e) were reprinted with permission from ref 169. Copyright 2012 American Chemical Society. (c), (d) and (f) were reprinted with permission from ref 170. Copyright 2019 Elsevier.

llic NWs with high aspect ratio for efficient MOR. The 3D structure of the INSAFs features a helical structure with a hollow core (diameter 2 nm), around which protofilaments rotate around each other. While the Pt NWs were grown along the inner surface of the INSAFs (Figure 1.25a-b),[169] the PtRh alloy was characterized by a vine-tree-like morphology, in which inner PtRh NWs acted as the rigid 'tree' and outer PtRh NPs were interconnected to form a 'vine' like spiral chain

structure (Figure 1.25c-d).[170] Cyclic voltammetry results showed larger ECSA values with the two materials relative to commercial Pt/C, indicating that the 1D structures provided more electrochemical active sites. In addition, the authors found that the Pt NWs exposed more Pt (110) facets, which is the most active low-index surface for methanol oxidation. The specific activity, mass activity, and stability of both materials outperformed Pt/C (Figure 1.25e-f). This simple route for synthesizing ultrathin NWs with excellent electrocatalytic performance suggests new possibilities for the construction of 1D nanomaterials.

Pd-based materials have been found to show higher activity than Pt-based catalysts towards EOR in alkaline conditions.[223,224] Controllable synthesis of Pd NMs with well-defined morphology and size is thus beneficial to construct anode material. Pang et al.[70] developed carbon-supported Pd NWs and Pd NPs using polyhedrin as a shape-directing agent. The polyhedron can self-assemble into a sparse framework under low protein concentration and a dense framework under high concentration, which leads to the formation of Pd NWs and Pd NPs respectively, as sparse framework has sufficient space for NP to aggregate into linear structures. The materials were dispersed on a carbon support to increase electron conductivity for the ethanol oxidation in alkaline conditions. It was noted that the onset potential toward ethanol oxidation of Pd NWs was lower than that of the Pd NPs and Pd/C, suggesting improved kinetic performance. Its stability also outperformed the later two. The one dimensional network is characterized by its high electron transport rate as a result of the path-directing effect of the structure anisotropy[169,225,226] as well as the large surface area provided by the protein support.[70] The polyhedrin was also reported to be a versatile template for the synthesis of PdCu alloy nanowire networks and further applied to methanol and ethanol electrooxidation.[168] By tuning the Pd-to-Cu ratio, it was found that with increasing Cu content, the catalytic activity also increased, which was attributed to the Cu modifying the d-band structure of Pd and thus changing the interatomic charge transfer between the two components. The alloy NWs showed excellent overpotential and long-time performance compared to the commercial Pd/C. However, the positive effect from the protein was not discussed.

1.3.4.3 Viruses as templates

In the report by Lee et al.[67] (section 1.2.4), the Au NWs on P8#9 was further utilized as a core template to prepare Au-Pt core-shell NWs with different Pt loadings, which were found to be highly efficient for EOR (Figure 1.26). Both cyclic voltammetry and chronoamperometry results

supported the enhanced EOR as compared to commercial Pt/C. The authors proposed the improved kinetics were due to the synergistic effect of Pt (110) catalyzing C-C bond cleavage and the partially exposed Au core with high activity for oxidizing CO, which could cause Pt poisoning.[67] Besides gene modification, M13 phage surface was also functionalized by bioconjugation. In a work by Sanchez's group,[144] the side amine groups on the pVIII protein on the phage surface were used to attach thiol groups, which then served as templates to nucleate Au, Ag and Pt nanoparticles to form 1D NWs. Both Au and Pt NP SH-M13 materials (without conducting support added) showed electroactivities close to the best reported values for Pt supported on conductive species for MOR.

1.3.5 Formic Acid Oxidation Reaction (FAOR)

Direct formic acid fuel cells (DFAFCs) also feature high power and energy densities, in which formic acid is oxidized at the anode to produce CO_2 and protons after complete oxidation.[227] Pd-based catalysts are widely used as efficient electrode materials for their higher abundance and stronger resistance to CO poisoning relative to Pt.[228] To efficiently utilize metal NPs for the reaction, suitable catalyst supports are required to well disperse NPs with high loading. Carbon materials such as graphene and carbon nanotubes are good catalyst supports because of their high electronic conductivities and large surface areas.[229,230] However, it remains difficult to directly deposit ultrasmall NPs on them with uniform distribution and high stability without aggregation, which are mainly caused by the lack of sufficient binding sites on these carbon materials.[231] To solve this issue, there have been some reports using natural DNA to modify the carbon surface.[171,172] DNA base pairs are rich in aromatic motifs, which can interact with graphene/nanotube by π-π conjugation.[232] In addition, the PO_4^{3-} backbone provides good anchor sites for Pd^{2+} binding,[233] leading to uniform growth of small Pd NPs along the DNA lattice. It was claimed that the nitrogen rich functional groups may also interact with Pd NPs.[171] As shown in Figure 1.27, a DNA-carbon-Pd nanosystem has shown higher ECSA, lower overpotential and increased peak current density when compared to the corresponding carbon-Pd composite, which demonstrated the important role of DNA molecules.[172] It acts a bridge to connect the carbon support and Pd NPs with high monodispersity and stability. Moreover, the nucleobases in DNA can be oxidized under positive potentials, which can help limit Pd oxidation, which deactivates the catalyst, and thus ensured high catalytic activity.[171]

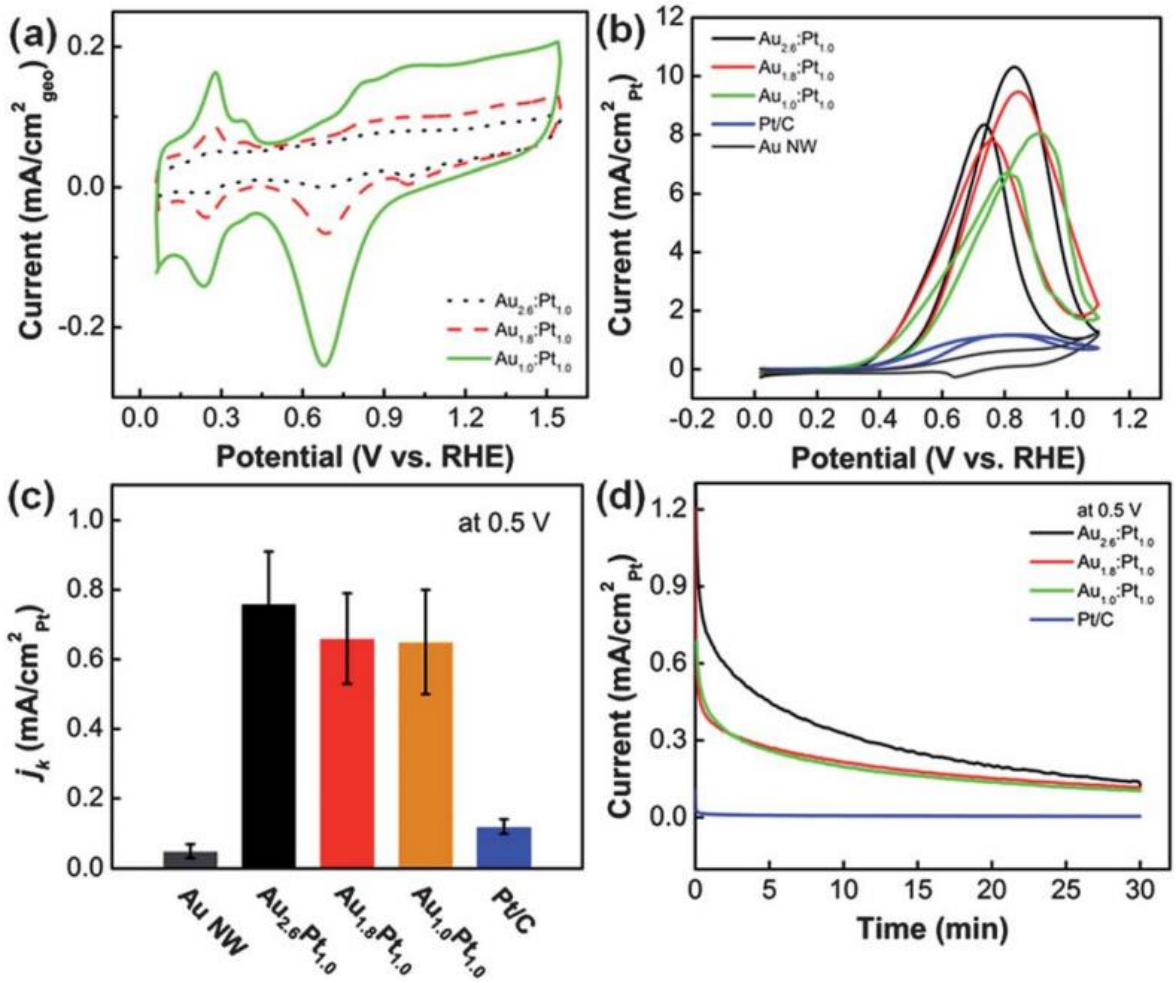

Figure 1.26: Comparison of ethanol oxidation of Au–Pt core–shell NW electrocatalysts with various compositions (Au : Pt) on GCE. (a) Cyclic voltammograms (after 25 cycles) of Au–Pt core–shell NWs on GCE (loading of $Au_{2.6}Pt_{1.0}$: 7.7 μg cm^{-2}, $Au_{1.8}Pt_{1.0}$: 9.7 μg cm^{-2} and $Au_{1.0}Pt_{1.0}$: 13.0 μg cm^{-2} and Pt–C: 9.8 μg cm^{-2}), in Ar-purged 0.1 M KOH at 50 mV s^{-1}; (b) Ethanol oxidation polarization curves of Au–Pt core–shell NWs, Au NWs, and a commercial Pt/C catalyst in 1.0 M ethanol and 0.1 M KOH at 50 mV s^{-1}; (c) Comparison of specific activity of the Au–Pt core–shell NWs and a commercial Pt/C catalyst at 0.5 V (vs. RHE). The specific activity is normalized by the electrochemically active surface area of Pt; (d) Chronoamperometry measurements of ethanol oxidation at 0.5 V on Au–Pt core–shell NWs and commercial Pt/C electrocatalyst on a GCE in 1.0 M ethanol and 0.1 M KOH. Reprinted with permission from ref 67. Copyright 2012 Royal Chemical Society.

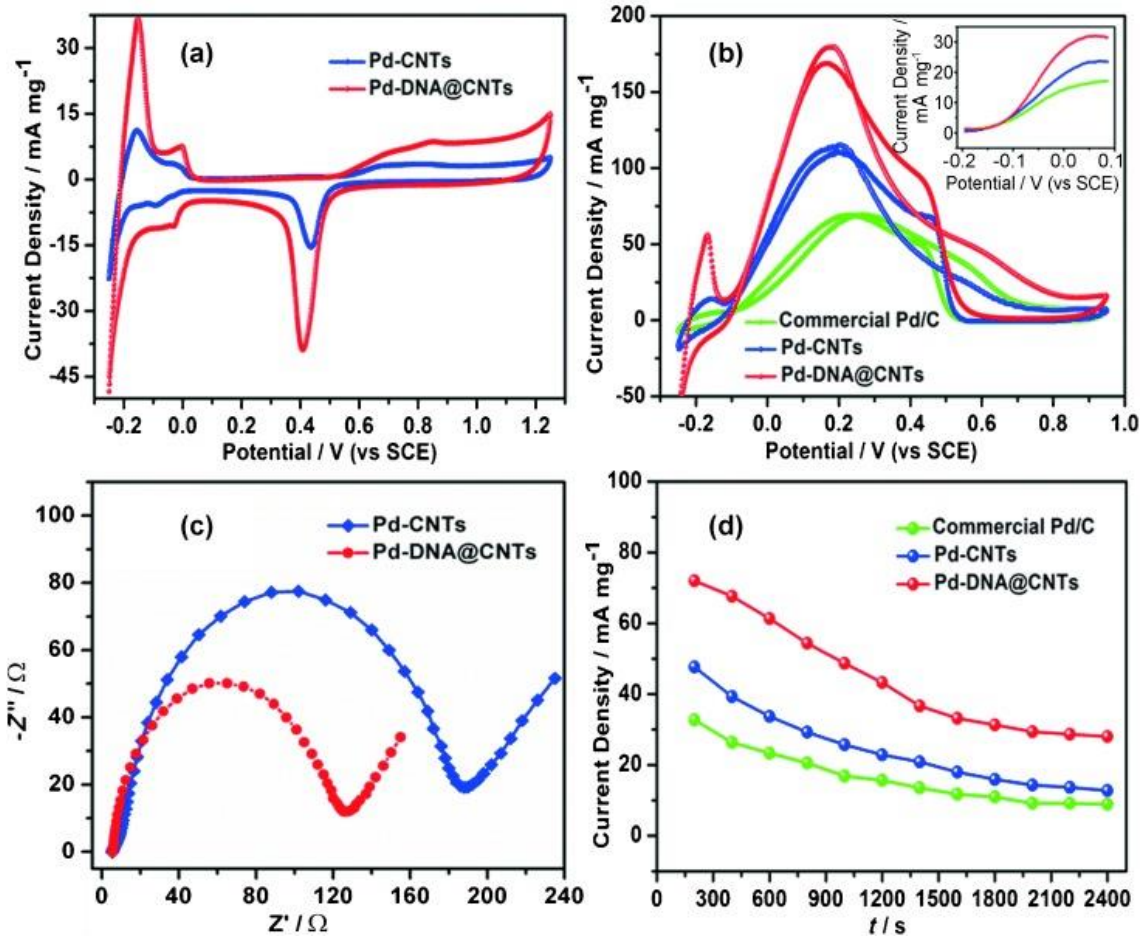

Figure 1.27: Voltammograms of various Pd-based electrocatalysts measured a) in N_2-saturated 0.5 M H_2SO_4 at 50 mV s^{-1} and b) in 0.5 M H_2SO_4 + 0.5 M HCOOH at 50 mV s^{-1} (inset shows steady-state polarization curves measured at 2 mV s^{-1}); c) Nyquist plots (note: c is unfortunately not plotted in orthogonal fashion) and d) Amperometric i–t curves for the different Pd-based electrocatalysts in 0.5 M H_2SO_4 + 0.5 M HCOOH electrolyte solution. Reprinted with permission from ref 172. Copyright 2014 Wiley.

1.3.6 Carbon Dioxide Reduction/Carbon Monoxide Oxidation Reaction (CO_2 RR/CO OR)

Carbon dioxide (CO_2) gas emission is the main cause for global climate change.[234] Transforming CO_2 into its reduced forms can produce useful chemicals and alleviates green house gas pollution simultaneously. Among the different routes for cycling CO_2, electrocatalytic reduction reaction (CO_2 RR) is considered as a green and economical method. Metals like Ag,[235,236] Au[237,238] and

Cu[239,240] have been found to be promising electrocatalysts for reducing CO_2 with high activity under appropriate conditions. Ag and Au NMs are of particular interest as they showed higher selectivtiy towards CO products compared to other metal catalysts.[241–243] High selectivty is important to avoid product separation processes and thus save cost in industrial applications. In the available literature, bio-templated MNMs are rarely used in CO_2 RR, which gives future opportunity to explore such an application. Very recently, our group reported the first example of using biosynthesized Ag nanorings for CO_2 RR.[100] A mixture of $AgNO_3$ and the disk assembly of TMV coat protein was illuminated by UV light, resulting in Ag nanorings assembled on the outer surface of the protein. Compared to bulk silver and silver NPs prepared by a chemical reduction method, the nanorings exhibited enhanced overpotential, CO Faradaic efficiency and long time stability (Figure 1.28). It was believed that the improved performance was related to the numerous functional groups on the protein such as arginine and thiol groups, which might influence the binding energies of the intermediates of the CO_2 RR and/or the side reaction HER.[100]

In the previous section on MOR/EOR (section 1.3.4), one important factor that affects Pt performance is poisoning from the CO intermediate, which strongly deactivates the Pt surface, resulting in higher overpotential and decreased activity.[244] It is therefore important to develop catalysts with high tolerance for CO for DAFCs. Au was found to be a good catalyst for CO oxidation. The aforementioned Au NWs (section 1.3.4.3) with different particle diameters were studied for CO oxidation.[67] Impressively, it was found that Au NWs with diameters of 40 nm gave current density about 10 times higher than NWs 30 nm and 20 nm in diameter (Figure 1.29). This could be due to the presence of more Au (110) facets on the 40 nm Au NW, since it was previously demonstrated that when using Au for CO oxidation the reactivity followed the trend Au (110) > Au (100) >> Au (111). In addition, 40 nm diameter Au NWs had a specific activity comparable to a (110) single-crystal Au surface, making it a good candidate for alloying Pt so that Pt adsorbs alcohol molecules and Au efficiently oxidizes CO to final products.[244]

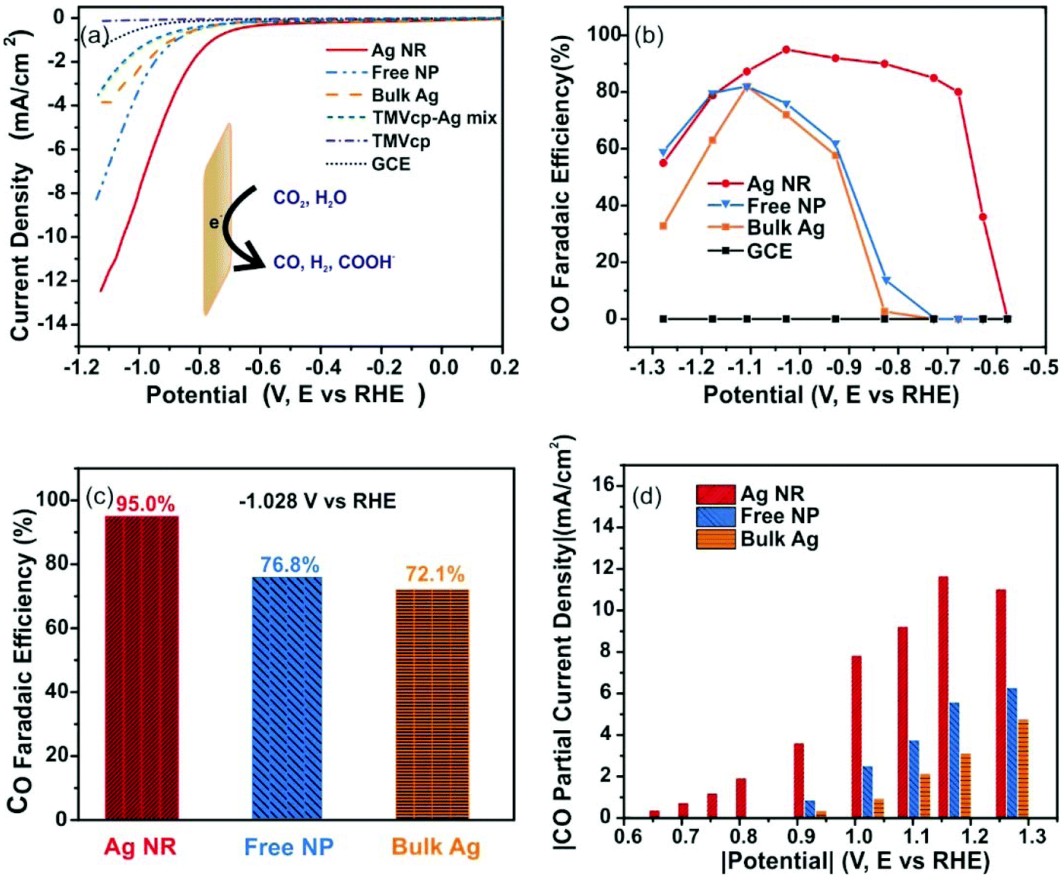

Figure 1.28: (a) CO_2 reduction cathodic LSV results; (b) Faradaic efficiencies (FEs) of CO at various applied potentials; (c) CO FEs at potential of -1.028 V; (d) CO Current density at various potentials. Reprinted from ref 99. Copyright 2019 Royal Society of Chemistry.

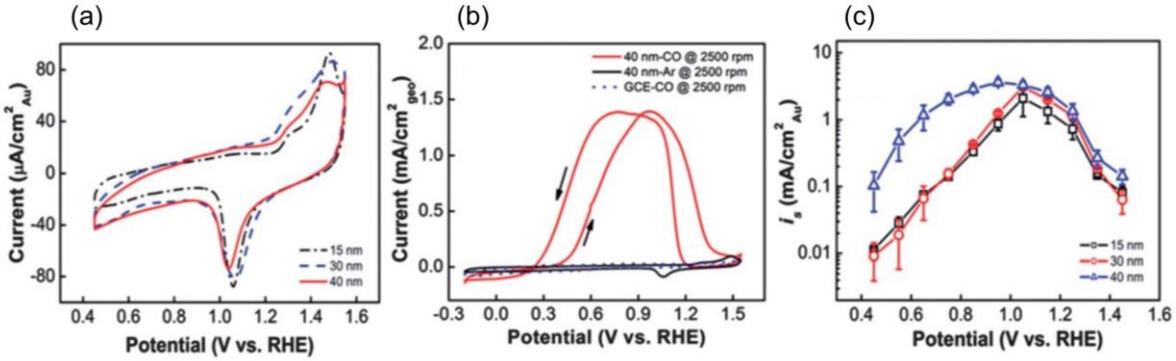

Figure 1.29: Cyclic voltammograms of Au NWs with 20 nm, 30 nm, 40 nm on GCE (loading of 16.3 μg cm^{-2}, 17.3 μg cm^{-2} and 12.2 μg cm^{-2}, respectively) in Ar purged 0.1 M KOH at 20 mV/s; (b) CO oxidation at 2500 rpm rotation rate in 0.1 M KOH electrolyte with 20 mV/s scan rate; (c) Specific activity of CO oxidation with different diameters of the Au NWs/GC RDE in CO saturated 0.1 M KOH at 1600 rpm with 20 mV s^{-1}. Reprinted with permission from ref 67. Copyright 2012 Royal Society of Chemistry.

1.4 Conclusions, Outlooks and Thesis Positioning

Nature is a great teacher, inspiring humans to pursue ingenious solutions in the fields of science and engineering. Particularly in material science, bioinspired methods have stimulated the rapid development of methods to synthesize and apply various kinds of innovative materials at the macro- and nano-scales. This chapter is aimed to present the most recent research progress in biological material templated MNM synthesis and their applications in electrocatalysis. Biological molecules including peptides, proteins, DNA, and whole viruses have proven themselves as outstanding candidates to support nanostructure nucleation and growth.

Among the bio-templates described in this review, peptides have found the widest application (ORR, HER, MOR, and EOR) in electrocatalysis, as displayed in some key examples above. Compared to other bio-templates, peptides are of low cost, and feature relatively simple amino acid sequences, which can be highly specific towards the target substrate through noncovalent interactions. Extension of this field relies on revealing a clear picture of atomic-level bio-interface to open new possibilities for the rational design of artificial peptide sequences with controllable structures and improved catalytic performance, which may serve as a great alternative to phage display technique with complicated process. It is worth noting that while some residues are responsible for anchoring to the nanoparticles, the remaining residues may also participate in providing optimal spatial arrangements to minimize the surface energy or interfacial energy. In addition, it is also necessary to optimize peptide length to simplify the peptide synthesis process, which is easier and cheaper for shorter peptides.

Regarding the emerging applications of bimetallic systems in electrocatalysis, peptides have also attracted attentions to serve as templates for the fabrication of alloy and core-shell structures. To this end, investigating the peptide-metal structure/function relationship will become even more difficult than in the single metal case, which poses great challenges and needs intensive collaboration between researchers from different fields. As these issues are solved, we believe that the application of peptide-based-nanocomposites can be further extended to more electrocatalytic reactions (such as EOR, CO_2 RR), as well as towards other applications such as electronic, sensing, imaging and biomedical areas.

Proteins have also been reported to be alternatives for constructing MNMs. They are made of larger chains of amino acids than peptides, resulting in different levels of structures. Moreover, proteins contain large numbers of functional groups such as -COOH, -NH_2, -SH, providing rich binding sites for interaction with metal cations. That said, protein self-assembly depends on the pH, ionic strength of the solution, making protein templates more sensitive to the environment when incubating with inorganic precursors. Hence, the use of protein templates can require careful control of the synthetic conditions to prevent denaturation and obtain the desired protein-nanocomposite with high stability.

Although many fabricated nanostructures were reported using proteins as templates, most of the resulting structures are used in organic catalysis. Only a few examples showed applications in electrocatalysis (MOR (section 1.3.4), CO_2RR (section 1.3.6) as discussed in this chapter), which is possibly due to the insulating property of the protein. Increasing electronic conductivity of the protein-metal system is one direction to pursue for enhancing electrocatalytic performance, which may be achieved by screening proteins with relatively good conductivity and/or modifying the protein with nanoparticles organized on the outer surface of the protein instead of being buried inside. Alternatively, if 1D or 2D MNMs are assembled on the protein in a stable pattern, it may be possible to remove the underlying insulated template by digesting without affecting the shape of metallic nanostructures.

As a biopolymer with rich phosphate backbones, DNA can chelate various metal cations, making it a good candidate to promote synthesis of uniform NPs with defined shape and size. However, DNA-metal complexes have not been widely reported as catalysts for electrocatalysis. In the examples discussed in section 1.3.5, DNA-nanoparticle complex systems were all immobilized on highly conductive carbon supports, which may be due to the poor conductivity of DNA molecules. In addition, most synthetic DNAs are expensive and difficult to produce in large scale, and the final yield of DNA-metal structures is usually low, limiting their further application in the catalysis field. In this regard, turning research endeavors to natural DNA can help enrich the available template library for effective MNM construction. Efforts should also be devoted to improving MNM yields if they are to be applied in more electrocatalytic reactions.

Compared to the biomolecules mentioned above, virus particles have more complex structures, consisting of DNA/RNA surrounded by many capsid proteins. It is more resistant to harsh

chemical /thermal conditions, with the resulted MNM possessing high stability. Through genetic modification or charge modification, the surface properties of these capsid proteins can be tuned to meet different requirements to generate various metal binding patterns, making them a versatile platform for MNM synthesis. In many cases, the binding residues are difficult to be accessed by the metal precursor, which then requires careful surface treatment to increase metallization efficiency. Viruses are the only template category that has already been used to synthesize structures from non-noble metals for electrocatalysis, in which metals like Ni and Co can be incorporated by electroless deposition methods. Virus-metal nanocomposites have been applied in both electro-oxidation and electro-reduction reactions in publications to date. Considering the hierarchical structure of virus, it maybe even more challenging to explain the NP assembly mechanism and fully characterize the formed bio-interface between the template and metal NP, which should be a research direction to focus on for future endeavors.

Both synchrotron-based and non-synchrotron-based techniques have been employed to explore the interactions between nanomaterials and biomolecule. For the former type, XAFS (X-ray absorption fine-structure spectroscopy) and HE-XRD (High energy X-ray diffraction) can be combined to provide key information on atomic-scale coordination and structural details.[245] Non-synchrotron-based tools such as QCM (quartz crystal microbalance), SPR (surface plasmon resonance), AFM (atomic force microscope) and CD (circular dichroism) have been employed.[29] For example, QCM and SPR are able to analyze the affinity of peptide to target metal by flowing the peptide solution over the metal-coated QCM/SPR sensor and extracting thermodynamic parameters.[246,247] AFM is a complementary method to image surface features of metal before and after adsorption of biomolecules, which can provide information on biomolecule surface coverage and assembly properties.[248] Compared to these three methods that normally require a 2D surface, CD is a powerful method to characterize the structural differences of biomolecules before and after metal adsorption in solution.[249] While these techniques enable us to acquire information about the affinity of biomolecules to metals, our understanding on the atomic level of the bio-interface formation mechanism is still rather limited. Advances in characterization tools such as in situ AFM are thus necessary to provide further insights and give a more complete picture.

Computational approaches hold great promise in interpreting experimental observations and guiding material design and optimization. Molecular dynamic (MD) simulations physically

modeled interactions between biomolecules and inorganic materials and revealed structure/function relationships.[29] Advanced sampling strategies with appropriate force fields provide reliable estimates of the biomolecule-metal adsorption free energies[250] and are critical to capture catalysis effects. If successful, MD simulation will be a good starting point for faster catalyst screening. Further progress is also necessary to model more complex systems such as multi-metal catalysts, which is an important material category for electrocatalysis. Besides modelling the existing template library, great achievements occurred in *de novo* design of artificial peptides and proteins complexed to metal cations, producing molecules with a larger number of binding functions or carrying out new catalytic transformations.[251] *De novo* design will lead to a programmable propensity expanding its application to more biomolecule-nanoparticle systems, in which specific catalytic properties/functions can be manipulated and confirmed by electrochemical measurements.

Both opportunities and challenges exist in employing useful bio-templates for MNM synthesis and applications in electrocatalysis, with the goal of developing materials with low cost, high catalytic activity and excellent durability, using simple synthetic protocols under environmentally benign conditions. On one hand, we expect more nano-biocomposites with outstanding performance to be demonstrated, enriching the current catalyst library, especially in developing inexpensive non-noble metal materials and even non-metal materials without sacrificing catalytic activity. On the other hand, characterization techniques and computational approaches need to be combined to enable a better understanding of the MNM formation mechanism, the bio-interface structural details at the molecular and atomic level, and how these properties further affect the resulting catalytic properties.

Although bioinspired MNMs nanocatalysis is a burgeoning area, a more enriched template library with outstanding catalytic efficiency is continually in demand. This thesis strives to serve this purpose. Specifically, a protein was used a versatile building block for fabrication of a series of nanometals, which combines the dual benefits of eco-friendly synthesis and excellent catalytic performance.

1.5 Thesis Outline

Chapter 2 outlines 1) the methodology and techniques necessary to characterize nanomaterials in this thesis; 2) related electrochemical techniques for evaluating electrocatalytic performance of nanocatalysts.

Chapter 3 discusses the biosynthesis of silver nanorings (Ag NRs) assembled on a tobacco mosaic virus coat protein (TMVCP). The Ag NR is examined as an electrocatalyst for carbon dioxide electroreduction. The catalytic performance is compared with Ag nanoparticles prepared by conventional chemical method, as well as a bulky Ag electrode. The electrocatalytic performance is evaluated regarding linear sweep voltammetry current density, carbon monoxide Faradaic efficiency and current density, and material long term operation durability. Possible origin for the enhanced performance of Ag NR is discussed.

Chapter 4 describes the biosynthesis of platinum nanorings (Pt NR) and isolated Pt nanoparticles (Pt NP) on TMVCP via under two different pH conditions. The two Pt materials are characterized by a series of techniques. They are then applied for the methanol electrooxidation reaction in acidic, neutral and alkaline supporting electrolytes. The catalytic performance is compared with a benchmarking commercial Pt on carbon catalyst. These three catalysts show different electrochemical responses regarding specific/mass activities, impedance and stability tests.

Chapter 5 involves the fabrication of metallic nanoparticles (Pt, Pd and Au NPs) on TMVCP A protein in alkaline buffer at room temperature. These materials are tested for two organic transformations in water, i.e., 4-nitrophenol reduction and olefinic alcohol hydrogenation. The kinetics of 4-nitrophenol reduction is probed via UV-vis monitoring to obtain the reaction constants. And the kinetics for olefinic alcohol hydrogenation is evaluated by NMR quantification to obtain turnover frequencies. Molecular dynamic simulation is then employed to a TMVCPA-Pd NP system to illustrate the role of TMCPA on the material catalysis behavior.

Chapter 6 presents the synthesis of bimetallic PdAu NPs on the TMVCPA, with different Pd-to-Au ratios. A series of characterization techniques are used to confirm the formation of PdAu nanoalloy homogeneously intermixed at nanoscale. Possible electrocatalytic applications of these alloy series are proposed.

Chapter 7 concludes this thesis and discusses possible future research directions.

1.6 References

[1] P. Peng, Z. Zhou, J. Guo and Z. Xiang, *ACS Energy Lett.*, 2017, **2**, 1308–1314.

[2] W. Xiao, W. Lei, M. Gong, H. L. Xin and D. Wang, *ACS Catal.*, 2018, **8**, 3237–3256.

[3] S. A. Grigoriev, M. S. Mamat, K. A. Dzhus, G. S. Walker and P. Millet, *Int. J. Hydrogen Energy*, 2011, **36**, 4143–4147.

[4] J. Wang, D. Gao, G. Wang, S. Miao, H. Wu, J. Li and X. Bao, *J. Mater. Chem. A*, 2014, **2**, 20067–20074.

[5] C. C. Pavel, F. Cecconi, C. Emiliani, S. Santiccioli, A. Scaffidi, S. Catanorchi and M. Comotti, *Angew. Chem. Int. Ed.*, 2014, **53**, 1378–1381.

[6] A. J. Bard, *J. Am. Chem. Soc.*, 2010, **132**, 7559–7567.

[7] S. Zhang, R. Geryak, J. Geldmeier, S. Kim and V. V Tsukruk, *Chem. Rev.*, 2017, **117**, 12942–13038.

[8] O. S. Kwon, H. S. Song, T. H. Park and J. Jang, *Chem. Rev.*, 2018, **119**, 36–93.

[9] G. Z. Gayda, O. M. Demkiv, N. Y. Stasyuk, R. Y. Serkiz, M. D. Lootsik, A. Errachid, M. V Gonchar and M. Nisnevitch, *Appl. Sci.*, 2019, **9**, 720.

[10] G. Liu, M. Lu, X. Huang, T. Li and D. Xu, *Sensors*, 2018, **18**, 4166.

[11] S. Bhatia, in *Natural polymer drug delivery systems*, Springer, 2016, pp. 33–93.

[12] S.-Y. Wang, H.-Z. Hu, X.-C. Qing, Z.-C. Zhang and Z.-W. Shao, *J. Cancer*, 2020, **11**, 69–82.

[13] B. Duncan, C. Kim and V. M. Rotello, *J. Control. Release*, 2010, **148**, 122–127.

[14] H. W. Tan, J. An, C. K. Chua and T. Tran, *Adv. Electron. Mater.*, 2019, **5**, 1800831.

[15] D. Son and Z. Bao, *ACS Nano*, 2018, **12**, 11731–11739.

[16] J. Kwon, H. Cho, H. Eom, H. Lee, Y. D. Suh, H. Moon, J. Shin, S. Hong and S. H. Ko, *ACS Appl. Mater. Interfaces*, 2016, **8**, 11575–11582.

[17] J. Park, T. Kwon, J. Kim, H. Jin, H. Y. Kim, B. Kim, S. H. Joo and K. Lee, *Chem. Soc. Rev.*, 2018, **47**, 8173–8202.

[18] C. Rogers, W. S. Perkins, G. Veber, T. E. Williams, R. R. Cloke and F. R. Fischer, *J. Am. Chem. Soc.*, 2017, **139**, 4052–4061.

[19] Z. W. She, J. Kibsgaard, C. F. Dickens, I. Chorkendorff, J. K. Nørskov and T. F. Jaramillo, *Science* 2017, **355,** eaad4998.

[20] W. Wang, C. F. Anderson, Z. Wang, W. Wu, H. Cui and C.-J. Liu, *Chem. Sci.*, 2017, **8**, 3310–3324.

[21] A. Heuer-Jungemann, N. Feliu, I. Bakaimi, M. Hamaly, A. Alkilany, I. Chakraborty, A. Masood, M. F. Casula, A. Kostopoulou and E. Oh, *Chem. Rev.*, 2019, **119**, 4819–4880.

[22] D. Huo, M. J. Kim, Z. Lyu, Y. Shi, B. J. Wiley and Y. Xia, *Chem. Rev.*, 2019, **119**, 8972–9073.

[23] V. K. Sharma, C. M. Sayes, B. Guo, S. Pillai, J. G. Parsons, C. Wang, B. Yan and X. Ma, *Nanotoxicology Sci. Total Environ.*, 2019, **653**, 1042–1051.

[24] S. Iravani, H. Korbekandi, S. V. Mirmohammadi and B. Zolfaghari, *Res. Pharm. Sci.*, 2014, **9**, 385–406.

[25] M. B. Dickerson, K. H. Sandhage and R. R. Naik, *Chem. Rev.*, 2008, **108**, 4935–4978.

[26] J. Xie, Y. Zheng and J. Y. Ying, *J. Am. Chem. Soc.*, 2009, **131**, 888–889.

[27] M. Mertig, L. Colombi Ciacchi, R. Seidel, W. Pompe and A. De Vita, *Nano Lett.*, 2002, **2**, 841–844.

[28] L. A. Lee, H. G. Nguyen and Q. Wang, *Org. Biomol. Chem.*, 2011, **9**, 6189–6195.

[29] T. R. Walsh and M. R. Knecht, *Chem. Rev.*, 2017, **117**, 12641–12704.

[30] M. Janczuk-Richter, I. Marinović, J. Niedziółka-Jönsson and K. Szot-Karpińska,

Electrochem. Commun., 2019, **99**, 11–15.

[31] J. Huang, L. Lin, D. Sun, H. Chen, D. Yang and Q. Li, *Chem. Soc. Rev.*, 2015, **44**, 6330–6374.

[32] E. Pazos, E. Sleep, C. M. Rubert Perez, S. S. Lee, F. Tantakitti and S. I. Stupp, *J. Am. Chem. Soc.*, 2016, **138**, 5507–5510.

[33] Y.-X. Pan, H.-P. Cong, Y.-L. Men, S. Xin, Z.-Q. Sun, C.-J. Liu and S.-H. Yu, *ACS Nano*, 2015, **9**, 11258–11265.

[34] K. Tomizaki, S. Wakizaka, Y. Yamaguchi, A. Kobayashi and T. Imai, *Langmuir*, 2014, **30**, 846–856.

[35] H. Acar, R. Genc, M. Urel, T. S. Erkal, A. Dana and M. O. Guler, *Langmuir*, 2012, **28**, 16347–16354.

[36] J. Yan, Y. Pan, A. G. Cheetham, Y. A. Lin, W. Wang, H. Cui and C. J. Liu, *Langmuir*, 2013, **29**, 16051–16057.

[37] R. Bhandari and M. R. Knecht, *Catal. Sci. Technol.*, 2012, **2**, 1360–1366.

[38] A. Jakhmola, R. Bhandari, D. B. Pacardo and M. R. Knecht, *J. Mater. Chem.*, 2010, **20,** 1522–1531.

[39] R. Bhandari, D. B. Pacardo, N. M. Bedford, R. R. Naik and M. R. Knecht, *J. Phys. Chem. C*, 2013, **117**, 18053–18062.

[40] J. M. Slocik and D. W. Wright, *Biomacromolecules*, 2003, **4**, 1135–1141.

[41] H. Yang, Z. Tang, W. Yan, L. Wang, Q. Wang, Y. Zhang, Z. Liu and S. Chen, *J. Alloys Compd.*, 2017, **702**, 146–152.

[42] X. Yuan, Y. Tay, X. Dou, Z. Luo, D. T. Leong and J. Xie, *Anal. Chem.*, 2013, **85**, 1913–1919.

[43] R. R. Naik, S. E. Jones, C. J. Murray, J. C. McAuliffe, R. A. Vaia and M. O. Stone, *Adv. Funct. Mater.*, 2004, **14**, 25–30.

[44] W. Yang, W. Guo, J. Chang and B. Zhang, *J. Mater. Chem. B*, 2017, **5**, 401–417.

[45] L. Ruan, H. Ramezani-Dakhel, C.-Y. Chiu, E. Zhu, Y. Li, H. Heinz and Y. Huang, *Nano Lett.*, 2013, **13**, 840–846.

[46] W. Wang, Z. Wang, M. Yang, C.-J. Zhong and C.-J. Liu, *Nano Energy*, 2016, **25**, 26–33.

[47] S. S. Bayram, O. K. Zahr, J. Del Re and A. S. Blum, *Nanotechnology*, 2016, **27**, 485603.

[48] O. K. Zahr and A. S. Blum, *Nano Lett.*, 2012, **12**, 629–633.

[49] G. Wei, F. Xu, Z. Li and K. D. Jandt, *J. Phys. Chem. C*, 2011, **115**, 11453–11460.

[50] R. A. McMillan, J. Howard, N. J. Zaluzec, H. K. Kagawa, R. Mogul, Y.-F. Li, C. D. Paavola and J. D. Trent, *J. Am. Chem. Soc.*, 2005, **127**, 2800–2801.

[51] D. Scott, M. Toney and M. Muzikár, *J. Am. Chem. Soc.*, 2008, **130**, 865–874.

[52] T. Yang, Z. Li, L. Wang, C. Guo and Y. Sun, *Langmuir*, 2007, **23**, 10533–10538.

[53] M. A. Lapierre-Devlin, C. L. Asher, B. J. Taft, R. Gasparac, M. A. Roberts and S. O. Kelley, *Nano Lett.*, 2005, **5**, 1051–1055.

[54] E. Spain, E. Brennan, H. McArdle, T. E. Keyes and R. J. Forster, *Anal. Chem.*, 2012, **84**, 6471–6476.

[55] J. Das and H. Yang, *J. Phys. Chem. C*, 2009, **113**, 6093–6099.

[56] S. Wu, H. Zhao, H. Ju, C. Shi and J. Zhao, *Electrochem. Commun.*, 2006, **8**, 1197–1203.

[57] J. T. Petty, J. Zheng, N. V Hud and R. M. Dickson, *J. Am. Chem. Soc.*, 2004, **126**, 5207–5212.

[58] J. F. Ohmura, F. J. Burpo, C. J. Lescott, A. Ransil, Y. Yoon, W. C. Records and A. M. Belcher, *Nanoscale*, 2019, **11**, 1091–1102.

[59] W. C. Records, Y. Yoon, J. F. Ohmura, N. Chanut and A. M. Belcher, *Nano Energy*, 2019, **58**, 167–174.

[60] A. A. A. Aljabali, F. Sainsbury, G. P. Lomonossoff and D. J. Evans, *Small*, 2010, **6**, 818–821.

[61] A. A. A. Aljabali, J. E. Barclay, G. P. Lomonossoff and D. J. Evans, *Nanoscale*, 2010, **2**, 2596–2600.

[62] M. Knez, A. M. Bittner, F. Boes, C. Wege, H. Jeske, E. Maiβ and K. Kern, *Nano Lett.*, 2003, **3**, 1079–1082.

[63] M. Ł. Górzny, A. S. Walton and S. D. Evans, *Adv. Funct. Mater.*, 2010, **20**, 1295–1300.

[64] K. Gerasopoulos, M. McCarthy, E. Royston, J. N Culver and R. Ghodssi, *J. Micromechanics Microengineering*, 2008, **18**, 104003.

[65] E. Royston, A. Ghosh, P. Kofinas, M. T. Harris and J. N. Culver, *Langmuir*, 2008, **24**, 906–912.

[66] A. S. Blum, C. M. Soto, C. D. Wilson, J. D. Cole, M. Kim, B. Gnade, A. Chatterji, W. F. Ochoa, T. Lin, J. E. Johnson and B. R. Ratna, *Nano Lett.*, 2004, **4**, 867–870.

[67] Y. Lee, J. Kim, D. S. Yun, Y. S. Nam, Y. Shao-Horn and A. M. Belcher, *Energy Environ. Sci.*, 2012, **5**, 8328–8334.

[68] Q. Wang, H. Yang, Z. Zhou, L. Wang, W. Yan, W. Wu, S. Chen, Z. Liu and Z. Tang, *Int. J. Hydrogen Energy*, 2017, **42**, 11295–11303.

[69] E. S. Kang, Y.-T. Kim, Y.-S. Ko, N. H. Kim, G. Cho, Y. H. Huh, J.-H. Kim, J. Nam, T. T. Thach, D. Youn, Y. D. Kim, W. S. Yun, W. F. DeGrado, S. Y. Kim, P. T. Hammond, J. Lee, Y.-U. Kwon, D.-H. Ha and Y. H. Kim, *ACS Nano*, 2018, **12**, 6554–6562.

[70] G. Pang, M. Sun, P. Liu, L. Hou and F. Gao, *RSC Adv.*, 2016, **6**, 19734–19741.

[71] W. J. Crookes-Goodson, J. M. Slocik and R. R. Naik, *Chem. Soc. Rev.*, 2008, **37**, 2403–2412.

[72] W. Wu, Z. Tang, K. Wang, Z. Liu, L. Li and S. Chen, *Electrochim. Acta*, 2018, **260**, 168–176.

[73] Z. Zong, K. Xu, D. Li, Z. Tang, W. He, Z. Liu, X. Wang and Y. Tian, *J. Catal.*, 2018, **361**, 168–176.

[74] M. S. Reddy, *Front. Microbiol.*, 2013, **4**, 314.

[75] Y. Cui, Y. Wang, R. Liu, Z. Sun, Y. Wei, Y. Zhao and X. Gao, *ACS Nano*, 2011, **5**, 8684–8689.

[76] B. Söptei, L. N. Nagy, P. Baranyai, I. Szabó, G. Mező, F. Hudecz and A. Bóta, *Gold Bull.*, 2013, **46**, 195–203.

[77] Y. Wang, Y. Cui, R. Liu, Y. Wei, X. Jiang, H. Zhu, L. Gao, Y. Zhao, Z. Chai and X. Gao, *Chem. Commun.*, 2013, **49**, 10724–10726.

[78] Y. Li, W. Gao, L. Ci, C. Wang and P. M. Ajayan, *Carbon N. Y.*, 2010, **48**, 1124–1130.

[79] R. Narayanan and M. A. El-Sayed, *J. Phys. Chem. B*, 2005, **109**, 12663–12676.

[80] I. Ahmad, F. Li, C. Kim, J.-M. Seo, G. Kim, J. Mahmood, H. Y. Jeong and J.-B. Baek, *Nano Energy*, 2019, **56**, 581–587.

[81] A. Jakhmola, R. Bhandari, D. B. Pacardo and M. R. Knecht, *J. Mater. Chem.*, 2010, **20**, 1522–1531.

[82] A.-P. Xu, P.-P. Yang, C. Yang, Y.-J. Gao, X.-X. Zhao, Q. Luo, X.-D. Li, L.-Z. Li, L. Wang and H. Wang, *Nanoscale*, 2016, **8**, 14078–14083.

[83] D. K. Clare and E. V Orlova, *J. Struct. Biol.*, 2010, **171**, 303–308.

[84] T. Peng, D. Paramelle, B. Sana, C. F. Lee and S. Lim, *Small*, 2014, **10**, 3131–3138.

[85] I. Gutsche, F. Coulibaly, J. E. Voss, J. Salmon, J. d'Alayer, M. Ermonval, E. Larquet, P. Charneau, T. Krey and F. Mégret, *Proc. Natl. Acad. Sci.*, 2011, **108**, 8003–8008.

[86] S. A. Cook, E. A. Hill and A. S. Borovik, *Biochemistry*, 2015, **54**, 4167–4180.

[87] H. Wei, Z. Wang, J. Zhang, S. House, Y.-G. Gao, L. Yang, H. Robinson, L. H. Tan, H. Xing, C. Hou, I. M. Robertson, J.-M. Zuo and Y. Lu, *Nat. Nanotechnol.*, 2011, **6**, 93.

[88] S. Kashyap, T. J. Woehl, X. Liu, S. K. Mallapragada and T. Prozorov, *ACS Nano*, 2014, **8**, 9097–9106.

[89] J. R. Henstock, M. Rotherham, H. Rashidi, K. M. Shakesheff and A. J. El Haj, *Stem Cells Transl. Med.*, 2014, **3**, 1363–1374.

[90] R. M. Kramer, C. Li, D. C. Carter, M. O. Stone and R. R. Naik, *J. Am. Chem. Soc.*, 2004, **126**, 13282–13286.

[91] J. S. Mohanty, P. L. Xavier, K. Chaudhari, M. S. Bootharaju, N. Goswami, S. K. Pal and T. Pradeep, *Nanoscale*, 2012, **4**, 4255–4262.

[92] N. Goswami, A. Giri, M. S. Bootharaju, P. L. Xavier, T. Pradeep and S. K. Pal, *Anal. Chem.*, 2011, **83**, 9676–9680.

[93] M. Liang, R. Su, R. Huang, W. Qi, Y. Yu, L. Wang and Z. He, *ACS Appl. Mater. Interfaces*, 2014, **6**, 4638–4649.

[94] X. He, D.-P. Yang, X. Zhang, M. Liu, Z. Kang, C. Lin, N. Jia and R. Luque, *Chem. Eng. J.*, 2019, **369**, 621–633.

[95] S.-L. Zhong, J. Zhuang, D.-P. Yang and D. Tang, *Biosens. Bioelectron.*, 2017, **96**, 26–32.

[96] Q. Ding, Z. Kang, X. He, M. Wang, M. Lin, H. Lin and D.-P. Yang, *Microchim. Acta*, 2019, **186**, 453.

[97] P. Guha Ray, P. Pal, P. K. Srivas, P. Basak, S. Roy and S. Dhara, *ACS Appl. Bio Mater.*, 2018, **1**, 985–998.

[98] O. K. Zahr and A. S. Blum, *Nano Lett.*, 2012, **12**, 629–633.

[99] O. K. Zahr and A. S. Blum, in *Virus Hybrids as Nanomaterials: Methods and Protocols*, eds. B. Lin and B. Ratna, Humana Press, Totowa, NJ, 2014, pp. 105–112.

[100] Y. Pan, W. J. Paschoalino, S. S. Bayram, A. S. Blum and J. Mauzeroll, *Nanoscale*, 2019, **11**, 18595–18603.

[101] A. S. Bommarius, J. K. Blum and M. J. Abrahamson, *Curr. Opin. Chem. Biol.*, 2011, **15**, 194–200.

[102] S. Manuguri, K. Webster, N. A. Yewdall, Y. An, H. Venugopal, V. Bhugra, A. Turner, L. J. Domigan, J. A. Gerrard and D. E. Williams, *Nano Lett.*, 2018, **18**, 5138–5145.

[103] F. Saccoccia, P. Di Micco, G. Boumis, M. Brunori, I. Koutris, A. E. Miele, V. Morea, P. Sriratana, D. L. Williams and A. Bellelli, *Structure*, 2012, **20**, 429–439.

[104] S. S. Bale, P. Asuri, S. S. Karajanagi, J. S. Dordick and R. S. Kane, *Adv. Mater.*, 2007, **19**, 3167–3170.

[105] R. Cao, R. Thapa, H. Kim, X. Xu, M. Gyu Kim, Q. Li, N. Park, M. Liu and J. Cho, *Nat. Commun.*, 2013, **4**, 2076.

[106] H. Bagheri, A. Afkhami, H. Khoshsafar, A. Hajian and A. Shahriyari, *Biosens. Bioelectron.*, 2017, **89**, 829–836.

[107] Z. Varpness, J. W. Peters, M. Young and T. Douglas, *Nano Lett.*, 2005, **5**, 2306–2309.

[108] D. Hebbalalu, J. Lalley, M. N. Nadagouda and R. S. Varma, *ACS Sustain. Chem. Eng.*, 2013, **1**, 703–712.

[109] J. Virkutyte and R. S. Varma, *Chem. Sci.*, 2011, **2**, 837–846.

[110] I. Willner, R. Baron and B. Willner, *Adv. Mater.*, 2006, **18**, 1109–1120.

[111] M. Zayats, R. Baron, I. Popov and I. Willner, *Nano Lett.*, 2005, **5**, 21–25.

[112] M. A. Komkova, E. E. Karyakina and A. A. Karyakin, *J. Am. Chem. Soc.*, 2018, **140**, 11302–11307.

[113] M. D. Nothling, Z. Xiao, A. Bhaskaran, M. T. Blyth, C. W. Bennett, M. L. Coote and L. A. Connal, *ACS Catal.*, 2019, **9**, 168–187.

[114] J. Wang, K. Wang, F.-B. Wang and X.-H. Xia, *Nat. Commun.*, 2014, **5**, 5285.

[115] C.-H. Lu, B. Willner and I. Willner, *ACS Nano*, 2013, **7**, 8320–8332.

[116] J. Zhang, S. Song, L. Wang, D. Pan and C. Fan, *Nat. Protoc.*, 2007, **2**, 2888–2895.

[117] S. J. Tan, M. J. Campolongo, D. Luo and W. Cheng, *Nat. Nanotechnol.*, 2011, **6**, 268.

[118] Q.-Y. Lin, J. A. Mason, Z. Li, W. Zhou, M. N. O'Brien, K. A. Brown, M. R. Jones, S. Butun, B. Lee, V. P. Dravid, K. Aydin and C. A. Mirkin, *Science*, 2018, **359**, 669-672.

[119] S. Kogikoski, W. J. Paschoalino, L. Cantelli, W. Silva and L. T. Kubota, *TrAC Trends Anal. Chem.*, 2019, **118**, 597–605.

[120] N. V Voigt, T. Tørring, A. Rotaru, M. F. Jacobsen, J. B. Ravnsbæk, R. Subramani, W.

Mamdouh, J. Kjems, A. Mokhir, F. Besenbacher and K. V. Gothelf, *Nat. Nanotechnol.*, 2010, **5**, 200.

[121] B. Liu and J. Liu, *Anal. Methods*, 2017, **9**, 2633–2643.

[122] S. Kogikoski and L. T. Kubota, *Electrochem. Commun.*, 2018, **90**, 51–55.

[123] G. J. Heddle, *Catalysts*, 2013, **3,** 683-708.

[124] H. Sun, J. Ren and X. Qu, *Acc. Chem. Res.*, 2016, **49**, 461–470.

[125] Q. Zhang, Y. Qiao, F. Hao, L. Zhang, S. Wu, Y. Li, J. Li and X.-M. Song, *Chem. – A Eur. J.*, 2010, **16**, 8133–8139.

[126] S. J. Kwon and A. J. Bard, *J. Am. Chem. Soc.*, 2012, **134**, 10777–10779.

[127] T.-T. Tsai, C.-A. Chen, N. Yi-Ju Ho, S. Yang and C.-F. Chen, *ACS sensors*, 2019, **4**, 2885–2892.

[128] A. M. Wen and N. F. Steinmetz, *Chem. Soc. Rev.*, 2016, **45**, 4074–4126.

[129] J. N. Culver, A. D. Brown, F. Zang, M. Gnerlich, K. Gerasopoulos and R. Ghodssi, *Virology*, 2015, **479**–**480**, 200–212.

[130] S. Chu, A. D. Brown, J. N. Culver and R. Ghodssi, *Biotechnol. J.*, 2018, **13**, 1800147.

[131] A. Klug, *Philos. Trans. R. Soc. Lond. B. Biol. Sci.*, 1999, **354**, 531–535.

[132] J.-S. Lim, S.-M. Kim, S.-Y. Lee, E. A. Stach, J. N. Culver and M. T. Harris, *J. Nanomater.*, 2010, **2010,** 62050.

[133] S. N. Shah, A. A. Khan, A. Espinosa, M. A. Garcia, W. Nuansing, M. Ungureanu, J. G. Heddle, A. L. Chuvilin, C. Wege and A. M. Bittner, *Langmuir*, 2016, **32**, 5899–5908.

[134] L. Marín-Caba, P. L. Chariou, C. Pesquera, M. A. Correa-Duarte and N. F. Steinmetz, *Langmuir*, 2018, **35**, 203–211.

[135] N. Kurgan and V. Karbivskyy, *Appl. Nanosci.*, 2019, 1–5.

[136] D. Oh, J. Qi, B. Han, G. Zhang, T. J. Carney, J. Ohmura, Y. Zhang, Y. Shao-Horn and A. M. Belcher, *Nano Lett.*, 2014, **14**, 4837–4845.

[137] D. Ghosh, Y. Lee, S. Thomas, A. G. Kohli, D. S. Yun, A. M. Belcher and K. A. Kelly, *Nat. Nanotechnol.*, 2012, **7**, 677–682.

[138] Y. Huang, C.-Y. Chiang, S. K. Lee, Y. Gao, E. L. Hu, J. De Yoreo and A. M. Belcher, *Nano Lett.*, 2005, **5**, 1429–1434.

[139] D. Oh, J. Qi, B. Han, G. Zhang, T. J. Carney, J. Ohmura, Y. Zhang, Y. Shao-Horn and A. M. Belcher, *Nano Lett.*, 2014, **14**, 4837–4845.

[140] D. Oh, J. Qi, Y.-C. Lu, Y. Zhang, Y. Shao-Horn and A. M. Belcher, *Nat. Commun.*, 2013, **4**, 1–8.

[141] K. T. Nam, D.-W. Kim, P. J. Yoo, C.-Y. Chiang, N. Meethong, P. T. Hammond, Y.-M. Chiang and A. M. Belcher, *Science*, 2006, **312**, 885–888.

[142] N. Nuraje, X. Dang, J. Qi, M. A. Allen, Y. Lei and A. M. Belcher, *Adv. Mater.*, 2012, **24**, 2885–2889.

[143] S. Y. Tee, K. Y. Win, W. S. Teo, L. Koh, S. Liu, C. P. Teng and M. Han, *Adv. Sci.*, 2017, **4**, 1600337.

[144] L. I. Vera-Robles, G. Van Tran Nhieu, C. Laberty-Robert, J. Livage and C. Sanchez, *Adv. Eng. Mater.*, 2013, **15**, 954–961.

[145] L. I. Vera-Robles, J. González-Gracida, A. Hernández-Gordillo and A. Campero, *Langmuir*, 2015, **31**, 9188–9197.

[146] X. Dang, H. Yi, M.-H. Ham, J. Qi, D. S. Yun, R. Ladewski, M. S. Strano, P. T. Hammond and A. M. Belcher, *Nat. Nanotechnol.*, 2011, **6**, 377–384.

[147] C. Rosant, B. Avalle, D. Larcher, L. Dupont, A. Friboulet and J.-M. Tarascon, *Energy Environ. Sci.*, 2012, **5**, 9936–9943.

[148] M. Janczuk, J. Niedziółka-Jönsson and K. Szot-Karpińska, *J. Electroanal. Chem.*, 2016, **779**, 207–219.

[149] J. H. Kang and Y. T. Ko, *Int. J. Nanomedicine*, 2015, **10**, 33.

[150] A. Luchini and G. Vitiello, *Front. Chem.*, 2019, **7**, 343.

[151] R. Bali, R. Siegele and A. T. Harris, *J. Nanoparticle Res.*, 2010, **12**, 3087–3095.

[152] H. L. Parker, E. L. Rylott, A. J. Hunt, J. R. Dodson, A. F. Taylor, N. C. Bruce and J. H. Clark, *PLoS One*, 2014, **9**, e87192.

[153] R. Ramanathan, A. P. O'Mullane, R. Y. Parikh, P. M. Smooker, S. K. Bhargava and V. Bansal, *Langmuir*, 2011, **27**, 714–719.

[154] H. Chen, L. Zhang, O.-W. Tareque, J. Huang, H. Wang, M. Fu, D. Sun and Q. Li, *Curr. Nanosci.*, 2014, **10**, 271–276.

[155] E. C. Dengler, J. Liu, A. Kerwin, S. Torres, C. M. Olcott, B. N. Bowman, L. Armijo, K. Gentry, J. Wilkerson and J. Wallace, *J. Control. Release*, 2013, **168**, 209–224.

[156] M. S. Bakshi, F. Possmayer and N. O. Petersen, *J. Phys. Chem. C*, 2007, **111**, 14113–14124.

[157] M. Nasrollahzadeh, S. Mahmoudi-Gom Yek, N. Motahharifar and M. Ghafori Gorab, *Chem. Rec.*, 2019, **19**, 2436–2479.

[158] R. K. Das and S. K. Brar, *Nanoscale*, 2013, **5**, 10155–10162.

[159] A. Fariq, T. Khan and A. Yasmin, *J. Appl. Biomed.*, 2017, **15**, 241–248.

[160] L. Ruan, E. Zhu, Y. Chen, Z. Lin, X. Huang, X. Duan and Y. Huang, *Angew. Chem. Int. Ed.*, 2013, **52,** 12577–12581.

[161] J. Bandak, J. Petzold, H. Hatahet, A. Prager, B. Kersting, C. Elsner and B. Abel, *RSC Adv.*, 2019, **9**, 5558–5569.

[162] B. Zhou, Z. Sun, D. Li, T. Zhang, L. Deng and Y.-N. Liu, *Nanoscale*, 2013, **5**, 2669–2673.

[163] A. Jindal, K. Tashiro, H. Kotani, T. Takei, S. Reichenberger, G. Marzun, S. Barcikowski, T. Kojima and Y. Yamamoto, *ACS Appl. Energy Mater.*, 2019, **2**, 6536–6541.

[164] Q. Wang, Z. Tang, L. Wang, H. Yang, W. Yan and S. Chen, *ChemistrySelect*, 2016, **1**, 6044–6052.

[165] J. Rho, S. Y. Lim, I. Hwang, J. Yun and T. D. Chung, *ChemCatChem*, 2018, **10**, 165–169.

[166] A. S. Schenk, S. Eiben, M. Goll, L. Reith, A. N. Kulak, F. C. Meldrum, H. Jeske, C. Wege

and S. Ludwigs, *Nanoscale*, 2017, **9**, 6334–6345.

[167] N. M. Bedford, A. R. Showalter, T. J. Woehl, Z. E. Hughes, S. Lee, B. Reinhart, S. P. Ertem, E. B. Coughlin, Y. Ren and T. R. Walsh, *ACS Nano*, 2016, **10**, 8645–8659.

[168] R. Chen, M. Sun, G. Pang, J. Zhou, L. Hou and F. Gao, *ChemElectroChem*, 2017, **4**, 1081–1087.

[169] L. Zhang, N. Li, F. Gao, L. Hou and Z. Xu, *J. Am. Chem. Soc.*, 2012, **134**, 11326–11329.

[170] L. Hou, Y. Niu, Y. Jiang, T. Jiao, Y. Guo, Y. Zhou and F. Gao, *Colloids Surf. A*, 2019, **573**, 6–13.

[171] K. Qu, L. Wu, J. Ren and X. Qu, *ACS Appl. Mater. Interfaces*, 2012, **4**, 5001–5009.

[172] L. Y. Zhang, C. X. Guo, H. Pang, W. Hu, Y. Qiao and C. M. Li, *ChemElectroChem*, 2014, **1**, 72–75.

[173] W. kyo Suh, P. Ganesan, B. Son, H. Kim and S. Shanmugam, *Int. J. Hydrogen Energy*, 2016, **41**, 12983–12994.

[174] K. Shinozaki, J. W. Zack, R. M. Richards, B. S. Pivovar and S. S. Kocha, *J. Electrochem. Soc.*, 2015, **162**, 1144–1158.

[175] A. Gómez-Marín, J. Feliu and T. Edson, *ACS Catal.*, 2018, **8**, 7931–7943.

[176] R. Zhou, Y. Zheng, M. Jaroniec and S. Z. Qiao, *ACS Catal.*, 2016, **6**, 4720–4728.

[177] J. Zhang, Z. Xia and L. Dai, *Sci. Adv.*, 2015, **1**, e1500564.

[178] S. Guo, S. Zhang and S. Sun, *Angew. Chem. Int. Ed.*, 2013, **52**, 8526–8544.

[179] G. Wu and P. Zelenay, *Acc. Chem. Res.*, 2013, **46**, 1878–1889.

[180] M. Shao, A. Peles and K. Shoemaker, *Nano Lett.*, 2011, **11**, 3714–3719.

[181] M. Yang, Z. Wang, W. Wang and C. Liu, *Nanoscale Res. Lett.*, 2014, **9**, 405.

[182] S. Shanmugam, J. Sanetuntikul, T. Momma and T. Osaka, *Electrochim. Acta*, 2014, **137**, 41–48.

[183] Y.-H. Li, T.-H. Hung and C.-W. Chen, *Carbon N. Y.*, 2009, **47**, 850–855.

[184] L. Ruan, C.-Y. Chiu, Y. Li and Y. Huang, *Nano Lett.*, 2011, **11**, 3040–3046.

[185] K.-C. Chen, W.-W. Wu, C.-N. Liao, L.-J. Chen and K. N. Tu, *Science*, 2008, **321**, 1066–1069.

[186] K. D. Gilroy, A. Ruditskiy, H. C. Peng, D. Qin and Y. Xia, *Chem. Rev.*, 2016, **116**, 10414–10472.

[187] M. Laskar and S. E. Skrabalak, *J. Mater. Chem. A*, 2016, **4**, 6911–6918.

[188] K. Tedsree, T. Li, S. Jones, C. W. A. Chan, K. M. K. Yu, P. A. J. Bagot, E. A. Marquis, G. D. W. Smith and S. C. E. Tsang, *Nat. Nanotechnol.*, 2011, **6**, 302–307.

[189] W. F. Lin, M. S. Zei, M. Eiswirth, G. Ertl, T. Iwasita and W. Vielstich, *J. Phys. Chem. B*, 1999, **103**, 6968–6977.

[190] P. Moseley and W. A. Curtin, *Nano Lett.*, 2015, **15**, 4089–4095.

[191] S. Yin, Z. Xie, X. Deng, W. Xuan, Y. Duan, S. Zhang and Y. Liang, *J. Electroanal. Chem.*, 2020, **856**, 113707.

[192] L. Liu, L.-X. Chen, A.-J. Wang, J. Yuan, L. Shen and J.-J. Feng, *Int. J. Hydrogen Energy*, 2016, **41**, 8871–8880.

[193] H.-Y. Park, T.-Y. Jeon, J. H. Jang, S. J. Yoo, K.-H. Choi, N. Jung, Y.-H. Chung, M. Ahn, Y.-H. Cho and K.-S. Lee, *Appl. Catal. B Environ.*, 2013, **129**, 375–381.

[194] F.-Q. Shao, X.-X. Lin, J.-J. Feng, J. Yuan, J.-R. Chen and A.-J. Wang, *Electrochim. Acta*, 2016, **219**, 321–329.

[195] J.-J. Feng, L.-X. Chen, X. Ma, J. Yuan, J.-R. Chen, A.-J. Wang and Q.-Q. Xu, *Int. J. Hydrogen Energy*, 2017, **42**, 1120–1129.

[196] X. Weng, Y. Liu, K.-K. Wang, J.-J. Feng, J. Yuan, A.-J. Wang and Q.-Q. Xu, *Int. J. Hydrogen Energy*, 2016, **41**, 18193–18202.

[197] S. Manivannan, Y. Seo and K. Kim, *J. Electrochem. Sci. Technol.*, 2019, **10**, 284–293.

[198] A. Higareda, S. Kumar-Krishnan, A. F. García-Ruiz, J. Maya-Cornejo, J. L. Lopez-Miranda, D. Bahena, G. Rosas, R. Pérez and R. Esparza, *Nanomaterials*, 2019, **9**, 1644.

[199] J.-H. Choi, K.-W. Park, I.-S. Park, K. Kim, J.-S. Lee and Y.-E. Sung, *J. Electrochem. Soc.*, 2006, **153**, A1812–A1817.

[200] J. Luo, P. N. Njoki, Y. Lin, L. Wang and C. J. Zhong, *Electrochem. commun.*, 2006, **8**, 581–587.

[201] B. R. Peelle, E. M. Krauland, K. D. Wittrup and A. M. Belcher, *Langmuir*, 2005, **21**, 6929–6933.

[202] A. Sengupta, C. K. Thai, M. S. R. Sastry, J. F. Matthaei, D. T. Schwartz, E. J. Davis and F. Baneyx, *Langmuir*, 2008, **24**, 2000–2008.

[203] R. R. Naik, S. J. Stringer, G. Agarwal, S. E. Jones and M. O. Stone, *Nat. Mater.*, 2002, **1**, 169.

[204] G. Yang, D. Chen, P. Lv, X. Kong, Y. Sun, Z. Wang, Z. Yuan, H. Liu and J. Yang, *Sci. Rep.*, 2016, **6**, 35252.

[205] D. Chen, C. Li, H. Liu, F. Ye and J. Yang, *Sci. Rep.*, 2015, **5**, 11949.

[206] L. Yang, M. B. Vukmirovic, D. Su, K. Sasaki, J. A. Herron, M. Mavrikakis, S. Liao and R. R. Adzic, *J. Phys. Chem. C*, 2013, **117**, 1748–1753.

[207] P. Strasser, S. Koh, T. Anniyev, J. Greeley, K. More, C. Yu, Z. Liu, S. Kaya, D. Nordlund and H. Ogasawara, *Nat. Chem.*, 2010, **2**, 454–460.

[208] L. Bu, N. Zhang, S. Guo, X. Zhang, J. Li, J. Yao, T. Wu, G. Lu, J.-Y. Ma and D. Su, *Science*, 2016, **354**, 1410–1414.

[209] J. Wu, P. Li, Y.-T. F. Pan, S. Warren, X. Yin and H. Yang, *Chem. Soc. Rev.*, 2012, **41**, 8066–8074.

[210] H. Dau, C. Limberg, T. Reier, M. Risch, S. Roggan and P. Strasser, *ChemCatChem*, 2010, **2**, 724–761.

[211] C. C. L. McCrory, S. Jung, J. C. Peters and T. F. Jaramillo, *J. Am. Chem. Soc.*, 2013, **135**,

16977–16987.

[212] M. W. Kanan and D. G. Nocera, *Science*, 2008, **321**, 1072–1075.

[213] Y. Liu, K. Ai and L. Lu, *Chem. Rev.*, 2014, **114**, 5057–5115.

[214] J. P. Park, M. Do, H.-E. Jin, S.-W. Lee and H. Lee, *ACS Appl. Mater. Interfaces*, 2014, **6**, 18653–18660.

[215] Y. Surendranath, M. Dinca and D. G. Nocera, *J. Am. Chem. Soc.*, 2009, **131**, 2615–2620.

[216] N. Dubouis and A. Grimaud, *Chem. Sci.*, 2019, **10**, 9165–9181.

[217] N. M. Markovića, S. T. Sarraf, H. A. Gasteiger and P. N. Ross, *J. Chem. Soc. Faraday Trans.*, 1996, **92**, 3719–3725.

[218] N. Mahmood, Y. Yao, J. Zhang, L. Pan, X. Zhang and J. Zou, *Adv. Sci.*, 2018, **5**, 1700464.

[219] R. Subbaraman, D. Tripkovic, D. Strmcnik, K.-C. Chang, M. Uchimura, A. P. Paulikas, V. Stamenkovic and N. M. Markovic, *Science*, 2011, **334**, 1256–1260.

[220] L. Wang, Y. Zhu, Z. Zeng, C. Lin, M. Giroux, L. Jiang, Y. Han, J. Greeley, C. Wang and J. Jin, *Nano energy*, 2017, **31**, 456–461.

[221] J. Bai, D. Liu, J. Yang and Y. Chen, *ChemSusChem*, 2019, **12**, 2117–2132.

[222] E. A. Monyoncho, S. N. Steinmann, C. Michel, E. A. Baranova, T. K. Woo and P. Sautet, *ACS Catal.*, 2016, **6**, 4894–4906.

[223] W. Du, K. E. Mackenzie, D. F. Milano, N. A. Deskins, D. Su and X. Teng, *ACS Catal.*, 2012, **2**, 287–297.

[224] E. A. Monyoncho, S. N. Steinmann, C. Michel, E. A. Baranova, T. K. Woo and P. Sautet, *ACS Catal.*, 2016, **6**, 4894–4906.

[225] H. Wang, C. Xu, F. Cheng and S. Jiang, *Electrochem. Commun.*, 2007, **9**, 1212–1216.

[226] Y. Xia, P. Yang, Y. Sun, Y. Wu, B. Mayers, B. Gates, Y. Yin, F. Kim and H. Yan, *Adv. Mater.*, 2003, **15**, 353–389.

[227] K. A. Schwarz, R. Sundararaman, T. P. Moffat and T. C. Allison, *Phys. Chem. Chem. Phys.*,

2015, **17**, 20805–20813.

[228] Z. Cui, P. J. Kulesza, C. M. Li and W. Xing, *Int. J. Hydrogen Energy*, 2011, **36**, 8508–8517.

[229] Z. M. Cui and C. M. Li, *Chem. Commun.*, 2011, **47**, 8418–8420.

[230] Y. Qiao, S.-J. Bao and C. M. Li, *Energy Environ. Sci.*, 2010, **3**, 544–553.

[231] C.-J. Zhong, J. Luo, B. Fang, B. N. Wanjala, P. N. Njoki, R. Loukrakpam and J. Yin, *Nanotechnology*, 2010, **21**, 62001.

[232] A. J. Patil, J. L. Vickery, T. B. Scott and S. Mann, *Adv. Mater.*, 2009, **21**, 3159–3164.

[233] Y. Hatakeyama, M. Umetsu, S. Ohara, F. Kawadai, S. Takami, T. Naka and T. Adschiri, *Adv. Mater.*, 2008, **20**, 1122–1128.

[234] J. K. Stolarczyk, S. Bhattacharyya, L. Polavarapu and J. Feldmann, *ACS Catal.*, 2018, 3602–3635.

[235] J. Rosen, G. S. Hutchings, Q. Lu, S. Rivera, Y. Zhou, D. G. Vlachos and F. Jiao, *ACS Catal.*, 2015, **5**, 4293–4299.

[236] Q. Lu, J. Rosen, Y. Zhou, G. S. Hutchings, Y. C. Kimmel, J. G. Chen and F. Jiao, *Nat. Commun.*, 2014, **5**, 1–6.

[237] F. Marques Mota, D. L. T. Nguyen, J.-E. Lee, H. Piao, J.-H. Choy, Y. J. Hwang and D. H. Kim, *ACS Catal.*, 2018, **8**, 4364–4374.

[238] Y. Chen, Y. Huang, T. Cheng and W. A. Goddard III, *J. Am. Chem. Soc.*, 2019, **141**, 11651–11657.

[239] T. K. Todorova, M. W. Schreiber and M. Fontecave, *ACS Catal.*, 2019, **10**, 1754–1768.

[240] G. L. De Gregorio, T. Burdyny, A. Loiudice, P. Iyengar, W. A. Smith and R. Buonsanti, *ACS Catal.*, 2020, **10**, 4854–4862.

[241] X. Lu, T. Yu, H. Wang, L. Qian and P. Lei, *ACS Catal.*, 2020, **10**, 8860–8869.

[242] N. Sharma, A. Bajpai, P. K. Yadav, S. Nellaiappan, S. Sharma, C. S. Tiwary and K. Biswas, *ACS Sustain. Chem. Eng.*, 2020, **8**, 12142–12150.

[243] J. Rosen, G. S. Hutchings, Q. Lu, S. Rivera, Y. Zhou, D. G. Vlachos and F. Jiao, *ACS Catal.*, 2015, **5**, 4293–4299.

[244] A. A. Permyakova, B. Han, J. O. Jensen, N. J. Bjerrum and Y. Shao-Horn, *J. Phys. Chem. C*, 2015, **119**, 8023–8031.

[245] N. M. Bedford, H. Ramezani-Dakhel, J. M. Slocik, B. D. Briggs, Y. Ren, A. I. Frenkel, V. Petkov, H. Heinz, R. R. Naik and M. R. Knecht, *ACS Nano*, 2015, **9**, 5082–5092.

[246] C. Tamerler, E. E. Oren, M. Duman, E. Venkatasubramanian and M. Sarikaya, *Langmuir*, 2006, **22**, 7712–7718.

[247] S. Brown, *Nat. Biotechnol.*, 1997, **15**, 269–272.

[248] C. R. So, C. Tamerler and M. Sarikaya, *Angew. Chem. Int. Ed.*, 2009, **48**, 5174–5177.

[249] R. Coppage, J. M. Slocik, M. Sethi, D. B. Pacardo, R. R. Naik and M. R. Knecht, *Angew. Chem. Int. Ed.*, 2010, **49**, 3767–3770.

[250] L. B. Wright, J. P. Palafox-Hernandez, P. M. Rodger, S. Corni and T. R. Walsh, *Chem. Sci.*, 2015, **6**, 5204–5214.

[251] I. V. Korendovych and W. F. DeGrado, *Q. Rev. Biophys.*, 2020, **53,** e3.

Chapter 2

Methodology of Nanomaterial Synthesis, Characterizations and Electrocatalytic Measurements

Chapter Preface

Chapter 2 describes the methodology of material synthesis, characterizations, and electrochemical techniques for electrocatalytic tests. This chapter serves as an introduction on the methods that are employed in the later chapters from Chapter 3 to 6 in this thesis. In Chapter 3 to 6, tobacco monsaic virus coat protein (TMVCP) was employed as a versatile bio-template to synthesize a series of metallic nanomaterials (MNMs) via "bottom-up" method. All syntheses were carried out at room temperature under mild conditions. Various means of microscopy and spectroscopy were implemented to characterize the as prepared MNMs in terms of size, shape, metal surface charge states, crystallinity, and optical properties. After synthesis, the materials were purified and prepared as catalyst ink on glassy carbon electrode for electrochemical tests. The electrocatalytic performance of the MNMs were evaluated mainly in three aspects including activity, selectivity, and stability. Different electrochemical characterization techniques were employed and Chapter 2 serves as a guide on how the data obtained from these techniques are used for assessing catalyst performance.

2.1 Synthesis of Protein-Templated Nanomaterials throughout the Thesis

The bio-template used in this thesis is the tobacco mosaic virus coat protein (TMVCP). Tobacco mosaic virus is a rod-shaped plant virus that consists of a single stranded RNA genome surrounded by ~2300 copies of identical coat protein subunits.[1,2] The RNA-free TMVCP self-assembles into different morphologies, depending on solution ionic strength and pH, as presented in Scheme 2.1. For example, in the pH range of 6.5 to 7.5, the dominant species is disk protein, with the diameter of the whole ring 18 nm and inner channel 4 nm. Increasing pH to alkaline conditions, the disk protein disassembles into A protein, which is a mixture of monomers and oligomers. In Chapter 2 and 3, the disk-shape protein was used as template to synthesize silver and platinum nanoring, respectively. In Chapter 4, 5 and 6, A protein was also employed to synthesize metallic nanoparticles. TMVCP expressed and purified from Tuner (DE3) pLysS competent cells and stored at -80 °C was first thawed to room temperature and dialyzed into solution with desired pHs.

Metallic salts were then incubated with the protein, in which the metal ions can bind with the protein via electrostatic interactions. In Chapter 3, the silver salts were reduced to zerovalent silver via photoreduction. In Chapter 4, 5 and 6, the metal salts were reduced by a chemical reagent sodium borohydride ($NaBH_4$).

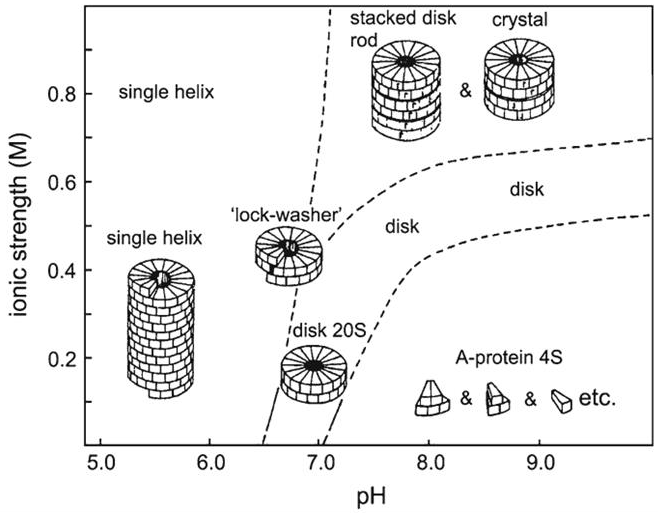

Scheme 2.1: Phase diagram of TMVCP under different solution pH and ionic strength conditions. Reprinted from ref.[3] . Copyright, Elsevier 2014.

2.2 MNM Characterizations

Characterization techniques of the as prepared MNMs in this thesis include ICP-OES (inductively coupled plasma optical emission spectroscopy), UV-vis (UV-visible spectroscopy), CD (circular dichroism spectroscopy), PXRD (powder x-ray diffraction), XPS (x-ray photoelectron spectroscopy), TEM (transmission electron diffraction), HR-TEM (high resolution TEM), SAED (selected area electron diffraction), and STEM-EDS (scanning transmission electron microscopy-energy dispersive x-ray spectroscopy). Table 2.1 summarizes the information obtained from different characterization techniques in this thesis.

Table 2.1: MNM characterization techniques and the derived information.

Characterization Methods	Main Information Extracted
ICP-OES	Element concentration in the sample
UV-vis	Material concentration, nanoparticle optical property
CD	Protein secondary structure
PXRD	Composition, crystal planes, sample purity
XPS	Element composition, electronic structure, valence states
TEM	Nanoparticle size, shape, size distribution, aggregation state
HR-TEM	Crystal lattice on single particle
SAED	Identify crystal structure on some particles in the selected area in TEM
STEM-EDS	Composition, elemental distribution and quantification

2.2.1 ICP-OES

ICP-OES is an analytical method used to determine the concentration of certain elements in the measured samples. In principle, the collision between argon atoms and electrons with high energies generates argon plasma, which can excite the electrons of the metal ions to higher energy levels.[4] When the electrons drop back to the lower energy states, the energy is released as photons at wavelengths characteristic of a particular element and the light intensity is proportional to the concentration of the elements. In Chapter 3 and 4, the MNMs were first digested into the corresponding metal cations. Standard metal cation solutions with known concentrations were prepared to generate the calibration curves, which was then used to calculate the concentration of metal cations in the digested sample.

2.2.2 UV-vis Spectroscopy

Ultraviolet and visible light can be used to excite the bonding and non-bonding electrons of molecules, which produces absorption peaks at certain wavelengths. The Beer-Lamber law demonstrates that the absorbance of the analyte is proportional to the concentration of the absorber in the sample, which can be used to quantify the concentration of the analyte. In this thesis, UV-

vis spectroscopy is employed as a facile and low-cost method to study the optical property of the formed MNMs. Noble metal NPs such as gold and silver NPs have the so-called localized surface plasmonic resonance (LSPR) effect.[5,6] The UV-vis light irradiation can stimulate and induce collective oscillation of the surface electrons of NPs, which is characterized by a surface plasmonic band at certain wavelength in the UV-vis spectrum. The shape and position of the plasmonic peak is related to the NP size, shape, binding ligand and agglomeration state.[7,8] In practice, solution samples were directly injected into a quartz cell for measurements.

2.2.3 CD Spectroscopy

CD spectroscopy is an excellent tool to extract information on the secondary structure of chiral biological molecules such as peptide, protein, and DNA.[9] In CD, a beam of light passes through a filter or prism to generate left-handed and right-handed circularly polarized light. When the polarized light travels in an optically active medium (e.g. protein solution), the chromophores of the protein interact with the left and right-circularly polarized light differently and results in unequal absorption in the spectrum.[10] Different secondary structures in the protein (α-helix, β-sheet, random coil) have their own characteristic CD spectrum,[11] which makes it possible to analyze the structure of the proteins and monitor their conformational change caused by environment stimulation or binding process. In Chapter 5, CD was employed to examine the secondary structure of TMVCP protein before and after binding to MNPs.

2.2.4 PXRD

PXRD is a widely used technique to characterize NMs as it can provide important information on sample composition, purity, material crystalline structure, lattice parameters and crystalline grain size.[12] When the x-rays produced by a diffractometer interact with the measured sample, the beam can be either reflected off the surface or diffracted by the atoms in the crystalline sample. The diffraction happens when the wavelength of the incident rays, the diffraction angle and the lattice spacing satisfy the Bragg's law.[13] In this thesis, PXRD was applied to identify the MNM composition, as well as a bulky complementary method to verify the crystalline information obtained from SAED that is only representative of a small number of particles. To prepare samples for PXRD measurement, the MNM suspension was desalted, washed with water by centrifuge, and then concentrated. Afterward, the concentrated suspension was dried on a glass substrate for

measurement. The PXRD data was compared to standard database (Joint Committee on Powder Diffraction Standards, JCPDS) to identify material composition.

2.2.5 XPS

XPS is a powerful tool to analyze the surface chemistry of MNMs, which can be used to detect the elemental composition, chemical state and electronic state of the material covered on the sample surface.[14] In XPS, monochromatic X-rays are used to irradiate the sample surface and the photons are absorbed an atom or molecule, which can eject some electrons. According to the photoelectric effect, the kinetic energies of the ejected electrons depend on the incident photon energy and the binding energy of the electrons.[15] Thus, the binding energy can be measured and is elemental specific. In this thesis, XPS was used to confirm the formation of zerovalent MNMs, as well as to detect any interaction between the MNM and TMVCP. Samples for XPS measurement were prepared in the same procedure as for the XRD in section 2.2.4, except the substrate was a silicon wafer instead of a piece of glass.

2.2.6 TEM, HR-TEM, SAED, and STEM-EDS

TEM is a microscopy technique that enables morphological characterization of materials at nanoscale due to the smaller de Brogile wavelength of electrons. A beam of electrons is transmitted through a specimen, and an image is formed from the interaction between the electrons and the sample on the grid.[15] HR-TEM image is obtained at higher magnification that can directly image the crystallographic structure of the sample at atomic level. SAED is an electron diffraction technique that can be performed inside a TEM instrument. The electron beam is diffracted by a chosen small area and can reveal the crystalline information of the material.[16] To prepare samples for these measurements, MNM suspensions were drop cast onto carbon-coated copper grids for ~5 min, after which the residues were removed with a filter paper. STEM-EDS is a powerful combined technique that can achieve atomic-resolution to map the location of individual elements in a given area.[17] It is especially useful in probing the composition and elemental distribution of nanomaterials composed of multiple components. To prepare samples, MNM suspensions were purified to remove the carbon residues, and then drop cast onto the silica-coated copper grids, to eliminate the effect from carbon contamination.

2.3 Electrochemical Methods for Evaluating MNM Catalytic Performance

In electrocatalysis, three key factors are commonly used to assess the performance of a catalyst: activity, selectivity and stability. Throughout this thesis, activity is mostly analyzed by CV (cyclic voltammetry), LSV (linear sweep voltammetry); Tafel analysis and impedance are also used to reveal kinetics information. Selectivity is evaluated by constant potential electrolysis and the product is quantified in combination with other non-electrochemical methods such as gas chromatographic (GC) and NMR (nuclear magnetic resonance), whereas stability is evaluated by chronoamperometry test.

2.3.1 Activity

2.3.1.1 CV, LSV and Underpotential Deposition

Activity of an electrocatalyst is normally assessed by CV and LSV. In general CV and LSV experiments, a potential is applied to the working electrode (WE) and is swept linearly versus time. While in LSV, the potential is ramped in only one direction and stops at the ending potential, it continues to be ramped in the opposite direction and returns to the initial value in CV. In both techniques, the current (I) at the WE is recorded and the final plot is a current (or current density) versus applied potential (E) curve. From a CV or LSV plot, onset potential (where the reaction starts) and the current density (J) at a given overpotential (η) are the two important electrochemical parameters for judging the catalytic activity. A smaller difference between the onset potential and the equilibrium potential of the redox couple means a smaller barrier to trigger the reaction. A higher current density is related to a higher reaction rate on the electrode. The current density can be reported by both specific activity (SA) and mass activity (MA), in which the measured current is normalized by the electrode surface area ($J = I/S$) or the mass of the catalyst ($J = I/m$). Nanocatalysts are characterized by their high surface-to-volume ratio and the electrochemically active surface area (ECSA) can be significantly larger than the geometric area of the WE.[18] Therefore, it is important to use the ECSA values as the real surface area for fair comparison between different nanocatalysts. In Chapter 3 and 4, ECSA of MNMs is estimated by underpotential deposition (UPD) method, in which a species electrodeposits a monolayer onto a

foreign substrate at a much less negative potential than its own reduction potential.[19] With this phenomenon, the ECSA can be calculated by running CV in a deoxygenated blank electrolyte using the following Eq. 2.1,

$$\mathrm{ECSA} = \frac{\mathrm{Q}}{\mathrm{C}} \tag{2.1}$$

where Q is the charge (integrated area of the adsorption/desorption region), C is the charge of full monolayer coverage of the atoms onto a clean electrode.

2.3.1.2 Tafel Analysis and Electrochemical Impedance Spectroscopy

Tafel analysis and electrochemical impedance spectroscopy (EIS) are widely used to study the kinetics of an electrode reaction. In experiment related to Tafel analysis, LSV is swept a low scan rate and the current-potential plot is transformed into logarithm of current density (log(j)) versus η plot. The linear portion of the plot can be fitted into the Tafel equation (Eq. 2.2), which describes the relationship between the η and the reaction rate:

$$\eta = \mathrm{a} + \mathrm{b}\log \mathrm{j} \tag{2.2}$$

Two important parameters that can be extracted from Eq. 2.2 are the slope b and the exchange current density (J_0), the current density when η = 0. While the Tafel slope is generally used to reveal information on the mechanism of the reaction and the rate determining step (RDS), J_0 is a parameter to compare the intrinsic rate of the electron transfer among different catalysts.[20]

Unlike all the above direct current (DC) techniques, EIS is an analytical method that applies an alternating signal of small magnitude as the perturbation source to the WE and observes its response. Due to its ability to unravel complex surface process in electrochemistry, EIS has wide applications in fuel cell,[21] batteries,[22] and corrosion,[23] etc. While in DC techniques, ohm's law defines that the resistance (R) is represented as E = i × R, it is E = i× Z in EIS, in which vector Z is the impedance of the circuit. In Chapter 3 and 4, the impedance is recorded as a response to an AC potential and the data is represented in Nyquist plot, which displays real (Z_{Re}) and imaginary (Z_{Im}) parts in x- and y-axis at different frequencies, respectively. Afterward, the plot is fitted into an equivalent circuit model composed of resistors and capacitors that enables the extraction of charge-transfer resistance (R_{ct}), which is a convenient index to gauge the electrode kinetics.

2.3.2 Selectivity

For electrode reactions that may involve multiple possible products, the measured overall current can have contributions from different reaction pathways.[24] It is thus important to separate the current contribution from reaction of interest to assess the selectivity of the catalyst. Faradaic Efficiency (FE) is an indicator of selectivity, which can be calculated as the ratio between the charge needed to form the specific amount of one product and the total charge passed during electrolysis, and a higher FE value means a higher selectivity.[25] In Chapter 3, FE is determined by electrolysis in combination with other non-electrochemical techniques for product distribution analysis. Specifically, the carbon dioxide electroreduction reaction is inevitably accompanied by the hydrogen evolution reaction in aqueous electrolyte. To evaluate the selectivity of Ag catalysts, constant potential electrolysis is applied for a specific amount of time, and the gaseous and liquid products are quantified with assistance of GC and NMR.

2.3.3 Stability

Durability is of vital importance for an electrocatalyst to be applied in practical electrocatalysis. Catalyst can degrade during long time operation, which is normally caused by nanoparticle aggregation, metal dissolution and gas evolution that leads to material's physical detachment from the electrode.[24] Chronoamperometry (CA) test is used to assess the catalyst stability in this thesis. A potential is applied to the WE and current is monitored as a function of time. A catalyst with higher durability will thus show less decay in current during operation. In addition, after the CA test, the catalyst can be further characterized by TEM and XPS to compare if there is any change in morphology and metal electronic states after durability test. Besides CA, other methods such as running CV or LSV for specific number of cycles are also protocols to test catalyst's long time stability.

2.4 Summary

This chapter outlines the workflow of practical electrocatalysis in this thesis, from MNM preparations, characterizations to electrochemical measurements. For bio-templated synthesis, care should be taken regarding the metal precursors to template ratio, reducing reagent, reaction

time and temperature. The characterization techniques used throughout the thesis are the most common methods for nanomaterial characterizations. To reveal a clearer picture of the bio-interface formed on the nanoparticle surface and reveal structure/function at atomic level, more advanced methods are required such as XAFS (x-ray absorption fine-structure spectroscopy). The electrochemical measurements introduced in this chapter are also the typical methods for bulk tests in electrocatalysis. More in-depth analysis in the electrode reaction mechanisms can be carried out if assisted by other methods such as in situ techniques and microscale measurements.

2.5 References

[1] H. Wu, D. Zhong, Z. Zhang, Y. Li, X. Zhang, Y. Li, Z. Zhang, X. Xu, J. Yang and Z. Gu, *Adv. Mater.*, 2020, **32**, 1904958.

[2] H. Hu, Y. Zhang, S. Shukla, Y. Gu, X. Yu and N. F. Steinmetz, *ACS Nano*, 2017, **11**, 9249–9258.

[3] O. K. Zahr and A. S. Blum, in *Virus Hybrids as Nanomaterials. Methods in Molecular Biology (Methods and Protocols)*, eds. B. Lin and B. Ratna, Humana Press, Totowa, NJ, 2014, pp. 105–112.

[4] M. He, B. Hu, B. Chen and Z. Jiang, *Phys. Sci. Rev.*, 2017, **2**, 1–37.

[5] K. M. Mayer and J. H. Hafner, *Chem. Rev.*, 2011, **111**, 3828–3857.

[6] E. Petryayeva and U. J. Krull, *Anal. Chim. Acta*, 2011, **706**, 8–24.

[7] Y. Hong, Y.-M. Huh, D. S. Yoon and J. Yang, *J. Nanomater.*, 2012, **2012**, 759830.

[8] H. Bin Jeon, P. V. Tsalu and J. W. Ha, *Sci. Rep.*, 2019, **9**, 13635.

[9] S. Beychok, *Science*, 1966, **154**, 1288–1299.

[10] N. J. Greenfield, *Nat. Protoc.*, 2006, **1**, 2876–2890.

[11] A. Micsonai, F. Wien, L. Kernya, Y.-H. Lee, Y. Goto, M. Réfrégiers and J. Kardos, *Proc. Natl. Acad. Sci.*, 2015, **112**, E3095–E3103.

[12] C. F. Holder and R. E. Schaak, *ACS Nano*, 2019, **13**, 7359–7365.

[13] M. Nasrollahzadeh, M. Atarod, M. Sajjadi, S. M. Sajadi and Z. Issaabadi, in *An Introduction to Green Nanotechnology*, eds. M. Nasrollahzadeh, S. M. Sajadi, M. Sajjadi, Z. Issaabadi and M. B. T.-I. S. and T. Atarod, Elsevier, 2019, vol. 28, pp. 199–322.

[14] S. Mourdikoudis, R. M. Pallares and N. T. K. Thanh, *Nanoscale*, 2018, **10**, 12871–12934.

[15] J. M. Hollander and W. L. Jolly, *Acc. Chem. Res.*, 1970, **3**, 193–200.

[16] W. F. Tivol, *Micros. Today*, 2010, **18**, 22–28.

[17] N. R. Lugg, G. Kothleitner, N. Shibata and Y. Ikuhara, *Ultramicroscopy*, 2015, **151**, 150–159.

[18] D. Voiry, M. Chhowalla, Y. Gogotsi, N. A. Kotov, Y. Li, R. M. Penner, R. E. Schaak and P. S. Weiss, *ACS Nano*, 2018, **12**, 9635–9638.

[19] E. Herrero, L. J. Buller and H. D. Abruña, *Chem. Rev.*, 2001, **101**, 1897–1930.

[20] T. Shinagawa, A. T. Garcia-Esparza and K. Takanabe, *Sci. Rep.*, 2015, **5**, 13801.

[21] S. Asghari, A. Mokmeli and M. Samavati, *Int. J. Hydrogen Energy*, 2010, **35**, 9283–9290.

[22] N. Meddings, M. Heinrich, F. Overney, J.-S. Lee, V. Ruiz, E. Napolitano, S. Seitz, G. Hinds, R. Raccichini, M. Gaberšček and J. Park, *J. Power Sources*, 2020, **480**, 228742.

[23] D. V Ribeiro and J. C. C. Abrantes, *Constr. Build. Mater.*, 2016, **111**, 98–104.

[24] J. Masa, C. Andronescu and W. Schuhmann, *Angew. Chem. Int. Ed.*, 2020, **59**, 15298–15312.

[25] R. Kas, R. Kortlever, A. Milbrat, M. T. M. Koper, G. Mul and J. Baltrusaitis, *Phys. Chem. Chem. Phys.*, 2014, **16**, 12194–12201.

Chapter 3

Biosynthesized Silver Nanoring as a Highly Efficient and Selective Electrocatalyst for CO_2 Reduction

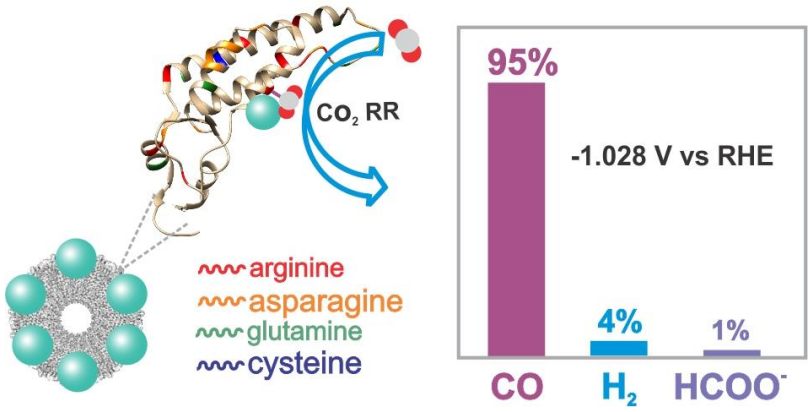

Chapter Preface

Scientific Contributions:

Chapter 3 presents the first example of applying a biosynthesized Ag nanoring material to catalyse CO_2 electroreduction. The synthesis features a simple, green and eco-friendly process. Furthermore, compared to spherical Ag nanoparticle made by pure chemical method and bulk Ag, Ag nanoring exhibits enhanced catalytic activity, reaction selectivity and material stability. Possible reasons for the excellent performance of the new material are discussed. This work provides new insight of exploring new bio-templates for fabricating green materials effective for CO_2 RR.

Public Information:

Chapter 3 is adapted from a previously published research article with permission from:

Y. Pan, W. J. Paschoalino, S. S. Bayram, A. S. Blum, J. Mauzeroll. Biosynthesized silver nanoring as a highly efficient and selective electrocatalysts for CO_2 reduction. *Nanoscale* **2019,** 11, 18595-18603.

Chapter Abstract

After the introductions of background and methodology in previous chapters, Chapter 3 presents our results in applying a bioinspired Ag material for electrocatalytic CO_2 reduction, which enriched the biotemplate library in this field. Inspiration from nature has driven the development and applications of greener inorganic nanomaterials prepared using bio-templates in the field of nanoscience. In Chapter 3, we report the superiority of using a biosynthesized silver nanoring material for CO formation in CO_2 saturated $KHCO_3$. Compared to bulk silver and free silver nanoparticles prepared by pure chemical reduction, this silver nanoring (assembled on tobacco mosaic virus coat protein) exhibits significantly enhanced activity and selectivity for the conversion of CO_2 to CO. The highest CO faradaic efficiency reaches 95.0% at an overpotential of 910 mV. Additionally, the CO partial current density is 2.7-fold higher than that of the free silver nanoparticles. The improved catalytic performance is believed to be related to the structuring ligand effect of the protein. The numerous functional groups on the protein may tune the reaction activity by influencing the binding energies of the intermediate species from CO_2 reduction or hydrogen evolution.

3.1 Introduction

Since the industrial revolution, the world has witnessed a rapid increase in carbon dioxide emission caused by the consumption of fossil fuels, leading to global climate change. While searching for alternatives to traditional fuels is important to solve the energy crisis, recycling carbon dioxide into useful chemical stocks and energy carriers can create a sustainable route.[1,2] As a stable chemical, converting carbon dioxide to other reduced carbon forms is difficult, and usually requires relatively harsh conditions like high temperature and pressure.[3–5] Amongst different methods, electrochemical CO_2 reduction is considered as a green, mild and economical route. Electricity can be easily accessed and is of low cost. However, CO_2 electroreduction is often challenged by a high reduction overpotential and poor selectivity.[6–8] In order to overcome these issues, different kinds of electrocatalysts have been developed aiming to decrease overpotential and improve reaction activity and selectivity.[8–12] Metals like gold,[13,14] silver,[15,16] and copper[17–20] are promising catalyst candidates for CO_2 reduction as they have weaker binding energy with *CO than with *H. In particular, Au and Ag have been demonstrated to be more selective towards the formation of carbon monoxide, an important chemical for the Fischer-Tropsch process.[21,22] Nanosized materials have attracted a lot of attention due to their unique surface and morphological properties compared to their bulk counterparts. Research attention has been devoted to searching for nanomaterials that have enhanced catalytic activity. Ag nanomaterials are excellent electrocatalysts with higher abundance and much lower cost than Au. For example, nanoporous Ag dealloyed from a Ag-Al precursor was synthesized and has shown extremely large surface area, creating large number of active step sites for CO_2 transformation.[15]

One classical method for producing well-defined nanomaterials is through chemical reduction. However, this is not an ecologically friendly, sustainable approach since it generally requires strong reducing agents to form nanoparticles, capping agents to stabilize them and relatively harsh conditions like elevated temperature in many cases.[23] These issues can be overcome by biological inspired reductions, which are nontoxic, greener and cleaner routes.[24] Some biological organisms contain natural reducing agents that can replace chemicals like sodium borohydride, hydrazine and hydrogen gas.[25] In addition, the synthesis can be carried out under very mild conditions. For instance, metallic nanoparticles prepared by using plant extracts represents an eco-friendly, easily-scaled up and inexpensive method.[26–28] There are also reports of fungus,[29,30] bacteria,[31–33] and algae[34] mediated synthesis of nanosilver. The enzymes in these microorganisms are responsible for the reduction of silver cations to form the nanoparticles. Due to the

special shape of the biological organisms, nanoparticles can be organized into ordered arrays that are difficult to achieve by traditional chemical methods.

Tobacco mosaic virus (TMV) is a plant virus with ~2130 identical coat protein subunits assembled around a single stranded RNA.[35] The RNA-free TMV coat protein (TMVCP) is capable of self-assembly into disk shapes in the pH range of 6.5 to 7.5, with the diameter of the whole ring 18 nm and inner channel 4 nm.[36] The disk shape TMVCP has previously been discovered to be an effective template to organize nanoparticles into different structures.[37–39] Under the mild neutral pH condition, the protein exposes a number of negatively charged residues, in particular aspartate and glutamate,[39] which allows electrostatic interactions with metal cations, triggering nanoparticle nucleation.

Initially, the motivation for developing bio-reduction methods is to increase the compatibility of nanomaterials in biological environment. In recent years, inspiration from nature has also driven people to apply biosynthesized metallic nanoparticles in various fields, including medicine for antimicrobial and anticancer activity,[40] organic catalysis,[41] sensors,[42] etc. However, the potential of using such materials in electrocatalysis has not been explored much. A few studies have shown that aside from the cleaner synthetic method to make bio-templated materials, some bio-supports can enhance the efficiency and energy density of electrocatalytic systems, since the well-organized structures allow better connection between the nanocatalyst and substrate.[43,44] To our knowledge, there is no prior report on applying biosynthesized silver nanostructure in electrocatalyzed CO_2 reduction.

In this chapter, a new approach for developing an electrocatalyst for the CO_2 reduction reaction is presented. A discrete silver nanoring (denoted as Ag NR) assembled on TMVCP was investigated as a catalyst, looking to improve the selectivity and current density for CO formation. Here, silver nitrate was incubated with the protein solution and then photoreduced to Ag(0) under UV light, forming a discrete ring structure. To assess the performance of the silver nanoring, comparison was made with bulk polycrystalline silver and free silver nanoparticles (denoted as Free NP) prepared by the chemical reduction method. These three materials were evaluated for electrochemical CO_2 reduction in $KHCO_3$ solution. Notably, compared to Free NP and bulk Ag, the Ag NR exhibited significantly improved CO product selectivity and current density, showing that the TMVCP plays an important role in improving the electrocatalytic performance of the assembled silver nanoring.

3.2 Experimental Section

3.2.1 Chemicals

$AgNO_3$ (99.0%), trisodium citrate (99.0%), $KHCO_3$ (99.7%), $Pb(NO_3)_2$ (99%), KCl (99.5%), nafion resin solution (~5 wt.% in mixture of lower aliphatic alcohol & H_2O), H_2SO_4 (98%) were purchased from Sigma Aldrich. $NaBH_4$ (98.0%) was from Acros. KCl (99.5%) and HNO_3 were from ACP Montreal and Caledon, separately. All chemicals are used without further purification. All solutions were prepared using Millipore MilliQ water (18.2 MΩ · cm).

3.2.2 Synthesis of Silver Nanoring on Wild Type TMV Coat Protein

TMVCP was expressed and purified according to a procedure published previously.[45] The purified protein stored at -80 °C in TEA buffer (20 mM, pH 7.2) was thawed to room temperature and then desalted into deionized water by desalting columns (Fisher Scientific). The protein concentration was determined by the absorbance at 282 nm (ε = 1.27 ml (mg cm)$^{-1}$) using UV/vis spectroscopy (Cary 100 Bio Spectrometer). The protein solution then sat at room temperature for 24 h. For nanoring synthesis, 1 mL of protein solution (0.3 mg/mL) was mixed with 125 µL of $AgNO_3$ solution (10 mM). The mixture was illuminated by UV light (365 nm) using a UVGL-55 lamp (6 W). The color changed to light pink within 1 minute. The mixture was purified by centrifugation twice and then resuspended in water. No thermal stability test of Ag NR was investigated, as all the related experiments were carried out under room temperature.

3.2.3 Synthesis of Free Silver Nanoparticles

Free silver nanoparticles were synthesized by a chemical reduction method.[45] 1 mL of ice cooled $NaBH_4$ solution (0.3 mM) was added to 98 mL of aqueous solution containing $AgNO_3$ (1.7 mg, 0.01 mmol) and trisodium citrate (25 mg, 0.01 mmol) under stirring. Stirring was continued for 3 h and the reaction mixture was then allowed to stand for 1 h. The mixture was purified and concentrated by centrifugation.

3.2.4 Material Characterizations

The optical property of the sample colloid was examined by UV-vis extinction spectra, which were collected using a Cary 100 Bio instrument. The TEM images were acquired using a Philips CM200 TEM at 200 kV. XPS was performed using a Thermo Scientific K-Alpha X-ray photoelectron spectroscopy system with a monochromatic Al Kα source ($\hbar\nu$ = 486.6 eV). PXRD patterns were recorded on a Bruker

D8 Advance diffractometer (Bruker AXS, Madison, WI) equipped with a Ni-filtered Cu-Kα (λ = 1.5406 Å) radiation source. The source was operated at 40 kV and 40 mA. 2θ was scanned from 20° to 90° (ħν = 1486.6 eV). Samples (*ca.* 200 µg, 180 µg Ag in Ag NR and Free NP respectively) were drop cast on clean glass substrates for characterization. ICP-OES (Agilent Technologies, 5000) was used to measure the actual amount of Ag in the colloid. Five standard solutions of Ag were prepared to generate the calibration curve used to calculate the concentration of the digested sample.

3.2.5 Working Electrode Preparation

40 µL of Ag NR suspension was mixed with nafion solution (6 µL) and then sonicated for 3 min to form a catalyst ink (Note: carbon black was not used in ink preparation). A glassy carbon electrode (GCE) of 3 mm in diameter was polished with alumina paste (from 3 µm to 1 µm to 0.05 µm) and thoroughly cleaned with Millipore MilliQ water (18.2 MΩ · cm). 5 µL of catalyst ink was loaded on GCE and dried under ambient conditions for 1 hour. Free Ag nanoparticle ink solution was prepared in the same way. The actual Ag loading amount of Ag NR and Free NP were 11.5 µg/cm^2 and 10.3 µg/cm^2 respectively. Bulk silver (99.99%, Goodfellow) was mechanically polished before use.

3.2.6 Electrochemical Surface Area Measurement

UPD of lead on silver was used to determine the electrochemical surface area. Cyclic voltammetry was conducted in a solution containing 5 mM $Pb(NO_3)_2$, 10 mM KCl and 10 mM HNO_3. The scan rate was 10 mV/s and the potential range was from 0 to -0.6 V (vs. SCE). The area was calculated by the Pb UPD corresponding to a charge of 600 µC/cm^2.[46]

3.2.7 CO_2 Reduction Reaction Test by Linear Sweep Voltammetry

All CO_2 electrochemical reduction experiments were conducted using an Interface 1000E potentiostat (Gamry Instruments). LSV was performed in an air-tight, three electrode electrochemical cell, with the cathode and anode separated by a nafion cation exchange membrane. Platinum wire and Ag/AgCl served as counter and reference electrode respectively. The electrolyte 0.5 M $KHCO_3$ was bubbled with CO_2 (99.5%, Air Liquid) for at least 1 hour to reach pH 7.2 before each measurement. LSV data was collected from -0.2 to -1.8 V (vs. Ag/AgCl) with a scan rate of 50 mV/s. The potential was converted to reversible hydrogen electrode (RHE) using the following equation: Potential (V. vs RHE) = Potential (V vs. Ag/AgCl) + 0.197 V + 0.0592 V × pH. Chronoamperometry tests were conducted at each fixed potential

for 1 hour. The electrolyte was stirred at a rate of 600 rpm with a magnetic stirring bar. After electrolysis, a small fraction of gaseous products were collected by an air tight syringe and quantified by gas chromatography (Shimadzu GC-2014) with a flame ionization detector (for CO and hydrocarbons) and another GC (Shimadzu GC-8A) with a thermal conductivity detector (for H_2). Helium (99.999%, Air Liquid) was used as the carrier gas. The amount of gas product was determined by calibration curves. Liquid products were collected from the 500 MHz ^{1}H NMR using dimethyl sulfoxide as an internal standard and D_2O as the deuterium solvent. Faradaic efficiency (FE, the ratio between the charge needed to form the specific amount of one product and the total charge passed during the electrolysis) was calculated from dividing the amount of charge needed for each product by the total charged passed during the one hour electrolysis (E.q 3.1). CO partial current density was calculated using Faraday's Law (Eq. 3.2).[47] Since the produced CO is toxic, the electrochemical cell was placed in a fume hood for post process cleaning.

$$\mathrm{FE(CO\ or\ H_2)} = \frac{2 \times \mathrm{F} \times \mathrm{n(CO\ or\ H_2)}}{\int_0^{3600} \mathrm{I_{(total)}\,dt}} \times 100\% \tag{3.1}$$

$$\mathrm{J\ (CO)} = \frac{2 \times \mathrm{n\ (CO)}}{\mathrm{F} \times \mathrm{S} \times 3600\mathrm{S}} \tag{3.2}$$

Where F is the Faraday constant, n is the mol of CO or H_2 calculated from GC results, I (total) is the current during electrolysis, S is the electrochemical active surface area.

3.2.8 Electrochemical Impedance Spectroscopy (EIS)

EIS experiments were performed in CO_2 saturated 0.5 M $KHCO_3$ solution. The experimental apparatus was the same as for LSV measurements. Nyquist plots were recorded at open circuit potential at a small (10 mV) AC voltage amplitude with a frequency range of 10^4 to 10^{-2} Hz using a VSP300 potentiostat (Biologic).

3.3 Results and Discussion

3.3.1 Ag NR and Free NP Synthesis

Studies have shown that Ag(I) has a favorable interaction with negatively charged amino acids,[48] and that the mechanism for its photoreduction is believed to be radical based.[49] The combination of carboxylate

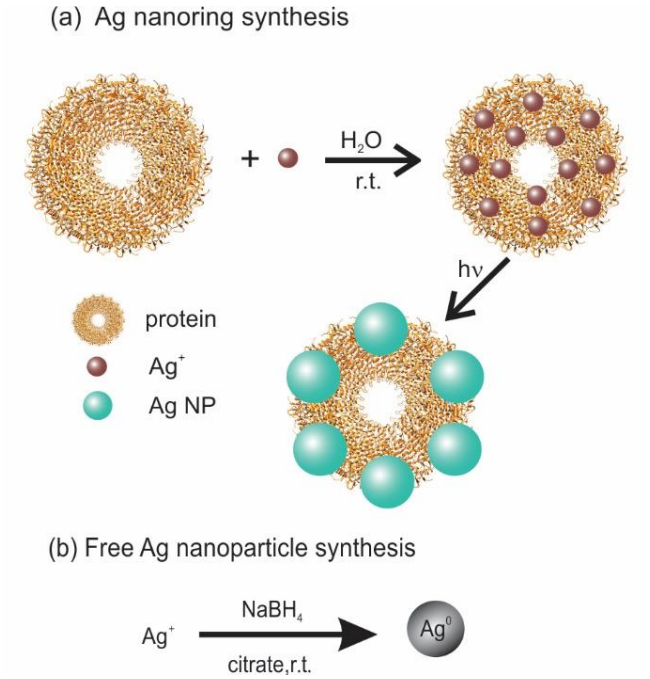

Figure 3.1: Synthesis Procedures of the Ag NR (a) and Free Ag nanoparticles (b).

groups present in the protein and UV radiation facilitate the reduction of silver ions into nanoparticles, in which carboxylate groups may act as the nucleation sites for the nanoparticle growth.[45] Figure 3.1a illustrates the preparation of the Ag NR. TMVCP (assembled in disk forms in water, Figure A1.1a in Appendix 1) was mixed with $AgNO_3$. Under UV illumination, Ag^+ is reduced to nanoparticles within 1 minute (the TMVCP alone remains as an intact disk after illumination under such a short time, see Figure A1.1b in Appendix 1). The whole process is straightforward and rapid compared to most chemical methods to make nanomaterials. Free NP was prepared by chemically reducing $AgNO_3$ with $NaBH_4$ in the presence of trisodium citrate (Figure 3.1b).

The optical properties of the synthesized Ag NR and Free NP colloids were examined by UV-vis spectroscopy (Figure 3.2). While Free NP shows the typical single absorbance of Ag at ~ 400 nm, the ring colloid not only shows the characteristic peak at 400 nm from the single particles in the ring, but also an additional broad surface plasmon resonance band centered at ~ 470 nm, likely arises from the in-plane coupling of the single particles on the ring.[45]

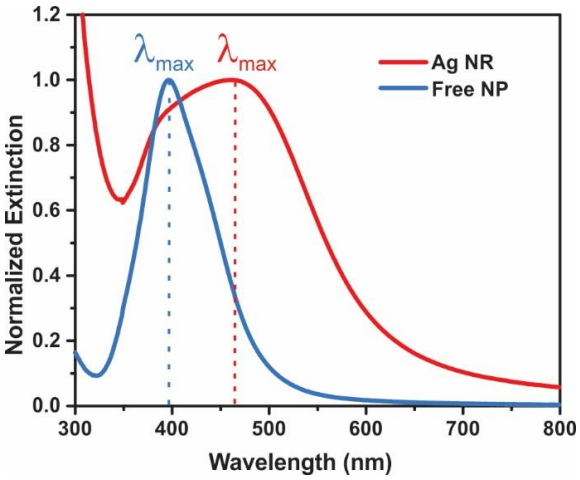

Figure 3.2: UV/vis spectra of Ag NR (red) and Free NP (blue).

The shape and size of the Ag NR was confirmed by TEM. It was found that three to six single nanoparticles were assembled on the protein (Figure 3.3a), forming a discrete ring structure. The outer diameter of the whole nanoring (protein included) has an average value of 30 nm (Figure 3.3c), with single particles on the ring 6~ 8 nm in diameter (Figure 3.3d), which is close to 8 nm Free NP as shown in Figure 3.3b, 3.3e.

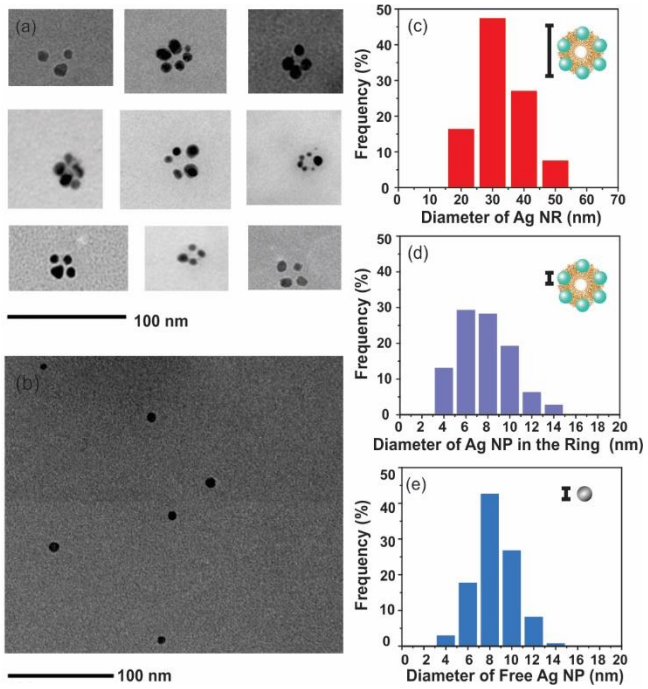

Figure 3.3: TEM images of Ag NR (a) and Free NP (b); Size distributions of the whole ring (c), the single particles in the ring (d) and Free NP (e).

XPS measurements were carried out to further identify the presence of Ag (0) (Figure 3.4a). By XPS, both Ag NR and Free NP yield clear spectra characteristic of Ag 3d peaks confirming the formation of silver nanoparticles. The peaks (at around 368.08 eV and 373.88 eV) are to some extent asymmetric, implying the small amount of Ag (I) species.[50] We also measured the S 2p and N 1s spectra in the pure TMVCP and Ag NR. For S 2p (Figure 3.4a, inset), the peak centered at around 162.0 eV (although not sharp) is associated with Ag NP-S intreaction.[51] In pure protein (Figure 3.4a, black), the peak is shifted to 163.5 eV and the ratio of this peak to peak at 169.0 eV is changed, which means the protein modifies the charging state of the Ag nanoparticle, inducing surface localization of the electrons. However, this peak could also originate from Ag cation-S interaction.

Nitrogen element is quite abundant in the protein (N is 16.12% atomic ratio as identified by XPS, Ag is 0.2%), the N 1s peaks in protein and Ag NR do not show a significant difference (Figure 3.4b). According to the structure of Ag NR, Ag only binds to the outer surface of the protein. Thus, compared to the massive amount of N atoms on the relatively inner part in the disk protein, only limited N atoms coordinate with Ag. This could be the reason why we do not see the obvious change in N 1s peak. In a study by Kim et

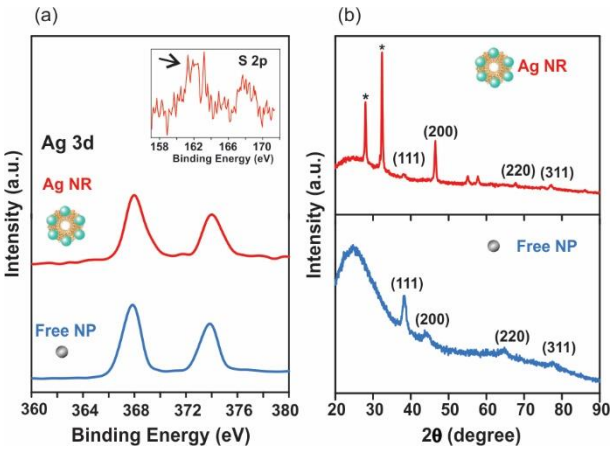

Figure 3.4: XPS spectra of Ag NR and Free NP (a); XRD data of Ag NR and Free NP (b).

al.,[52] it was also found that the oleylamine capped Ag NPs could not give clear N peak, due to the limited Ag-N coordination.

XRD was used to characterize the crystallinity of the Ag materials (Figure 3.4b). Results indicate that the synthesized Ag NR and Free NP are face-centered cubic Ag crystal structures with four distinct diffraction peaks at 37.08°, 44.61°, 64.78°, and 78.83°, corresponding to (1 1 1), (2 0 0), (2 2 0), and (3 1 1) planes respectively (JCPDS file no. 84-0713 and 04-0783). Compared to Free NP, Ag NR shows additionally two strong peaks at 27.99°, 32.40° and two minor peaks between 55.00° and 60.00° (marked with stars), which suggests the presence of a crystalline biophase coexisting with the silver nanocrystals in the structure. Similar results were reported in several studies on synthesizing silver nanoparticle by using coleus aromaticus leaf extract,[53] geranium leaf extract,[54] and mushroom extract.[55] Since the protein in much higher in content than the Ag, the two peaks related to the crystalline biophase around 30° gave stronger intensity than the Ag peaks. The above four Ag peaks in Ag NR and Free NP showed comparable intensity since the Ag amount are similar.

3.3.2 Electrochemical CO_2 Reduction Performance

To evaluate the CO_2 reduction activity of Ag NR and Free NP, catalyst inks were used to make the working electrodes as described in the methods section. The catalytic activities of Ag NR, Free NP, TMVCP and Free NP mixture, pure TMVCP, and bare GCE were assessed under identical conditions by linear sweep voltammetry (LSV) from 0.200 V to -1.128 V vs RHE in CO_2 saturated $KHCO_3$ (0.5 M).

Figure 3.5a compares the results from all six electrodes. Notably, a much more positive onset potential was observed for Ag NR and its overall current density (normalized by electrochemically active surface area, Figure A1.2 in Appendix 1) was approximately 1.5-fold and 3-fold higher than those of Free NP and Bulk Ag, respectively. Pure TMVCP showed even lower current density than glass carbon, which means the CO_2 reduction activity is not coming from pure protein. Mixing the protein with Free NP did not give higher activity than Free NP. The more positive onset potential, as well as the increase in current density, indicates the higher reaction activity of Ag NR.

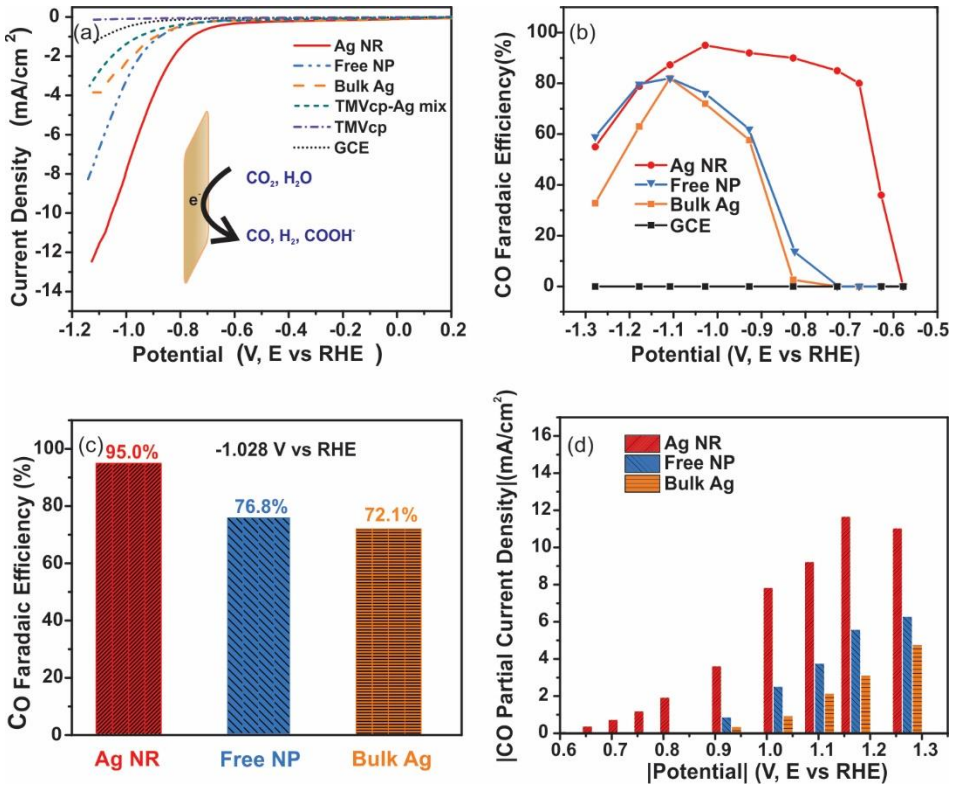

Figure 3.5: CO_2 reduction Cathodic LSV results (a); Faradaic efficiencies (FEs) of CO at various applied potentials (b); CO FEs at fixed potential of -1.028 V (c); CO partial current density (d).

While the LSV signal is indicative of enhanced activity, the overall current density includes contributions from both CO_2 reduction and the inevitable hydrogen evolution reaction in an aqueous environment, leading to the formation of different possible products. In order to examine the fractional product distribution and study the reaction selectivity by assessing the Faradaic efficiency, potentiostatic electrolysis was carried out for one hour at various potentials from -0.578 V to -1.278 V and the results

are shown in Figure A1.3 in Appendix 1. After each 1 h electrolysis, the gaseous products from the headspace of the electrochemical cell were quantified by gas chromatograph (GC). For the silver-based materials, carbon monoxide, from CO_2 reduction, and hydrogen gas, from water reduction, are the only gaseous products formed. Liquid products were determined by ^1H NMR, with trace amounts of formate detected at highly negative potentials (FE is less than 1%), indicating higher selectivity for CO production rather than formate.

In Figure 3.5b, CO FE was plotted against different potentials. Only H_2 gas was detected from GCE under all the potentials tested, confirming that the glassy carbon support does not contribute to CO FE, and that the total yield of CO comes from the silver-based materials. For Ag NR, CO FE reached 36.0% at -0.628 V (overpotential η = 518 mV, compared to the CO_2/CO equilibrium potential at -110 mV vs RHE). In contrast, for Free NP and bulk Ag, CO formation required an overpotential of 718 mV, which is a remarkable 248 mV cathodic shift relative to Ag NR. One can see that the presence of the protein ligand improves the CO_2 reduction rate. Sweeping to the more negative potentials, CO FE for all three materials increased significantly, indicating the predominance of CO formation over hydrogen evolution. After reaching the maximum point (-1.028 V for Ag NR, -1.178 V for Free NP and bulk Ag), the CO FE began to decrease and HER increased gradually, which is due to the concentration depletion at the catalytic interface caused by the dilution effects related to H_2 generation. The highest CO FEs were 95.0%, 78.5%, 74.7% for Ag NR, Free NP, and bulk Ag, respectively, with Ag NR achieving the maximum selectivity toward CO at η = 918 mV, 100 mV lower as compared to Free NP and bulk Ag, which could be related to the well-organized structure of the TMVCP template that improves the selectivity and efficiency of the silver-based bioelectrocatalyst. It is worth noting that while Free NP and bulk Ag are both sensitive to the applied potentials, Ag NR maintains high CO FE over a much wider range, being above 80% from -0.678 V to -1.108 V, illustrating the more stable CO production capability of Ag NR. When CO FEs are compared (Figure 3.5c) at -1.028 V (where Ag NR has the highest CO FE), the value for Ag NR is 18.5% higher than Free NP, and 22.9% higher than bulk Ag, likely due to the nanostructure, which can improve the CO_2 adsorption and give higher CO production.

Calculated from the chronoamperometry testing results, potential dependent CO partial current densities are reported in Figure 3.5d. At all applied potentials, both Ag nanomaterials showed enhancement in current densities compared to bulk Ag. In the potential range -0.928 V to -1.278 V, Ag NR had a CO partial current density increase of 2.7 times on average compared to Free NP and 5.7 times compared to

bulk Ag. After -1.178 V, further increase in overpotential did not give higher CO partial current density, instead, it promoted the formation of H_2. This can also be observed in the decrease in CO FE at potentials more negative than -1.178 V. Furthermore, as seen in Figure A1.4a in Appendix 1, the mass activity of Ag NR and Free NP followed a similar trend with the CO partial current density, with Ag NR outperforming Free NP. Taken together, the significantly enhanced reaction selectivity and activity towards CO formation by the Ag NR demonstrate the great potential of using biosynthesized Ag nanomaterial for application in CO_2 electrochemical reduction.

The time stability of the catalyst is a major concern in electrocatalyzed CO_2 reduction. To investigate the durability of the materials, electrolysis was performed with the three materials at -1.028 V for 5 h. The amount of CO and H_2 were quantified by GC every 1 h and the results are summarized in Figure A1.7 in Appendix 1. While the current densities did not change much over 5 h for all the three under the applied potential, the trends in the CO FE versus time are quite different. Based on the CO FE, Ag NR is more durable than Free NP and bulk Ag. The CO FE declined from 72.1% to 56.2% for bulk Ag after 5 h. However, for the Ag NR, it decreased only by 1.7% (from 95.1% to 93.4%), demonstrating a remarkably enhanced stability. Free NP also showed a relatively good stability, with a 6.9% decrease. For all the samples, the loss of CO FE was assigned to the formation of H_2, as can been seen in the increase of H_2 FE over time. Longer time chronoamperometry test performed for 12 h (Figure A1.8a in Appendix 1) found that Free NP and bulk Ag experienced current density decreases of around 34% and 32% respectively (calculated from average values of first 3 h and last 3h). However for Ag NR, the current density remained stable after 12 h (from 7.29 mA/cm^2 to 7.51 mA/cm^2). In addition, TEM image and XPS data taken after electrolysis showed no appreciable morphological and elemental changes, which demonstrates the remarkable stability of Ag NR (Figure A1.8b in Appendix 1). For bulk Ag and Free NP, these results are likely caused by surface modifications of these materials over time during electrolysis. While the polarized bulk silver electrode has its surface modified; the Free NP can be aggregated due to the applied potential and environmental conditions.[23]

In addition, the catalytic performance of the Ag NR is also excellent compared to some other reported nanosized silver materials (Table A1.1 in Appendix 1), for example, 10 nm Ag on carbon support (CO FE of 72.6%, η = 0.790 V), spherical Ag NP (CO FE of 65.4%, η = 0.846 V), but still it is not as efficient as silver triangular nanoplates (CO FE 96.8%, η = 0.746 V), which is due to the predominant shape effect. This can inspire further development of nanoparticles with different shapes on biomolecules.

3.3.3 Possible Origins for the Enhancement for Electroreducing CO_2 with Ag NR

In order to compare kinetic performance of Ag NR and Free NP, Electrochemical impedance spectroscopy was employed to evaluate the charge-transfer resistance. Nyquist plots were recorded in CO_2 saturated $KHCO_3$ solution (Figure A1.6 in Appendix 1). The resistance of the system decreases substantially when the nanoparticles are supported on the TMVCP, which corroborates with the electrocatalysis results, where Ag NR presented much higher activity for CO_2 reduction reaction. Tafel plots could also provide information on kinetics of CO_2 reduction to CO. Ag NR showed a Tafel slope of 110 mv dec^{-1}, slightly lower than Free NP of 124 mv dec^{-1} (Figure A1.4b in Appendix 1). Both values are close to 118 mv dec^{-1} expected for the single-electron rate determining step (RDS) of CO_2 reduction, with CO_2 receiving one electron to form an adsorbed *COO-.[51] As such, the RDS is not changed whether the Ag nanoparticles are capped by citrate or supported on the protein. However, the exchange current density of Ag NR exhibited an 8 times enhancement compared to that of Free NP. The higher exchange current density can indicate a higher intrinsic rate of electron transfer between the electrode and electrolyte.[51] While the underlying mechanism for the enhancement for CO_2 reduction with Ag NR is not totally understood due to the significant challenges involved in the detailed characterization of the bio-interface fabricated on the nanoparticle and also in resolving how the protein conformation affects the reaction process, we speculate the following possible origins based on our results and some relevant literature studies.

A report by Liu et al.[47] showed the shape dependent CO_2 reduction activity on silver triangular nanoplates and spherical nanoparticles with similar sizes, demonstrating that the triangular Ag nanoplates can provide optimum edge-to-corner ratio that can lower the energy to initiate the RDS, which significantly improved CO_2 reduction selectivity and overpotential. Besides shape effects, it has also been illustrated that silver nanoparticles with different sizes can yield different CO_2 reduction performance.[51] In our study, TEM results revealed that the single particles in the Ag NR have similar size and shape to that of the Free NP, which suggests that in our work, the nanoparticle morphology factor is not the reason for the higher performance of Ag NR compared to Free NP.

Therefore, it is highly possible that the protein plays a vital role in tuning the catalytic activity of the silver nanoparticles. There have been some studies investigating how small organic molecules on metallic nanoparticle surfaces can modify their chemical properties, thus affecting the catalytic activity in CO_2 electrochemical reduction.[56] For example, a 3,5-diamino-1,2,4-triazole modified silver electrode increased CO FE by weakening CO binding strength.[57] Silver nanoparticles grown on carbon support with

a cysteamine anchoring agent have shown enhanced ability to stabilize the crucial COOH intermediate, improving overpotential for CO formation.[51] Kim et al. prepared silver nanoparticles with different surface capping agents containing amine, thiol, carboxyl groups separately.[52] Results showed that compared to thiol and carboxyl, the amine functional group was able to further increase the CO FE by destabilizing the hydrogen bonding and suppressing HER, which was supported by DFT study. These studies have indicated that effective functional groups in surface-bound molecules can assist the reaction activity by reducing the overpotential or increasing the CO FE.

In our case, while carboxyl groups are the major functional groups responsible for the nucleation and growth of silver nanoparticles on the protein, the Ag NP can also have interactions with other functional groups containing nitrogen or sulfur. According to the disk protein structure, Ag nanoparticles bind to the surface (Figure 3.6). Arginine, Asparagine, and glutamate are relatively abundant on the surface of the protein.[45] As such, it is possible that some -NH- groups on the surface can have direct interaction with Ag NPs, while some don't (a bit buried inside) and they are only part of the peptide chains that use carboxyl to bind to Ag NPs. In that study by Kim et al.,[52] the amine groups in the capping agent has been demonstrated to suppress HER by destabilizing hydrogen binding energies.[52]

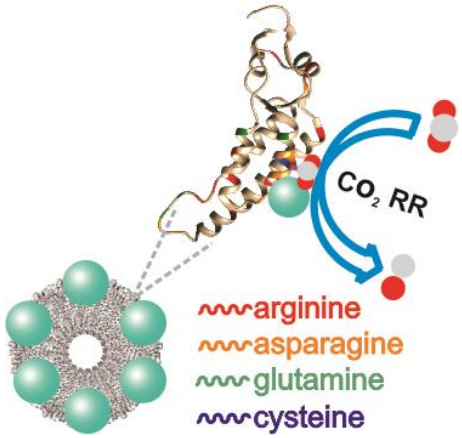

Figure 3.6: Illustration of different amino acids on the protein promoting CO_2 reduction to CO.

It is also suggested in another study that, from a geometric view, although N is not the direct binding site on the capping agent, the -NH_2 group from the cysteamine could geometrically stabilize chemisorbed CO_2, facilitating CO_2 activation to reduce overpotential.[58] This agrees with some protein related studies,[59] in which amine groups are thought to be responsible for enhanced capture of CO_2 by the protein. Thus,

possible reasons for the improvement of the Ag NR can be from the -NH- groups in the above three amino acids, which suppress HER activity or geometrically stabilize chemisorpted CO_2 onto the electrode, accelerating the reaction rate and thus showing higher reaction activity.

Cysteines are the ones in TMVCP that has thiol groups, which possibly results in thiol-Ag NP interaction, as suggested by the XPS data (Figure 3.4a). However, compared to the other three amino acids, cysteines are a bit more buried inside. Thus, the peak at 162.3 eV could also originate from the already existing Ag cation-thiol interaction. Ag-S interaction has been proved to influence the binding energies and stabilize the intermediate species, resulting in improved reaction activity.[54] For Free NP, the capping agent citrate also contains carboxylate groups, but the sole interaction from carboxyl groups may not be strong enough to affect the performance. Besides the chemical properties of the functional groups, their three-dimensional arrangement into ring structures may also be able to modify the charging states of the surface on the silver nanoparticle.

Understanding the exact binding event on the biointerface between the silver nanoparticles and the protein is crucial to determine the structural details and the modified chemical properties of the silver surface, which result in the corresponding catalytic behavior. In this regard, combining high resolution imaging techniques at molecular level with computational modeling and analysis is needed to gain further insight on the conformational and charging effects from the protein controlling the reaction activity.

3.4 Conclusions

The biosynthesized Ag NR was utilized as a successful catalyst for CO_2 electroreduction. Compared to the bulk Ag electrode and Free NP prepared by pure chemical reduction routes, the Ag NR exhibits superior reaction selectivity as 95.0 % of CO FE. Moreover, it has a lower onset potential and higher current density for CO formation. A durability test over 5 hours demonstrates its enhanced stability. Thus, we propose this bioinspired nanomaterial approach as a powerful strategy for CO_2 RR, which combines the ecologically benign synthetic conditions with excellent catalytic properties. The origin for the observed improvement is likely due to surface modification of the silver nanoparticles by the protein template. While it is very challenging to determine intrinsic structure/property relationship of the biointerface, several factors can contribute to the improvement of Ag NR for CO_2 RR, which may include

1) the -NH- groups destabilizing hydrogen bonding to suppress HER and/or enhancing the adsorption of CO_2 and 2) the thiol functional groups on the protein forming Ag-S bond with Ag, resulting in increased stability of intermediates. For future work, it will be necessary to utilize more advanced experimental and computational techniques to understand the detailed mechanism. We anticipate this study will provide new insights to the chemistry community for fabricating and applying new bioinspired nanomaterials to research fields like catalysis, energy conversion and biomedical technologies.

3.5 References

[1] J. H. Montoya, L. C. Seitz, P. Chakthranont, A. Vojvodic, T. F. Jaramillo and J. K. Nørskov, *Nat. Mater.*, 2016, **16**, 70–81.

[2] W. Zhang, Y. Hu, L. Ma, G. Zhu, Y. Wang, X. Xue, R. Chen, S. Yang and Z. Jin, *Adv. Sci.*, 2018, **5**, 1700275.

[3] V. Singh, H. Muroyama, T. Matsui, S. Hashigami, T. Inagaki and K. Eguchi, *J. Power Sources*, 2015, **293**, 642–648.

[4] D. Liu, R. Lau, A. Borgna and Y. Yang, *Catal. Today*, 2009, **358**, 110–118.

[5] C.-S. Chen, W.-H. Cheng and S.-S. Lin, *Appl. Catal. A Gen.*, 2003, **238**, 55–67.

[6] J. K. Stolarczyk, S. Bhattacharyya, L. Polavarapu and J. Feldmann, *ACS Catal.*, 2018, **8**, 3602–3635.

[7] R. Francke, B. Schille and M. Roemelt, *Chem. Rev.*, 2018, **118**, 4631–4701.

[8] B. Khezri, A. C. Fisher and M. Pumera, *J. Mater. Chem. A*, 2017, **5**, 8230–8246.

[9] M. Azuma, H. Kazuhito, H. Masahiro, W. Masahiro and T. Sakata, *J. Electrochem. Soc.*, 1990, **137**, 1772–1778.

[10] B. A. Rosen, A. Salehi-Khojin, M. R. Thorson, W. Zhu, D. T. Whipple, P. J. A. Kenis and R. I. Masel, *Science*, 2011, **334**, 643–644.

[11] J. Huang and R. Buonsanti, *Chem. Mater.*, 2019, **31**, 13–25.

[12] P. Kang, S. Zhang, T. J. Meyer and M. Brookhart, *Angew. Chem. Int. Ed.*, 2014, **53**, 8709–8713.

[13] Y. Chen, C. W. Li and M. W. Kanan, *J. Am. Chem. Soc.*, 2012, **134**, 19969–19972.

[14] H. E. Lee, K. D. Yang, S. M. Yoon, H. Y. Ahn, Y. Y. Lee, H. Chang, D. H. Jeong, Y. S. Lee, M. Y. Kim and K. T. Nam, *ACS Nano*, 2015, **9**, 8384–8393.

[15] Q. Lu, J. Rosen, Y. Zhou, G. S. Hutchings, Y. C. Kimmel, J. G. Chen and F. Jiao, *Nat. Commun.*, 2014, **5**, 1–6.

[16] J. Huang, M. Mensi, E. Oveisi, V. Mantella and R. Buonsanti, *J. Am. Chem. Soc.*, 2019, **141**, 2490–2499.

[17] Z. Wang, G. Yang, Z. Zhang, M. Jin and Y. Yin, *ACS Nano*, 2016, **10**, 4559–4564.

[18] R. Reske, H. Mistry, F. Behafarid, B. Roldan Cuenya and P. Strasser, *J. Am. Chem. Soc.*, 2014, **136**, 6978–6986.

[19] S. Y. Lee, H. Jung, N. K. Kim, H. S. Oh, B. K. Min and Y. J. Hwang, *J. Am. Chem. Soc.*, 2018, **140**, 8681–8689.

[20] C.-T. Dinh, T. Burdyny, M. G. Kibria, A. Seifitokaldani, C. M. Gabardo, F. Pelayo García De Arquer, A. Kiani, J. P. Edwards, P. De Luna, O. S. Bushuyev, C. Zou, R. Quintero-Bermudez, Y. Pang, D. Sinton and E. H. Sargent, *Science*, 2018, **360**, 783–787.

[21] S. Zhao, R. Jin and R. Jin, *ACS Energy Lett.*, 2018, **3**, 452–462.

[22] M. Mikkelsen, M. Jørgensen and F. C. Krebs, *Energy Environ. Sci.*, 2010, **3**, 43–81.

[23] V. K. Sharma, C. M. Sayes, B. Guo, S. Pillai, J. G. Parsons, C. Wang, B. Yan and X. Ma, *Nanotoxicology Sci. Total Environ.*, 2019, **653**, 1042–1051.

[24] M. J. Firdhouse and P. Lalitha, *J. Nanotechnol.*, 2015, 829526.

[25] S. Iravani, H. Korbekandi, S. V. Mirmohammadi and B. Zolfaghari, *Res. Pharm. Sci.*, 2014, **9**, 385–406.

[26] S. Iravani, *Green Chem.*, 2011, **13**, 2638–2650.

[27] A. A. Abdelhamid, M. A. Al-Ghobashy, M. Fawzy, M. B. Mohamed and M. M. S. A. Abdel-

Mottaleb, *ACS Sustain. Chem. Eng.*, 2013, **1**, 1520–1529.

[28] L. Jia, Q. Zhang and Q. Li, *Nanotechnology*, 2007, **18**, 105104.

[29] P. Mukherjee, A. Ahmad, D. Mandal, S. Senapati, S. R. Sainkar, M. I. Khan, R. Parishcha, P. V Ajaykumar, M. Alam, R. Kumar and M. Sastry, *Nano Lett.*, 2001, **1,** 515-519.

[30] M. Kitching, P. Choudhary, S. Inguva, Y. Guo, M. Ramani, S. K. Das and E. Marsili, *Enzyme Microb. Technol.*, 2016, **95**, 76–84.

[31] M. Zhang, K. Zhang, B. De Gusseme, W. Verstraete and R. Field, *Biofouling*, 2014, **30**, 347–357.

[32] T. Klaus, R. Joerger, E. Olsson and C.-G. Ran Granqvist, *Proc. Natl. Acad. Sci.*, 1999, **23**, 13611–13614.

[33] S. Gurunathan, K. Kalishwaralal, R. Vaidyanathan, V. Deepak, S. Ram, K. Pandian, J. Muniyandi, N. Hariharan and S. H. Eom, *Colloids Surf. B*, 2009, **74**, 328–335.

[34] T. N. V. K. V. Prasad, V. S. R. Kambala and R. Naidu, *J. Appl. Phycol.*, 2013, **25**, 177–182.

[35] O. K. Zahr and A. S. Blum, *Nano Lett.*, 2012, **12**, 629–633.

[36] A. Klug, *Philos. Trans. R. Soc. Lond. B. Biol. Sci.*, 1999, **354**, 531–535.

[37] E. Dujardin, C. Peet, G. Stubbs, J. N. Culver and S. Mann, *Nano Lett.*, 2003, **3**, 413–417.

[38] N. Liu, C. Wang, W. Zhang, Z. Luo, D. Tian, N. Zhai, H. Zhang, Z. Li, X. Jiang, G. Tang and Q. Hu, *Nanotechnology*, 2012, **23**, 335602.

[39] K. T. Nam, Y. J. Lee, E. M. Krauland, S. T. Kottmann and A. M. Belcher, *ACS Nano*, 2008, **2**, 1480–1486.

[40] R. Sankar, A. Karthik, A. Prabu, S. Karthik, K. Subramanian Shivashangari and V. Ravikumar, *Colloids. Surf. B*, 2013, **108**, 80–84.

[41] A. Gangula, R. Podila, R. M, L. Karanam, C. Janardhana and A. M. Rao, *Langmuir*, 2011, **27**, 15268–15274.

[42] C. Liu, X. Yang, H. Yuan, Z. Zhou and D. Xiao, *Sensors*, 2007, **7**, 708–718.

[43] A. S. Schenk, S. Eiben, M. Goll, L. Reith, A. N. Kulak, F. C. Meldrum, H. Jeske, C. Wege and S.

Ludwigs, *Nanoscale*, 2017, **9,** 6334–6345.

[44] Y. Lee, J. Kim, D. S. Yun, Y. S. Nam, Y. Shao-Horn and A. M. Belcher, *Energy Environ. Sci.*, 2012, **5**, 8328–8334.

[45] N. Liu, C. Wang and W. Zhang, *Nanotechnology*, 2016, **27**, 485603.

[46] Y. Yoon, A. S. Hall and Y. Surendranath, *Angew. Chem. Int. Ed*, 2016, **55**, 15282–15286.

[47] S. Liu, H. Tao, L. Zeng, Q. Liu, Z. Xu, Q. Liu and J. L. Luo, *J. Am. Chem. Soc.*, 2017, **139**, 2160–2163.

[48] H. Li and R. Guevremont, *J. Am. Soc. Mass Spectrom.*, 1998, **9**, 760–766.

[49] A. Abedini, A. R. Daud, M. A. A. Hamid, N. K. Othman and E. Saion, *Nanoscale Res. Lett.*, 2013, **8**, 1–10.

[50] C. Battocchio, I. Fratoddi, L. Fontana, E. Bodo, F. Porcaro, C. Meneghini, I. Pis, S. Nappini, S. Mobilio, M. V. Russo and G. Polzonetti, *Phys. Chem. Chem. Phys.*, 2014, **16**, 11719–11728.

[51] C. Kim, H. S. Jeon, T. Eom, M. S. Jee, H. Kim, C. M. Friend, B. K. Min and Y. J. Hwang, *J. Am. Chem. Soc.*, 2015, **137**, 13844–13850.

[52] C. Kim, T. Eom, M. S. Jee, H. Jung, H. Kim, B. K. Min and Y. J. Hwang, *ACS Catal.*, 2017, **7**, 779–785.

[53] M. Vanaja and G. Annadurai, *Appl. Nanosci.*, 2013, **3**, 217–223.

[54] S. S. Shankar, A. Ahmad and M. Sastry, *Biotechnol. Prog.*, 2003, **19**, 1627–1631.

[55] D. Philip, C. Unni, S. A. Aromal and V. K. Vidhu, *Spectrochim. Acta - Part A Mol. Biomol. Spectrosc.*, 2011, **78**, 899–904.

[56] H. K. Lim, H. Shin, W. A. Goddard, Y. J. Hwang, B. K. Min and H. Kim, *J. Am. Chem. Soc.*, 2014, **136**, 11355–11361.

[57] K. G. Schmitt and A. A. Gewirth, *J. Phys. Chem. C*, 2014, **118**, 17567–17576.

[58] Z. Wang, L. Wu, K. Sun, T. Chen, Z. Jiang, T. Cheng and W. A. Goddard, *J. Phys. Chem. Lett.*, 2018, **9**, 3057–3061.

[59] M. Imtiaz-Ul-Islam, H. Liang and T. Langrish, *Chem. Eng. J.*, 2011, **171**, 1069–1081.

Chapter 4

Tunable Assembly of Protein Enables Fabrication of Platinum Nanostructures with Different Catalytic Activity

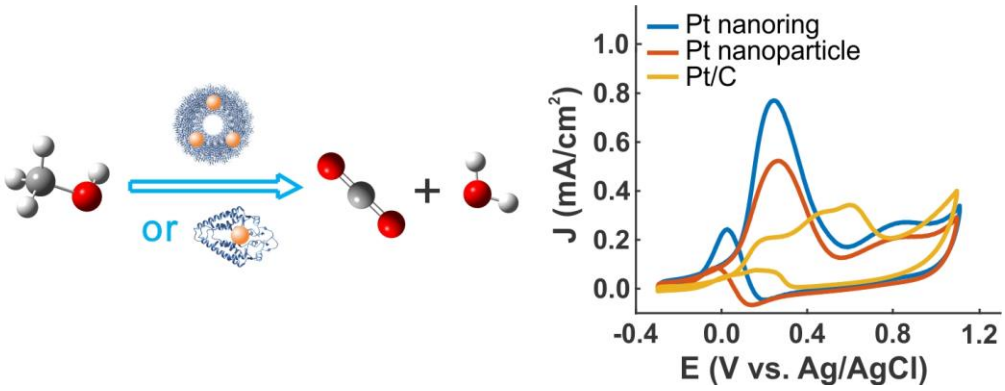

Chapter Preface

Scientific Contributions:

Chapter 3 employed TMVCP disk protein as a template to fabricate Ag NRs around the edge of the ring template via photoreduction. Given the excellent catalytic performance of Ag NR in CO_2 reduction, Chapter 4 further explores the potential of TMVCP as the shape directing template to prepare nanosized Pt materials, the most widely used metal in electrocatalysis. Taking advantage of the assembly properties of TMVCP, Pt nanorings and discrete Pt nanoparticles were prepared under different pH conditions. Both materials were applied in methanol electrooxidation and compared to bench marking Pt/C catalyst. Possible reasons for the different performance of the three nanocatalysts were discussed. This chapter demonstrates that the tunable assembly state of TMVCP enables modulation of interparticle spacing and have impact on the catalytic performance. We anticipate our results in Chapter 4 can stimulate more research on exploring the potential of various natural ligands for construction of nanomaterials with tailorable structures and properties.

Publication Information:

Chapter 4 is adapted from a previously published research article with permission from:

Y. Pan, A. S. Blum, J. Mauzeroll. Tunable assembly of protein enables fabrication of platinum nanostructures with different catalytic activity. *ACS Applied Materials & Interfaces,* **2021,** 13, 52588-52597.

Chapter Abstract

Proteins are promising bio-functional units for the construction of nanomaterials (NMs) due to their abundant binding sites, intriguing self-assembly properties and mild NM synthetic conditions. TMVCP is a protein capable of self-assembly into distinct morphologies depending on the solution pH and ionic strength. Chapter 4 reports the use of TMVCP as a building block to organize nanosized platinum into discrete nanorings and isolated nanoparticles by varying the solution pH to modulate the protein assembly state. Compared with a commercial Pt/C catalyst, the TMVCP templated platinum materials exhibited

significant promotion of the catalytic activity and stability towards methanol electrooxidation in both neutral and alkaline conditions. The enhanced catalytic performance is likely facilitated by the protein support. Additionally, Pt nanorings outperformed isolated nanoparticles, although they are both synthesized on TMVCP templates. This could be due to the higher mechanical stability of the protein disk structure and possible cooperative effects between adjacent nanoparticles in the ring with narrow interparticle spacing. In Chapter 4 we expanded the scope of TMVCP template to Pt nanomaterials. Specifically in Chapter 4, we investigated the effect of protein template morphology on the material catalytic behavior.

4.1 Introduction

Direct methanol fuel cells (DMFCs) represent a promising power generation technology to meet the demand of clean and green energy production thanks to their high energy density, easy liquid storage and low pollutant emission.[1–5] The anode component of DMFCs is the methanol electrooxidation reaction (MOR), which is a six-electron transfer reaction if the methanol is completely converted to carbon dioxide (CO_2). The complete reaction of methanol oxidation to form CO_2 in acidic and basic media follows:

Acidic media: $CH_3OH + H_2O \rightarrow CO_2 + 6H^+ + 6e^-$

Basic media: $CH_3OH + 6OH^- \rightarrow CO_2 + 5H_2O + 6e^-$

At present, platinum (Pt) is the most widely used material for MOR due to its excellent electrocatalytic activity.[6,7] A widely accepted mechanism for the Pt catalyzed MOR process to form CO_2[8,9] is that methanol molecules go through several dehydrogenation steps to form CO adsorbed on the metal surface, Pt-$(CO)_{ads}$ (Eq. 4.2). Adsorbed H_2O then dissociates into hydroxy species (OH_{ads}) on the Pt surface to generate Pt-$(OH)_{ads}$ (Eq. 4.2), which can further oxidize neighbouring Pt-$(CO)_{ads}$ species to produce CO_2 via Langmuir-Hishelwood (L-H) mechanism (Eq. 4.3).[8] In alkaline electrolytes, some CO_{ads} can also react with the free OH^- through Eley-Ridel (E-R) pathway.[10] Besides CO_2, significant quantities of other products such as HCHO and HCOOH are also produced through a parallel pathway in which weakly or non-adsorbing intermediate species diffuse away from the electrode and form the partially oxidized products.[11]

$$Pt + CH_3OH \rightarrow Pt\text{-}(CO)_{ads} + 4H^+ + 4e^- \qquad (4.1)$$

$$Pt + H_2O \rightarrow Pt\text{-}(OH)_{ads} + H^+ + e^- \quad (4.2)$$

$$Pt\text{-}(CO)_{ads} + Pt\text{-}(OH)_{ads} \rightarrow 2Pt + CO_2 + H^+ + e^- \quad (4.3)$$

Despite its great promises, Pt alone as a catalyst suffers from high cost, slow kinetics, and surface poisoning caused by absorbed intermediate species such as carbon monoxide (CO), which can lead to diminished current density during long term operation.[6] Developing Pt nanocatalysts with fast kinetics and high durability is thus critical to improve electrode performance. Much encouraging research progress has been achieved. For example, alloying Pt with a second metal can increase Pt utilization efficiency and attenuate its CO poisoning (eg., PtRu,[12] PtRh[13] and PtNi,[14] etc). These oxophilic metals facilitate the decomposition of water molecules to form hydroxy species (OH), which can promote the oxidation of CO on neighbouring Pt sites to free these active sites for further methanol oxidation.[15] Apart from alloying nanometals, metal oxides,[16] metal carbides,[17] and metal nitrides[18] are good candidates to support Pt catalysts owing to their reasonable cost, good mechanical and chemical stability against corrosion in acidic environments.[19,20] To further increase nanoparticle dispersity and electrode conductivity, nanocatalysts are generally loaded on various kinds of carbon supports, such as mesoporous carbon black, graphene, multiwall and single-wall carbon nanotubes, etc.[21–25]

In recent years, biological scaffolds including peptides,[26,27] proteins,[28,29] nucleic acids[30,31] and bacteriophages[32,33] are emerging as attractive supports for nanomaterial nucleation and growth into well-defined structures. Compared to conventional chemical synthetic routes, these biobased methods hold some key advantages:[34–36] 1) eco-friendly synthetic conditions without use of non-natural surfactants, organic solvents and elevated temperature; 2) large diversity of structures to organize nanoparticles into different morphologies such as wires, rings, networks, etc; 3) precise control over site-specific functionalization via surface group manipulation by genetic modification or bioconjugation. Among the different bio-templates, proteins are of particular interest due to their intriguing self-assembly features and highly complex hierarchical structures, which can provide versatile platforms for fabrication of nanoarchitectures with various dimensions.[28,37]

In this study, we take advantage of the self-assembly properties of tobacco mosaic virus coat protein (TMVCP) to serve as a shape-directing support to functionalize Pt nanoparticles (NPs) into different patterns. Tobacco mosaic virus (TMV) is a plant virus with a single stranded RNA genome surrounded by 2130 identical coat protein (CP) subunits, forming a 300 nm long nanotube, with its outer diameter

and inner diameter 18 nm and 4 nm, respectively.[38,39] This filamentous geometry makes TMV and its VLP (virus like particles) facile templates for construction of one-dimensional nanowires coated by various kinds of nanocomposites, such as copper,[40] gold,[41] platinum-pallidum alloy,[42] and iron oxide,[40] etc. Interestingly, the RNA-free coat protein self-assembles into different morphologies based on the solution environment. As shown in Scheme 1a, under neutral pH conditions, the dominant species are in hollow disk forms, with the two-layer disk consisting of 34 copies of protein subunit.[43] Increasing solution pH leads to disassembly of disks into A protein, which is a mixture of monomers and oligomers. This tuneable geometry makes TMVCP a facile template to potentially direct the organization of nanoparticles into diverse target structures. Moreover, mutation at specific residues can provide even more possibilities for efficient nano-object decoration.[44,45] For instance, Zhang and co-workers functionalized the internal channel of TMVCP with thiol groups via genetic modification, which enables highly efficient and uniform construction of nanochains coated by Au NPs and Ag_2S quantum dots.[46]

Herein, we demonstrate that Pt NPs can be either immobilized onto the wild type disk protein to form a discrete ring (denoted as Pt NR, although not a continuous metallic ring formation[45,47]) or supported on the A protein to obtain well dispersed individual nanoparticles (denoted as Pt NP), depending on the solution pH. To explore the electrocatalytic potential of the as synthesized two Pt materials, comparison was made with commercial Pt on carbon (Pt/C) for MOR in acidic, neutral and alkaline media, respectively. Remarkably, compared to Pt/C, Pt NR exhibited significantly enhanced current density in all the three media. Pt NP also outperformed Pt/C in neutral and alkaline media, however we obtained the opposite result in acidic media. In addition, Pt NR showed better performance than Pt NP, suggesting that when nanosized Pt particles are assembled in a closely packed pattern, they may show emergent collective properties that are not displayed by individually dispersed nanoparticles. Our results demonstrate that both the protein support and the inter-nanoparticle interactions play critical roles in influencing the electrocatalytic performance.

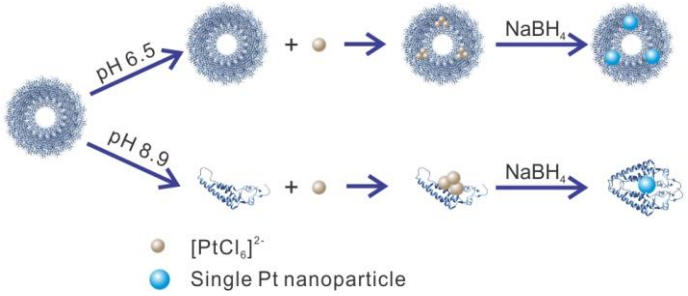

Scheme 4.1: Synthetic scheme of Pt NRs and Pt NPs under different conditions.

4.2 Experimental Section

4.2.1 Materials

Chloroplatinic acid (H_2PtCl_6•$6H_2O$), sodium hexachloroplatinate (Na_2PtCl_6•$6H_2O$), sodium borohydride ($NaBH_4$), methanol (CH_3OH), Tris Base, Nafion resin solution (5 wt% in a mixture of low aliphatic alcohol and water), hydrochloric acid (HCl), disodium phosphate (Na_2HPO_4), monosodium phosphate (NaH_2PO_4), dipotassium phosphate (K_2HPO_4), monopotassium phosphate (KH_2PO_4), perchloric acid ($HClO_4$, 70%), sodium hydroxide (NaOH) were purchased from Sigma Aldrich. Carbon black (Vulcan XC-72) and Pt/C catalyst (10 wt% loading of Pt on carbon black) were obtained from Fuel Cell Store. All chemicals were used as received without further purification. Millipore MilliQ water (18.2 MΩ·cm) was used to prepare solutions.

4.2.2 Synthesis of Pt NR and Pt NP and Catalyst Preparation

Wild type TMVCP was expressed from Tuner (DE3) pLysS competent cells and purified according to a previously published protocol.[39] The protein stored at -80 °C was thawed to room temperature, and then dialyzed into pH 6.5 (PBS buffer, 80 mM) and pH 8.9 (Tris-HCl buffer, 15 mM) separately. The dialysis was carried out at room temperature overnight using cellulose membrane tubing (12-14 k MWCO, Spectra/Pro). The protein concentration was then determined by the absorbance at 282 nm (1.27 m (mg cm)$^{-1}$) using UV-visible (UV-Vis) spectroscopy (Cary 100 Bio Spectrometer). To fabricate Pt NRs, 24 μL of H_2PtCl_6•H_2O (0.1 M) was incubated with 575 μL of protein solution in PBS buffer (0.4 mg/mL) for three hours. 48 μL of freshly prepared $NaBH_4$ solution (0.15 M) was added to the above solution to induce reduction of metal precursors. Stirring was continued for one hour and the mixture was then

allowed to stand for another one hour. To prepare the catalyst ink, the reaction mixture was purified by desalting, centrifuge and then suspended in water. Afterward, 5 μL of solution was mixed with 45 μL of carbon suspension (2 mg/mL) and 2 μL of Nafion solution (0.5%). The mixture was sonicated to form a homogeneous catalyst ink. Pt NPs were synthesized with the same procedure using $Na_2PtCl_6 \cdot 6H_2O$ as the precursor with the reaction buffer Tris-HCl (pH 8.9, 15 mM).

4.2.3 Material Characterizations

All TEM, HR-TEM, and SAED measurements were conducted on a Talos 300 TEM operating at 200 kV. To prepare samples, 10 μL of material suspensions were drop-cast onto TEM mesh grids for 5 min. The residues were then removed with a filter paper. Negatively stained samples were prepared by applying an additional drop of phosphotungstic acid (2%, adjusted to pH 7) for ~1 min, which was then blotted off and dried. PXRD)patterns were collected on a Bruker D8 Advance diffractometer (Bruker AXS, Madison, WI) with a Ni-filtered Cu-Kα ($\lambda = 0.15406$ nm) radiation source, which was operated at 40 mA and 40 kV. Prior to characterization, the samples were concentrated and dried on glass substrates. The 2θ angular scan was from 20° to 90° ($\hbar\nu = 1486.6$ eV). To analyze surface electronic states of the target element, XPS characterizations were carried out on a Thermal Scientific K-Alpha XPS instrument using a monochromatic Al Kα source. The binding energies were referenced to C 1s peak at 284.5 eV. The actual platinum concentration in the catalyst ink was determined by ICP-OES (Agilent Technologies, 5000).

4.2.4 Electrochemical Measurements

A three-electrode system was employed for all electrochemical characterizations, with Ag/AgCl and Pt wire serving as reference electrode and counter electrode, respectively. The working electrode was prepared by loading 8 μL of catalyst ink onto a clean glassy carbon electrode (GCE, diameter 4 mm) and dried overnight to form a homogeneous film. All electrolyte solutions were deoxygenated by purging with Argon for at least 30 min before the tests. CV, LSV and CA experiments were conducted using an ELProScan1 system (HEKA, German; bipotentiostat model PG340). Blank CV (scan rate, 50 mV/s) were performed in each electrolyte to stabilize the electrode surface and measure the ECSAs. The areas were estimated via integrating charges associated with the hydrogen underpotential deposition region (double layer correction applied), assuming a charge of 210 $\mu C/cm^2$ for hydrogen monolayer adsorption on Pt surface. Electrochemical impedance spectra were recorded at a small AC voltage amplitude (10 mV) with

a frequency of 100 kHz ~ 10 mHz using a VSP300 potentiostat (Biologic). All experiments were carried out at room temperature.

4.3 Results and Discussion

4.3.1 Pt NR and Pt NP Synthesis

As illustrated in Scheme 4.1, TMVCP was buffered in pH 6.5 phosphate buffer solution (PBS) and pH 8.9 Tris-HCl solution to form the disk and A protein, respectively. When the Pt precursors were introduced to the solution, the functional groups on the TMVCP provided binding sites to sequester these Pt complexes onto the protein surface via electrostatic interactions.[38] Adding an excess amount of $NaBH_4$ leads to the *in situ* formation of zerovalent nanometals supported on the template. For the disk protein, the nucleation sites determine the nanoparticle arrangement due to spatial confinement, resulting in neighbouring nanoparticles anchored on the disk surface. This confinement is removed in the free A protein, which then leads to the formation of isolated dispersed nanoparticles as expected. The resultant solutions were characterized by UV-vis spectroscopy, and the featureless spectra (Figure A2.1 in Appendix 2) are typical of Pt^0 materials, indicating full reduction of Pt salts.

The final assembly patterns were verified by TEM and typical images are shown in Figure 4.1. For the Pt NR, three single nanoparticles were immobilized onto the disk surface surrounding the central hole to form a triangular trimer (Figure 4.1a, low magnification TEM image was displayed in Figure A2.2 in Appendix 2). They are close to each other without obvious aggregation (two and four particles were also observed occasionally), with one single particle having a diameter of ca. 3.23 ± 0.52 nm (Figure 4.1g). When using the A protein, single Pt NPs with uniform size distributions were observed (Figure 4.1b), with an average particle size of ca. 2.91 ± 0.49 nm (Figure 4.1h). HR-TEM images (Figure 4.1c-d) suggest that (111) is the main facet for both Pt NR and Pt NP. Additionally, the SAED patterns (Figure 4.1e-f) suggest that both materials are polycrystalline features. Calculation of d-spacing indicates the existence of lattice planes associated with (111), (200), (200), (311) and (222) of Pt face-centered cubic structures. The crystalline properties were also characterized by XRD in Figure 4.2a. The diffraction patters of the two Pt materials are the same, with five distinct peaks at approximately 38.99°, 44.55°, 67.95°, 82.62° and 88.82°, which can be assigned to (111), (200), (220), (311) and (222) planes, respectively (JCPDS file no. 04-0802). The XRD results corroborate the conclusion from SAED patterns.

XPS measurements were conducted to compare the electronic states of the two Pt materials (Survey spectra presented in Figure A2.3 in Appendix 2). Figure 4.2b displays the high resolution spectrum of core level Pt 4f peaks of Pt NR. In the deconvoluted curves, the double peaks with binding energies of 71.01 eV and 74.38 eV are assigned to Pt^0 $4f_{7/2}$ and Pt^0 $4f_{5/2}$, respectively, confirming the formation of zerovalent metallic Pt. Additionally, the two peaks with higher binding energies (72.20 eV and 75.93 eV) indicate a small amount of oxidation during sample preparation. The Pt NP showed a similar Pt 4f spectrum, with two Pt^0 peaks located at 70.84 eV and 74.11 eV, and the oxidized species centered at 72.18 eV and 75.69 eV, respectively. Overall, the above microscopic and spectroscopic results demonstrate that Pt nanostructures were successfully synthesized on the TMVCP template, and that the single particles in the Pt NR and the Pt NP are quite close in physical properties.

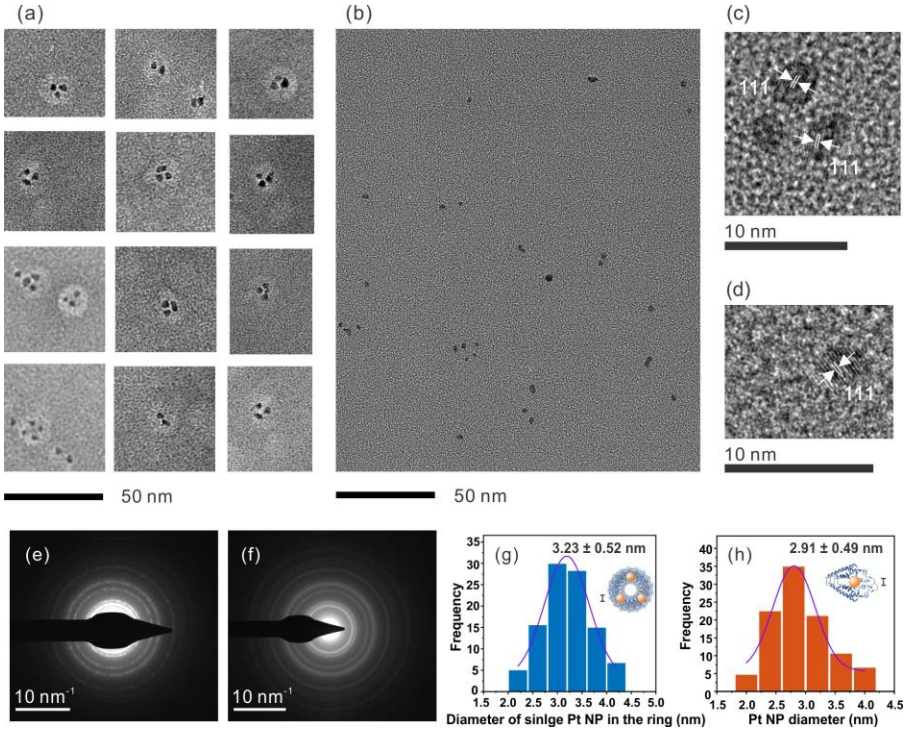

Figure 4.1: Representative TEM images (negatively stained) (a, b), HR-TEM images (c, d), SAED patterns (e, f) of Pt NRs (a, c, e) and Pt NPs (b, d, f); Size distributions of single Pt nanoparticle on the Pt NRs (g) and the Pt NPs (h).

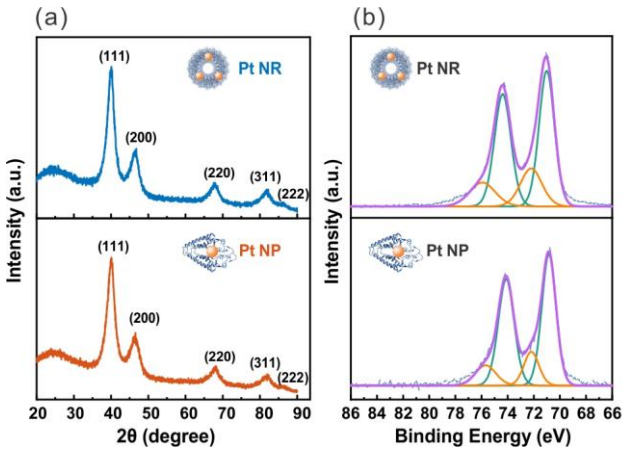

Figure 4.2: XRD patterns of Pt NRs and Pt NPs (a); XPS spectra of Pt 4f from Pt NRs and Pt NPs (b).

4.3.2 Electrocatalytic Methanol Oxidation Reaction Performance

Platinum is known to catalyze MOR efficiently in both acidic and alkaline environment. Herein, we investigated the catalytic behaviors of the two Pt nanomaterials in acidic, neutral and alkaline solutions, and comparison was made with benchmarking commercial Pt/C catalyst under same test conditions. ECSA values were first determined by running CV in background electrolytes without methanol and the results are listed in Table A2.1 in Appendix 2. The calculated values of the three platinum materials in all three different electrolytes follow the order Pt NP > Pt NR > Pt/C, which could be attributed to the slightly smaller sizes of Pt NP and Pt NR (Pt/C size: ca. 3.32 nm), as well as their high dispersity.

Figure 4.3a compares the CV results of Pt NR, Pt NP and Pt/C in $HClO_4$ electrolyte with 1.0 M methanol, with the current densities normalized to the relative ECSAs. All CV curves consist of two strong oxidation peaks in the forward (~0.65 V vs. Ag/AgCl) and backward (~0.42 V vs. Ag/AgCl) scans. The forward peak was used to evaluate the MOR catalytic activity. Among all three materials, Pt NR exhibited the highest current density (1.51 mA/cm^2), which was approximately 2-fold and 1.3-fold higher than those of Pt NP (0.77 mA/cm^2) and Pt/C (1.16 mA/cm^2), respectively. Interestingly, the peak value for Pt NP was lower than that for Pt/C. However, opposite results were detected when the environment was changed to neutral and alkaline media as shown in Figure 4.3b and c, in which Pt NP outperformed Pt/C in specific activity (SA). Still, Pt NR delivered the best catalytic activity in both PBS and NaOH electrolytes. Specifically, its SA in PBS buffer was ~1.4 and ~3.7 times higher than Pt NP and Pt/C, respectively. While in NaOH, the SA of Pt NR (4.04 mA/cm^2) brought ~1.63 times enhancement compared to Pt/C

(2.48 mA/cm^2). The value of Pt NP (3.69 mA/cm^2) is also higher than Pt/C with ~ 1.48 times increase. These data signified the much faster MOR reaction rate for Pt NR when compared to that of Pt/C standard. Furthermore, the same trends were observed for mass activity (MA) when the current density was normalized to Pt mass (Figure 4.3d-f), with the highest Pt utilization efficiency achieved by Pt NR. Overall, these data indicate that the TMVCP can have a drastic impact on the catalytic activity of Pt.

In Figure 4.3g, the peak MA and SA values for the MOR with each Pt material were compared in three electrolytes. It can be seen that all Pt catalysts displayed higher activities in 0.1 M NaOH than in 0.1 M $HClO_4$. Furthermore, in PBS the peak values were significantly lower than either in acid or base, even when buffered at a high concentration (0.75 M), demonstrating a strongly pH-dependent effect on electrode performance. The main advantage of using alkaline medium is its increased MOR kinetics, since OH^- can be easily absorbed onto the Pt surface to trigger the oxidation of intermediate species.[49] Additionally, metal corrosion is much easier in acidic media, leading to relatively faster degradation of the catalyst. However, alkaline media also have drawbacks such as carbonation, in which CO_3^{2-}/HCO_3^- (CO_2 reacts with OH^-) formed in solution gradually changes the electrolyte environment and induces a drop in pH, thus causing a voltage loss.[49] As a pH neutral electrolyte, the PBS medium is free from these drawbacks possessed by acid and base type MOR, which may meet the need for secure and bio-compatible electrochemical devices.[50,51] However, MOR under neutral conditions suffers from slower kinetics than the other two media. This may stimulate future research endeavors towards engineering catalysts highly active in pH neutral media. Noteworthy, our TMVCP supported Pt catalysts show great potential with their substantial improvement in MA and SA as compared to Pt/C.

The concentration of methanol has a large impact on the reaction rate. Figure A2.4-2.6 in Appendix 2 display the CVs of three Pt catalysts with constant electrolyte concentrations and varied MeOH concentrations, ranging from 0.1 M to 1.0 M. The SA monotonically increases as the MeOH concentration increases in $HClO_4$ and PBS media, which demonstrates that the observed oxidation peaks are indeed from MOR. In NaOH, the same trend was observed until MeOH reached 0.5 M, after which the SA had little change when the concentration was further increased to 0.75 M and 1.0 M. This suggests that at concentrations above 0.5 M, the MOR rate is no longer controlled by the diffusion of methanol in solution, but instead by the reaction itself.[52]

CA was employed to evaluate the operation durability of each Pt catalyst in different media. As shown in Figure 4.4a, initial rapid deceases in MA were observed for all the three materials in $HClO_4$, which can

be caused by the accumulation of strongly adsorbed surface poisoning species. The current densities then decreased slowly and gradually reached pseudosteady values. Although Pt NR had a higher initial current density than Pt/C, it decayed faster, indicating a decreased stability. Furthermore, the MA of Pt NP after 1 h was the lowest among the three. The relatively lower MOR stability in $HClO_4$ for Pt NR and Pt NP may discourage their application in acidic media. The reason may be attributed to the TMVCP, which can be denatured in extremely acidic pH solutions (pH = 1.2 for 0.1 M $HClO_4$). Moreover, the A protein is likely to undergo faster denaturation than the disk protein, since the disk is more rigid in shape. This may also explain why the Pt NP has the lowest current density for MOR in $HClO_4$ (Figure 4.3a), since the protein denaturing can lead to support loss and thus particle aggregation. Nevertheless, both Pt NR and

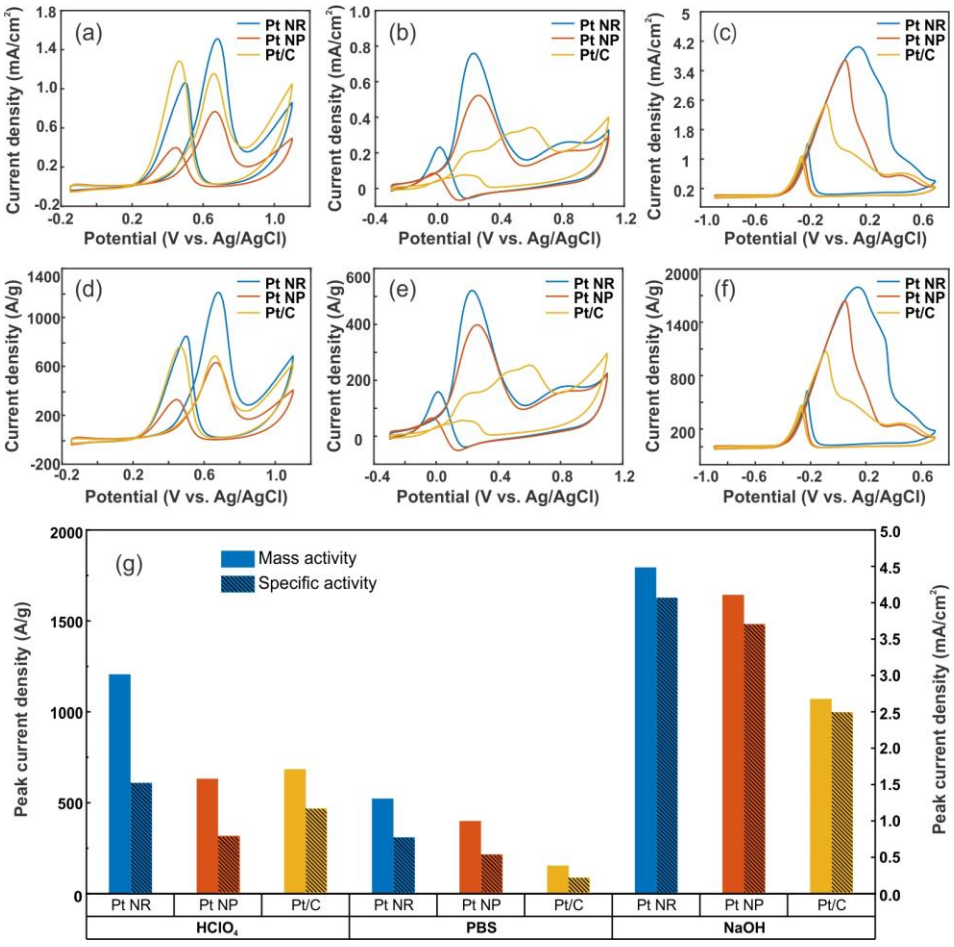

Figure 4.3: Cyclic voltammogram (CV) of Pt NRs, Pt NPs, and Pt/C for MOR in 0.1 M $HClO_4$/1.0 M MeOH (pH 1.2) (a, d), 0.75 M PBS/1.0 M MeOH (pH 6.5) (b, e) and 0.1 M NaOH/0.5 M MeOH (c, f), respectively; (g) Comparison of MOR peak current density of the three Pt catalysts in the above three electrolytes, with CV peak current values normalized to Pt mass (left axis) and ECSA (right axis). All CVs were recorded at a scan rate of 50 mV/s.

Pt NP exhibited higher durability in neutral and basic media. In particular, the final MAs after 1h electrolysis were close for these two Pt catalysts in both media; and the values were improved by ca. 3 times and 1.5 times compared with Pt/C in PBS (Figure 4.4b) and NaOH solutions (Figure 4.4c), respectively. These results conclude that TMVCP templated Pt nanostructures have better tolerance to poisoning effects and thus improved stability in neutral and alkaline pH environments. Taking the CV and CA results into account, the two TMVCP templated Pt materials are better for MOR in neutral and alkaline media than under acidic conditions. Therefore, subsequent experiments were carried out only in neutral and alkaline conditions.

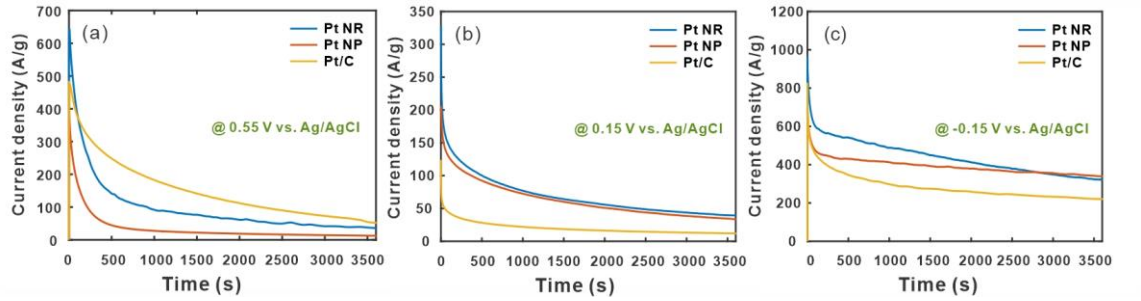

Figure 4.4: The chronoamperometry (CA) MOR tests of the three Pt catalysts in 0.1 M $HClO_4$ (a), 0.75 M PBS (b) and 0.1 M NaOH (c) at constant applied potentials for 1 h.

The relationship between SA and scanning rate in the CV is used to reveal the kinetics. Figure 4.5a shows the case of Pt NR in PBS, with CV conducted at different scan rates (from 10 mV/s to 125 mV/s). It is apparent that the anodic peak current density increases and the peak potential shifts positively as the scan rate increases, indicating a diffusion-controlled process.[11] A linear trend was observed with regard to peak current density vs. square root of scanning rate (Figure 4.5b). The slope value can reflect electron transfer rate in the rate-determining step.[45] Figure A2.7 in Appendix 2 shows the data for Pt NP and Pt/C in PBS, respectively. Also, the results from all the three Pt catalysts in NaOH are given in Figure A2.8 in Appendix 2. It can be seen that in all cases, Pt NR has the largest slope values, demonstrating its enhanced kinetics for MOR, which agrees well with the CV results in Figure 4.3.

Impedance was further adopted to investigate the kinetics of MOR under these two conditions. Figure 4.5c-d compare the Nyquist plots of the three Pt catalysts in both PBS and NaOH electrolytes at the corresponding fixed potentials. The diameter of the semicircle in the medium-

frequency range can be used to indicate the charge transfer resistance (R_{ct}). To estimate R_{ct} values, the plots were fitted by an equivalent circuit (Figure A2.9 in Appendix 2). Specifically, the R_{ct} values follow the order that Pt NR (5402 Ω) < Pt NP (9412 Ω) < Pt/C (14317 Ω) in PBS. The comparison in NaOH followed the same order. The lowest R_{ct} of Pt NR indicates that it has the highest intrinsic ability for methanol oxidation.

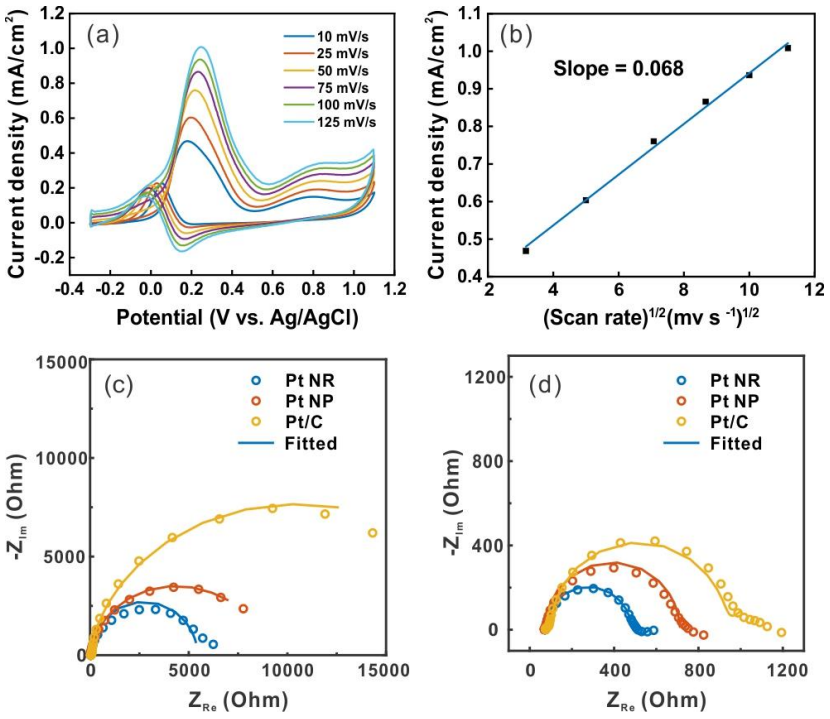

Figure 4.5: (a) CVs of Pt NR catalyzed MOR in 0.75 M PBS/1.0 M MeOH with increasing scan rates; (b) The corresponding plot of forward peak current density versus the square root of the scan rate; Nyquist plots of the Pt NR, Pt NP and Pt/C in 0.75 M PBS/1M MeOH (c) and 0.1 M NaOH/0.5 M MeOH solution (d) at -0.05 V and -0.4 V vs. Ag/AgCl, respectively.

The aforementioned findings demonstrate that TMVCP supported Pt materials exhibit improved catalytic performance compared to Pt/C in PBS and NaOH, suggesting that the protein has a profound effect on Pt catalytic activity. The interaction between TMVCP and Pt enables the formation of Pt NR and Pt NP with uniform sizes. Furthermore, their highly uniform particle dispersion and slightly smaller diameters compared to Pt/C contributes to their larger active surface areas, thus resulting in superior mass activity. In addition, the protein is rich in hydrophilic functional groups such as carboxyl, amino, hydroxy. As stated previously for MOR mechanism,

the OH_{ads} from H_2O dissociation oxidizes the CO_{ads} to form the final product. With abundant functional groups on the protein support, the hydrophilicity of the catalyst system increased, which may make it easier for water to access the catalyst surface and thus facilitating H_2O dissociation to promote oxidation of intermediates such as CO_{ads}. The benefit of adding hydrophilicity of the support was also seen in other systems such as reduced graphene oxide.[54,55] Notably, these two TMVCP-Pt catalysts also showed higher alkaline MOR activity compared to some previously reported Pt-based NMs, as listed in Table A2.2 in Appendix 2. For instance, the mass activities (although under higher alkaline concentrations) were 939 A/g, 1200 A/g and 132 A/g for Pt NPs supported on multiple-layered graphene,[56] PtNi alloy NPs,[57] Au-Pt coreshell NPs,[58] respectively. These values are all lower than TMVCP-Pt NRs and Pt NPs, illustrating the great promise of TMVCP as a building block for fabrication of highly efficient electrocatalysts.

It was also noted that Pt NR outperformed Pt NP for MOR. This difference demonstrates that the structure of TMVCP plays an essential role in influencing the material catalytic activity. These two Pt materials showed almost same individual particle size, shape, UV-vis, XPS and XRD results. Thus, the main difference between Pt NR and Pt NP is their particle distribution pattern. For the Pt NR, the particles were immobilized on the protein ring surface and are in close proximity to each other, with an average edge-to-edge distance of 0.94 ± 0.54 nm (according to TEM). For Pt NP, the individual particles are isolated and capped by bulky A protein subunits, with the distance between particles at least two layer of protein units, which is much larger than 1 nm, according to our previous model.[59]

It has been demonstrated in some studies that the catalytic activity of NPs can be strongly related to particle distribution patterns regarding the interparticle spacing (IP).[13,60–65] For example, Mistry et al.[65] reported tailoring copper (Cu) NP interparticle distance to modulate the product selectivity for CO_2 electroreduction. The authors claimed that when the IP distance of the NPs is small, the desorbed reaction intermediate CO on one Cu NP can readsorb on the adjacent particle, which then continues to be reduced further to the hydrocarbon products, thus affecting the reaction selectivity.[65] In another report by Fabbri et al.,[64] it was also found that the Pt NP distribution has a strong impact on its catalytic performance towards oxygen electroreduction reaction. One important finding is that when the catalyst distribution changed from highly dispersed Pt NPs to closely packed layers with a narrow IP distance, it decreased the absorption energy for OH_{ads}. This

make the Pt surface active sites less blocked by the adsorbates and thus promote the specific activity.[64] Furthermore, Nesselbeger and coworkers' study revealed that when the edge-to-edge interparticle distance between Pt NPs diminished below 1 nm, the SA for ORR boosted significantly.[60] This was explained by the overlap of electric double layers between neighbouring particles, which altered the potential at the compact layer and the adsorption strength of the adsorbed ions.[60] Based on these previous observations, we tentatively attribute the distinct catalytic performance of Pt NR and Pt NP mainly to the IP distance. It is possible that for Pt NR, the individual particles in the ring are close enough to induce a cooperative effect as seen in the abovementioned studies. The detailed effect could be related to a change in the adsorption energy of some oxygenated species (eg. OH_{ads}), which promotes the oxidation of the CO_{ads} (eq 2) and thus accelerate the kinetics of the overall reaction. It is also possible that some desorbed intermediate species can readsorb on a neighbouring particle and undergo further oxidation, leading to an overall increased reaction rate through a more complete six-electron pathway. Further research combining experimental evidence and theoretical calculation is necessary to fully reveal the nature of this structure-activity relationship.

4.4 Conclusions

In summary, we have demonstrated that by varying solution pH, Pt nanorings and isolated Pt nanoparticles can be successfully immobilized on TMVCP disk templates and A protein, respectively. The synthetic processes are straightforward and carried out under mild conditions. The two Pt nanocatalysts as prepared exhibited substantially improved catalytic activity and stability towards methanol electrooxidation in neutral and alkaline media, compared to the benchmarking Pt/C catalyst. The enhanced performance is likely related to the well-defined NP formation and the higher hydrophilicity of protein molecules. Moreover, Pt NR showed even better performance than Pt NP, which is possibly due to particle distribution effects. Using Pt catalyst as an example in this study, we demonstrate that biological scaffold has the potential of modulating nanoparticle organization pattern via tuning the self-assembly state, which can impact on the final nanomaterial catalytic property. With the goal of further improving Pt catalyst performance, one future direction is to alloy Pt with another more oxophilic metal to construct bio-templated bimetallic systems for MOR.

4.5 References

[1] N. Kakati, J. Maiti, S. H. Lee, S. H. Jee, B. Viswanathan and Y. S. Yoon, *Chem. Rev.*, 2014, **114**, 12397–12429.

[2] X. Bai, J. Geng, S. Zhao, H. Li and F. Li, *ACS Appl. Mater. Interfaces*, 2020, **12**, 23046–23050.

[3] L. Yang, G. Li, R. Ma, S. Hou, J. Chang, M. Ruan, W. Cai, Z. Jin, W. Xu, G. Wang, J. Ge, C. Liu and W. Xing, *Nano Res.*, 2021, **14**, 2853–2860.

[4] X. Wang, S. Xi, W. S. V. Lee, P. Huang, P. Cui, L. Zhao, W. Hao, X. Zhao, Z. Wang, H. Wu, H. Wang, C. Diao, A. Borgna, Y. Du, Z. G. Yu, S. Pennycook and J. Xue, *Nat. Commun.*, 2020, **11**, 4647.

[5] H. Huang and X. Wang, *J. Mater. Chem. A*, 2014, **2**, 6266–6291.

[6] R. Zeng, Y. Yang, T. Shen, H. Wang, Y. Xiong, J. Zhu, D. Wang and H. D. Abruña, *ACS Catal.*, 2020, **10**, 770–776.

[7] C. Yang, Q. Jiang, W. Li, H. He, L. Yang, Z. Lu and H. Huang, *Chem. Mater.*, 2019, **31**, 9277–9287.

[8] S. Lu, H. Li, J. Sun and Z. Zhuang, *Nano Res.*, 2018, **11**, 2058–2068.

[9] J. S. Spendelow, G. Q. Lu, P. J. A. Kenis and A. Wieckowski, *J. Electroanal. Chem.*, 2004, **568**, 215–224.

[10] K. Zhang, H. Wang, J. Qiu, J. Wu, H. Wang, J. Shao, Y. Deng and L. Yan, *Chem. Eng. J.*, 2021, **421**, 127786.

[11] V. K. Puthiyapura, W.-F. Lin, A. E. Russell, D. J. L. Brett and C. Hardacre, *Top. Catal.*, 2018, **61**, 240–253.

[12] L. Huang, X. Zhang, Q. Wang, Y. Han, Y. Fang and S. Dong, *J. Am. Chem. Soc.*, 2018, **140**, 1142–1147.

[13] P. Serp, *Nanoscale*, 2021, **13**, 5985–6004.

[14] M. Li, K. Duanmu, C. Wan, T. Cheng, L. Zhang, S. Dai, W. Chen, Z. Zhao, P. Li, H. Fei, Y. Zhu, R. Yu, J. Luo, K. Zang, Z. Lin, M. Ding, J. Huang, H. Sun, J. Guo, X. Pan, W. A. Goddard, P. Sautet, Y. Huang and X. Duan, *Nat. Catal.*, 2019, **2**, 495–503.

[15] X. Chen, W. Wang, X. Chen, X. Liao, Z. Lyu, K. Liu and S. Xie, *Nanoscale*, 2021, **13**, 2632–2638.

[16] E. Antolini, *Appl. Catal. B Environ.*, 2018, **237**, 491–503.

[17] S. T. Hunt, M. Milina, A. C. Alba-Rubio, C. H. Hendon, J. A. Dumesic and Y. Román-Leshkov, *Science*, 2016, **352**, 974–978.

[18] B. Anasori, M. R. Lukatskaya and Y. Gogotsi, *Nat. Rev. Mater.*, 2017, **2**, 1–17.

[19] A. Yuda, A. Ashok and A. Kumar, *Catal. Rev.*, 2020, 1–103.

[20] G. M. Alvarenga and H. M. Villullas, *Curr. Opin. Electrochem.*, 2017, **4**, 39–44.

[21] J.-J. Lv, Y. Li, S. Wu, H. Fang, L.-L. Li, R.-B. Song, J. Ma and J.-J. Zhu, *ACS Appl. Mater. Interfaces*, 2018, **10**, 11678–11688.

[22] I. C. Gerber and P. Serp, *Chem. Rev.*, 2020, **120**, 1250–1349.

[23] Z. Cai, M. Kamiko, I. Yamada and S. Yagi, *ACS Appl. Nano Mater.*, 2021, **4**, 1445–1454.

[24] M. Liu, R. Zhang and W. Chen, *Chem. Rev.*, 2014, **114**, 5117–5160.

[25] Z. A. C. Ramli and S. K. Kamarudin, *Nanoscale Res. Lett.*, 2018, **13**, 410.

[26] E. S. Kang, Y.-T. Kim, Y.-S. Ko, N. H. Kim, G. Cho, Y. H. Huh, J.-H. Kim, J. Nam, T. T. Thach, D. Youn, Y. D. Kim, W. S. Yun, W. F. DeGrado, S. Y. Kim, P. T. Hammond, J. Lee, Y.-U. Kwon, D.-H. Ha and Y. H. Kim, *ACS Nano*, 2018, **12**, 6554–6562.

[27] Z. Zong, K. Xu, D. Li, Z. Tang, W. He, Z. Liu, X. Wang and Y. Tian, *J. Catal.*, 2018, **361**, 168–176.

[28] L. Hou, Y. Niu, Y. Jiang, T. Jiao, Y. Guo, Y. Zhou and F. Gao, *Colloids Surfaces A Physicochem. Eng. Asp.*, 2019, **573**, 6–13.

[29] L. Zhang, N. Li, F. Gao, L. Hou and Z. Xu, *J. Am. Chem. Soc.*, 2012, **134**, 11326–11329.

[30] K. Qu, L. Wu, J. Ren and X. Qu, *ACS Appl. Mater. Interfaces*, 2012, **4**, 5001–5009.

[31] L. Y. Zhang, C. X. Guo, H. Pang, W. Hu, Y. Qiao and C. M. Li, *ChemElectroChem*, 2014, **1**, 72–75.

[32] L. I. Vera-Robles, G. Van Tran Nhieu, C. Laberty-Robert, J. Livage and C. Sanchez, *Adv. Eng. Mater.*, 2013, **15**, 954–961.

[33] Y. Lee, J. Kim, D. S. Yun, Y. S. Nam, Y. Shao-Horn and A. M. Belcher, *Energy Environ. Sci.*, 2012, **5**, 8328–8334.

[34] J. Huang, L. Lin, D. Sun, H. Chen, D. Yang and Q. Li, *Chem. Soc. Rev.*, 2015, **44**, 6330–6374.

[35] Y. Pan, W. J. Paschoalino, A. Szuchmacher Blum and J. Mauzeroll, *ChemSusChem*, 2021, **14**, 758–791.

[36] L. A. Lee, H. G. Nguyen and Q. Wang, *Org. Biomol. Chem.*, 2011, **9**, 6189–6195.

[37] R. Chen, M. Sun, G. Pang, J. Zhou, L. Hou and F. Gao, *ChemElectroChem*, 2017, **4**, 1081–1087.

[38] E. Dujardin, C. Peet, G. Stubbs, J. N. Culver and S. Mann, *Nano Lett.*, 2003, **3**, 413–417.

[39] A. Klug, *Philos. Trans. R. Soc. London. Ser. B Biol. Sci.*, 1999, **354**, 531–535.

[40] W. Shenton, T. Douglas, M. Young, G. Stubbs and S. Mann, *Adv. Mater.*, 1999, **11**, 253–256.

[41] K. M. Bromley, A. J. Patil, A. W. Perriman, G. Stubbs and S. Mann, *J. Mater. Chem.*, 2008, **18**, 4796–4801.

[42] K. Zhou, Y. Zhou, H. Yang, H. Jin, Y. Ke and Q. Wang, *Angew. Chem. Int. Ed.*, 2020, **59**, 18249–18255.

[43] O. K. Zahr and A. S. Blum, in *Virus Hybrids as Nanomaterials. Methods in Molecular Biology (Methods and Protocols)*, eds. B. Lin and B. Ratna, Humana Press, Totowa, NJ, 2014, pp. 105–112.

[44] J. T. Zhang, J. Ma, R. K. Kankala, Q. Yu, S. Bin Wang and A. Z. Chen, *ACS Appl. Bio Mater.*, 2021, **4**, 4039–4048.

[45] J. Zhang, K. Zhou, Y. Zhang, M. Du and Q. Wang, *Adv. Mater.*, 2019, **31**, 1901485.

[46] J. Zhang, R. K. Kankala, J. Ma, Y. Zhou, S. Bin Wang and A. Z. Chen, *Biomacromolecules*, 2021, **22**, 540–545.

[47] O. K. Zahr and A. S. Blum, *Nano Lett.*, 2012, **12**, 629–633.

[48] O. K. Zahr and A. S. Blum, *Nano Lett.*, 2012, **12**, 629–633.

[49] M. A. F. Akhairi and S. K. Kamarudin, *Int. J. Hydrogen Energy*, 2016, **41**, 4214–4228.

[50] L. Li, Z. Wu, S. Yuan and X.-B. Zhang, *Energy Environ. Sci.*, 2014, **7**, 2101–2122.

[51] J. P. Esquivel, M. Castellarnau, T. Senn, B. Löchel, J. Samitier and N. Sabaté, *Lab Chip*, 2012, **12**, 74–79.

[52] S. Xie, X. L. Tong, G. Q. Jin, Y. Qin and X. Y. Guo, *J. Mater. Chem. A*, 2013, **1**, 2104–2109.

[53] F. Wang, B. Fang, X. Yu and L. Feng, *ACS Appl. Mater. Interfaces*, 2019, **11**, 9496–9503.

[54] A. Ali and P. K. Shen, *J. Mater. Chem. A*, 2019, **7**, 22189–22217.

[55] R. Baronia, J. Goel, S. Tiwari, P. Singh, D. Singh, S. P. Singh and S. K. Singhal, *Int. J. Hydrogen Energy*, 2017, **42**, 10238–10247.

[56] C. Berghian-Grosan, T. Radu, A. R. Biris, M. Dan, C. Voica, F. Watanabe, A. S. Biris and

A. Vulcu, *J. Energy Chem.*, 2020, **40**, 81–88.

[57] Q. Jiang, L. Jiang, S. Wang, J. Qi and G. Sun, *Catal. Commun.*, 2010, **12**, 67–70.

[58] N. S. K. Gowthaman, B. Sinduja, S. Shankar and S. A. John, *Sustain. Energy Fuels*, 2018, **2**, 1588–1599.

[59] Y. Pan, A. S. Blum, L. Simine and J. Mauzeroll, *Appl. Catal. B Environ.*, 2021, **298**, 120540.

[60] M. Nesselberger, M. Roefzaad, R. Fayçal Hamou, P. Ulrich Biedermann, F. F. Schweinberger, S. Kunz, K. Schloegl, G. K. H. Wiberg, S. Ashton, U. Heiz, K. J. J. Mayrhofer and M. Arenz, *Nat. Mater.*, 2013, **12**, 919–924.

[61] X. Wang, A. S. Varela, A. Bergmann, S. Kühl and P. Strasser, *ChemSusChem*, 2017, **10**, 4642–4649.

[62] Z. Jusys, J. Kaiser and R. J. Behm, *Langmuir*, 2003, **19**, 6759–6769.

[63] Y. E. Seidel, A. Schneider, Z. Jusys, B. Wickman, B. Kasemo and R. J. Behm, *Langmuir*, 2010, **26**, 3569–3578.

[64] E. Fabbri, S. Taylor, A. Rabis, P. Levecque, O. Conrad, R. Kötz and T. J. Schmidt, *ChemCatChem*, 2014, **6**, 1410–1418.

[65] H. Mistry, F. Behafarid, R. Reske, A. S. Varela, P. Strasser and B. Roldan Cuenya, *ACS Catal.*, 2016, **6**, 1075–1080.

Chapter 5

Nanometals Templated by Tobacco Mosaic Virus Coat Protein with Enhanced Catalytic Activity

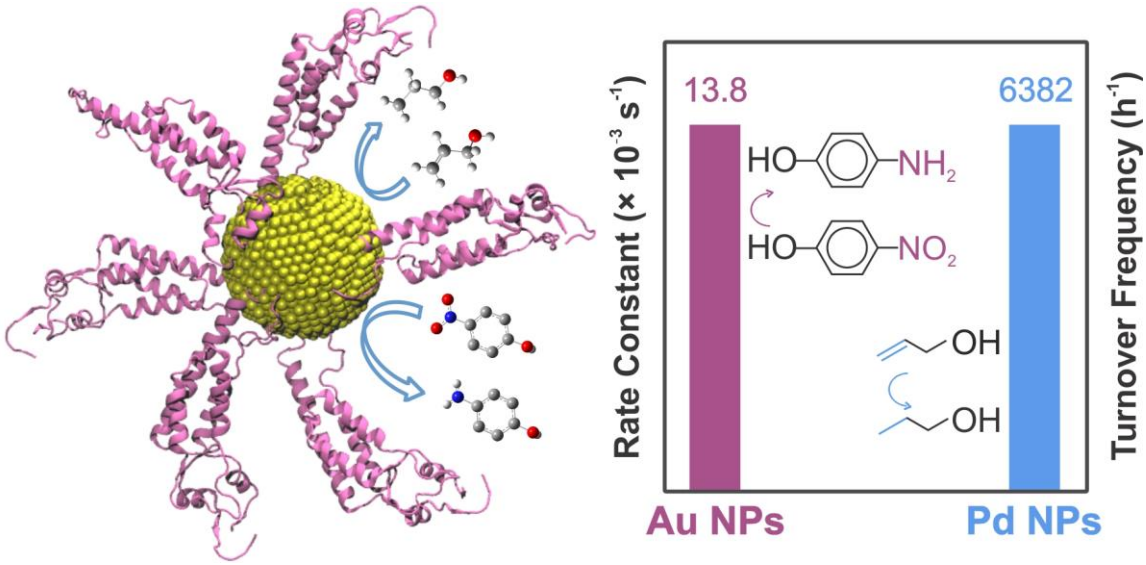

Chapter Preface

Scientific Contributions:

Chapter 5 explores the potential of TMVCP A protein as a template for synthesis of spherical metallic nanoparticles (MNPs, Pd, Pt, Au) in alkaline environment at room temperature. The as prepared nanoparticles were evaluated in two industrially important organic reactions, i.e., 4-nitrophenol and unsaturated alcohol hydrogenation. Our results showed that these MNPs exhibited superior catalytic activity compared to materials synthesized by conventional chemical reductions. The insight into the enhanced performance was studied via molecular dynamic simulations and the possible origins were proposed. The results in this chapter may stimulate more research on developing natural bulky ligands to protect nanostructures for heterogeneous catalysis.

Public Information:

This chapter is adapted from a previously published research article with permission from:

Y. Pan, A. S. Blum, L. Simine, J. Mauzeroll. Nanometals templated by tobacco mosaic virus coat protein with enhanced catalytic activity. *Applied Catalysis B: Environmental.* **2021,** 298, 120540.

Chapter Abstract

Bio-nano hybrid materials feature eco-friendly synthesis, various self-assembly patterns and numerous possibilities for surface functionalization. With these unique advantages, biological scaffolds have been regarded as green alternatives to fabricate metallic nanomaterials. Herein, a bulky TMVCP was employed as a versatile template to synthesize metallic nanoparticles at room temperature. These materials exhibited exceptional performance for organic transformations under green conditions. Remarkably, while Au NPs showed rapid kinetics in pollutant 4-nitrophenol reduction, Pd NPs demonstrated superior catalytic activity towards hydrogenation of unsaturated alcohols. The enhanced performance is likely related to the protein. To ascertain the protein structure-function effect on the catalytic performance, an in-depth analysis was performed for a TMVCP-Pd NP system via molecular dynamic (MD) simulations. Our results suggest that due to

minimal passivation of bulky protein, a large portion of the Pd NP surface remains approachable for the reactants, thus resulting in high reaction rate. While Chapter 3 and 4 explored the electrocatalytic applications, Chapter 5 broadens the scope of application to organic reactions using TMVCPA template-metal hybrids (Pd, Pt and Au).

5.1 Introduction

Nanosized noble metals have opened unprecedented opportunities for wide range of chemical applications, such as organic synthesis, electrocatalysis, photocatalysis, etc.[1–5] Their catalytic performance is significantly influenced by surface composition, size, morphology and facet availability. Controllable synthesis of nanocatalysts with desired functions has long been a goal in the field of nanoscience and chemical catalysis. In the classical 'bottom up' route to prepare metallic nanomaterials (MNMs), metal salts are reduced to zerovalent nanometals and dispersed by stabilizers, which are used to prevent material aggregation caused by the high surface energy. Citrate, thioethers and alkanethiolate ligands are typical caping reagents used to protect nanometals, in which electrostatic repulsion or steric effects are used to increase colloid stability. Unfortunately, this 'bottom-up' method frequently involves the use of non-natural stabilizers, organic solvents and elevated temperatures to generate structures with specific features. To alleviate high energy input and address environmental concerns, green catalytic systems with excellent reaction activities are highly desired.

In recent years, NMs fabricated via biologically-inspired approaches are emerging as attractive candidates for applications in many research fields such as lithium ion batteries,[6,7] catalysis,[8,9] electronics,[10,11] bio-imaging,[12,13] and drug delivery,[14,15] etc. Such approaches hold some inherent advantages over traditional chemical methods. Biobased synthesis can be much more energy efficient. The reactions are generally carried out under ecologically benign conditions (room temperature, water as the solvent) and employ green and renewable sources as supports/capping agents, which mainly include peptides,[16–18] proteins,[19–21] DNA,[22,23] and some microorganisms.[24–26] Additionally, the self-assembly properties of some biomolecules make them facile templates to organize nanoparticles (NPs) into different patterns by varying the solution conditions. Moreover, the abundant surface functional groups on such bio-templates can be modified through genetic

modification and bioconjugation to provide numerous possibilities for nucleation events. For example, a series of genetically engineered filamentous M13 bacteriophages have served as versatile building blocks for the fabrication of nanowires and nanonetworks,[27–30] which are difficult to synthesize using nonbiological methods under mild conditions.

Among the bio-templates mentioned above, peptides are the most extensively explored for biocatalyst fabrication due to their ready availability, simple structure and easy modification. Compared to most peptides, proteins have longer sequences of amino acid and more complex hierarchical structures, thus providing more diverse patterning for NPs. From a catalysis perspective, some bulkier protein structures may passivate the NP surface to a lesser extent, thus exposing a larger surface area for the approach of small reactant molecules to improve catalysis efficiency.

TMVCP is the capsid protein of TMV. This plant virus is a rod-shaped particle, with a single stranded RNA genome surrounded by 2130 identical coat protein subunits forming a helical tube.[31,32] Interestingly, the morphology of the RNA-free coat protein is dependent on the pH and ionic strength of the solution.[33] For example, it self-assembles predominantly into disk forms in pH 6.5~7.5. In higher pH solutions, the disk disassembles into smaller A-protein (a mixture of monomers and oligomers, a single subunit contains 158 amino acid residues). The complete virion form[34,35] and the RNA free disk protein[36,37] have been successfully utilized as versatile building blocks for 3D metallic nanomaterial growth/deposition. However, A-protein remains less explored for mediating the production of nanoarchitectures.

In this chapter, we demonstrate that A-protein (hereafter denoted as TMVCPA) is able to support the growth of highly active green catalysts. Specifically, near spherical Pd, Pt and Au NPs were produced under ambient conditions. These metallic nanoparticles (MNPs) were tested for two organic reactions in aqueous media, i.e., 4-nitrophenol (4-NP) reduction and olefinic alcohol hydrogenation. The kinetic results showed that Au and Pd NPs exhibited exceptional catalytic efficiency towards 4-NP reduction and allyl alcohol hydrogenation, respectively. Studies have shown that these two organic reactions follow the heterogeneous-type mechanism when catalyzed by nanometals rather than the atom/ion leaching mechanism.[38,39] The nanometals aided the electron transfer process between the two reactants to lower the kinetic barrier. In the heterogeneous mechanism, reactant molecules in solution must first penetrate through the

protective ligand layer to reach the NP surface in order to drive the reaction to form products. Therefore, reaction activity is a function of the available surface area of the NPs, with a larger free surface area giving more rapid kinetics. In this regard, densely packed ligands that interact strongly with the NP surface not only block some metal surface but also hinder the diffusion rate of reagents, leading to diminished reaction rate.[40]

One key advantage of using TMVCPA-templated catalysts we explored in this chapter is that the bulky protein has rather minimal passivation of the metal surface in spite of the induced high NP colloid stability, which is of great significance for heterogeneous catalytic systems. We demonstrate this mechanism via a combination of experimental evidence and computational simulations. Our circular dichroism results indicate that the conformation of protein is generally conserved well before and after binding to the nanoparticle. In order to gain further insights on this binding regime and explore the molecular details, an atomistic molecular dynamic (MD) simulation of a TMVCPA-Pd NP-water-propanol system was performed for allyl alcohol hydrogenation reaction. Our simulations revealed that even in the presence of proteins, a large catalytically active surface area is exposed to solvent and small solutes. Moreover, from this simulation, the number of propanol molecules adsorbed on one Pd NP surface was quantified and was shown to be in good agreement with the number derived from experimental turnover frequency (TOF), which further confirms the high catalytic activity of the catalyst. Overall, we conclude that this protein-NP system has the combined benefit of an eco-friendly synthetic method and outstanding structure-activity performance for heterogeneous catalysis.

5.2 Experimental Section

5.2.1 Materials

Na_2PdCl_4, $Na_2PtCl_6 \cdot 6H_2O$, $NaAuCl_4 \cdot 2H_2O$, $NaBH_4$, allyl alcohol, 3-buten-ol, 3-methyl-2-buten-1-ol, crotyl alcohol, 2-methyl-3-buten-2-ol, acrylic acid, acrylic amide, N-iso-propylacrylamide, 4-nitrophenol, sodium borohydride, dimethyl sulfoxide and deuterium oxide were purchased from Sigma Aldrich. Tris Base and hydrochloric acid were acquired from Fisher Scientific. All chemicals were used as received without further purification. Millipore MilliQ water (18.2 MΩ·cm) was used throughout.

5.2.2 Fabrication of TMVCPA-Templated MNPs

TMVCP was expressed and purified according to a previously reported procedure.[37] The purified protein stored at -80 °C in PBS (20 mM, pH 7.0) was thawed to room temperature and dialyzed into pH 8.9. Dialysis was carried out over 24 h in Tris-HCl buffer (15 mM) using dialysis membrane tubing with 12 k-14 k MWCO (Spectra/Pro). The protein concentration was determined by the absorbance at 282 nm (1.27 ml (mg cm)$^{-1}$) using UV-vis spectroscopy. To synthesize Pd NPs, 15 μL of Na_2PdCl_4 solution (50 mM) was incubated with 400 μL of protein (0.24 mg/mL in 15 mM Tris-HCl buffer, pH 8.9) and gently stirred for 3 hours. 15 μL of freshly prepared $NaBH_4$ solution (150 mM) was then added to the above solution. The mixture turned dark brown immediately. Stirring was continued for 1 h and the reaction mixture was then allowed to stand for another 1 h before characterizations or catalysis tests. Pt NPs and Au NPs were prepared with the same procedure as the Pd NPs, using $Na_2PtCl_6 \cdot 6H_2O$ and $NaAuCl_4 \cdot 2H_2O$ as the metal precursors, respectively.

5.2.3 Material Characterizations

All UV-vis spectra were obtained with an Evolution 260 Bio UV-vis spectrometer employing a 1.0 cm quartz cuvette. The TEM, HR-TEM, and SAED images were acquired using a Talos 300 TEM operating at 200 kV. The samples were prepared by drop-casting 10 μL of nanomaterial suspensions onto carbon-coated copper grids (Ted Pella) for 5 min, after which the residues were removed with a filter paper. Size distributions of MNPs were measured by counting at least 300 random particles using ImageJ software. The crystallinity of MNPs was analyzed from HR-TEM and SAED patterns. XPS spectra were recorded on a Thermo Scientific K-Alpha XPS system with a monochromatic Al Kα source ($\hbar\nu$ = 1486.6 eV). CD characterization was performed at room temperature using an Applied Photophysics CD spectrometer. 350 μL of sample solutions were injected into a quartz cell with a 5 mm path length. A total of seven scans (scan rate: 2 nm/s) were performed for each sample and averaged. The signal of pure Tris-HCl buffer was subtracted. ^{1}H NMR spectra were obtained on a Bruker 500 MHz NMR spectrometer.

5.2.4 MNP-Catalyzed 4-Nitrophenol Reduction

The procedure for MNP catalyzed 4-nitrophenol reduction was adapted from previously published literature.[41,42] In a 1.0 cm cuvette, 15 μL of as synthesized Pd NP solution was diluted with 785 μL of MilliQ water into 800 μL. For catalyst tests with other amounts, sufficient water was added to keep a total volume of 800 μL. 120 μL of freshly prepared $NaBH_4$ solution (0.1 M) was then mixed with the above suspension and left undisturbed for 7 min. After that, 400 μL of 4-nitrophenol solution (200 μM) was added. Immediately after the addition, time dependent UV-vis absorption spectra were recorded from 500 nm to 250 nm, with a time interval of 7 s for 4 min. To determine activation energy, experiments were conducted at temperatures ranging from 8 to 39 °C. The catalyst concentration was calculated from the initial reagent concentration. Catalytic experiments using Pt and Au NPs were carried out under identical conditions.

5.2.5 MNP-Catalyzed Allyl Alcohol Hydrogenation

In a 10 mL round bottom flask, 14.6 μL of Pd NP (0.05 mol% loading) solution was diluted with water into 4 mL. The suspension was bubbled with hydrogen gas for ~10 min at a flow rate of 15 mL/min and the flask was then sealed with a rubber stopper and parafilm. To initiate the reaction, 3.05 mg of allyl alcohol in 1 mL of water was injected into the suspension and stirred at room temperature. To calculate TOF values, 500 μL aliquots were extracted at predetermined time points and prepared for ^1H NMR measurements. Dimethyl sulfoxide served as the internal standard to quantify the product. D_2O was the deuterium solvent. Experiments with Pt NPs and Au NPs followed the same procedure.

5.2.6 Molecular Dynamic Simulations

MD simulations were run on the combined system of six TMVCPA subunits surrounding one Pd NP and one thousand dissolved propanol molecules in a 30^3 nm^3 water box. This initial configuration was constructed based on experimental concentrations and chemical intuition. It remained stable for the duration of the production simulations (30 ns) with only minor fluctuations in the adsorption patterns. We chose to simulate propanol rather than the allyl alcohol because propanol is the product of the hydrogenation reaction of allyl alcohol and the two structures occupy a similar area on the surface of the Pd NP. Thus, for the purpose of our simulation, these two are

interchangeable and propanol was chosen due to readily available forcefield parameters.[43] GROMACS/2020.4 was used as our MD engine with the OPLS-AAM forcefield with SPC/E water.[44] Propanol was modelled using the forcefield developed by Jorgensen et al.,[43] and the Pd NP was modelled using the Interface MD parameters for fcc Pd reported in the work by Heinz et al.[45] In all simulations, the Verlet cut-off scheme was used with 1 nm cut-offs for nonbonded interactions, and the Particle Mesh Ewald (PME) for long-range electrostatics was used with a PME order of 4, and a Fourier spacing of 0.16. Following the initial minimization and preliminary equilibration preparatory simulations, the production NVT run was performed with a Berendsen thermostat at 300 K for 30 ns with 2 fs time-steps and molecular configurations were recorded for analysis at 10 ps intervals. A Python module was used to analyze the data.[46]

5.3 Results and Discussion

5.3.1 Synthesis and Characterizations of TMVCPA-Templated MNPs

Pd, Pt and Au NPs were prepared in a facile two-step process as shown in Figure 5.1a. Metal salts were first incubated with protein in Tris-HCl buffer, in which amino acid residues on the TMVCPA with can bind with the metal-chloro complexes through electrostatic interaction.[34,47] Adding excess amount of $NaBH_4$ leads to a rapid solution color change from pale yellow to dark brown (Pd and Pt) or purple (Au), indicating the formation of zerovalent nanomaterials. No obvious precipitation was observed, suggesting that the TMVCPA enables NP high colloid stability. The reduction process was monitored by UV-vis spectroscopy as displayed in Figure 5.1b. In the pre-reaction spectra (Figure 5.1b), the absorbance peaks in the range of 300~400 nm come from the unreduced metal salts (same features with metal salts alone in Tris-HCl buffer, Figure A3.1 in Appendix 3). In the post-reaction spectra (Figure 5.1c), the metal peaks disappeared, indicating the reduction of metal ions. Specifically, for Au NPs, there is an absorbance band centered around 540 nm, which is typical of plasmonic Au NPs larger than 2 nm.[48] Upon exposure to light, the surface conduction electrons of Au NPs are stimulated and induces a localized collective oscillation of electron cloud, resulting in a plasmonic band in the visible frequency of UV-vis spectrum.[49] Additionally, the absorbance at around 280 nm for both Au and Pd NPs is from the protein, while it is more

featureless in the Pt NPs. Compared to pure protein, the higher absorbance values at ~280 nm are attributed to the scattering effect of NPs.

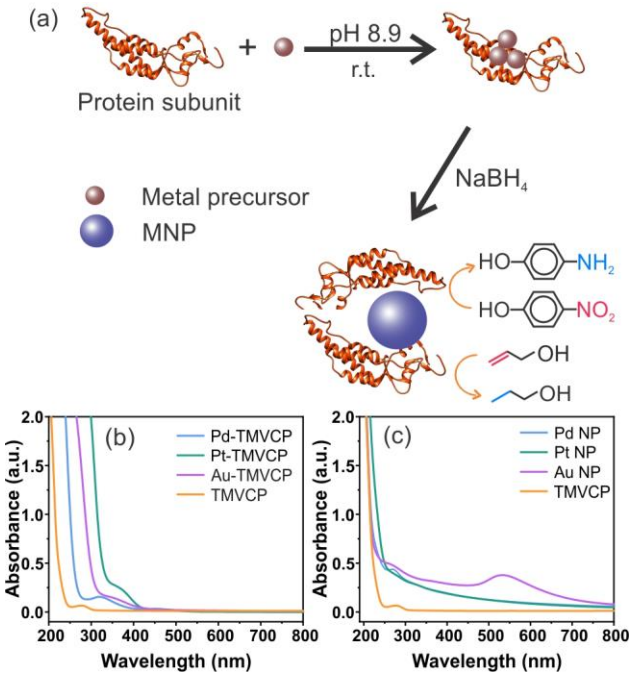

Figure 5.1: (a) Synthetic scheme of TMVCPA-templated MNPs and catalytic applications for 4-nitrophenol reduction and allyl alcohol hydrogenation; (b) UV-vis spectra of metal precursors incubated with protein in Tris-HCl buffer at pH 8.9 prior to reduction; (c) UV-vis spectra of reaction mixture after reduction by $NaBH_4$.

The size, shape and crystallinity of the as synthesized MNPs were characterized by transmission electron microscopy (TEM), high-resolution TEM (HR-TEM) and selected area electron diffraction (SAED). Representative TEM images confirmed the formation of MNPs in Figure 5.2a-c. For all the three materials, near spherical NPs with uniform size distribution were observed, demonstrating that the TMVCPA can well control the growth of NPs. The particle size distribution histograms (Figure 5.2g-i) revealed that the average diameters of Pd, Pt and Au NPs are 3.44 ± 0.51 nm, 3.05 ± 0.49 nm, 2.86 ± 0.49 nm, respectively. $NaBH_4$ is a strong reducing agent that often leads to formation of nanoparticles with small sizes. No obvious change in morphology and size was observed with slightly varying ratios of the metal salts to protein and incubation time. For example, with higher concentrations of Na_2PdCl_4 or longer incubation time, similar sizes were obtained for Pd NPs (Figure A3.2 in Appendix 3). HR-TEM images (insets) showed that [111] is

the dominant facet for all the three materials by measuring the interlayer spacings. In addition, all the SAED results (Figure 5.2d-f) displayed Scherrer ring patterns assigned to [111], [200], [220] and [311] planes, suggesting the formation of fcc crystal lattice of MNPs.

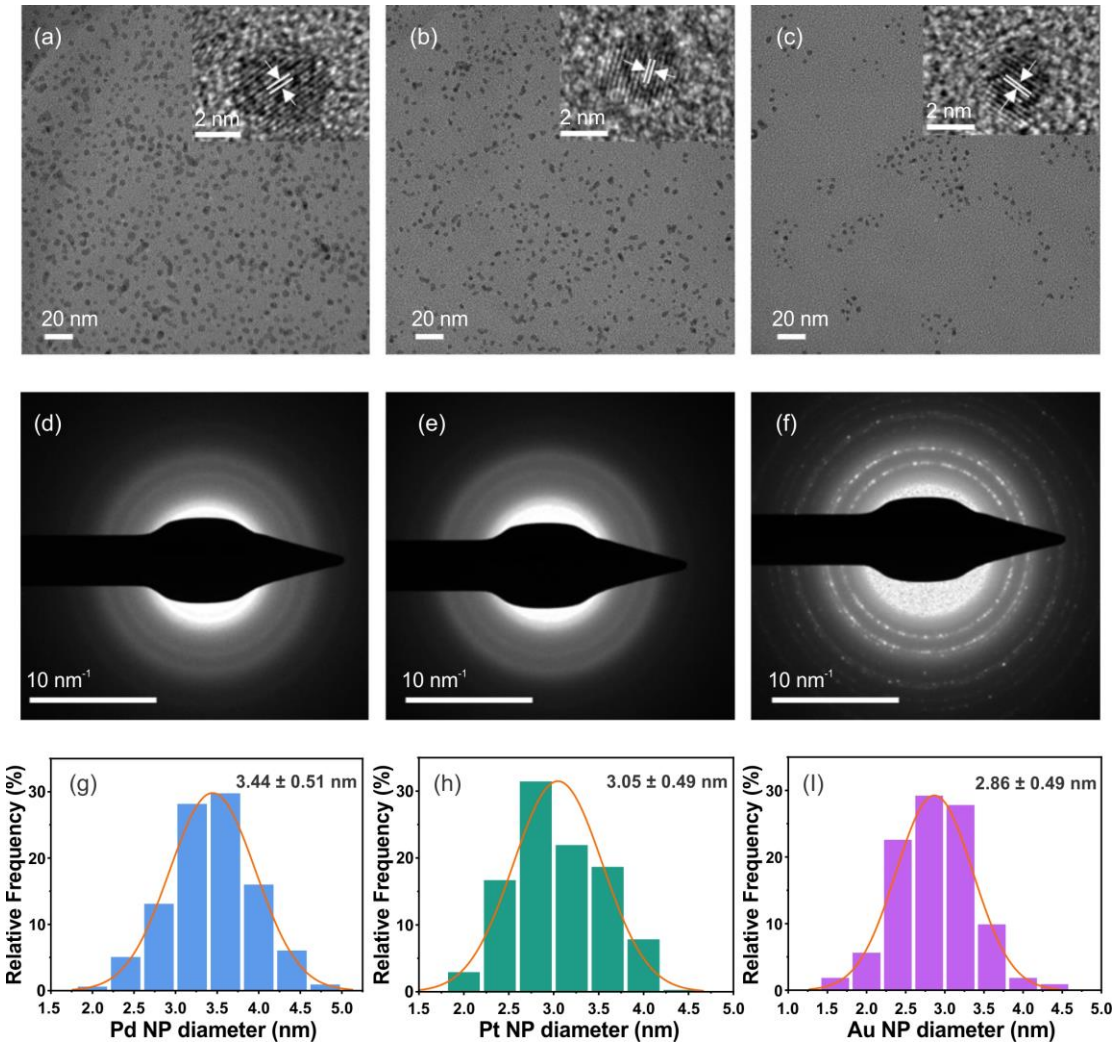

Figure 5.2: Morphology and crystallinity characterizations of MNPs. TEM image of Pd (a), Pt (b) and Au (c) NPs, the inset shows the HR-TEM results; SAED patterns of Pd (d), Pt (e) and Au (f) NPs; Size distribution histograms of Pd (g), Pt (h) and Au (i) NPs.

X-ray photoelectron spectroscopy (XPS) measurements were carried out to probe the surface composition and electronic state of the protein-templated MNPs. Figure 5.3a-c shows the XPS spectra of core level Pd 3d, Pt 4f and Au 3d peaks, respectively (survey spectra in Figure A3.3 in Appendix 3). Deconvolution of the fitted data reveals that the metals have different charging states

on the protein. In the deconvoluted Pd 3d spectrum, the doublet peaks located at 335.32 eV and 340.52 eV can be assigned to the zerovalent Pd $3d_{5/2}$ and $3d_{3/2}$ respectively, confirming the formation of NPs. In addition, peaks with higher binding energies (orange peaks at 337.32 eV and 342.42 eV) are also observed, which indicates small amount of oxidation during sample preparation after synthesis. Similar result was obtained for Pt NPs, in which Pt^0 $4f_{7/2}$ and $4f_{5/2}$ have binding energies at 71.01 eV and 74.36 eV respectively, while the oxidized species locate at 72.51 eV and 75.80 eV. Compared to Pd and Pt NPs, Au NPs have a smaller amount of oxidation, as indicated by its smaller area ratio of the orange peaks. The spectrum deconvolution result in Au^0 at 83.39 eV and 87.08 eV, Au oxides at 85.48 eV 88.78 eV.

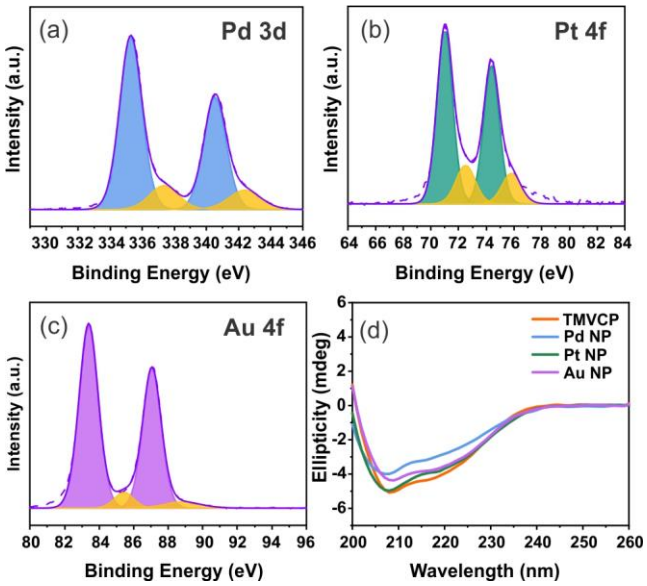

Figure 5.3: XPS and CD analysis of MNPs. XPS spectra of Pd 3d from Pd NP (a), Pt 4f from Pt NP (b) and Au 4f from Au NP (c); CD spectra of TMVCPA and MNPs in Tris-HCl buffer (d).

The secondary structural composition of the TMVCPA was examined by circular dichroism (CD) spectroscopy in Figure 5.3d. The protein spectrum is similar to results in several previous reports,[50,51] in which the negative band at 208 nm and the shoulder around 220 nm suggest the dominant presence of α-helix conformations. In the protein-MNP mixture spectra, the features of the band shape remained relatively constant, indicating that the protein conformation in general conserves well after binding to MNPs (the difference in ellipticity magnitude might be due to slight difference in concentration). However, the CD results are not able to provide enough information

on the detailed binding patterns of TMVCP on the metal surface. To uncover the role of protein's structural aspects in the catalysis, computational studies were conducted which will be discussed later.

5.3.2 Catalytic 4-Nitrophenol Reduction

Nitrophenols are commonly used in the synthesis of pesticides, plasticizers and dyes, which can cause serious environmental concerns with their release into wastewater.[52] Reduction of nitroaromatics is an efficient method both for eliminating hazardous pollutants and for producing aromatic amines, which are significant chemicals in industrial applications (e.g., as corrosion inhibitors, and as intermediates for pharmaceuticals, etc). The reduction of 4-NP is one of the most widely adopted model reactions to evaluate the catalytic activity of nanocatalysts since 1) there are no by-products formed; 2) the reaction can be carried out in water at room temperature; 3) the reaction rate can be easily monitored via time resolved UV-vis spectroscopy for kinetic studies.[53]

Studies have demonstrated that mechanistically, the reduction takes place directly on the NP surface.[39] Addition of $NaBH_4$ to the catalyst solution can produce active hydrogen species on the metal surface. This hydrogen then reacts with the newly added 4-NP to form an unstable intermediate 4-nitrosophenol, which is then converted to 4-hydroxyaminophenol and finally 4-aminophenol (4-AP). Figure 5.4a presents the time-dependent UV-vis monitoring of the 4-NP reduction catalyzed by 20 μM Au NPs in water at room temperature. In alkaline pH, 4-NP deprotonates to 4-nitropheonlate ion with a strong absorbance peak at 400 nm. As the reaction time increased, its peak intensity gradually decreased, and accompanied by the emergence of a new peak at 310 nm corresponding to the generation of 4-aminophenol. The spectrum was recorded for about 4 min when the reaction was complete as the 400 nm peak reached almost zero. This was confirmed by the solution color change from initial bright yellow to light purple in the end. In the control experiment without any catalyst, only little change in peak intensity at 400 nm was observed (see Figure A3.4 in Appendix 3.4), indicating that $NaBH_4$ alone could not efficiently reduce 4-NP and catalyst was necessary to lower the kinetic barrier.

Given that $NaBH_4$ is in significant excess amount (150-fold in molar) compared to 4-nitrophenol, the reaction can be regarded as a pseudo-first-order reaction with respect to the 4-nitrophenol concentration. Therefore, the reaction rate constant (k) is used to evaluate the catalytic activity of

MNPs. To study the kinetics, $\ln(C/C_0)$ (data taken from absorbance values at 400 nm) was plotted against reaction time and comparison was made between Au and Pd NPs at room temperature, as shown in Figure 5.4b (our preliminary results showed that compared to Au and Pd NPs, Pt NPs were much slower for 4-NP reduction, thus no further experiments with Pt were continued). C is the 4-NP concentration at time t and C_0 is its initial concentration. According to Eq. 5.1, k is the slope value of the fitted linear region. The obtained k values for Pd NPs and Au NPs are 6.32×10^{-3} s^{-1} and 13.80×10^{-3} s^{-1} (same catalyst concentration), respectively. This suggests that Au NP has higher catalytic activity than Pd NPs. To check the effect of catalyst concentration, different amounts of both catalysts were applied to the reaction (Figure 5.4c). As expected for both materials, larger k values were obtained at higher catalyst concentrations.

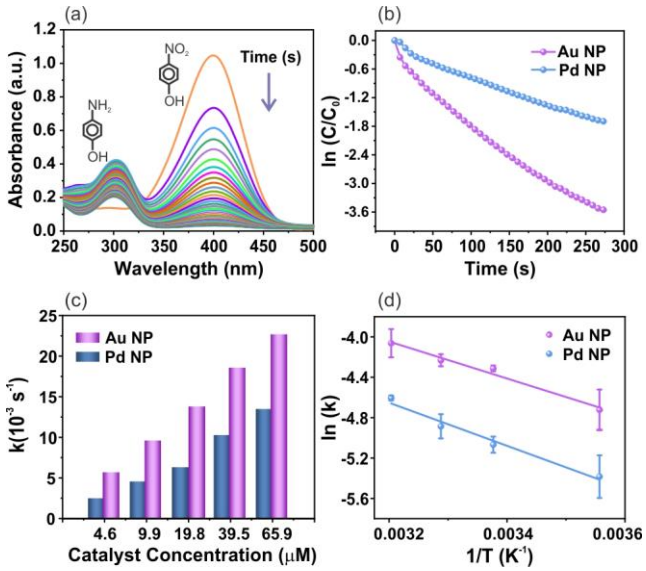

Figure 5.4: Kinetic results of Au and Pd NPs catalyzed 4-NP reduction. (a) UV-vis spectra evolution of 20 μM Au NPs catalyzed 4-NP reduction; (b) ln (C/C_0) vs. time to calculate pseudo first order reaction rate constants k for Au and Pd NPs, with a catalyst concentration of 19.8 μM; (c) Dependence of k on the catalyst concentration; (d) The Arrhenius plots at different temperatures to calculate E_a for Au and Pd NPs, catalyst concentration 19.8 μM. In (a), (b) and (c), reactions were all carried out at room temperature.

In addition, Au NPs exhibited higher activity than Pd NPs for all measured concentrations.

$$-kt = \ln\left(\frac{C_t}{C_0}\right) \tag{5.1}$$

$$\ln k = \ln A - \frac{E_a}{RT} \quad (5.2)$$

To further compare the performance of Au NPs and Pd NPs, the activation energy (E_a) was determined by carrying out experiments at four different temperatures from 8 to 39 °C. Table 5.1 presents the results of k at each temperature for Au and Pd NPs with the same concentration, each averaged from triplicates. For all four temperatures, Au NPs outperform Pd NPs with larger k values. ln (k) was then plotted as a function of 1/T (temperature in Kelvin) in Figure 5.4d and a linear relationship was observed for both materials. E_a (in kJ/mol) was then calculated from the slope of the fitted trend line, which follows the Arrhenius equation (Eq. 5.2). A is the pre-exponential factor and R is the gas constant. E_a values of 17.74 and 15.22 kJ/mol were obtained for the 4-NP reduction catalyzed by Pd NPs and Au NPs, respectively. This indicates that Au NPs are able to drive the reaction more easily than Pd NPs. Combining the results of rate constant and activation energy, we can be confident that among all three protein-templated MNPs, Au NPs exhibited the best performance towards catalyzing 4-NP reduction. As mentioned above, in 4-NP reduction, the BH_4^- adsorbs on the metal surface and directly transfers the H^- onto the metal surface, which then attacks the 4-NP substrate. During this process, the electronic property of the metal plays an important role. The higher k values of Au maybe partially explained by its faster electron transfer rate with an electron-rich surface.[54,55] In addition, Au NPs have the smallest size among the three catalyst, which can be the second reason for their higher activity. Nevertheless, other factors such as adsorption rate of 4-NP/BH_4^- and desorption rate of 4-AP product can also differ among the metals. The present outcome may be ascribed to multiple factors. At this moment, a full interpretation of the activity order Au > Pd > Pt is challenging and needs further studies on each step during 4-NP reduction.

The recyclability of Au and Pd NPs were examined by running the 4-NP reduction for six times and the resultant k values were shown in Figure A3.5 in Appendix 3. For Au NPs, the k value was as high as 96% in the 6th cycle, demonstrating their good cycling potential. Pd NPs showed lesser stability, maintaining ~72% in the 6th cycle. The decrease in the k may be attributed to the gradual accumulation of 4-AP product on the NP surface that can block some active sites.[56] TEM and XPS were further employed to characterize the morphology and surface charge of the recovered two catalysts after cycling tests. It was observed by TEM (Figure A3.6 in Appendix 3) that both MNPs remained almost unaltered in particle shape and size, in which Au NPs showed an average diameter

of 3.00 ± 0.56 nm, and Pd NPs gave 3.53 ± 0.65 nm. Interestingly, XPS (Figure A3.7 in Appendix 3) results showed that the binding energies of Au^0 $4f_{5/2}$ and Pd^0 $3d_{3/2}$ decreased by around 0.6 eV and 1.0 eV, respectively. The decrease in the binding energy may be attributed to the 4-AP product, which absorbed onto the NP surface as a ligand and induces change in the electronic states of the NP surface.[57] Also, some BH_4^- (electron donor) might be still absorbed on the NP surface and resulted in an electron enriched metal state.

In order to compare the catalytic activity of TMVCPA-Au NPs with literature results, k was normalized by amount of Au elements (μmol) to obtain k_{nor}. Table 5.2 listed the comparison of k_{nor} and E_a with some representative sub 15 nm Au nanocatalysts. It can be seen that Au NPs with smaller sizes (entries 1, 3-6, 8) generally give higher k_{nor} compared to those with larger sizes (entries 2, 7), which can be attributed to the higher surface-to-volume ratio with smaller NPs. However, size is not the only decisive parameter for catalytic performance. As compared in entries 5, 6, 8, NPs with diameters 2~4 nm showed different k_{nor} and E_a values, suggesting that the template has great impact on catalytic activity. Overall, our TMVCPA templated Au catalyst exhibited excellent activity, as demonstrated by its higher k_{nor} and lower E_a values compared to typical Au NPs stabilized by polymer (entry 1), carbon support (entry 2), peptides (entries 3-6), and ESM (entry 7).

Table 5.1: Au and Pd NP catalyzed 4-NP reduction at different temperatures.

	Catalyst [k ($10^{-3}s^{-1}$)]	
Temperature	Au NP	Pd NP
10 ºC	14.74 ± 0.35	7.22 ± 0.78
22 ºC	18.62 ± 1.24	9.64 ± 0.25
30 ºC	21.60 ± 0.61	11.40 ± 0.34
39 ºC	25.13 ± 0.68	13.61 ± 0.93
Ea (kJ/mol)	**13.32 ± 0.41**	**15.95 ± 0.67**

Table 5.2: Comparison of catalytic activities of different Au nanocatalysts for the 4-NP reduction.

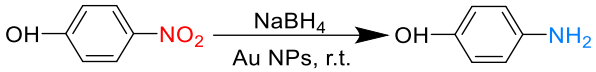

Entry	Particle size / shape [a]	Stabilizer / support	$NaBH_4$/4-NP/Au (molar ratio)	k ($\times 10^{-3}$ s^{-1})	k_{nor} ($\times 10^{-3}$ s^{-1} μmol^{-1})	E_a (kJ/mol)	Ref
1	6 nm / SN	PVP	800/6/1	3.7	72.6	-[b]	62
2	14.6 nm / SN	Graphene hydrogel	165/2.30/1	3.2	26	-	63
3	6.7 nm / NPN	R5 peptide	133/0.71/1	11 ± 2	46 ± 0.8	29 ± 1.4	64
4	5.2 nm / SN	Amyloid-β peptide	75/0.75/1	12.8	64	14.2	41
5	2.3 nm / SN	A3 peptide	75/0.75/1	8	40	20 ± 1.0	65
6	3.3 nm / SN	AuBP2 peptide	75/0.75/1	14.8	74	26.2 ± 0.9	42
7	11.7 nm / SN	Egg shell membrane	200/1/-	-	22 ± 2	-	66
8	**2.8 nm / SN**	**TMVCP**	**460/3/1**	**13.8 ± 0.4**	**527 ± 15**	**15.22 ± 1.5**	**This work**

[a]SN: near spherical nanoparticle; NC: nanocluster; NPN: nanoparticle network. [b]Data not available.

5.3.3 MNP Catalyzed Olefinic Alcohol Hydrogenation

Pd based nanocatalysts are known to be highly active for a series of organic reactions, such as hydrogenation, cross couplings, alkylation, etc.[58–61] In this chapter, TMVCPA-templated Pd NPs were assessed for catalyzing hydrogenation of olefinic alcohols, which are important reactions for producing useful saturated alcohols in fine chemical and pharmaceutical synthesis. The simplest structure allyl alcohol was first used as the model substrate. Similar to NP catalyzed 4-NP reduction, the allyl alcohol hydrogenation occurs on the metal surface, via a Pd-alkyl mechanism.[38] Molecular hydrogen dissociates on the Pd surface to form a Pd-H species, which then coordinates with the π-bond of the allyl alcohol. With an anti-Markovnikov insertion pattern, hydrogen atom is added to the α carbon and forms the linear Pd-alkyl intermediate and finally produces n-propanol. The Pd surface was saturated with hydrogen species by bubbling H_2 gas into Pd NPs dispersed in water, followed by rapid injection of allyl alcohol to initiate the reaction. The catalytic activity was

evaluated by TOF values, which were calculated by extracting certain amount of reaction mixture at different time points for NMR quantification. Significantly, with a 0.05 mol% metal loading, Pd NPs achieved a high TOF value of 6382 ± 258 mol product (mol Pd × h)$^{-1}$ (see Figure A3.8 in Appendix 3 for TOF determination). No product was produced in the absence of Pd NPs, confirming the catalytic activity of the material. Note that during the reaction, a small amount of the isomerization product propionaldehyde was also observed in NMR. Nevertheless, it was fully converted to the n-propanol afterwards, therefore the TOF value also contains the propionaldehyde contribution for easy comparison with previous studies. Pt and Au NPs were also tested for the allyl alcohol hydrogenation. Interestingly, while Pt NPs gave small TOF (740 mol product (mol Pt × h)$^{-1}$), Au NPs could not catalyze the reaction. This can be attributed to their lower capacity to dissociate molecular dihydrogen on the metal surface, as well as the weaker interaction with C=C bond in the allyl alcohol, which resulted in a rather high reaction barrier to activate C=C bond and thus lower reaction rate.[67–69]

According to the TOF value for allyl alcohol hydrogenation, the catalytic activity of TMVCPA-templated Pd NPs exceed any reported Pd nanocatalysts with similar size, shape and hydrogenation conditions (see Table A3.1 in Appendix 3). For example, a variety of Pd NPs embedded in polyelectrolyte (PEI) films,[70,71] supported on solid composites[71] and stabilized by organic ligands[40,72] have been employed for allyl alcohol hydrogenation. One early study of 1.7 nm Pd NPs encapsulated into poly(amidoamine) dendrimers reported a TOF of 480 mol H_2 (mol Pd × h)$^{-1}$,[73] whereas thiolate ligands such as S-alkythiosulfates can be relatively densely packed on the NP surface and lead to diminished activity (310 mol product (mol Pd × h)$^{-1}$.[40] Pd NPs capped by bio-templates such as peptides have also been studied for this reaction and generally showed higher TOFs. For instance, Knect's group has successfully developed a series of peptides[74] and peptoids[75] to support Pd NP growth. Specifically, spherical Pd NPs were capped by Pd4 peptide and a series of analogues, with one optimized analogue achieving the highest TOF 6100 ± 200 mol product (mol Pd × h)$^{-1}$.[74] They also employed a R5 peptide to produce Pd nanostructures with different morphologies, the TOF values were all around 3000 mol product (mol Pd × h)$^{-1}$.[76]

To explore the scope of the protein-Pd NP system for hydrogenation reactions, unsaturated alcohols with different shapes and sizes were tested under the same reaction conditions, as shown in entries 2-7 in Table 5.3. The TOFs varied depending on the molecule size and substituents. As

Table 5.3: TOFs for hydrogenation of various olefins.

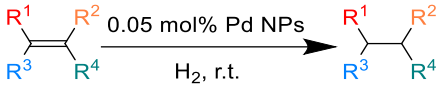

Entry	Substrate	Product	TOF[a]
1			6382 ± 258
2			4529 ± 1230
3			4797 ± 251
4			1185 ± 149
5	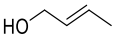	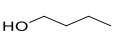	1147 ± 122
6	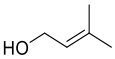	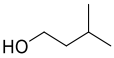	110 ± 11
7			2630 ± 30
8			3909 ± 153
9	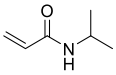	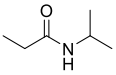	4448 ± 845

[a]mol product (mol Pd × h)$^{-1}$. Values are the sum of TOFs for hydrogenation and isomerization.

expected, the substitution pattern of the carbon-carbon double bond has more impact on TOF than that of the α-carbon of the double bond. For example, for entries 2-3 with C=C monosubstitution, adding more alky groups on the α-carbon of the C=C resulted in slightly lower TOF values. However, when it becomes a disubstitution on C=C (entries 4-5), TOFs were lowered to ca. 1000 mol product (mol Pd × h)$^{-1}$. In particular, when it is a tri-substitution (entry 6), the TOF was significantly reduced to only 110 ± 11 mol product (mol Pd × h)$^{-1}$. Compared to allyl alcohol, these decreases in TOFs can be attributed to the larger steric hindrance that lower the reaction rate of Pd-H coordinating with C=C bond. It can also be caused by the lower solubility and diffusion rate of longer and more branched alky chains in water. Besides olefinic alcohols, Pd NPs also showed

good activity for catalyzing unsaturated carboxylic acid and amides when it is a C=C mono-substitution, as demonstrated in entries 7-9.

5.3.4 Insights from MD Simulations into the Enhanced Catalytic Activity with TMVCPA-Pd NPs

Based on the results discussed above, we have shown that the TMVCPA enables formation of green MNPs that are highly active towards 4-NP reduction and olefinic alcohol hydrogenation. The enhanced performance is likely related to the protein ligand effect. To get a clearer picture of the protein structure-function relationship, we used TMVCPA-Pd NP for further theoretical analysis. It has been demonstrated by Knecht's group that the reaction rate of allyl alcohol hydrogenation is proportional to the available surface area on the Pd NP surface.[74] Building on this insight we hypothesized that proteins surrounding the Pd NP do not significantly restrict access of solvent and small solutes to the surface. We tested this idea using an atomistic molecular dynamics simulation as computational microscope. For technical details please see the Experimental Section.

Our initial simulations of the Pd NP surrounded by six protein subunits in water lead to two important observations: 1) The TMVCPAs form stable complexes with the Pd NP through direct interaction with only a handful of residues; whereas the rest of the protein remain unchanged, which is likely the reason for the little conformation change after binding as shown in the previous CD results. The small 'footprint' of the contact is demonstrated in Figure 5.5a with the protein residues within 0.6 nm of the NP highlighted in blue. 2) The proteins maintain rather rigid and bulky conformations during the simulation and as a consequence, steric conflicts make dense packing impossible. Figure 5.5b provides the evidence of conformational stability for a representative protein by tracking its radius of gyration throughout the simulation.

These preliminary observations set the stage for addressing the main question we posed to our simulation: To what extent do solute molecules have access to the surface of the nanoparticles? In order to answer this question, we added propanol to our simulation box and quantified its accumulation at the surface of the nanoparticles. Since we were not interested in concentration dependent effects, we used solute concentration a bit higher than the experimental (0.0615 mmol/mL) and kept track of the solute within 0.6 nm from the surface of the NP. Figure 5.5c

shows an illustration of the NP surface covered with propanol molecules everywhere except the areas occupied by the protein. The number of propanols at the surface as a function of time is depicted in Figure 5.5d. Starting from the initial condition with propanols randomly distributed throughout the simulation box, the number of propanols at the surface grows steadily until it settles

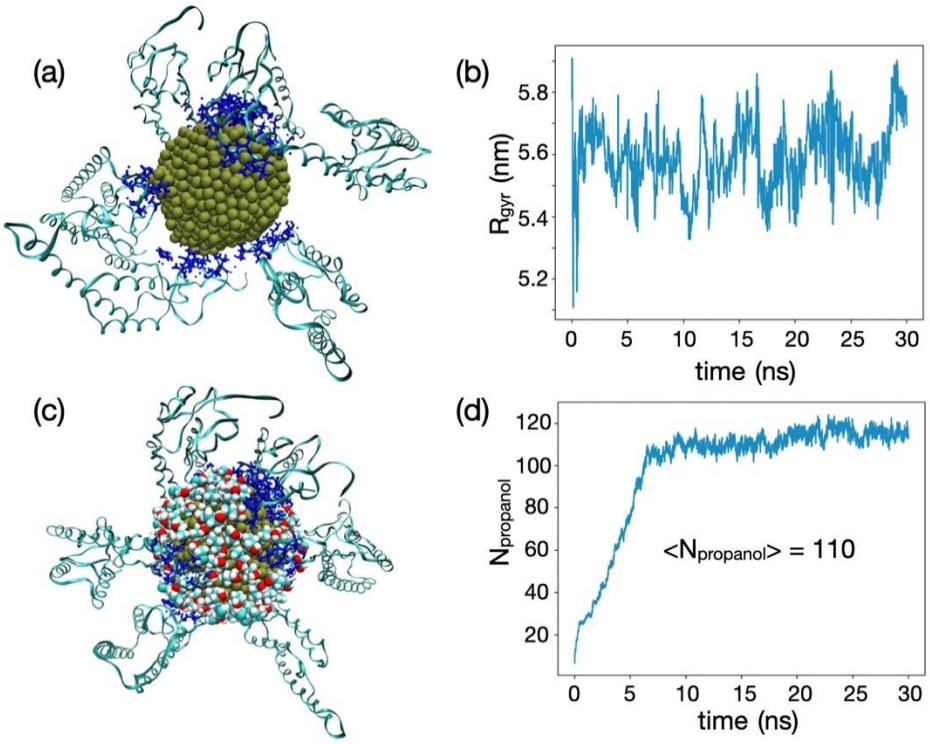

Figure 5.5: Computational modelling of the 6-TMVCPA-Pd NP system. (a) A snapshot from the simulation trajectory demonstrating that only a handful of residues in each TMVCPA form direct contacts with the surface of the NP. The residues in contact are shown in blue, the water and propanol are hidden; cut-off distance of 0.6 nm was used to define a contact; (b) The radius of gyration of one single TMVCPA in the simulation is shown to be stable throughout the simulation fluctuating mildly about 5.6 nm; other proteins behaved similarly; (c) An illustration of the adsorption of the propanol solute onto the surface of the NP. The blue TMVCPA residues clearly displace any solute from the surface locally, but the area that is accessible to the solute remains large; (d) The number of propanol molecules adsorbed onto the NP surface throughout the simulation. The average number over the plateau region is $N_{propanol} = 110$.

into a stable plateau fluctuating between 100 and 120 molecules on the Pd NP with an average of 110 propanols on the surface (averaged over the stable plateau region). This number is in a quantitative agreement with the theoretically expected 107 ± 4 propanols at the surface of the Pd NP. The theoretical value was obtained by rearranging the Eq. 5.3:[74]

$$\mathrm{TOF} = \mathrm{C} \times \frac{\mathrm{N_{solute}}}{\mathrm{N_{NP}}} \quad (5.3)$$

where the C is the dimensionless constant (chose as C = 90000),[74] N_{NP} is the number of Pd atoms in one particle , and TOF is taken from the experimental value for allyl alcohol hydrogenation (6382 ± 258 mol product (mol Pd × h)$^{-1}$). Overall, the simulation results suggested that there are only a few protein residues having direct contact with the Pd NP, and the bulk protein subunits have minimal surface passivation which allows efficient access for small reactant molecules. Since A-protein is often a mixture of monomers and oligomers, it is also possible that the bulkier oligomers would bring more steric hindrance to make the NP surface even less passivated.

5.4 Conclusions

TMVCPA was successfully employed as a biological scaffold for the fabrication of green catalysts under environmentally benign conditions. The as prepared bio-nanocomposites demonstrated exceptional performance towards heterogeneous catalysis for 4-nitrophenol reduction and olefinic alcohol hydrogenation. To interpretate the improved catalytic activity, experiments and computational modelling with TMVCPA-Pd NP were combined to reveal the structure/function relationship. We demonstrate that due to the moderate interaction of the protein-metal and the bulkiness of protein ligands, the Pd nanoparticle surface is minimally passivated while maintaining good colloid stability. The nanoparticle exposes a sufficient number of catalytically active sites for adsorption of small reactant molecules to initiate subsequent transformation to products. The results are important as this strategy combines eco-friendly synthesis with unique biomolecule binding properties to enlarge nanometal's available surface area for approach of reactant molecules. We anticipate that this work will bring new opportunities for the rational design and applications of bioinspired in heterogeneous catalysis and other related fields.

5.5 References

[1] C. Gao, F. Lyu and Y. Yin, *Chem. Rev.*, 2021, **121**, 834–881.

[2] D. Wang and D. Astruc, *Chem. Soc. Rev.*, 2017, **46**, 816–854.

[3] X. Jin, R. Tsukimura, T. Aihara, H. Miura, T. Shishido and K. Nozaki, *Nat. Catal.*, 2021, **4**, 312–321.

[4] C. C. Lima, M. V. F. Rodrigues, A. F. M. Neto, C. R. Zanata, C. T. G. V. M. T. Pires, L. S. Costa, J. Solla-Gullón and P. S. Fernández, *Appl. Catal. B Environ.*, 2020, **279**, 119369.

[5] S. Deng, B. Zhang, P. Choo, P. J. M. Smeets and T. W. Odom, *Nano Lett.*, 2021, **21**, 1523–1529.

[6] C. Gong, S. Sun, Y. Zhang, L. Sun, Z. Su, A. Wu and G. Wei, *Nanoscale*, 2019, **11**, 4147–4182.

[7] K. T. Nam, D.-W. Kim, P. J. Yoo, C.-Y. Chiang, N. Meethong, P. T. Hammond, Y.-M. Chiang and A. M. Belcher, *Science*, 2006, **312**, 885–888.

[8] Y. Guo, Y. Sun, D.-P. Yang, J. Dai, Z. Liu, Y. Chen, J. Huang and Q. Li, *ACS Appl. Mater. Interfaces*, 2020, **12**, 2469–2480.

[9] H. Tabe, H. Takahashi, T. Shimoi, S. Abe, T. Ueno and Y. Yamada, *Appl. Catal. B Environ.*, 2018, **237**, 1124–1129.

[10] M. Li, L. Zong, W. Yang, X. Li, J. You, X. Wu, Z. Li and C. Li, *Adv. Funct. Mater.*, 2019, **29**, 1901798.

[11] Z. Wang, J. Xu, P. Wang, Y. Zhang, J. You and C. Li, *ACS Nano*, 2020, **14**, 828–834.

[12] S. Zhang, X. Zhang and Z. Su, *J. Mater. Chem. B*, 2020, **8**, 4176–4194.

[13] Y. Gao, Y. Liu, R. Yan, J. Zhou, H. Dong, X. Hua and P. Wang, *Anal. Chem.*, 2020, **92**, 13595–13603.

[14] G. Yang, Y. Liu, H. Wang, R. Wilson, Y. Hui, L. Yu, D. Wibowo, C. Zhang, A. K. Whittaker, A. P. J. Middelberg and C.-X. Zhao, *Angew. Chem. Int. Ed.*, 2019, **58**, 14357–

14364.

[15] J. Huang, L. Lin, D. Sun, H. Chen, D. Yang and Q. Li, *Chem. Soc. Rev.*, 2015, **44**, 6330–6374.

[16] H. Inaba, M. Yamada, M. R. Rashid, A. M. R. Kabir, A. Kakugo, K. Sada and K. Matsuura, *Nano Lett.*, 2020, **20**, 5251–5258.

[17] R. L. Lawrence, B. Scola, Y. Li, C.-K. Lim, Y. Liu, P. N. Prasad, M. T. Swihart and M. R. Knecht, *ACS Nano*, 2016, **10**, 9470–9477.

[18] M. A. Nguyen, Z. E. Hughes, Y. Liu, Y. Li, M. T. Swihart, M. R. Knecht and T. R. Walsh, *J. Phys. Chem. C*, 2018, **122**, 11532–11542.

[19] Q. Ding, Z. Kang, X. He, M. Wang, M. Lin, H. Lin and D.-P. Yang, *Microchim. Acta*, 2019, **186**, 453.

[20] S. Manuguri, K. Webster, N. A. Yewdall, Y. An, H. Venugopal, V. Bhugra, A. Turner, L. J. Domigan, J. A. Gerrard and D. E. Williams, *Nano Lett.*, 2018, **18**, 5138–5145.

[21] H. Bagheri, A. Afkhami, H. Khoshsafar, A. Hajian and A. Shahriyari, *Biosens. Bioelectron.*, 2017, **89**, 829–836.

[22] S. Huo, N. Gong, Y. Jiang, F. Chen, H. Guo, Y. Gan, Z. Wang, A. Herrmann and X.-J. Liang, *Sci. Adv.*, 2019, **5**, eaaw6264.

[23] X. Luo, C. Lachance-Brais, A. Bantle and H. F. Sleiman, *Chem. Sci.*, 2020, **11**, 4911–4921.

[24] C. E. Benjamin, Z. Chen, P. Kang, B. A. Wilson, N. Li, S. O. Nielsen, Z. Qin and J. J. Gassensmith, *J. Am. Chem. Soc.*, 2018, **140**, 17226–17233.

[25] R. R. Nasaruddin, T. Chen, Q. Yao, S. Zang and J. Xie, *Coord. Chem. Rev.*, 2021, **426**, 213540.

[26] Y. Choi, T. J. Park, D. C. Lee and S. Y. Lee, *Proc. Natl. Acad. Sci. U. S. A.*, 2018, **115**, 5944–5949.

[27] D. Oh, J. Qi, B. Han, G. Zhang, T. J. Carney, J. Ohmura, Y. Zhang, Y. Shao-Horn and A. M. Belcher, *Nano Lett.*, 2014, **14**, 4837–4845.

[28] E. H. Koh, C. Mun, C. Kim, S.-G. Park, E. J. Choi, S. H. Kim, J. Dang, J. Choo, J.-W. Oh and D.-H. Kim, *ACS Appl. Mater. Interfaces*, 2018, **10**, 10388–10397.

[29] S. Kilper, T. Jahnke, M. Aulich, Z. Burghard, D. Rothenstein and J. Bill, *Adv. Mater.*, 2019, **31**, 1805597.

[30] W. C. Records, Y. Yoon, J. F. Ohmura, N. Chanut and A. M. Belcher, *Nano Energy*, 2019, **58**, 167–174.

[31] H. Hu, Y. Zhang, S. Shukla, Y. Gu, X. Yu and N. F. Steinmetz, *ACS Nano*, 2017, **11**, 9249–9258.

[32] H. Wu, D. Zhong, Z. Zhang, Y. Li, X. Zhang, Y. Li, Z. Zhang, X. Xu, J. Yang and Z. Gu, *Adv. Mater.*, 2020, **32**, 1904958.

[33] A. Klug, *Philos. Trans. R. Soc. London. Ser. B Biol. Sci.*, 1999, **354**, 531–535.

[34] E. Dujardin, C. Peet, G. Stubbs, J. N. Culver and S. Mann, *Nano Lett.*, 2003, **3**, 413–417.

[35] A. J. Love, V. Makarov, I. Yaminsky, N. O. Kalinina and M. E. Taliansky, *Virology*, 2014, **449**, 133–139.

[36] J. Zhang, K. Zhou, Y. Zhang, M. Du and Q. Wang, *Adv. Mater.*, 2019, **31**, 1901485.

[37] O. K. Zahr and A. S. Blum, *Nano Lett.*, 2012, **12**, 629–633.

[38] E. Sadeghmoghaddam, H. Gu and Y.-S. Shon, *ACS Catal.*, 2012, **2**, 1838–1845.

[39] K. Zhang, J. M. Suh, J.-W. Choi, H. W. Jang, M. Shokouhimehr and R. S. Varma, *ACS Omega*, 2019, **4**, 483–495.

[40] D. J. Gavia and Y.-S. Shon, *Langmuir*, 2012, **28**, 14502–14508.

[41] Y. Feng, H. Wang, J. Zhang, Y. Song, M. Meng, J. Mi, H. Yin and L. Liu, *Biomacromolecules*, 2018, **19**, 2432–2442.

[42] B. D. Briggs, Y. Li, M. T. Swihart and M. R. Knecht, *ACS Appl. Mater. Interfaces*, 2015, **7**, 8843–8851.

[43] W. L. Jorgensen, D. S. Maxwell and J. Tirado-Rives, *J. Am. Chem. Soc.*, 1996, **118**, 11225–

11236.

[44] M. J. Robertson, J. Tirado-Rives and W. L. Jorgensen, *J. Chem. Theory Comput.*, 2015, **11**, 3499–3509.

[45] H. Heinz, R. A. Vaia, B. L. Farmer and R. R. Naik, *J. Phys. Chem. C*, 2008, **112**, 17281–17290.

[46] N. Michaud-Agrawal, E. J. Denning, T. B. Woolf and O. Beckstein, *J. Comput. Chem.*, 2011, **32**, 2319–2327.

[47] K. N. Avery, J. E. Schaak, R. E. Schaak, T. Pennsyl, V. State, V. Uni, U. V Park and V. Pennsyl, *Chem.Mater.*, 2009, **14**, 2176–2178.

[48] A. Zinchenko, Y. Miwa, L. I. Lopatina, V. G. Sergeyev and S. Murata, *ACS Appl. Mater. Interfaces*, 2014, **6**, 3226–3232.

[49] W. Zhou, X. Gao, D. Liu and X. Chen, *Chem. Rev.*, 2015, **115**, 10575–10636.

[50] A. M. Arutyunyan, E. R. Rafikova, V. A. Drachev and E. N. Dobrov, *Biochem.*, 2001, **66**, 1378–1380.

[51] V. N. Orlov, A. M. Arutyunyan, S. V Kust, E. A. Litmanovich, V. A. Drachev and E. N. Dobrov, *Biochem.*, 2001, **66**, 154–162.

[52] R. D. Neal, Y. Inoue, R. A. Hughes and S. Neretina, *J. Phys. Chem. C*, 2019, **123**, 12894–12901.

[53] E.-M. Felix, M. Antoni, I. Pause, S. Schaefer, U. Kunz, N. Weidler, F. Muench and W. Ensinger, *Green Chem.*, 2016, **18**, 558–564.

[54] M. M. Nigra, J.-M. Ha and A. Katz, *Catal. Sci. Technol.*, 2013, **3**, 2976–2983.

[55] R. Ciganda, N. Li, C. Deraedt, S. Gatard, P. Zhao, L. Salmon, R. Hernández, J. Ruiz and D. Astruc, *Chem. Commun.*, 2014, **50**, 10126–10129.

[56] T. B. Nguyen, C. P. Huang and R. an Doong, *Appl. Catal. B Environ.*, 2019, **240**, 337–347.

[57] C. Wang, R. Ciganda, L. Salmon, D. Gregurec, J. Irigoyen, S. Moya, J. Ruiz and D. Astruc,

Angew. Chem. Int. Ed., 2016, **55**, 3091–3095.

[58] R. Li, Y. Yue, Z. Chen, X. Chen, S. Wang, Z. Jiang, B. Wang, Q. Xu, D. Han and J. Zhao, *Appl. Catal. B Environ.*, 2020, **279**, 119348.

[59] B. Sun, L. Ning and H. C. Zeng, *J. Am. Chem. Soc.*, 2020, **142**, 13823–13832.

[60] K. Kim, Y. Jung, S. Lee, M. Kim, D. Shin, H. Byun, S. J. Cho, H. Song and H. Kim, *Angew. Chem. Int. Ed.*, 2017, **56**, 6952–6956.

[61] C. B. Reddy, R. Bharti, S. Kumar and P. Das, *ACS Sustain. Chem. Eng.*, 2017, **5**, 9683–9691.

[62] M. Guo, J. He, Y. Li, S. Ma and X. Sun, *J. Hazard. Mater.*, 2016, **310**, 89–97.

[63] J. Li, C. Liu and Y. Liu, *J. Mater. Chem.*, 2012, **22**, 8426–8430.

[64] R. Bhandari and M. R. Knecht, *Catal. Sci. Technol.*, 2012, **2**, 1360–1366.

[65] Y. Li, Z. Tang, P. N. Prasad, M. R. Knecht and M. T. Swihart, *Nanoscale*, 2014, **6**, 3165–3172.

[66] Y. Li, X. Geng, W. Leng, P. J. Vikesland and T. Z. Grove, *New J. Chem.*, 2017, **41**, 9406–9413.

[67] J. Zhao, L. Ge, H. Yuan, Y. Liu, Y. Gui, B. Zhang, L. Zhou and S. Fang, *Nanoscale*, 2019, **11**, 11429–11436.

[68] R. Ouyang and D. Jiang, *ACS Catal.*, 2015, **5**, 6624–6629.

[69] G. Budroni and A. Corma, *J. Catal.*, 2008, **257**, 403–408.

[70] S. Kidambi and M. L. Bruening, *Chem. Mater.*, 2005, **17**, 301–307.

[71] S. Bhattacharjee and M. L. Bruening, *Langmuir*, 2008, **24**, 2916–2920.

[72] T. R. Sibakoti, J. B. Jasinski, M. H. Nantz and F. P. Zamborini, *Nanoscale*, 2020, **12**, 12027–12037.

[73] Y. Niu, L. K. Yeung and R. M. Crooks, *J. Am. Chem. Soc.*, 2001, **123**, 6840–6846.

[74] N. M. Bedford, H. Ramezani-Dakhel, J. M. Slocik, B. D. Briggs, Y. Ren, A. I. Frenkel, V. Petkov, H. Heinz, R. R. Naik and M. R. Knecht, *ACS Nano*, 2015, **9**, 5082–5092.

[75] N. A. Merrill, F. Yan, H. Jin, P. Mu, C.-L. Chen and M. R. Knecht, *Nanoscale*, 2018, **10**, 12445–12452.

[76] R. Bhandari, D. B. Pacardo, N. M. Bedford, R. R. Naik and M. R. Knecht, *J. Phys. Chem. C*, 2013, **117**, 18053–18062.

Chapter 6

Tobacco Mosaic Virus Coat Protein-Templated PdAu Nanoalloys for Electrocatalytic Applications

Chapter Preface

Scientific Contributions:

As an extension of the work in previous chapters, Chapter 6 investigated the formation of alloy nanoparticles on TMVCPA template via simple co-reduction of metal precursors. Gold-palladium (PdAu) alloys were deposited on the TMVCPA, as confirmed by a series of characterization techniques. This chapter shows the first example of successful fabrication of bimetallic PdAu nanocatalysts on protein under ambient conditions. The objective of this work is to apply the as prepared PdAu alloys in electrocatalysis and identify the best metal-to-metal ratio for largest increase in catalytic activity and longevity, as compared to the monometallic counterparts. At the time of writing this thesis, the evaluation of catalytic performance has not been carried out yet. This chapter thus mainly presents the results of material synthesis and characterizations.

Chapter Abstract

A variety of monometallic nanomaterials are highly active catalysts for numerous catalytic reactions. In pursuit of further enhancing catalytic efficiencies, multicomponent nanomaterials have been designed and explored for their unique properties. In this regard, biomolecules have attracted research interest for their great potential as versatile templates to effectively deposit nanostructures with uniform size, tunable morphology and interesting optical properties. Nevertheless, literature reports of protein templated bimetallic nanometals for electrocatalysis remain limited. In Chapter 6, we report the fabrication of bimetallic PdAu nanostructures on TMVCPA template, with different Au-to-Pd ratios. To confirm the formation of alloy structures, a series of microscopic and spectroscopic techniques were used to characterize the as prepared materials. Possible electrocatalytic applications of these alloys were then discussed. Chapter 3, 4 and 5 used single component metal catalysts on the protein template. Chapter 6 expands the scope to protein-bimetal systems for electrocatalytic reactions.

6.1 Introduction

Nanosized metallic materials are widely used as catalysts in various electrocatalytic reactions, thanks to their high surface area-to-volume ratios and unique electronic properties at the nanoscale.[1–5] The electrocatalytic activity of nanocatalysts are strongly affected by the nanoparticle composition, size, morphology, surface facet and ligands.[6] Tremendous efforts have been devoted to optimizing these parameters aiming to improve the electrode performance, and they can be either through modulating the size, shape and surface facets of pure MNPs or constructing multicomponent materials, bimetallic catalysts in particular.[7–11] Bimetallic materials generally demonstrate some distinct advantages over their single component counterpart: 1) it can reduce the loading amount of the metal of higher cost and thus increases the utilization efficiency; 2) while being mixed together, the surface electronic property of the metal can be modulated due to charge transfer;[12,13] 3) different metals exhibit synergistic effect that can alter the adsorption of specific species involved in the reaction and thus contribute to enhanced catalytic performance.[14,15] For instance, Pt is the most widely used metal in electrocatalysis; however, its limited resource and high cost drives the need to alloy it with a second metal to reduce the overall material cost.[16,17]

As an excellent alternative to Pt, Pd also plays important roles in electrocatalytic reactions such as ORR, OER and FAOR in fuel cells.[18–22] To further improve its activity, an effective strategy is to construct Pd-based bimetallic platforms (alloy, core-shell).[12,23] For example, Yin et al. synthesized a series of oleic acid and oleylamine stabilized bimetallic PdAu NPs, which feature a Pd-enriched shell and Au-enriched core structure.[24] Catalysts with different component ratios were tested for MOR and the most active $Pd_{30}Au_{70}$ exhibited almost 5-fold increase in peak current density as compared to Pd/C. The origin of the improved activity was explained by the twinned structure that possesses strain effect and more defects.[24] It could also be due to the synergistic effect from Au, which promotes CO oxidation and thus the overall MOR performance.[24] Besides MOR, PdAu NPs with controlled compositions have also shown impressive performance in other renewable energy conversion related reactions such as CO_2 RR,[25–27] ORR,[28,29] HER,[30,31] and FAOR.[32,33]

Yet despite the research progress in the development of bimetallic PdAu NPs, the synthetic methods of the catalysts mentioned above generally involve the use of non-natural capping agents

and solvents, elevated temperature and complicated synthetic steps. Controllable production of PdAu NPs with concise fabrication process, uniform sizes, mild synthetic conditions and excellent catalytic performance are highly desired. In this regard, biomolecule-directed synthetic methods for bimetallic NPs are emerging as promising alternatives to the traditional chemistry-based bottom-up routes, although examples are still limited to date, as reviewed in Chapter 1. Among the different bio-templates, only limited examples have employed peptides for the fabrication of nanosized PdAu electrocatalysts,[34–36] leveraging the known knowledge that some specific peptide sequences have affinity to Pd and Au surfaces, respectively. For example, Bedford's group fabricated a series of PdAu NPs with Pd- and Au-binding peptides, as well a hybrid peptide that contains anchoring sites for both metals.[34] The NPs were studied for MOR and results demonstrated the critical role of peptide sequences on the material's catalytic performance. In another report by Zong et al., Au@Pd core-shell structures with different metal ratios were constructed on a FlgA3 peptide, which contains an A3 domain for Au binding and a Flg domain for Pd binding.[35] It was found that among the series, $Au@Pd_{1.0}$ exhibited superior ORR activity and durability compared to Pt/C and Pd/C. The bimetallic NPs are also effective catalysts towards HER. The enhanced performance can be attributed to the lattice strain effect induced by the core-shell structure, which alters the d-band center and affect the molecule-sorption strength.[35]

Compared to peptides, proteins have more complicated organization patterns and may bring new material properties to enlarge the bio-templates library for bimetallic electrocatalyst systems. Given that both Pd NPs and Au NPs can be anchored on the TMVCPA as seen in Chapter 5, we further explore the potential of the protein to construct PdAu NPs under similar fabrication conditions. In Chapter 6, successful preparation of TMVCPA-templated PdAu alloy NPs with homogenous mixing at nanoscale was achieved. The alloys were then characterized by UV-vis, TEM, HR-TEM, SAED and STEM-EDS mapping. The as prepared catalysts will be tested for electrocatalysis, and if successful, this would be the first example of protein-templated PdAu alloy as efficient electrocatalyst.

6.2 Experimental Section

6.2.1 Chemicals

$NaAuCl_4 \bullet 2H_2O$, Na_2PdCl_4, and $NaBH_4$ were purchased from Sigma-Aldrich. Tris Base and hydrochloric acid were supplied by Fisher Scientific. All materials were used as received without further purification. Millipore MilliQ water (18.2 MΩ·cm) was used for all aqueous experiments.

6.2.2 Synthesis of TMVCPA-Templated AuPd Bimetallic Nanomaterials

TMVCP was dialyzed into pH 8.9 (Tris-HCl buffer, 15 mM) over 24 h, using dialysis membrane tubing (12 k-14 k MWCO, Spectra/Pro). The protein concentration was determined by the absorbance at 282 nm (1.27 mL $(mg\ cm)^{-1}$) using UV-vis spectroscopy. To fabricate the bimetallic nanoparticles, Pd:Au ratio was 0:100, 30:70, 50:50, 70:30, or 100:0. Specifically, to 400 µL of protein solution (0.24 mg/mL) was added 40 µL, 28 µL, 20 µL, 12 µL or 0 µL of $NaAuCl_4 \cdot 2H_2O$ (25 mM) under gentle stirring. Next, 0 µL, 12 µL, 20 µL, 28 µL, or 40 µL of Na_2PdCl_4 solution was added to the above solution. Stirring was continued for 3 h. Afterward, 20 µL of freshly prepared $NaBH_4$ solution (0.15 M) was added to the reaction mixture and the mixture turned into dark brown immediately. The mixture was stirred for 1 h and then left undisturbed for another 1 h before purification and subsequent characterization. All experiment throughout this chapter were carried out at room temperature.

6.2.3 Material Characterizations

UV-vis measurements were carried out using Evolution 260 Bio UV-vis spectrometer. TEM, HR-TEM, SAED, and STEM images were obtained from Talos 200 TEM coupled with HAADF-STEM imaging and EDS system, operating at an accelerating voltage of 200 kV. Samples for TEM, HR-TEM and SAED were prepared onto carbon coated copper grids, while specimens for STEM-EDS characterizations were prepared onto silicon oxide coated copper grids to reduce the carbon contamination. 10 µL of suspension was drop cast onto TEM grids and allowed to sit for 5 min before blotting with a filter paper. The average sizes of NPs were obtained by random selection of at least 300 particles on the TEM images using software ImageJ. XPS spectra were acquired on a Thermo Scientific K-Alpha XPS system, with Al Kα as the monochromatic source.

6.3 Results and Discussion

The TMVCPA was first incubated with palladium and gold metal precursors with different metal loading ratios, in which the amino acid residues on the protein can bind with the precursors through electrostatic interactions.[37,38] The zerovalent NPs were then obtained by reduction of $NaBH_4$. Figure 6.1 presents the UV-vis spectra of the PdAu NPs with different Pd-to-Au ratios, i.e., $Pd_{30}Au_{70}$, $Pd_{50}Au_{50}$ and $Pd_{70}Au_{30}$. Interestingly, the characteristic plasmonic peak of Au NPs at around 540 nm (Figure 5.1c) was not found in all the three materials, which strongly indicates that the NPs are composed of alloys instead of phase-separate Au and Pd NPs. This phenomenon was consistent with previous reports on bimetallic PdAu NP systems.[35,39]

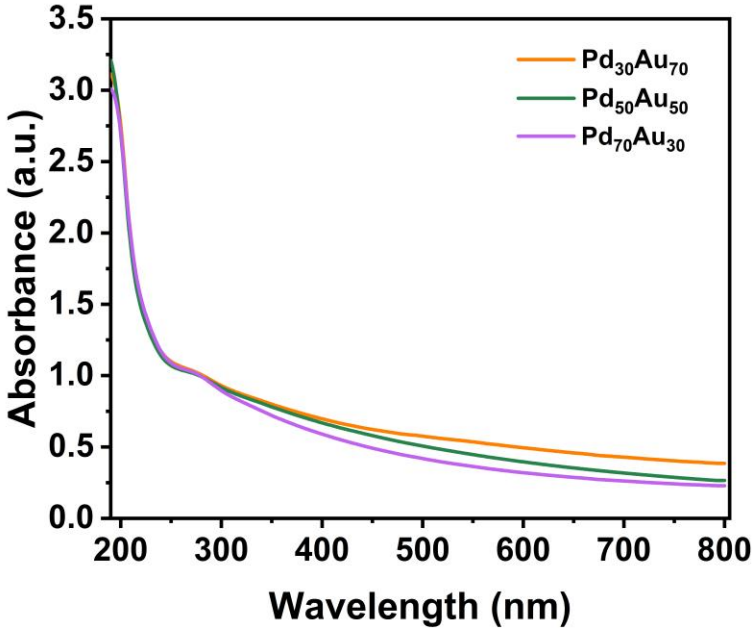

Figure 6.1: UV-vis spectra of PdAu NPs with different stoichiometric ratios.

EDS was then used to quantify the actual Pd-to-Au ratio in the NPs (Figure A4.1 in Appendix 4), and the results are $Pd_{33}Au_{67}$, $Pd_{52}Au_{48}$, and $Pd_{72}Au_{28}$, respectively, which are close to the corresponding stoichiometric ratios of the precursors. TEM was used to analyze the size and shape of the protein-templated NPs. As shown in Figure 6.2a-c, near spherical particles were observed with all the three materials, confirming the formation of MNPs. The sizes of $Pd_{33}Au_{67}$, $Pd_{52}Au_{48}$

and $Pd_{72}Au_{28}$ NPs are close to each other, and the diameters are 3.50 ± 0.85 nm, 3.47 ± 0.79 nm, and 3.15 ± 0.64 nm, respectively, indicating some degree of polydispersity. HR-TEM and SAED were then used to further examine the crystalline property of the NPs, as displayed in Figure 6.2d and 6.2e for the representative $Pd_{52}Au_{48}$ sample. HR-TEM shows well-defined lattice fringes, with a d-spacing of 0.233 nm, indicating a (111) dominant facet. Notably, this value is between the value of Pd (111) (0.224 nm, JCPDS-46-1043) and Au (111) (0.235 nm, JCPDS-04-0784), which further suggests the PdAu alloy formation.[36,40] The alloy formation was also supported by SAED result in Figure 6.2e, which shows four bright and clear diffraction patterns close to the center of the image and reveals polycrystalline nature of the material. The patterns correspond to the [111], [200], [220] and [311] planes, respectively. The four distinct rings clearly suggest that the Pd and Au are well alloyed instead of separately metallized, since separate phases of the two metals will produce eight separate ring patterns. In addition, the lattice parameters are in between of those of Pd and Au. For example, the [200] plane is 0.200 nm, it is between that of Pd (200) (0.195 nm, JCPDS-46-1043) and Au (200) (0.203 nm, JCPDS-04-0784).

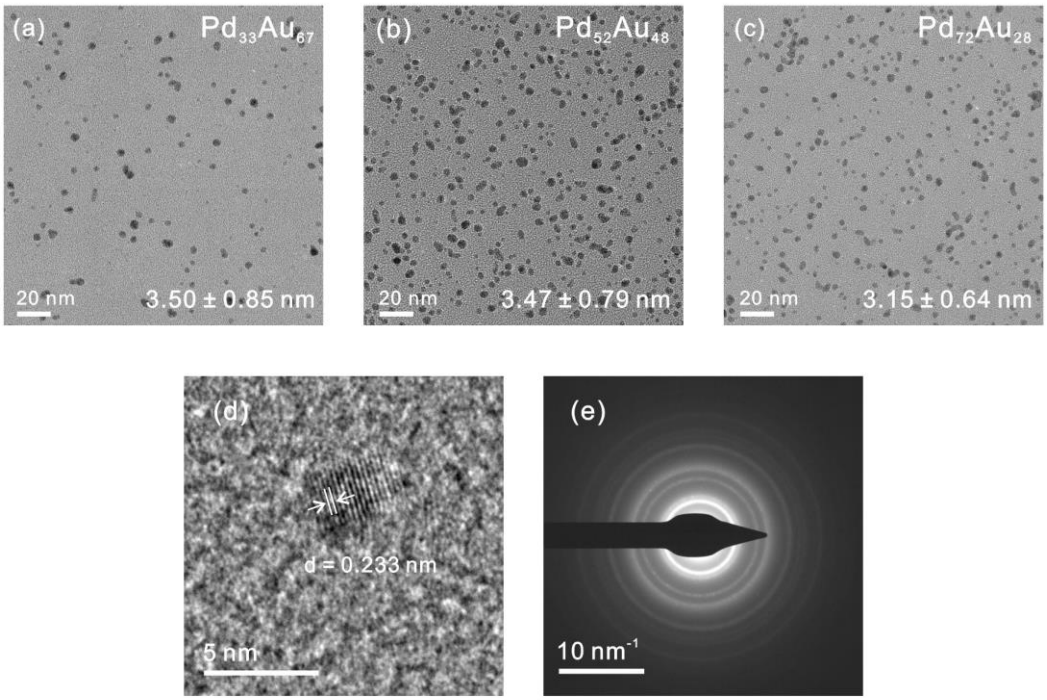

Figure 6.2: TEM images of $Pd_{33}Au_{67}$ (a), $Pd_{52}Au_{48}$ (b) and $Pd_{72}Au_{28}$ (c); HR-TEM image (d) and SAED image (e) of $Pd_{52}Au_{48}$.

To visualize the elemental distribution on the NP, HAADF-STEM-EDS mapping was employed on both Au and Pd. The HAADF-STEM image of a representative $Pd_{52}Au_{48}$ sample is displayed in Figure 6.3a. Elemental mapping of the metals clearly matches the contributions from green Pd (Figure 6.3b) and red Au (Figure 6.3c) plots. Moreover, the overlay mapping of Pd and Au reveals an even overall distribution and thus confirms the well intermixing of the two metals, as displayed in Figure 6.3d. EDS-STEM line-scan (Figure 6.3e) was also performed on a single particle as marked by the while line in Figure 6.3d. The line profile clearly illustrates that the single particle is composed of both Pd and Au, and the two metals are alloyed homogeneously at atomic scale, since they show similar intensities across the line positions.

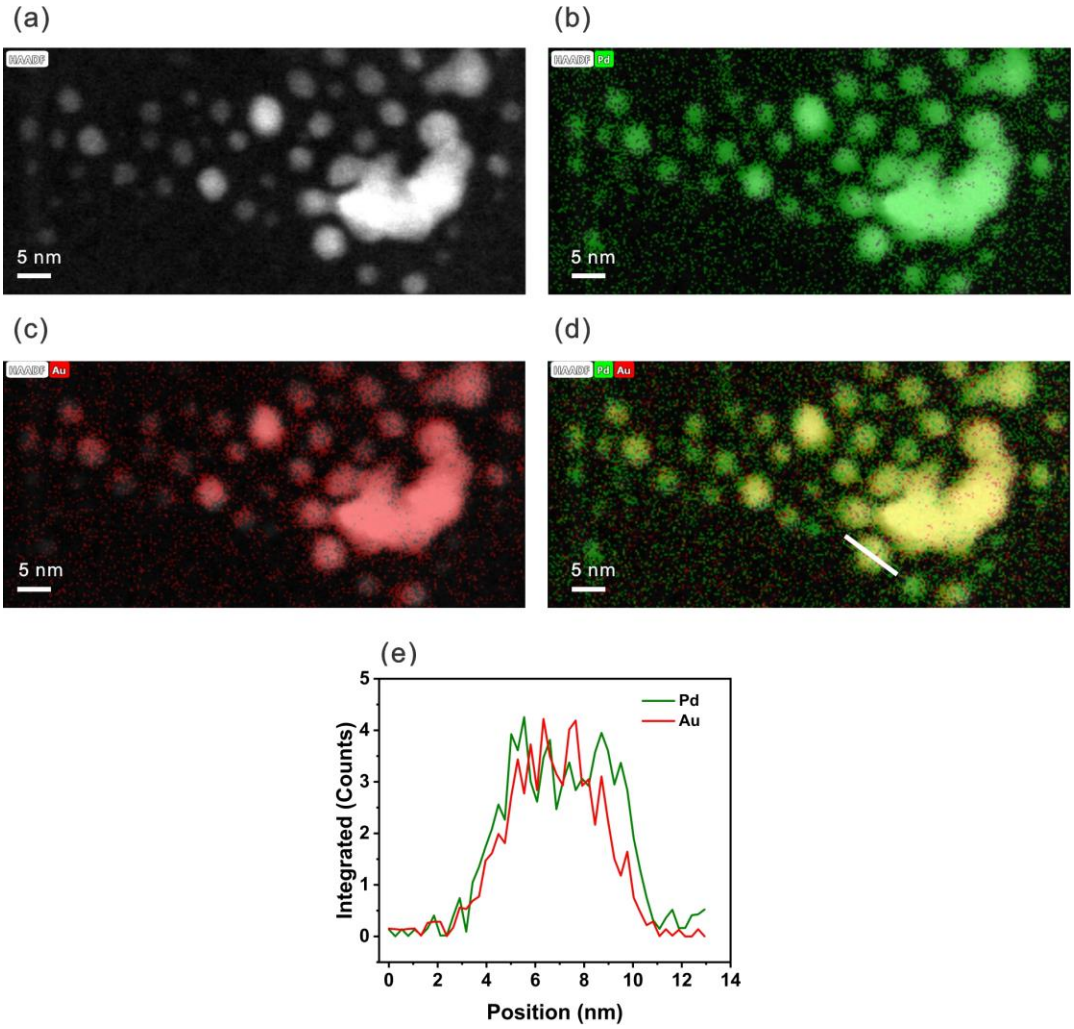

Figure 6.3: Representative HAADF-STEM image of $Pd_{52}Au_{48}$(a); Corresponding EDS mapping of Pd (b) and Au (c); Overlay of Pd and Au mapping (d); EDS line-scan profile of a single particle (e).

XPS measurement was carried out on $Pd_{52}Au_{48}$ nanoalloy to probe the surface chemistry and the valence-electronic state. Figure 6.4a and 6.4b present the high-resolution spectra of Pd 3d and Au 4f, respectively (survey spectrum in Figure A4.2 in Appendix 4). For Pd 3d, the spectrum can be deconvoluted into two pair of doublet peaks. The doublet peaks with binding energies of 324.44 eV and 339.73 eV are ascribed to the zerovalent Pd $3d_{5/2}$ and $3d_{3/2}$, respectively. Interestingly, these values shift negatively towards lower binding energies compared to the monometallic Pd NPs (see section 5.3.1). The other pair of doublet peaks located at 337.21 eV and 341.68 eV suggests the Pd with higher valence states, which probably arises from small amount of material oxidation during sample purification and drying. Similarly, in the deconvoluted spectrum of Au 4f (Figure 6.4b), the binding energies of 82.89 eV and 86.56 eV can be assigned to Au_0 $4f_{5/2}$ and $4f_{7/2}$, which also shift negatively by ~0.5 eV in comparison with TMVCPA-templated Au NPs. The negative shifts in binding energies of both Pd and Au in the bimetallic NP were also reported on some other AuPd nanoalloys and bulk alloys,[41,42] in which the phenomenon was explained by a redistribution of occupied valence shells.[43,44]

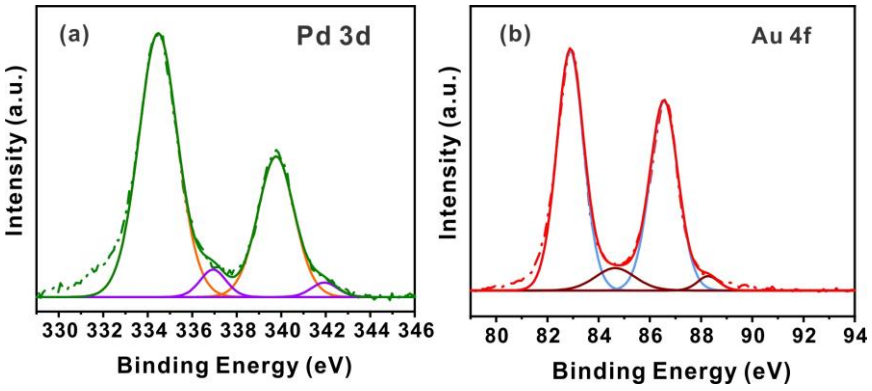

Figure 6.4: High-resolution XPS spectra of Pd 3d (a) and Au 4f (b) of $Pd_{52}Au_{48}$.

6.4 Conclusions and Outlooks

In Chapter 6, we demonstrate that TMVCPA is not only a facile building block for NP formation with single component but also capable of directing successful construction of bimetallic systems. Under mild synthetic conditions, PdAu nanoalloys can be synthesized with homogeneous intermixing compositions, as suggested by the data obtained from microscopic and spectroscopic

characterizations. To further obtain quantitative information at atomic- scale, other x-ray techniques such as EXAFS (extended X-ray absorption fine structure) may be necessary.[45] Remaining work of this chapter would be to apply the nanoalloy series in electrocatalytic reactions. Potential reactions worth trying include ORR, HER and FOAR, which have been discovered to be efficiently catalyzed by bimetallic PdAu systems in a great many literature reports. Practically, PdAu with different component ratios will be subjected to LSV or CV tests to identify the best candidate; comparisons with pure Pd, Au and other reported PdAu NPs are also necessary. Specifically, typical parameters including onset potential, specific activity and mass activity are to be analyzed. Moreover, durability tests by CA or continued CV cycling and post characterizations of materials are to be investigated. Discussions on possible origins for the catalytic performance are also necessary.

6.5 References

[1] C. Gao, F. Lyu and Y. Yin, *Chem. Rev.*, 2021, **121**, 834–881.

[2] L. Liu and A. Corma, *Chem. Rev.*, 2018, **118**, 4981–5079.

[3] P. J. Kulesza, I. S. Pieta, I. A. Rutkowska, A. Wadas, D. Marks, K. Klak, L. Stobinski and J. A. Cox, *Electrochim. Acta*, 2013, **110**, 474–483.

[4] M. A. Montiel, F. J. Vidal-Iglesias, V. Montiel and J. Solla-Gullón, *Curr. Opin. Electrochem.*, 2017, **1**, 34–39.

[5] C. Zhang, X. Shen, Y. Pan and Z. Peng, *Front. Energy*, 2017, **11**, 268–285.

[6] Y. Tang and W. Cheng, *Nanoscale*, 2015, **7**, 16151–16164.

[7] W. Zhu, B. M. Tackett, J. G. Chen and F. Jiao, *Top. Curr. Chem.*, 2018, **376**, 41.

[8] I. Roger, M. A. Shipman and M. D. Symes, *Nat. Rev. Chem.*, 2017, **1**, 3.

[9] S. Jiao, X. Fu, L. Zhang, Y.-J. Zeng and H. Huang, *Nano Today*, 2020, **31**, 100833.

[10] X. Li, C. Wang, H. Xue, H. Pang and Q. Xu, *Coord. Chem. Rev.*, 2020, **422**, 213468.

[11] M. Liang, T. Xia, H. Gao, K. Zhao, T. Cao, M. Deng, X. Ren, S. Li, H. Guo and R. Wang, *Nano Res.*, 2021, DOI:10.1007/s12274-021-3629-z.

[12] J. Fan, H. Du, Y. Zhao, Q. Wang, Y. Liu, D. Li and J. Feng, *ACS Catal.*, 2020, **10**, 13560–13583.

[13] S. Seraj, P. Kunal, H. Li, G. Henkelman, S. M. Humphrey and C. J. Werth, *ACS Catal.*, 2017, **7**, 3268–3276.

[14] M. A. Ehsan, A. S. Hakeem and A. Rehman, *Sci. Rep.*, 2020, **10**, 14469.

[15] A. K. Singh and Q. Xu, *ChemCatChem*, 2013, **5**, 652–676.

[16] L. Wang, A. Holewinski and C. Wang, *ACS Catal.*, 2018, **8**, 9388–9398.

[17] C. Wang, N. M. Markovic and V. R. Stamenkovic, *ACS Catal.*, 2012, **2**, 891–898.

[18] G. V Fortunato, E. Pizzutilo, E. S. F. Cardoso, M. R. V Lanza, I. Katsounaros, S. J. Freakley, K. J. J. Mayrhofer, G. Maia and M. Ledendecker, *J. Catal.*, 2020, **389**, 400–408.

[19] M. Wang, X. Qin, K. Jiang, Y. Dong, M. Shao and W.-B. Cai, *J. Phys. Chem. C*, 2017, **121**, 3416–3423.

[20] K. S. Joya, M. A. Ehsan, N.-U.-A. Babar, M. Sohail and Z. H. Yamani, *J. Mater. Chem. A*, 2019, **7**, 9137–9144.

[21] R. P. Jansonius, P. A. Schauer, D. J. Dvorak, B. P. MacLeod, D. K. Fork and C. P. Berlinguette, *Angew. Chem. Int. Ed.*, 2020, **59**, 12192–12198.

[22] T. Shen, J. Zhang, K. Chen, S. Deng and D. Wang, *Energy & Fuels*, 2020, **34**, 9137–9153.

[23] T. Wang, A. Chutia, D. J. L. Brett, P. R. Shearing, G. He, G. Chai and I. P. Parkin, *Energy Environ. Sci.*, 2021, **14**, 2639–2669.

[24] Z. Yin, M. Chi, Q. Zhu, D. Ma, J. Sun and X. Bao, *J. Mater. Chem. A*, 2013, **1**, 9157–9163.

[25] Y. Wang, L. Cao, N. J. Libretto, X. Li, C. Li, Y. Wan, C. He, J. Lee, J. Gregg, H. Zong, D. Su, J. T. Miller, T. Mueller and C. Wang, *J. Am. Chem. Soc.*, 2019, **141**, 16635–16642.

[26] X. Yuan, L. Zhang, L. Li, H. Dong, S. Chen, W. Zhu, C. Hu, W. Deng, Z.-J. Zhao and J. Gong, *J. Am. Chem. Soc.*, 2019, **141**, 4791–4794.

[27] S. Zhu, Q. Wang, X. Qin, M. Gu, R. Tao, B. P. Lee, L. Zhang, Y. Yao, T. Li and M. Shao, *Adv. Energy Mater.*, 2018, **8**, 1802238.

[28] K. Sasaki, H. Naohara, Y. Choi, Y. Cai, W.-F. Chen, P. Liu and R. R. Adzic, *Nat. Commun.*, 2012, **3**, 1115.

[29] H. Erikson, A. Sarapuu, J. Kozlova, L. Matisen, V. Sammelselg and K. Tammeveski, *Electrocatalysis*, 2015, **6**, 77–85.

[30] L. Rakočević, S. Štrbac and I. Srejić, *Int. J. Hydrogen Energy*, 2021, **46**, 9052–9063.

[31] Y. Jiang, Y. Yan, Y. Han, H. Zhang and D. Yang, *RSC Adv.*, 2017, **7**, 43373–43379.

[32] D. W. Yuan and Z. R. Liu, *J. Power Sources*, 2013, **224**, 241–249.

[33] Y. Wang, Z. Xiong and Y. Xia, *RSC Adv.*, 2017, **7**, 40462–40469.

[34] N. M. Bedford, A. R. Showalter, T. J. Woehl, Z. E. Hughes, S. Lee, B. Reinhart, S. P. Ertem, E. B. Coughlin, Y. Ren and T. R. Walsh, *ACS Nano*, 2016, **10**, 8645–8659.

[35] Z. Zong, K. Xu, D. Li, Z. Tang, W. He, Z. Liu, X. Wang and Y. Tian, *J. Catal.*, 2018, **361**, 168–176.

[36] D. Li, Z. Tang, S. Chen, Y. Tian and X. Wang, *ChemCatChem*, 2017, **9**, 2980–2987.

[37] E. Dujardin, C. Peet, G. Stubbs, J. N. Culver and S. Mann, *Nano Lett.*, 2003, **3**, 413–417.

[38] K. N. Avery, J. E. Schaak, R. E. Schaak, T. Pennsyl, V. State, V. Uni, U. V Park and V. Pennsyl, *Chem.Mater.*, 2009, **14**, 2176–2178.

[39] J. Lim, S. Kim, S. Lee, E. A. Stach, J. N. Culver and M. T. Harris, *J. Nanomater.*, 2010, 620506.

[40] J.-N. Zheng, S.-S. Li, X. Ma, F.-Y. Chen, A.-J. Wang, J.-R. Chen and J.-J. Feng, *J. Power Sources*, 2014, **262**, 270–278.

[41] X. Zhu, Q. Guo, Y. Sun, S. Chen, J. Q. Wang, M. Wu, W. Fu, Y. Tang, X. Duan, D. Chen and Y. Wan, *Nat. Commun.*, 2019, **10**, 1–11.

[42] P. A. P. Nascente, S. G. C. de Castro, R. Landers and G. G. Kleiman, *Phys. Rev. B*, 1991, **43**, 4659–4666.

[43] R. E. Watson, J. Hudis and M. L. Perlman, *Phys. Rev. B*, 1971, **4**, 4139–4144.

[44] M. B. Griffin, A. A. Rodriguez, M. M. Montemore, J. R. Monnier, C. T. Williams and J. W. Medlin, *J. Catal.*, 2013, **307**, 111–120.

[45] N. A. Merrill, T. T. Nitka, E. M. McKee, K. C. Merino, L. F. Drummy, S. Lee, B. Reinhart, Y. Ren, C. J. Munro, S. Pylypenko, A. I. Frenkel, N. M. Bedford and M. R. Knecht, *ACS Appl. Mater. Interfaces*, 2017, **9**, 8030–8040.

Chapter 7

Conclusions and Future Work

Chapter Preface

Chapter 7 provides a summary of each chapter separately. The summary includes a discussion on scientific contributions, conclusions, as well as existing challenges. Furthermore, some final thoughts and suggestions for future research directions are described.

7.1 Summary and Conclusions by Chapter

7.1.1 Chapter 1

As an introduction chapter, Chapter 1 first discussed the main advantages of bioinspired MNM synthesis over traditional chemical and physical based methods. It then summarized various fabrication methods of MNMs supported on different biological scaffolds, including peptides, proteins, DNA and viruses. Chapter 1 also focused on the applications of bio-directed MNMs in electrocatalytic reactions related to energy conversion fields. Moreover, analysis was made to compare the advantages and disadvantages of electrocatalysts supported on each bio-template. As reviewed in Chapter 1, although bioderived MNMs with fascinating properties have received wide research interest, they did not find immediate applications in electrocatalysis until only around ten years ago, and the existing examples in literature are not as many as other types of electrocatalysts. Given the large library of biological scaffolds, there presents lots of research opportunities in discovering suitable candidates to be applied in electrocatalysis.

7.1.2 Chapter 3

Chapter 3 reported the first example of utilizing a bioinspired Ag nanomaterial as an electrocatalyst for electro CO_2 RR. Although there are a number of literature reports on Ag-based NMs with excellent performance for catalysing CO_2 RR,[1–3] many of them fabricate the materials with multi-steps of synthesis, use non-natural ligands, hazardous solvents and require high thermal input, which is both energy intensive and environmentally unfriendly. The Ag NR in Chapter 3 addressed this common issue, since the reaction uses water as the solvent, is carried out at room temperature and is of simple synthetic step by photoreduction.

CO_2 RR test results showed that the Ag NR exhibited much improved catalytic activity, selectivity and stability compared to Ag NP prepared by conventional chemical reduction method and a bulky Ag electrode. Kinetic results by impedance spectra and Tafel plots further supported the faster intrinsic reaction rate with Ag NRs. In addition, its activity and CO FE are also excellent in comparison with some other reported Ag NMs.

Due to limitations in characterizing the bio-interface between the Ag NR and TMVCP, discussions on possible origins for the improved CO_2 RR performance were based on the current experimental evidence and relevant literature studies. Our hypothesis for this improvement is that the protein ligand has a large impact, in which the amine groups may suppress HER activity or stabilize chemisorpted CO_2, and the thiol functional groups may influence the binding energies and stabilize intermediate species.

7.1.3 Chapter 4

Building on Chapter 3, Chapter 4 described the work to expand the versatility of TMVCP in fabricating nanosized Pt materials in the form of both discrete nanorings and isolated particles, taking the advantage of the protein self-assembly properties under different pH conditions. The Pt NMs were prepared via incubation with TMVCP at neutral and alkaline solutions, and then reduced by $NaBH_4$. TEM characterizations showed that while in neutral solution, particles were embedded onto the disk protein surface and possess a close interparticle spacing, isolated particles were assembled on the protein subunit TMVCPA in alkaline condition.

The two Pt NMs were utilized as electrocatalysts for MOR and comparisons were made to Pt/C in acidic, neutral and alkaline electrolytes. Electrochemical data showed that both Pt NRs and Pt NPs had much improved activity and stability than Pt/C in neutral and alkaline conditions, which is probably due to the well-defined NP formation and increased hydrophilicity brought by the protein template. Moreover, the Pt NRs outperformed Pt NPs. We proposed that their distinct behaviors can be attributed to the different particle packing patterns. In Pt NRs, the distances between single particles are short enough that they induce a collectively positive impact on the readsorption of intermediate species onto neighboring particles, thus improving the overall reaction kinetics. Unfortunately, although the two Pt catalysts have excellent performance in neutral and alkaline

electrolytes, their stabilities in acid electrolytes are less satisfactory compared to Pt/C. The weaker stability could be related to the TMVCP template, that the protein may undergo denaturing during electrochemical tests in the extreme acidic pH electrolyte.

7.1.4 Chapter 5

Chapter 5 expanded on the application avenue and incorporated two organic reactions that have great significance in industrial processes, i.e., 4-nitrophenol reduction and allyl alcohol hydrogenation. For NM catalyzed these two reactions, they follow heterogeneous-type mechanism, in which the kinetics is strongly impacted by the NP's available surface area. Higher surface area facilitates the approach of reactant molecules to reach the catalytic sites and thus enables a faster reaction rate.

In this chapter, TMVCPA acted as the capping ligand to stabilize the growth of spherical Pt, Pd, and Au NPs. Compared to small organic capping ligands and peptide molecules that tightly binds to NPs, TMVCPA has a bulkier structure, which causes larger steric hindrance when capping the NP and maintains limited passivation over the surface. This brings great catalysis benefits when applied in a heterogenous-type reaction. Kinetic data demonstrated exceptional reaction rates of Au NP catalyzed 4-NP reduction and Pd NP catalyzed olefin hydrogenation, as compared to NPs capped by organic molecules and peptides.

The hypothesized protein structure-function relationship was supported by MD simulation results on one single Pd NP surrounded by TMVCPAs. As expected, it was observed that the protein interacts with the NP by only a small number of amino acid residues and the rest of the protein remains unaltered in structure. Moreover, the steric hindrance indeed makes it impossible for protein to densely pack onto the NP surface, thus exposing a large portion of NP surface to the solvent. Therefore, the small reactant molecules can easily access the catalytically active site and promotes reaction kinetics.

7.1.5 Chapter 6

Chapter 6 explored the potential of TMVCPA to template the formation of bimetallic systems. All previous chapters dealt with the synthesis of single metallic nanocatalysts and proved the

versatility of the protein template, which make the natural transition of expecting it to also be a good candidate to support growth of bimetallic catalysts. Compared to single component catalyst, bimetallic systems often show distinct advantages of higher material utilization efficiency, as well as synergistic behaviors between metals that may contribute positively to the final catalytic performance.

In Chapter 6, bimetallic PdAu was chosen as the target bimetallic catalyst, since PdAu bimetallic materials in both alloy and core-shell forms have been widely reported as effective catalysts towards a variety of reactions. The synthesis followed the same protocols as in previous chapters, except the precursors were added sequentially with Au and Pd salts. The successful bimetallic NP synthesis was supported by UV-vis and XPS characterizations. While in UV-vis spectra, the characteristic gold plasmonic band disappeared, XPS data showed that the binding energies of both metals shifted negatively, as compared to the corresponding single metal NPs. Furthermore, by TEM and STEM-EDS mapping measurements, the bimetallic PdAu NPs were confirmed to be in an alloy composition, with Pd and Au distributed uniformly in the particles.

Future work of Chapter 6 includes applying the PdAu NPs in electrocatalysis. One potential reaction worth trying would be formate oxidation, which is the anode reaction for FAOR fuel cell. NPs with diverse stoichiometries are to be screened to identify the best candidate and study the trend of the catalytic performance with varying Pd content. Also, this relationship between Pd content and activity needs further investigation to reveal the possible mechanisms.

7.2 Future Work

7.2.1 Understanding the Biointerface Characteristics between TMVCP and NP

The interaction between NP and biomacromolecules generally results in a biointerface that is critically important to maintain the colloid stability, as well as the exquisite control over the final NP morphology and organization patterns.[4] Fundamental understanding of the biointerface structural regime at atomic scale is imperative to reveal many properties that arise from this

binding event, which in turn can have drastic impact on the overall catalytic activity. Nevertheless, the biointerface faces significant challenges in term of characterizations.[4]

In this thesis, the TMVCP-NPs are mainly characterized by routine techniques such as UV-vis, TEM, SAED, and x-ray based XPS, XRD, all of which are more concerned with the inorganic NPs. Future work can involve the characterizations that focused on the structural details of the bio-interface. Some techniques are worth exploration, such as QCM,[5–7] SPR,[8–10] XAFS,[11] etc. While QCM and SPR can provide information on the binding affinity of metal to the biomolecule surface, synchrotron based XAFS can be used to analyze the metal coordination by the non-metal elements in the protein. Specifically, take Chapter 4 as an example, the two Pt catalysts on TMVCP and TMVCPA are utilized for MOR and show different catalytic behaviors. Although we tentatively proposed that the reason likely lies in the interparticle spacing between adjacent particles, the bio-interface may be also different. It is possible that in disk protein, the Pt particle lies onto the surface and the top part of the NP is exposed to the environment; at higher pH, the Pt NPs are surrounded by the A proteins instead. How this different protein assembly geometry affect the binding affinity and the NP exposed surface area needs investigation, in which QCM may provide some insights.

In Chapter 5, MD simulations are carried out on TMVCPA-Pd NP system to model the binding regimes of the A proteins capping a single NP and calculate the number of small reactants that can reach the NP surface. This leads to the natural thought of future work on simulating the binding event of metallic nanorings on the disk protein, including Ag NRs (Chapter 3) and Pt NRs (Chapter 4). In Chapter 3, the enhanced performance of Ag NRs was attributed to the protein ligand that its abundant functional groups facilitate the CO_2 RR. Via simulation, it might be possible to probe the binding sites that used to nucleate silver nanoparticles. Nevertheless, given that the disk protein consists of 34 protein subunits and assembled in two layers, the computational cost would be rather high and it is unclear whether this can be realized with current simulation power, which needs cooperation with computational chemists.

7.2.2 Enlarging TMV Family for Directing Synthesis of Bio-Nano Hybrid Electrocatalysts

Wild-type TMVCP was used throughout this thesis. In the process of developing disk protein templated nanoring synthesis, Ag NR and Pt NR were successfully prepared. Gold precursors were also tried for incubation with TMVCP and reduced by sodium borohydride, which unfortunately did not lead to efficient ring formation. As promising materials, gold nanorings may find important applications in various fields including electrocatalysis. To realize in situ gold nanoring formation on TMVCP, a good direction would be to engineer the genetic sequence and express mutated proteins to introduce thiol groups.[12–14] There have been some examples using TMVCP mutants to assemble nanostructures. For instance, Zhang et al. used a T103C-TMV disk to convert the threonine around the inner cavity into cysteine in its inner cavity, and thus immobilized S-S bonds between neighboring protein subunits, which can be activated into thiol groups and act as binding sites to interact with presynthesized gold NPs, forming chainlike nanostructures under low pH buffer.[14] To enable in situ fabrication of Au nanoparticles onto the ring or outer edge of the disk protein, it is necessary to introduce thiol groups or other functional groups at the corresponding position to induce site specific binding.

It is noted that both Ag NRs and Pt NRs consist of discrete nanoparticles forming a ring shape. From an electrocatalysis perspective, contiguous ring shape have the advantage of higher electron conductivity. Thus, another suggestion would be to design variants that possesses more binding sites in a contiguous manner and realize formation of contiguous nanoring.

According to phase diagram of TMVCP, nanorods form when solution in slightly acidic conditions. The 300 nm long TMV in has been utilized as a robust 1D template for in situ metallization in both its internal channel and outer surfaces. Nevertheless, the RNA-free nanorods are less explored. Nanowires are characterized by their high aspect ratios and electronic conductivity, which are beneficial to electrocatalytic activities.[15–17] To build such 1D electrocatalyst, it could be either first dialyze the variant TMVCP into slightly acidic conditions then carry out mineralization, or first assemble nanoparticles on the outer surface of TMVCP disk protein first, then explore assembly conditions to form the corresponding nanowires.

7.2.3 Incorporation of Earth-Abundant Nanocomposites on TMVCP

Precious metals such as platinum, palladium and silver are widely used electrocatalysts, which are also the target metals for TMVCP mineralization in this thesis. However, given the relatively high cost and low abundance of these metals, it is imperative to find more economical alternatives that can show catalytic performance comparable to those of noble metals, with the ultimate goal of achieving inexpensive and green electrochemical reactions. Popular candidates include compounds containing elements such as nickel,[18,19] cobalt,[20,21] as well as some transition metal oxides,[22] nitride,[23] carbides.[24] There have been numerous literature reports on employing these materials for electrocatalysis, using chemically based fabrication methods.[24] To this end, we envision the prospects of transitioning to the TMVCP-templated earth-abundant inorganic electrocatalyst. Two examples successfully implemented TMV virion and its variant as platform for cobalt and nickel nanowire formation via electroless deposition.[25,26] It is therefore worth exploring the potential of the coat protein to direct the co-deposition of noble-metal and non-noble metal, or deposition of sole earth-abundant materials. For instance, Pt is of high cost and suffers from CO poisoning when applied in MOR, as stated in Chapter 4. One future direction of this work could be to incorporate $Ni(OH)_2$ to form TMVCP-Pt-$Ni(OH)_2$ nanocomposite, since nanosized $Ni(OH)_2$ has been demonstrated to show excellent performance in removing CO.[27,28]

7.2.4 Exploring Applications beyond Electrocatalysis

As stated in section 7.2.2, 1D nanowires feature high aspect ratio and electronic conductivity, which may make them promising materials not limited to electrocatalysis, but can be extended to other electrochemistry related areas, such as electronic devices, battery electrodes, electrochemical sensors, etc. Applications in these fields are worth exploring once the rod-like TMVCP can be successfully decorated by the inorganic components.

Additionally, in Chapter 5, we presented the promising application of TMVCP-NP complex in organic synthesis to expand into the non-electrochemistry fields. For future work, more heterogeneous catalysis maybe involved. Unfortunately, proteins can be denatured when exposed in organic solvents, which may limit the reaction scope organic transformations to those can be carried out in aqueous solutions.

7.2.5 Other Promising Bio-Templates

While this thesis deals with the TMVCP and strives to push its full potential for MNM fabrications, it still has some limitations. For example, the conductivity of the protein is not sufficient, as seen in Chapter 4 that the two Pt catalysts need to be mixed with carbon ink to achieve good electrode conductivity. Also, the protein is prone to denature in very acidic electrolytes and pure organic solvents, which requires careful solvent choice when applied in certain catalytic reactions. These specific challenges also apply to many other protein molecules and may need research endeavors to address these issues, either by modifying the proteins themselves, or developing more of the other effective bio-templates to enlarge this library for applications in various fields.

7.3 References

[1] S. Zhao, R. Jin and R. Jin, *ACS Energy Lett.*, 2018, **3**, 452–462.

[2] S. Liu, H. Tao, L. Zeng, Q. Liu, Z. Xu, Q. Liu and J. L. Luo, *J. Am. Chem. Soc.*, 2017, **139**, 2160–2163.

[3] W. Zhang, Y. Hu, L. Ma, G. Zhu, Y. Wang, X. Xue, R. Chen, S. Yang and Z. Jin, *Adv. Sci.*, 2018, **5**, 1700275.

[4] T. R. Walsh and M. R. Knecht, *Chem. Rev.*, 2017, **117**, 12641–12704.

[5] C. Tamerler, E. E. Oren, M. Duman, E. Venkatasubramanian and M. Sarikaya, *Langmuir*, 2006, **22**, 7712–7718.

[6] J. P. Palafox-Hernandez, Z. Tang, Z. E. Hughes, Y. Li, M. T. Swihart, P. N. Prasad, T. R. Walsh and M. R. Knecht, *Chem. Mater.*, 2014, **26**, 4960–4969.

[7] C. Tamerler, M. Duman, E. E. Oren, M. Gungormus, X. Xiong, T. Kacar, B. A. Parviz and M. Sarikaya, *Small*, 2006, **2**, 1372–1378.

[8] U. O. S. Seker, B. Wilson, D. Sahin, C. Tamerler and M. Sarikaya, *Biomacromolecules*, 2009, **10**, 250–257.

[9] M. Hnilova, E. E. Oren, U. O. S. Seker, B. R. Wilson, S. Collino, J. S. Evans, C. Tamerler and M. Sarikaya, *Langmuir*, 2008, **24**, 12440–12445.

[10] U. O. S. Seker, B. Wilson, J. L. Kulp, J. S. Evans, C. Tamerler and M. Sarikaya, *Biomacromolecules*, 2014, **15**, 2369–2377.

[11] N. A. Merrill, T. T. Nitka, E. M. McKee, K. C. Merino, L. F. Drummy, S. Lee, B. Reinhart, Y. Ren, C. J. Munro, S. Pylypenko, A. I. Frenkel, N. M. Bedford and M. R. Knecht, *ACS Appl. Mater. Interfaces*, 2017, **9**, 8030–8040.

[12] J. Zhang, K. Zhou, Y. Zhang, M. Du and Q. Wang, *Adv. Mater.*, 2019, **31**, 1901485.

[13] J. T. Zhang, J. Ma, R. K. Kankala, Q. Yu, S. Bin Wang and A. Z. Chen, *ACS Appl. Bio Mater.*, 2021, **4**, 4039–4048.

[14] J. Zhang, R. K. Kankala, J. Ma, Y. Zhou, S. Bin Wang and A. Z. Chen, *Biomacromolecules*, 2021, **22**, 540–545.

[15] Y. Li, A. Morel, D. Gallant and J. Mauzeroll, *Anal. Chem.*, **93**, 9657–9662.

[16] Y. Zhu, L. Bu, Q. Shao and X. Huang, *ACS Catal.*, 2019, **9**, 6607–6612.

[17] D. Raciti, M. Mao, J. H. Park and C. Wang, *Catal. Sci. Technol.*, 2018, **8**, 2364–2369.

[18] V. Vij, S. Sultan, A. M. Harzandi, A. Meena, J. N. Tiwari, W.-G. Lee, T. Yoon and K. S. Kim, *ACS Catal.*, 2017, **7**, 7196–7225.

[19] M. Gong, D.-Y. Wang, C.-C. Chen, B.-J. Hwang and H. Dai, *Nano Res.*, 2016, **9**, 28–46.

[20] T. Ling, D.-Y. Yan, H. Wang, Y. Jiao, Z. Hu, Y. Zheng, L. Zheng, J. Mao, H. Liu and X.-W. Du, *Nat. Commun.*, 2017, **8**, 1–7.

[21] H. Jin, J. Wang, D. Su, Z. Wei, Z. Pang and Y. Wang, *J. Am. Chem. Soc.*, 2015, **137**, 2688–2694.

[22] Y. Xue, S. Sun, Q. Wang, Z. Dong and Z. Liu, *J. Mater. Chem. A*, 2018, **6**, 10595–10626.

[23] J. Xie and Y. Xie, *Chem. Eur. J.*, 2016, **22**, 3588–3598.

[24] W.-F. Chen, J. T. Muckerman and E. Fujita, *Chem. Commun.*, 2013, **49**, 8896–8909.

[25] M. Knez, A. M. Bittner, F. Boes, C. Wege, H. Jeske, E. Maiβ and K. Kern, *Nano Lett.*, 2003, **3**, 1079–1082.

[26] E. Royston, A. Ghosh, P. Kofinas, M. T. Harris and J. N. Culver, *Langmuir*, 2008, **24**, 906–912.

[27] K. Zhang, H. Wang, J. Qiu, J. Wu, H. Wang, J. Shao, Y. Deng and L. Yan, *Chem. Eng. J.*, 2021, **421**, 127786.

[28] W. Huang, H. Wang, J. Zhou, J. Wang, P. N. Duchesne, D. Muir, P. Zhang, N. Han, F. Zhao, M. Zeng, J. Zhong, C. Jin, Y. Li, S.-T. Lee and H. Dai, *Nat. Commun.*, 2015, **6**, 10035.

Appendix 1

Biosynthesized Silver Nanoring as a Highly Efficient and Selective Electrocatalyst for CO_2 Reduction

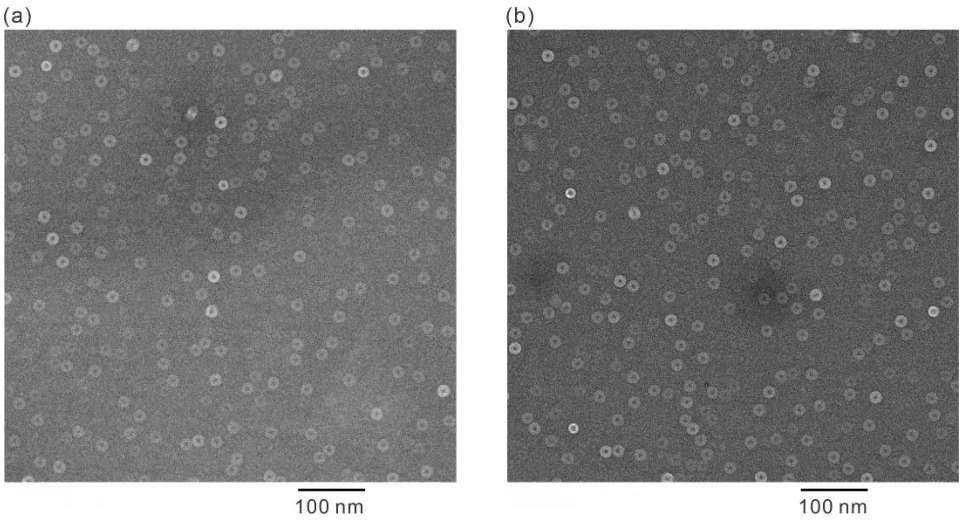

Figure A1.1: TEM image of the wild type TMV-cp in water before (a) and after (b) UV illumination, the dominant species is in disk form.

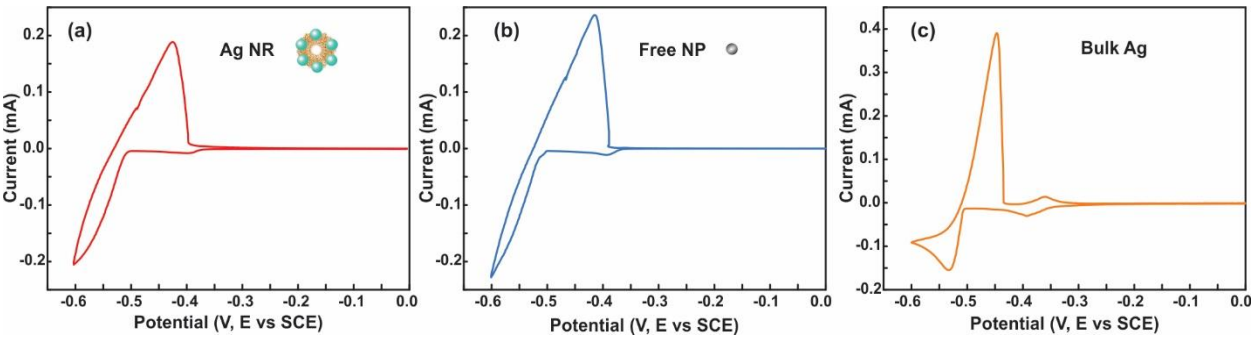

Figure A1.2: Cyclic voltammograms of UPD and bulk deposition of lead in 5 mM $Pb(NO_3)_2$, 10 mM HNO_3 and 10 mM KCl, with a scan rate of 10 mV/s.

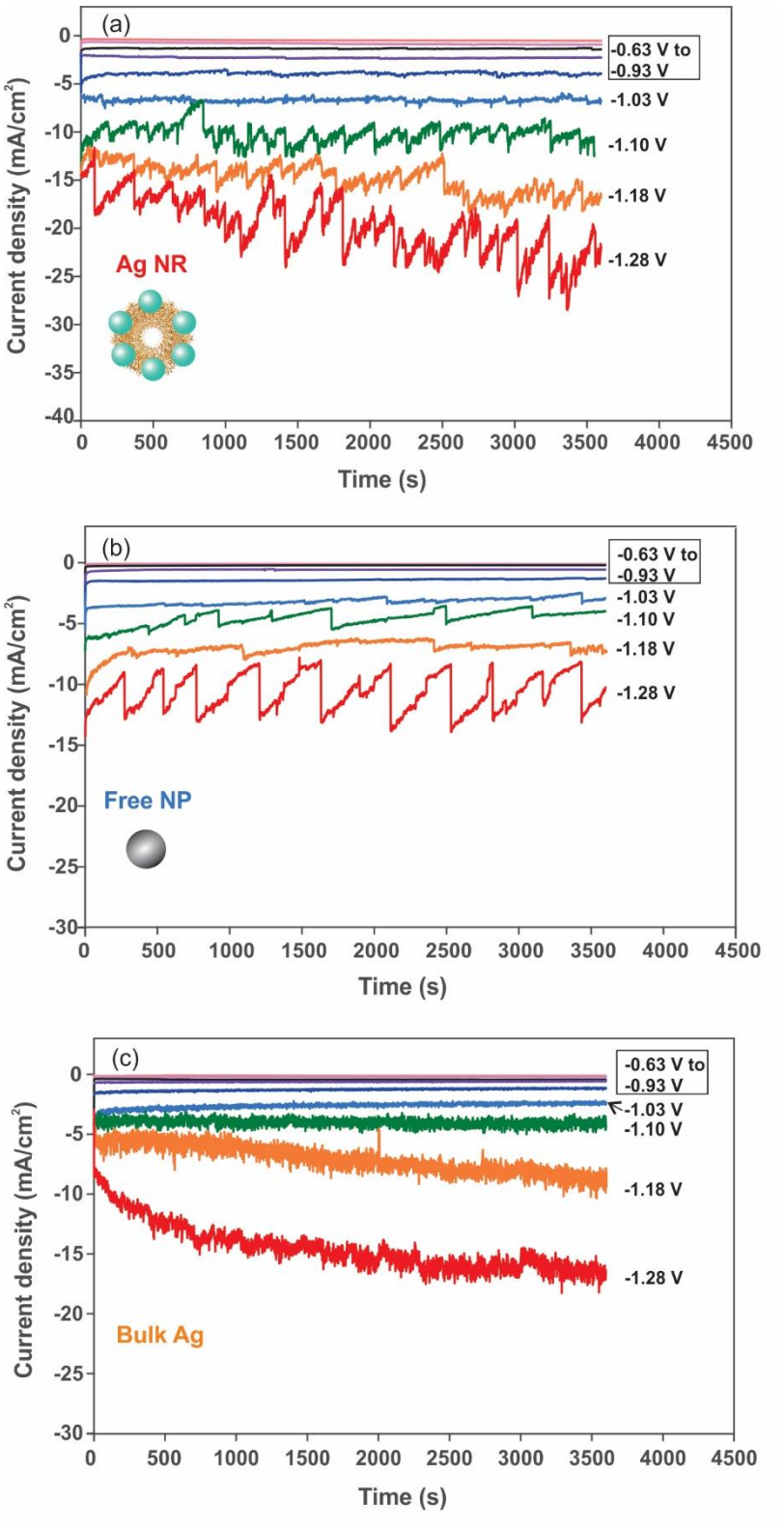

Figure A1.3: Current densities over time at different applied potentials of Ag NR (a); Free NP (b); and bulk Ag (c).

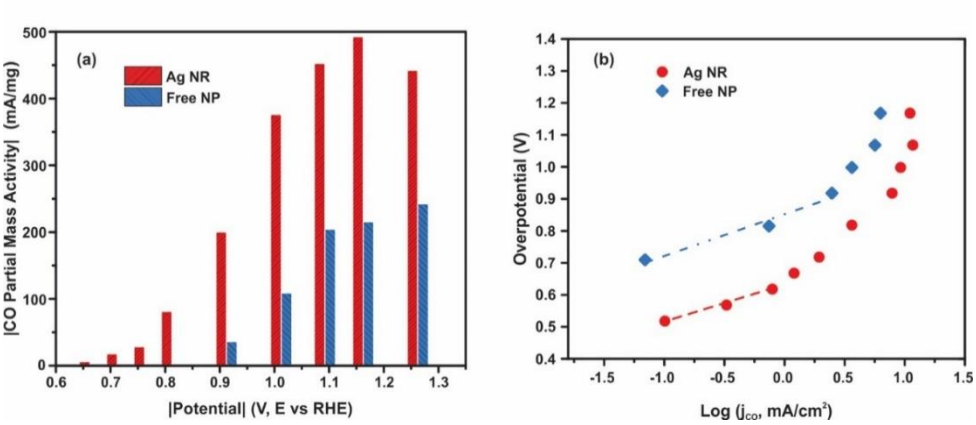

Figure A1.4: CO mass activity of Ag NR and Free NP under different applied potentials (a); Tafel plots of prepared Ag NR and Free NP (b).

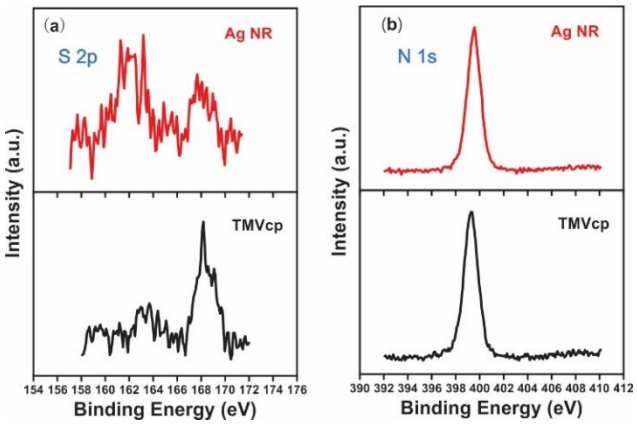

Figure A1.5: XPS spectra of S 2p (a) and N 1s (b) from Ag NR and pure TMVCP.

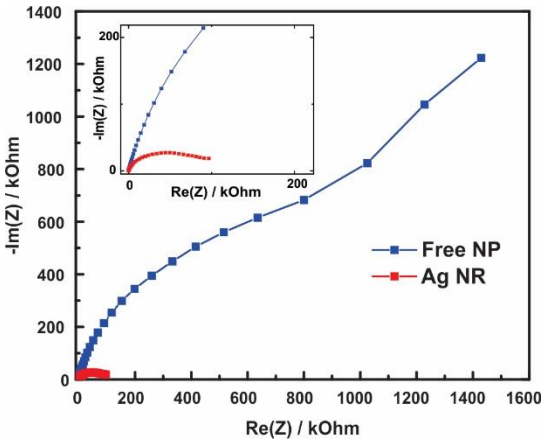

Figure A1.6: Nyquist plot of Ag NR and Free NP recorded at open circuit potential in CO_2 saturated 0.5 M $KHCO_3$ solution.

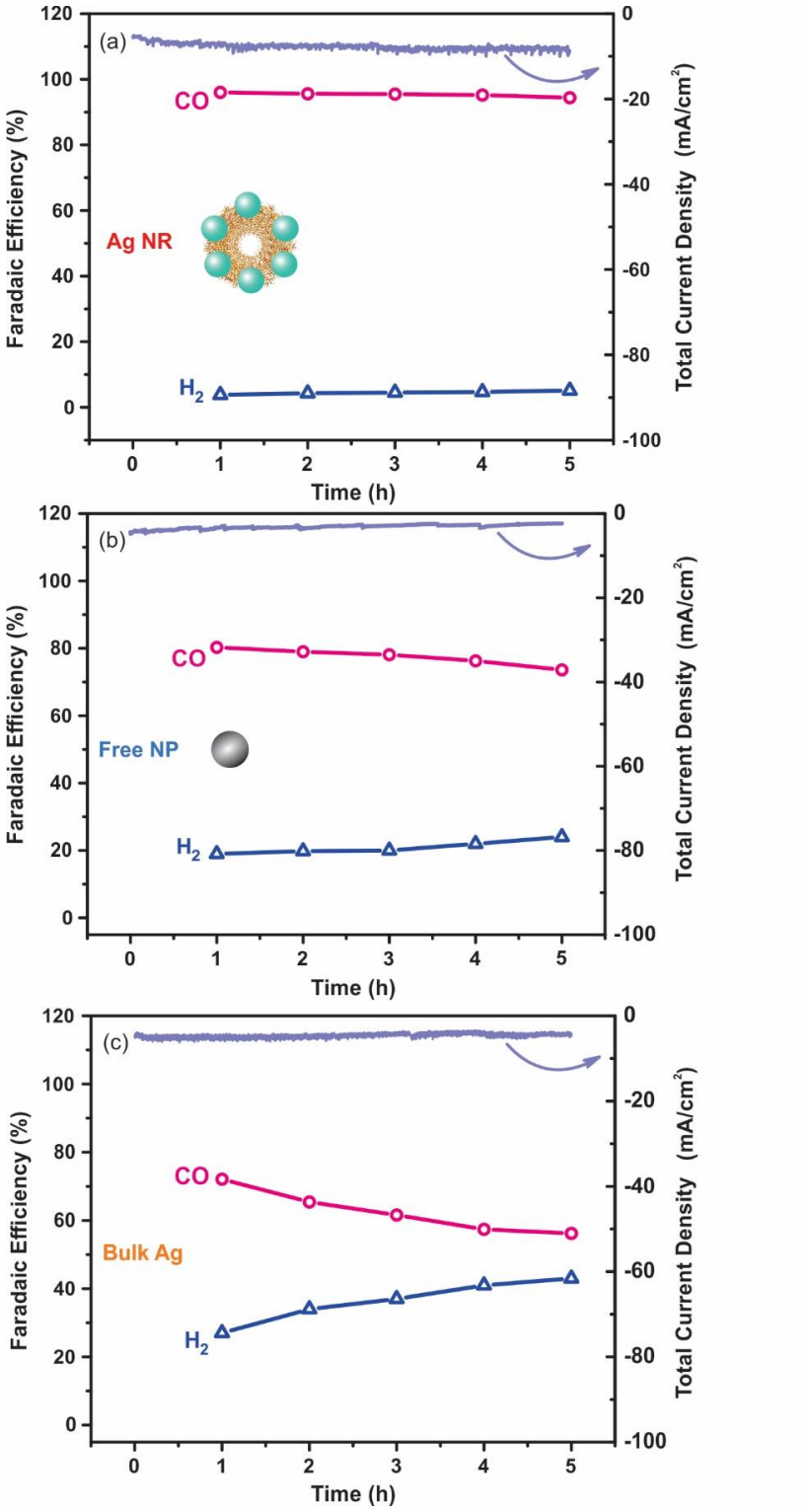

Figure A1.7: Five hours durability test at a potential of -1.028 V from Ag NR (a); Free NP (b); and Bulk Ag (c). FEs of CO and H_2 (left axis) versus time and total current densities (right axis) versus time.

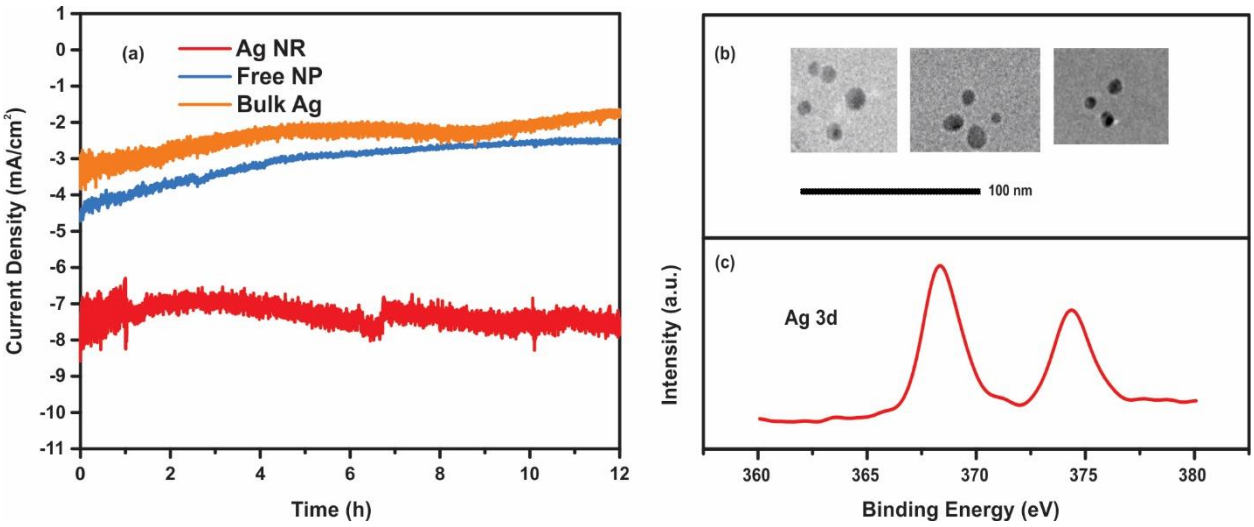

Figure A1.8: Twelve hours durability test at a potential of -1.028 V from Ag NR, Free NP and Bulk Ag (a); post electrolysis characterization of Ag NR by TEM (b) and XPS spectrum (c).

Table A1.1: Comparison of some Ag catalysts for CO_2 reduction to CO.

Material	Electrolyte	pH	Highest CO FE	Overpotential[a]	j_{CO}[b] (mA/cm^2)	Ref.
Ag NR	0.5 M $KHCO_3/CO_2$	7.2	95 %	0.918 V	7.8	This work
8 nm Ag	0.5 M $KHCO_3/CO_2$	7.2	82%	0.998 V	3.8	This work
Bulk Ag	0.5 M $KHCO_3/CO_2$	7.2	82%	0.998 V	2.1	This work
3 nm Ag/C	0.5 M $KHCO_3/CO_2$	7.0	76.8%	0.790 V	6.0	R1
5 nm Ag/C	0.5 M $KHCO_3/CO_2$	7.0	79.2%	0.640 V	6.0	R1
10 nm Ag/C	0.5 M $KHCO_3/CO_2$	7.0	72.6%	0.790 V	3.0	R1
Triangular Ag nanoplate	0.1 M $KHCO_3/CO_2$	7.0	96.8%	0.746 V	1.2	R2
Spherical Ag NP	0.1 M $KHCO_3/CO_2$	7.0	65.4%	0.846 V	1.7	R2
Ag plate	0.5 M $KHCO_3/CO_2$	7.2	~ 60%	0.79 V~ 0.99 V	-	R3
35 nm Ag nanowire	0.5 M $KHCO_3/CO_2$	7.2	78.0%	0.790 V	-	R3

[a]The overpotential that needed at highest CO FE. [b]The CO current density under the overpotential in the left column.

References

[1] C. Kim, H. S. Jeon, T. Eom, M. S. Jee, H. Kim, C. M. Friend, B. K. Min and Y. J. Hwang, *J. Am. Chem. Soc.*, 2015, **137**, 13844–13850.

[2] S. Liu, H. Tao, L. Zeng, Q. Liu, Z. Xu, Q. Liu and J. L. Luo, *J. Am. Chem. Soc.*, 2017, **139**, 2160–2163.

[3] W. Xi, R. Ma, H. Wang, Z. Gao, W. Zhang and Y. Zhao, *ACS Sustain. Chem. Eng.*, 2018, **6**, 7687–7694.

Appendix 2

Tunable Assembly of Protein Enables Fabrication of Platinum Nanostructures with Different Catalytic Activity

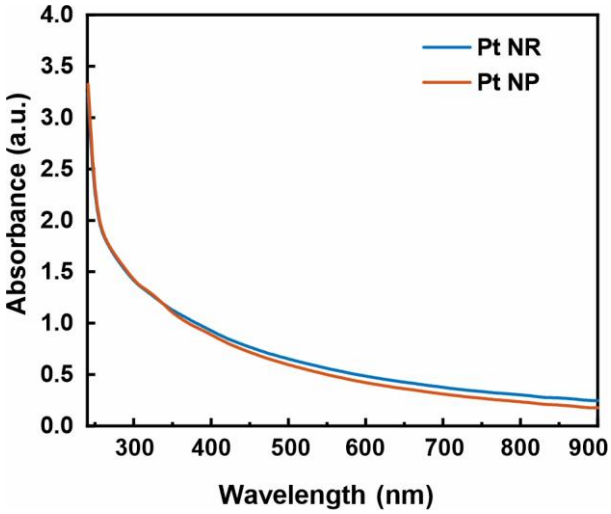

Figure A2.1: UV-vis spectra of Pt NR and Pt NP.

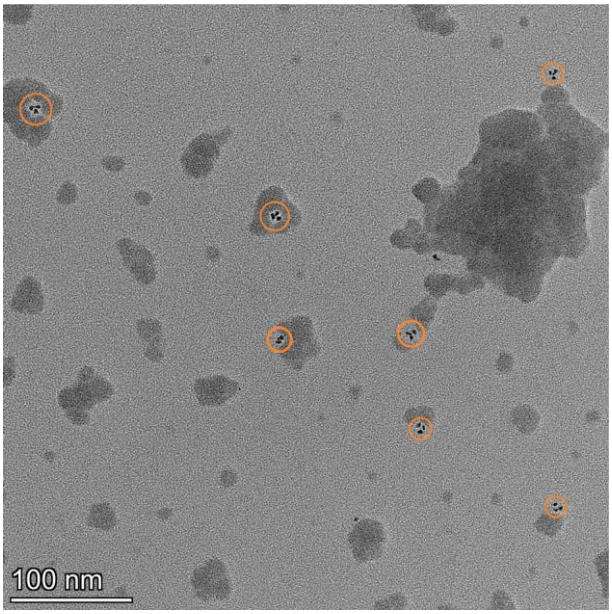

Figure A2.2: Representative low magnification TEM image of Pt NR (stained).

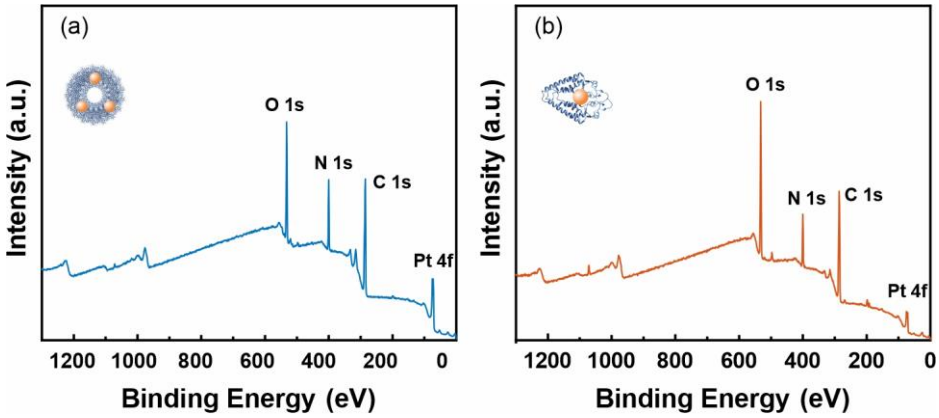

Figure A2.3: XPS survey spectra of Pt NRs (a) and Pt NPs (b).

Table A2.1: ECSA values of Pt NR, Pt NP and Pt/C in different electrolytes.

	Electrolyte		
Catalyst	**0.1 M $HClO_4$**	**0.75 M PBS**	**0.1 M NaOH**
Pt NR	792.4 cm^2/mg	685.5 cm^2/mg	442.1 cm^2/mg
Pt NP	822.6 cm^2/mg	761.1 cm^2/mg	448.4 cm^2/mg
Pt/C	591.5 cm^2/mg	618.1 cm^2/mg	433.3 cm^2/mg

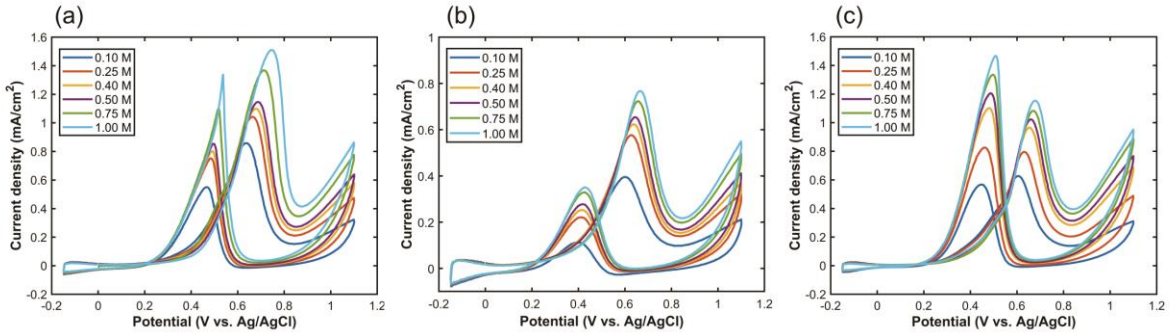

Figure A2.4: CVs of Pt NR (a), Pt NP(b) and Pt/C (c) catalyzed MOR in 0.1 M $HClO_4$ with various MeOH concentrations.

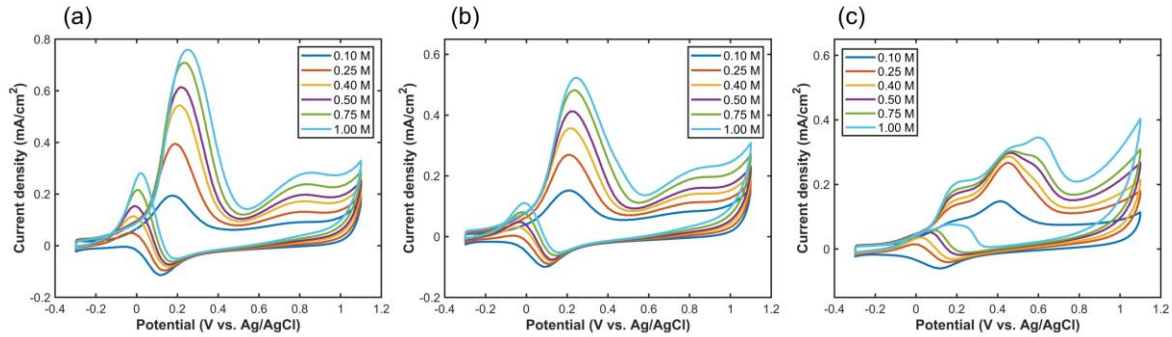

Figure A2.5: CVs of Pt NR (a), Pt NP(b) and Pt/C (c) catalyzed MOR in 0.75 M PBS with various MeOH concentrations.

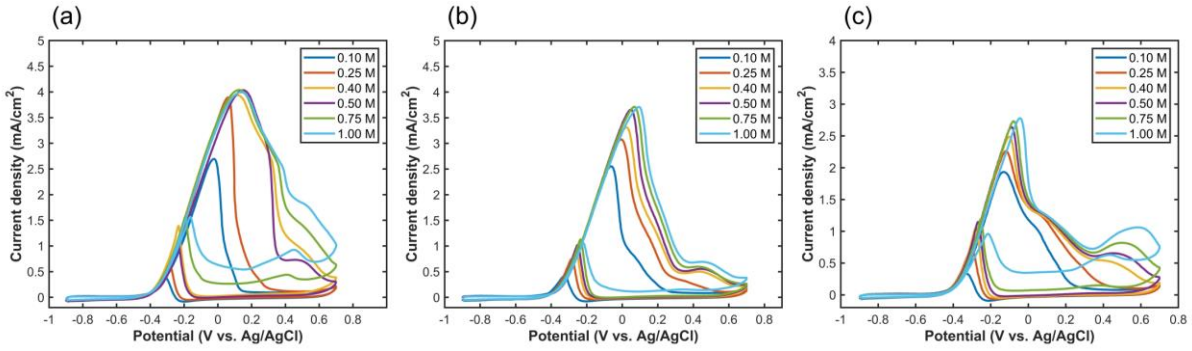

Figure A2.6: CVs of Pt NR (a), Pt NP(b) and Pt/C (c) catalyzed MOR in 0.1 M NaOH with various MeOH concentrations.

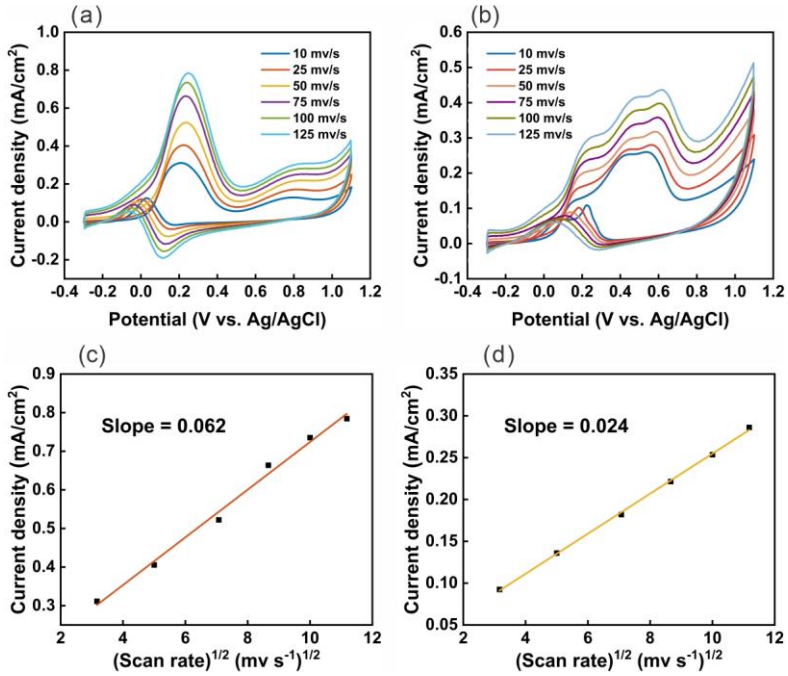

Figure A2.7: CVs of Pt NP (a) and Pt/C (b) catalyzed MOR in 0.75 M PBS/1 M MeOH at different scan rates; The corresponding plots of forward peak current density versus square root of scan rates, with (c) from Pt NP and (d) from Pt/C.

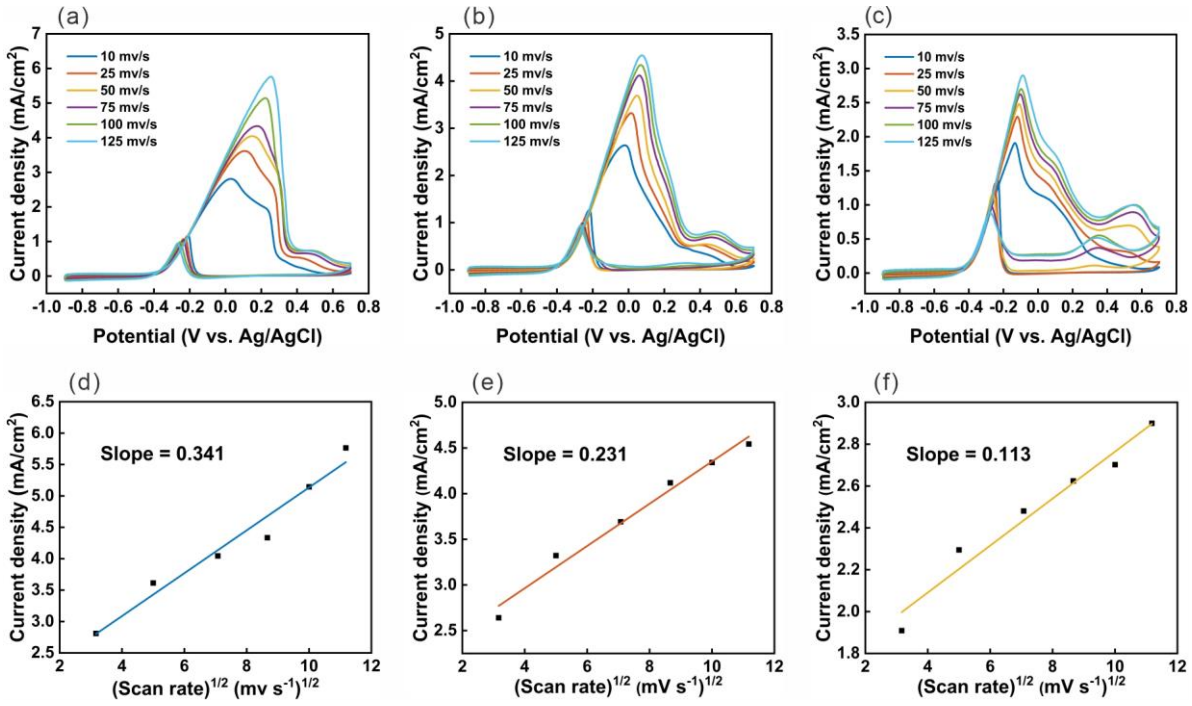

Figure A2.8: CVs of Pt NR (a) Pt NP (b) and Pt/C (c) catalyzed MOR in 0.1 M NaOH/0.5 M MeOH at different scan rates; The corresponding plots of forward peak current density versus square root of scan rates, with (d) from Pt NR, (e) from Pt NP and (f) from Pt/C.

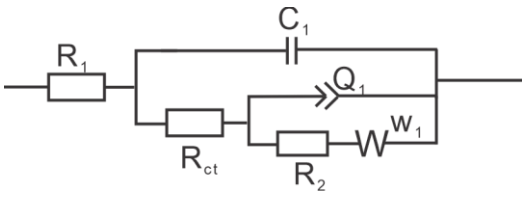

Figure A2.9: Proposed equivalent circuit for the methanol oxidation Nyquist plots in PBS and NaOH electrolytes.

For the above equivalent circuit, R_1 represents solution resistance, C_1 is the double layer capacitance, R_{ct} corresponds to the charge transfer resistance from the methanol oxidation, Q_1 is a constant phase element of the methanol oxidation, R_2 may be related to the contact resistance between catalyst and the glassy carbon electrode, W_1 is the Warburg impedance related to diffusion.

Table A2.2: Comparison of some representative Pt-based nanomaterials for alkaline methanol electrooxidation.

Entry	Electrocatalyst	Support/template	Electrolyte	Scan rate (mV/s)	Peak current density[a]	Ref
1	Pt NPs	Graphene-vanadium carbonitride	0.5 M MeOH/ 1.0 M KOH	50	1.15 mA/cm^2	1
2	Pt NPs	Multiple layers of graphene	1.0 M MeOH/ 1.0 M NaOH	50	939 A/g	2
3	Pt NPs	Carbon nanohorns	1.0 M MeOH/ 1.0 M KOH	50	490 A/g	3
4	Pt NPs	3D graphene polyaniline	1.0 M MeOH/ 1.0 M NaOH	100	1172 A/g	4
5	PtNi NPs	Carbon	1.0 M MeOH/ 1.0 M NaOH	50	1200 A/g	5
6	PtBi NPs	Electrodeposition on GCE	1.0 M MeOH/ 1.0 M NaOH	50	1400 A/g	6
7	Au@Pt NPs	HDA[b]/GCE	1.0 M MeOH/ 1.0 M KOH	50	132 A/g	7
8	Au/PtCu	-	1.0 M MeOH/ 1.0 M KOH	50	1500 A/g	8
9	Pt NPs	TMVCP	0.5 M MeOH/ 0.1 M NaOH	50	3.68 mA/cm^2 1641 A/g	This work
10	Pt NRs	TMVCP	0.5 M MeOH/ 0.1 M NaOH	50	4.04 mA/cm^2 1793 A/g	This work

[a]Specific activity normalized to ECSA, mass activity normalized to Pt mass.

[b]HDA: 1,6-hexanediamine

References

[1] T. Huang, S. Mao, G. Zhou, Z. Zhang, Z. Wen, X. Huang, S. Ci and J. Chen, *Nanoscale*, 2015, **7**, 1301–1307.

[2] C. Berghian-Grosan, T. Radu, A. R. Biris, M. Dan, C. Voica, F. Watanabe, A. S. Biris and A. Vulcu, *J. Energy Chem.*, 2020, **40**, 81–88.

[3] C. Zhu, D. Liu, Z. Chen, L. Li and T. You, *J. Colloid Interface Sci.*, 2018, **511**, 77–83.

[4] Y. Wang, Z. Li, S. Xu, Y. Xie and S. Lin, *Mater. Res. Bull.*, 2018, **102**, 172–179.

[5] Q. Jiang, L. Jiang, S. Wang, J. Qi and G. Sun, *Catal. Commun.*, 2010, **12**, 67–70.

[6] M. Yang, *J. Power Sources*, 2013, **229**, 42–47.

[7] N. S. K. Gowthaman, B. Sinduja, S. Shankar and S. A. John, *Sustain. Energy Fuels*, 2018,

2, 1588–1599.

[8] W. Hong, J. Wang and E. Wang, *Small*, 2014, **10**, 3262–3265.

Appendix 3

Nanometals Templated by Tobacco Mosaic Virus Coat Protein with Enhanced Catalytic Activity

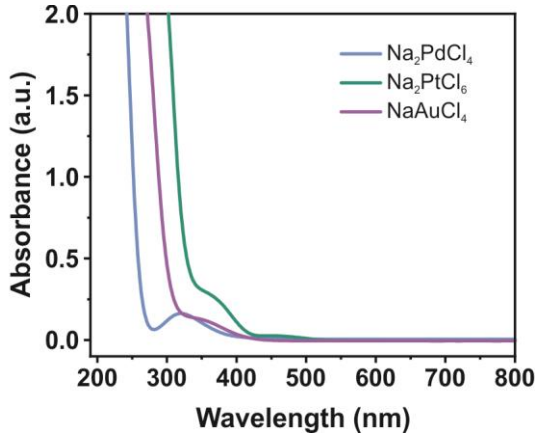

Figure A3.1: UV-vis spectra of metal salts in Tris-HCl buffer.

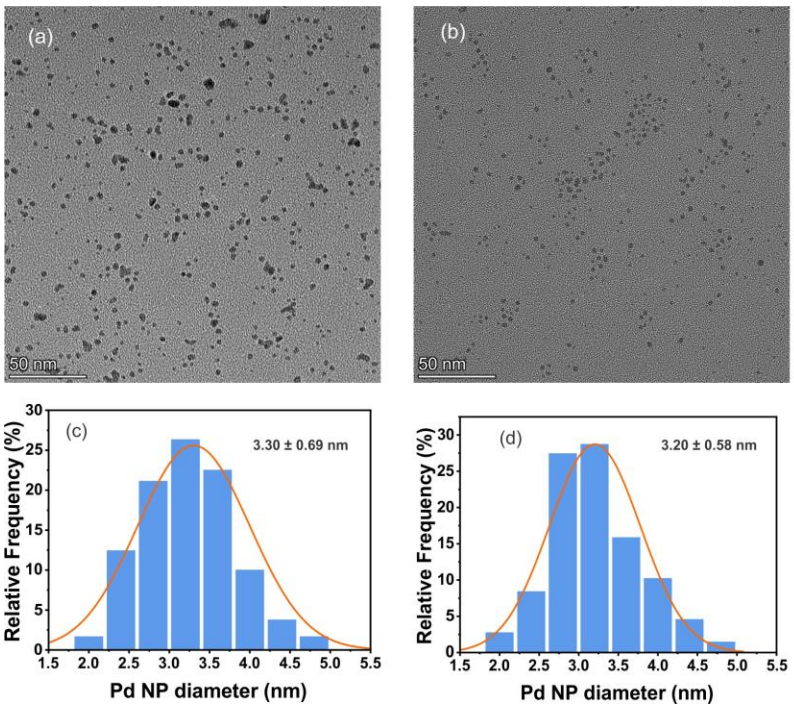

Figure A3.2: TEM image (a) of Pd NPs with higher concentration of Na_2PdCl_4 (3.4 mM) and the size distribution histogram (c); TEM image (b) of Pd NPs with 8 hrs metal-protein incubation time and the size distribution histogram (d).

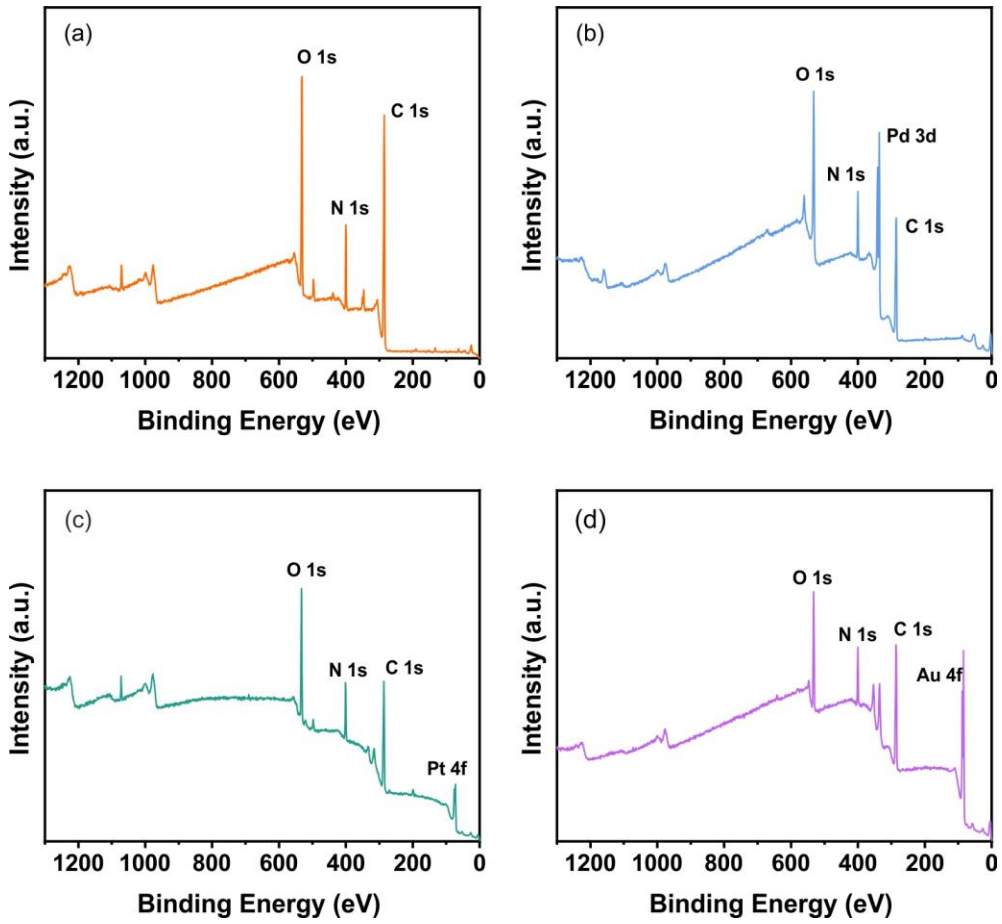

Figure A3.3: XPS survey spectra of TMVCP (a), TMVCP-templated Pd NPs (b), Pt NPs (c) and Au NPs (d).

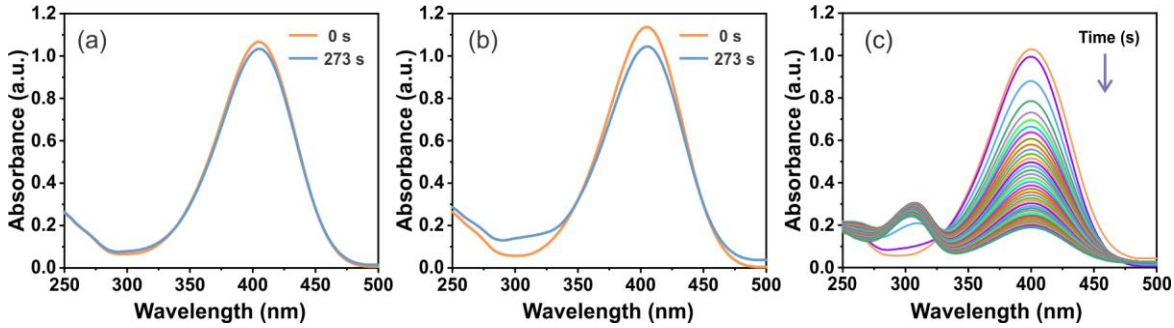

Figure A3.4: Control experiment of $NaBH_4$ mixed with 4-NP without any catalyst (a), and with only TMVCP (b); (c) UV-vis spectra evolution of 20 μM Pd NPs catalyzed 4-NP reduction at room temperature.

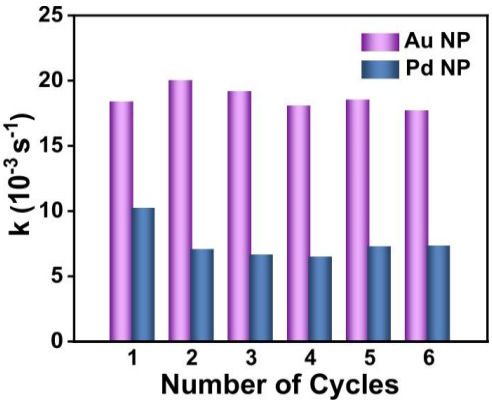

Figure A3.5: The reusability of 39.5 μM Au and Pd NPs for 4-NP reduction.

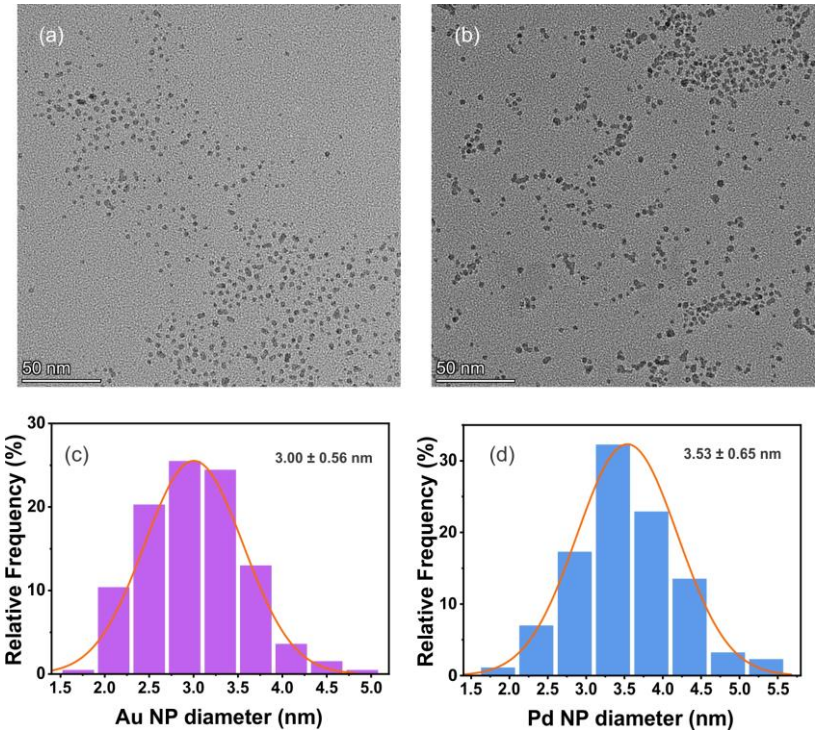

Figure A3.6: TEM image of Au NPs (a) and Pd NPs (b) after 4-NP reduction cycling tests; The corresponding particle size histogram of Au NPs (c) and Pd NPs (d).

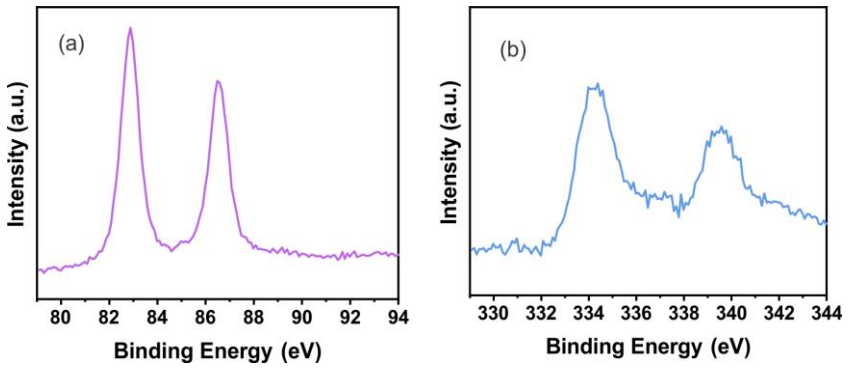

Figure A3.7: XPS spectra of Au 4f from Au NPs (a), and Pd 3d from Pd NPs (b) after 4-NP reduction cycling tests.

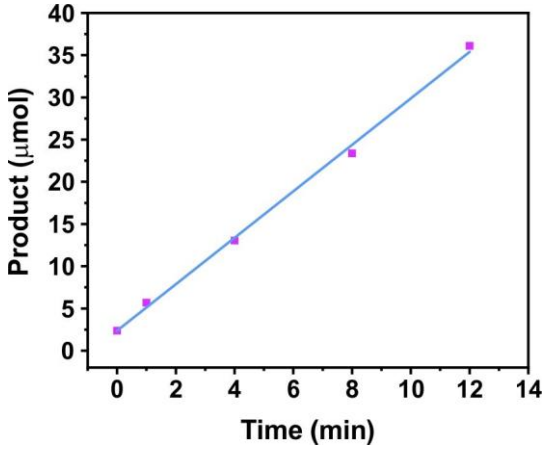

Figure A3.8: TOF determination of Pd NP (0.05% mol) catalyzed allyl alcohol hydrogenation. The amount of product was quantified by NMR and TOF was calculated by linear fitting of the curve to obtain the slope.

Table A3.1: Comparison of some representative palladium nanoparticles for allyl alcohol hydrogenation.

Entry	Particle size / shape	Support / template	TOF [mol product (mol Pd h)$^{-1}$]	Ref
1	1.69 nm / spherical	6-mercaptohexanocic acid	480	[1]
2	1.7 nm / spherical	Poly(amidoamine) dendrimers	480[a]	[2]
3	1.66 nm / spherical	S-alkythiosulfate	310	[3]
4	2.6 nm / spherical	Gluathione	131	[4]
5	2.1 nm / spherical	Polyelectrolyte film	5300 ± 500	[5]
6	3.0 nm / spherical	R5 peptide	2983 ± 162	[6]
7	5.7 nm / nanoparticle network	Peptoid membrane	3465 ± 585	[7]
8	5.0 nm / nanoparticle chain	Peptoid fiber	5423 ± 1057	[7]
9	3.5 nm / spherical	TMVCP	6382 ± 258	This work

[a]Reaction solvent was MeOH-H_2O (4:1 v/v), TOF was calculated on the basis of H_2 uptake.

References

[1] D. J. Gavia, M. S. Maung and Y.-S. Shon, *ACS Appl. Mater. Interfaces*, 2013, **5**, 12432–12440.

[2] Y. Niu, L. K. Yeung and R. M. Crooks, *J. Am. Chem. Soc.*, 2001, **123**, 6840–6846.

[3] D. J. Gavia and Y.-S. Shon, *Langmuir*, 2012, **28**, 14502–14508.

[4] T. R. Sibakoti, J. B. Jasinski, M. H. Nantz and F. P. Zamborini, *Nanoscale*, 2020, **12**, 12027–12037.

[5] S. Bhattacharjee and M. L. Bruening, *Langmuir*, 2008, **24**, 2916–2920.

[6] R. Bhandari, D. B. Pacardo, N. M. Bedford, R. R. Naik and M. R. Knecht, *J. Phys. Chem. C*, 2013, **117**, 18053–18062.

[7] N. A. Merrill, F. Yan, H. Jin, P. Mu, C.-L. Chen and M. R. Knecht, *Nanoscale*, 2018, **10**, 12445–12452.

Appendix 4

Tobacco Mosaic Virus Coat Protein-Templated PdAu Nanoalloys for Electrocatalytic Applications

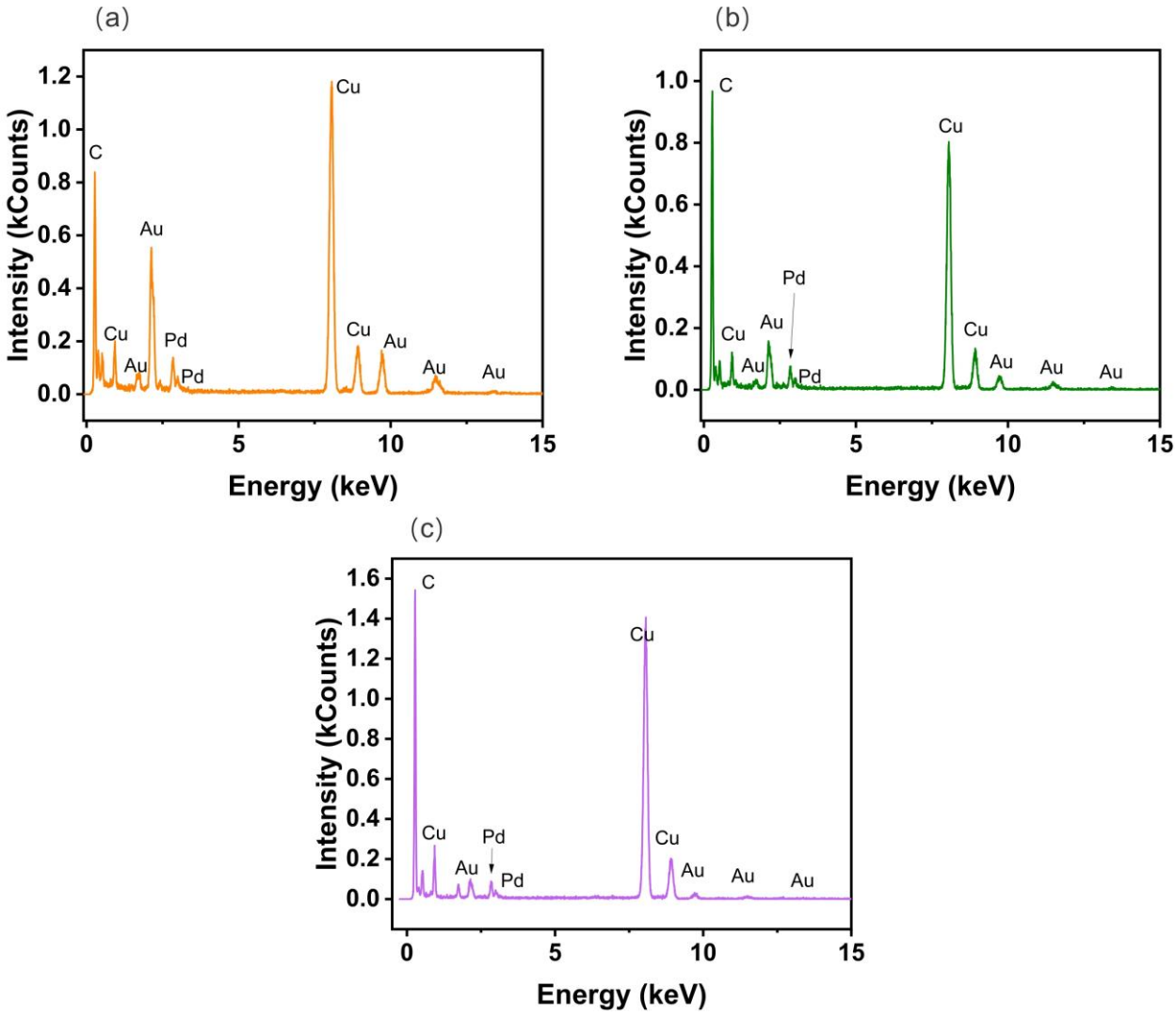

Figure A4.1: Representative EDS spectrum of $Pd_{33}Au_{67}$ NPs (a), $Pd_{52}Au_{48}$ NPs (b) and $Pd_{72}Au_{28}$ NPs (c).

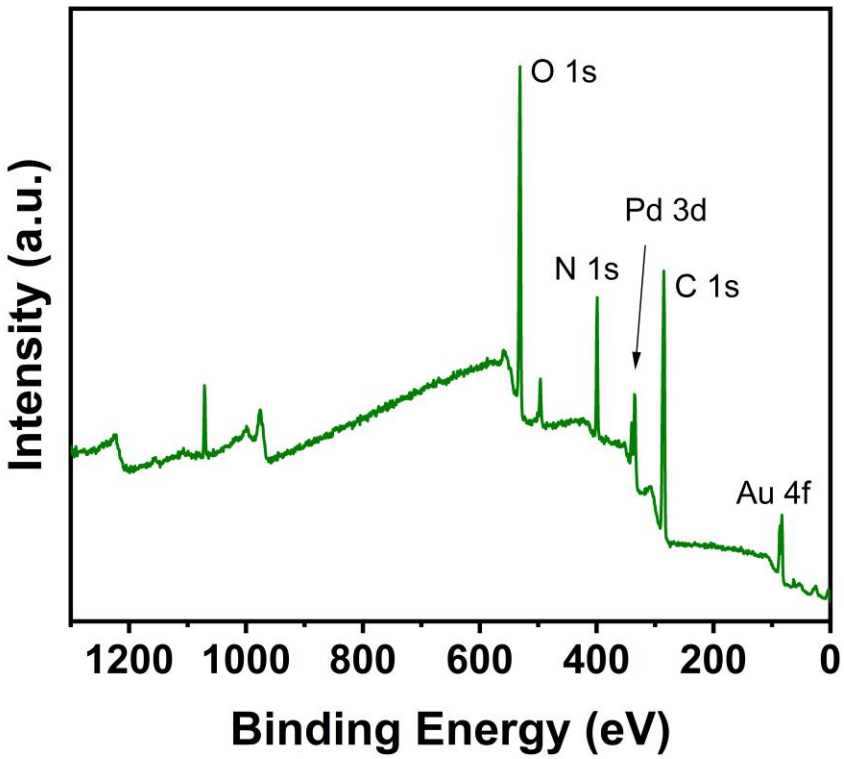

Figure A4.2: XPS survey spectrum of $Pd_{52}Au_{48}$ NP.

Appendix 5

Copyrights Permission

Scheme 2.1

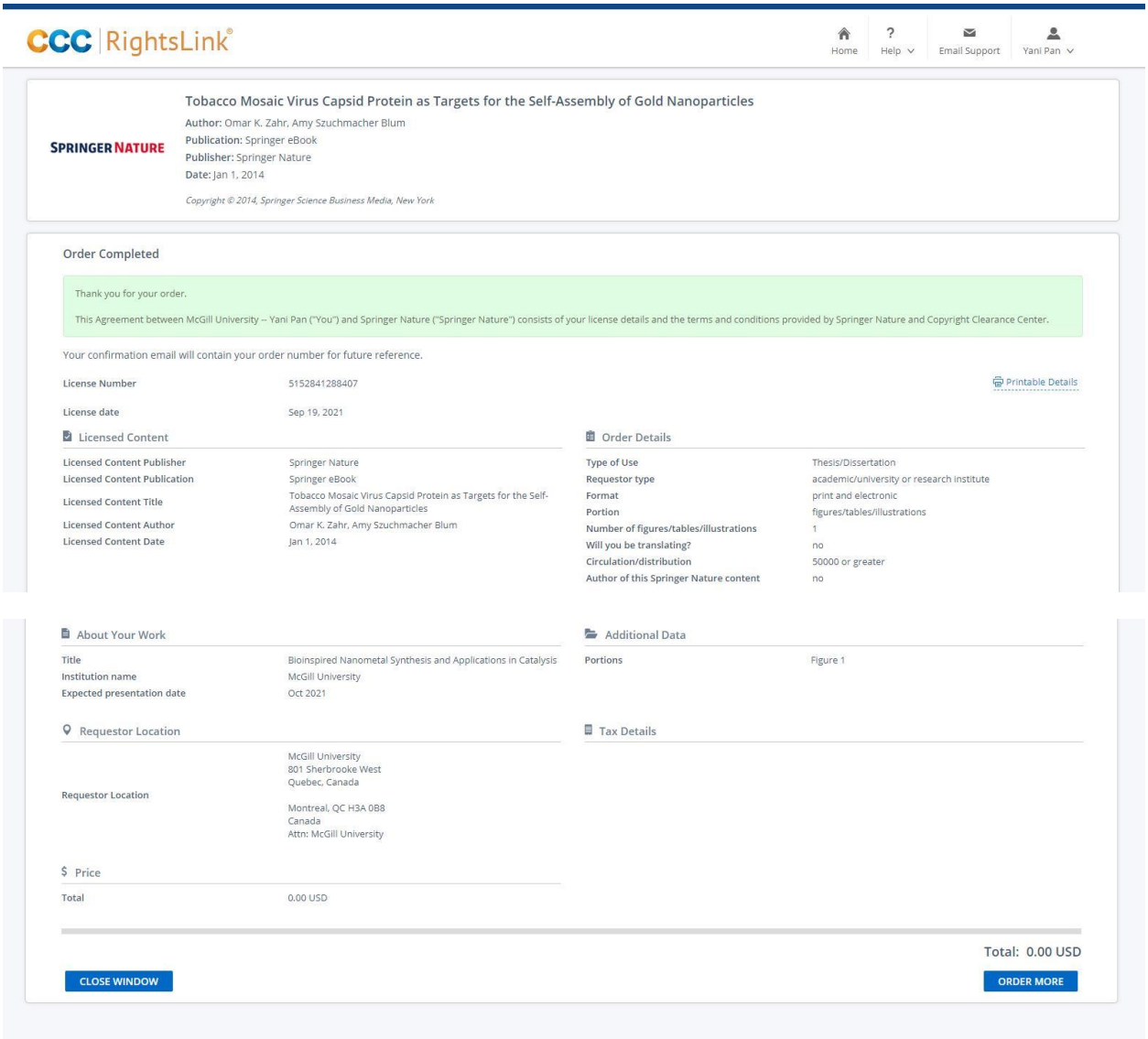

CCC | RightsLink

Home | Help | Email Support | Yani Pan

SPRINGER NATURE

Tobacco Mosaic Virus Capsid Protein as Targets for the Self-Assembly of Gold Nanoparticles

Author: Omar K. Zahr, Amy Szuchmacher Blum
Publication: Springer eBook
Publisher: Springer Nature
Date: Jan 1, 2014

Copyright © 2014, Springer Science Business Media, New York

Order Completed

Thank you for your order.

This Agreement between McGill University -- Yani Pan ("You") and Springer Nature ("Springer Nature") consists of your license details and the terms and conditions provided by Springer Nature and Copyright Clearance Center.

Your confirmation email will contain your order number for future reference.

Printable Details

License Number	5152841288407
License date	Sep 19, 2021

Licensed Content

Licensed Content Publisher	Springer Nature
Licensed Content Publication	Springer eBook
Licensed Content Title	Tobacco Mosaic Virus Capsid Protein as Targets for the Self-Assembly of Gold Nanoparticles
Licensed Content Author	Omar K. Zahr, Amy Szuchmacher Blum
Licensed Content Date	Jan 1, 2014

Order Details

Type of Use	Thesis/Dissertation
Requestor type	academic/university or research institute
Format	print and electronic
Portion	figures/tables/illustrations
Number of figures/tables/illustrations	1
Will you be translating?	no
Circulation/distribution	50000 or greater
Author of this Springer Nature content	no

About Your Work

Title	Bioinspired Nanometal Synthesis and Applications in Catalysis
Institution name	McGill University
Expected presentation date	Oct 2021

Additional Data

Portions	Figure 1

Requestor Location

Requestor Location	McGill University 801 Sherbrooke West Quebec, Canada Montreal, QC H3A 0B8 Canada Attn: McGill University

Tax Details

Price

Total	0.00 USD

Total: 0.00 USD

CLOSE WINDOW

ORDER MORE

Appendix 5

Chapter 1

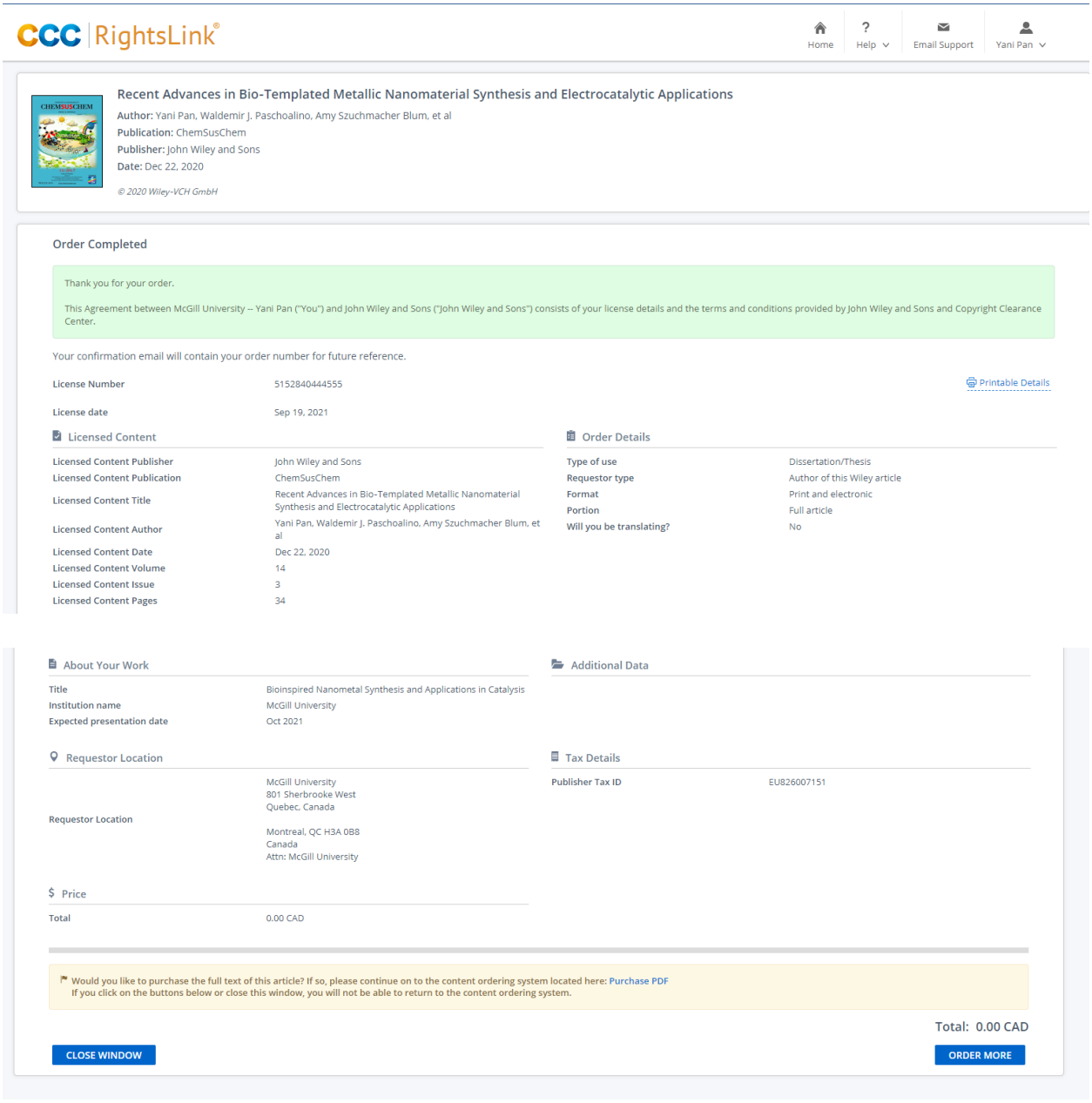

CCC | RightsLink®

Home | Help | Email Support | Yani Pan

Recent Advances in Bio-Templated Metallic Nanomaterial Synthesis and Electrocatalytic Applications

Author: Yani Pan, Waldemir J. Paschoalino, Amy Szuchmacher Blum, et al
Publication: ChemSusChem
Publisher: John Wiley and Sons
Date: Dec 22, 2020

© 2020 Wiley-VCH GmbH

Order Completed

Thank you for your order.

This Agreement between McGill University -- Yani Pan ("You") and John Wiley and Sons ("John Wiley and Sons") consists of your license details and the terms and conditions provided by John Wiley and Sons and Copyright Clearance Center.

Your confirmation email will contain your order number for future reference.

Printable Details

License Number	5152840444555
License date	Sep 19, 2021

Licensed Content

Licensed Content Publisher	John Wiley and Sons
Licensed Content Publication	ChemSusChem
Licensed Content Title	Recent Advances in Bio-Templated Metallic Nanomaterial Synthesis and Electrocatalytic Applications
Licensed Content Author	Yani Pan, Waldemir J. Paschoalino, Amy Szuchmacher Blum, et al
Licensed Content Date	Dec 22, 2020
Licensed Content Volume	14
Licensed Content Issue	3
Licensed Content Pages	34

Order Details

Type of use	Dissertation/Thesis
Requestor type	Author of this Wiley article
Format	Print and electronic
Portion	Full article
Will you be translating?	No

About Your Work

Title	Bioinspired Nanometal Synthesis and Applications in Catalysis
Institution name	McGill University
Expected presentation date	Oct 2021

Additional Data

Requestor Location

Requestor Location	McGill University 801 Sherbrooke West Quebec, Canada Montreal, QC H3A 0B8 Canada Attn: McGill University

Tax Details

Publisher Tax ID	EU826007151

Price

Total	0.00 CAD

Would you like to purchase the full text of this article? If so, please continue on to the content ordering system located here: Purchase PDF
If you click on the buttons below or close this window, you will not be able to return to the content ordering system.

Total: 0.00 CAD

CLOSE WINDOW | ORDER MORE

Appendix 5

Chapter 3

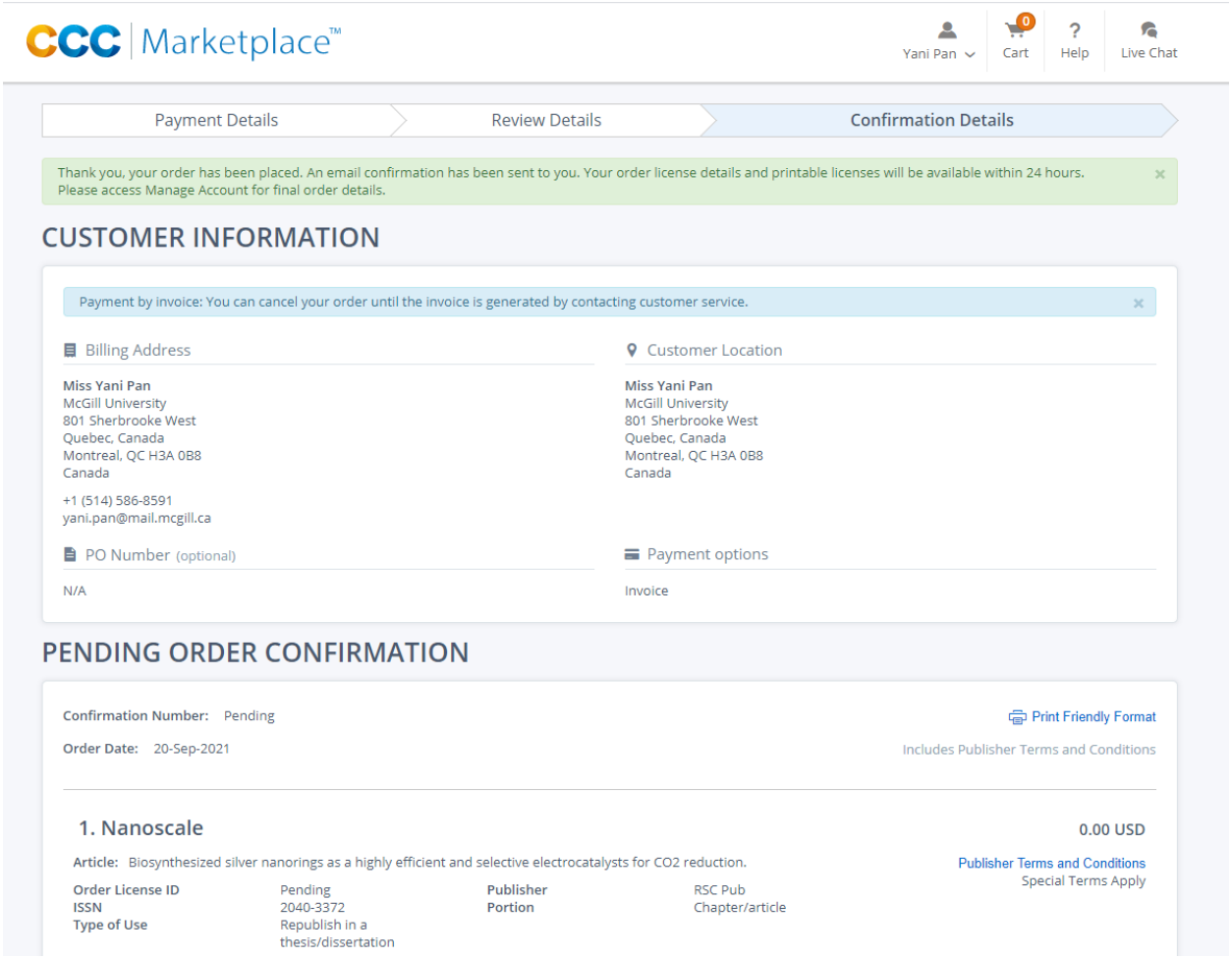

CCC Marketplace™

Yani Pan | Cart 0 | Help | Live Chat

Payment Details > Review Details > Confirmation Details

Thank you, your order has been placed. An email confirmation has been sent to you. Your order license details and printable licenses will be available within 24 hours. Please access Manage Account for final order details.

CUSTOMER INFORMATION

Payment by invoice: You can cancel your order until the invoice is generated by contacting customer service.

Billing Address

Miss Yani Pan
McGill University
801 Sherbrooke West
Quebec, Canada
Montreal, QC H3A 0B8
Canada

+1 (514) 586-8591
yani.pan@mail.mcgill.ca

Customer Location

Miss Yani Pan
McGill University
801 Sherbrooke West
Quebec, Canada
Montreal, QC H3A 0B8
Canada

PO Number (optional)

N/A

Payment options

Invoice

PENDING ORDER CONFIRMATION

Confirmation Number: Pending

Order Date: 20-Sep-2021

Print Friendly Format

Includes Publisher Terms and Conditions

1. Nanoscale

0.00 USD

Article: Biosynthesized silver nanorings as a highly efficient and selective electrocatalysts for CO2 reduction.

Publisher Terms and Conditions
Special Terms Apply

Order License ID	Pending	**Publisher**	RSC Pub
ISSN	2040-3372	**Portion**	Chapter/article
Type of Use	Republish in a thesis/dissertation		

Appendix 5

LICENSED CONTENT

Publication Title	Nanoscale	**Publication Type**	e-Journal
Article Title	Biosynthesized silver nanorings as a highly efficient and selective electrocatalysts for CO2 reduction.	**Start Page**	18595
		End Page	18603
Author/Editor	National Center for Nanoscience and Technology., Royal Society of Chemistry (Great Britain)	**Issue**	40
		Volume	11
		URL	http://www.rsc.org/Publishing/Journal...
Date	01/01/2009		
Language	English		
Country	United Kingdom of Great Britain and Northern Ireland		
Rightsholder	Royal Society of Chemistry		

REQUEST DETAILS

Portion Type	Chapter/article	**Rights Requested**	Main product
Page range(s)	18595-18603	**Distribution**	Worldwide
Total number of pages	9	**Translation**	Original language of publication
Format (select all that apply)	Print, Electronic	**Copies for the disabled?**	No
Who will republish the content?	Academic institution	**Minor editing privileges?**	Yes
Duration of Use	Life of current edition	**Incidental promotional use?**	No
Lifetime Unit Quantity	Up to 999	**Currency**	USD

NEW WORK DETAILS

Title	Bioinspired Nanometal Synthesis and Applications in Catalysis	**Institution name**	McGill University
		Expected presentation date	2021-10-05
Instructor name	Janine Mauzeroll		

ADDITIONAL DETAILS

Order reference number	N/A	**The requesting person / organization to appear on the license**	Yani Pan/Mcgill Unversity

REUSE CONTENT DETAILS

Title, description or numeric reference of the portion(s)	Chapter 3 - Biosynthesized silver nanoring as a highly efficient and selective electrocatalysts for CO2 reduction	**Title of the article/chapter the portion is from**	Biosynthesized silver nanorings as a highly efficient and selective electrocatalysts for CO2 reduction.
Editor of portion(s)	PAN, YANI; Paschoalinojunior, Waldemir; Bayram, Serene; Blum, Amy Szuchmacher; Mauzeroll, Janine	**Author of portion(s)**	PAN, YANI; Paschoalinojunior, Waldemir; Bayram, Serene; Blum, Amy Szuchmacher; Mauzeroll, Janine
		Issue, if republishing an article from a	40

REUSE CONTENT DETAILS

Title, description or numeric reference of the portion(s)	Chapter 3 - Biosynthesized silver nanoring as a highly efficient and selective electrocatalysts for CO2 reduction	**Title of the article/chapter the portion is from**	Biosynthesized silver nanorings as a highly efficient and selective electrocatalysts for CO2 reduction.
Editor of portion(s)	PAN, YANI; Paschoalinojunior, Waldemir; Bayram, Serene; Blum, Amy Szuchmacher; Mauzeroll, Janine	**Author of portion(s)**	PAN, YANI; Paschoalinojunior, Waldemir; Bayram, Serene; Blum, Amy Szuchmacher; Mauzeroll, Janine
Volume of serial or monograph	11	**Issue, if republishing an article from a serial**	40
Page or page range of portion	18595-18603	**Publication date of portion**	2019-01-01

Print License

Total Items: 1 **Total Due: 0.00 USD**

Accepted: All Publisher and CCC Terms and Conditions

Continue Shopping

Appendix 5

Chapter 4

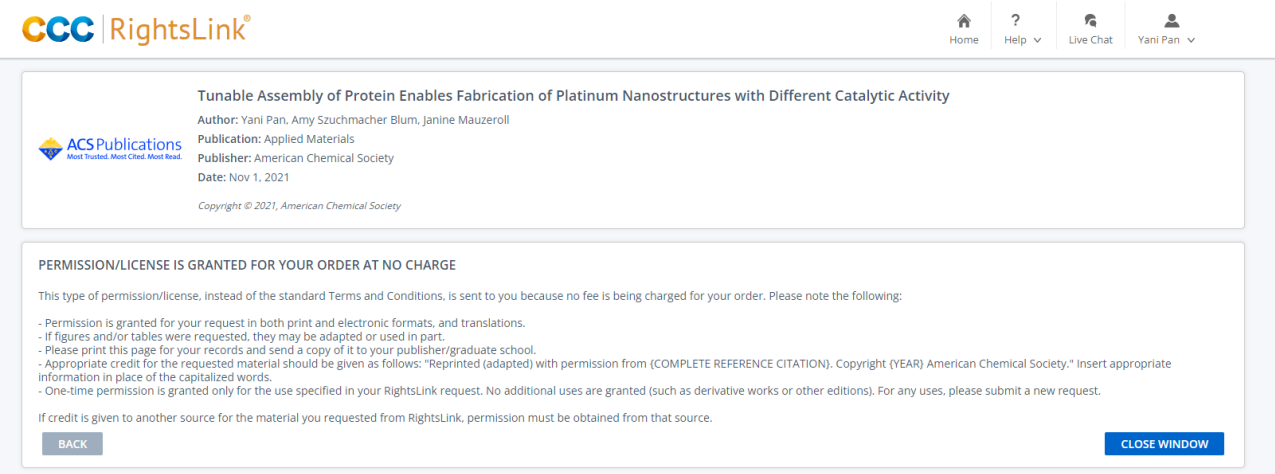

Chapter 5